EXAMINANDO UN *MARS ROVER*
EN CONDICIONES DE "ALTA TROPICALIDAD"

EDITOR

E. ALTSHULER
Facultad de Física, Universidad de la Habana
ealtshuler@fisica.uh.cu

EDICIÓN ELECTRÓNICA

J. J. GONZÁLEZ, C. GANDARILLA
Facultad de Física, Universidad de la Habana
jjgonzalez@fisica.uh.cu, cgandarilla@fisica.uh.cu

E. MARTÍNEZ
NTNU, Norway
martinez.etien@gmail.com

O. ALMORA
University Erlangen-Nuremberg
osbel.almora@fau.de

D. MIRAVET
Centro Atómico Bariloche & Instituto Balseiro
dmiravet@cab.cnea.gov.ar

EDITORES ASOCIADOS

A. J. BATISTA-LEYVA
INSTEC, La Habana
abatista@instec.cu,

W. BIETENHOLZ
UNAM, México
wolbi@nucleares.unam.mx

G. ROJAS-LORENZO
INSTEC, La Habana
german@instec.cu

J. O. FOSSUM
NTNU, Noruega
Jon.fossum@ntnu.no

J. –P. GALAUP
Lab. A. Cotton (CNRS) & Univ. Paris-Sud
Jean-pierre.galaup@lac.u.-psud.fr

J. LLOVERA
CUJAE, La Habana
llovera@electrica.cujae.edu.cu

O. de MELO, R. MULET
Facultad de Física, Universidad de La Habana
omelo@fisica.uh.cu, mulet@fisica.uh.cu

P. MUNÉ
Facultad de Ciencias, Universidad de Oriente
mune@cnt.uo.edu.cu

T. PÖSCHEL
University Erlangen-Nuremberg
thorsten.poeschel@fau.de

E. RAMÍREZ-MIQUET
HiFiBiO Therapeutics, France
e.ramirez@hifibio.com

T. SHINBROT
Rutgers University
shinbrot@soemail.rutgers.edu

C. A. ZEN-VASCONCELOS
Univ. Federal Rio Grande du Sul
cesarzen@cesarzen.com

LA REVISTA CUBANA DE FÍSICA ES UNA PUBLICACIÓN SEMESTRAL DE LA SOCIEDAD CUBANA DE FÍSICA

WHERE IS OUR JOURNAL RIGHT NOW? UP-TO-DATE BIBLIOMETRICS AND PROGRESS OF REVISTA CUBANA DE FÍSICA

¿DÓNDE ESTÁ NUESTRA REVISTA EN ESTOS MOMENTOS? BIBLIOMETRÍA ACTUALIZADA Y PROGRESO DE LA REVISTA CUBANA DE FÍSICA

E. E. Ramírez-Miquet and E. Altshuler

Editorial Committee, Revista Cubana de Física

As the Cuban Physical Society flagship publication, the Revista Cubana de Física (RCF) serves the local and foreign physicists with original articles, communications, reviews and comments. The RCF publishes physics articles in both English and Spanish and provides a platform that serves the ibero-american and other scientific communities, processing submissions from all continents, with prominent presence from Hispanic countries.

After thirty years of almost uninterrupted publishing, 2011 marked an inflexion point in the pathway of RCF, with renewed efforts in the style, types of articles, inclusion of new sections, and formal applications for indexing in a set of worldwide recognized science databases. As a result, in recent years RCF was indexed by Scopus, the Emerging Sources Citation Index (ESCI)/Web of Science (WoS) of Clarivate Analytics (formerly Thompson Reuters), Scimago Journal Ranking, DOAJ, REDIB, ROAD, Latindex, ResearchGate and Google Scholar. Of these, mainly Scopus, Scimago and WoS provide verifiable bibliometrics of the journal evolution and progress. We hereby provide an up-to-date analysis of RCF and check its activity and performance relative to national physics publications from foreign communities.
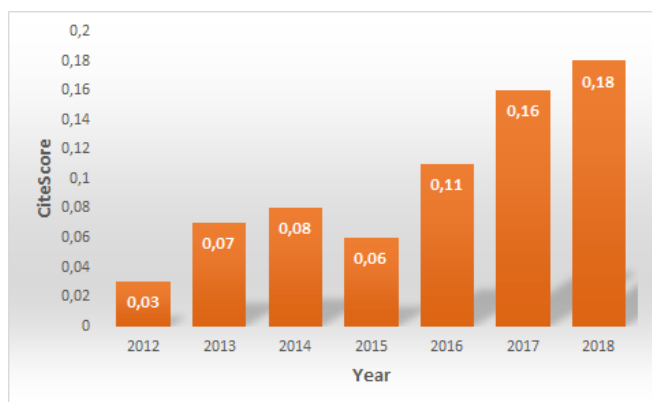
Figure 1. CiteScore progression over the last seven years. Data extracted from Scopus database.

Since 2011 RCF content and metadata are indexed in Scopus –the search engine powered by Elsevier– and bibliometric data is regularly calculated. After an in-depth look into this set of information, we offer a global view of where we currently are and what we foresee as a potential future for our journal as a venue for professional physics content. Scopus quantifies the quality of a journal using its CiteScore, a statistical descriptor of the performance of a given publication. It is determined by the sum of citations received in a given year for papers published in the previous three years divided by the number of published papers in the preceding three years. RCF received its first CiteScore quantification in 2012 and reached a maximum yearly-calculated value in 2018. The last update of the CiteScore Tracker 2019 reaches 0.09 as of July 8th, 2019 with 10 citations this year for papers from 2016-2018. The CiteScore evolution for the period 2012-2018 is presented in Fig. 1, and it clearly evidences the progress of the journal, tripling by now the score it held in 2015. This positive progression, in other words, is a quantification of how RCF is now more cited with respect to the number of articles that are published in the preceding three years.
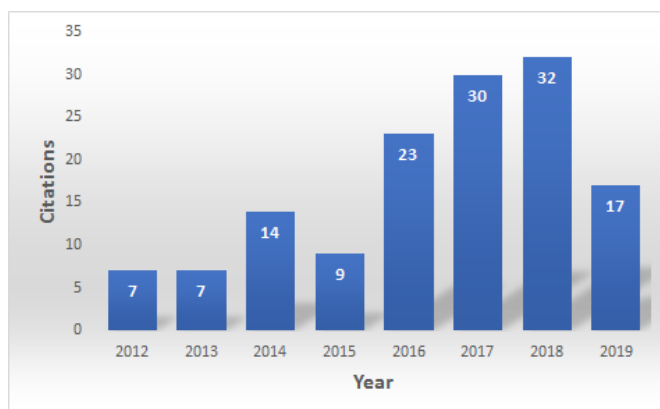
Figure 2. Citations received by RCF articles within the last 8 years. Data extracted from Scopus database.

Still, this indicator is low for a wide-scope physics journal as RCF is and it's critical to ensure that the peer-review process yields accepted papers based, above all, on their significance. Our editorial processes must be focused on assessing deeply the novelty and significance of each submitted manuscript, as these two features will increase the number of citations the journal receives in the years following the publication online.

But we must keep the delicate balance between significance and rejection rate.

As mentioned above, RCF is also part of the large collection Emerging Sources Citation Index powered by Clarivate Analytics. This is a first step in the direction of having an impact factor assigned and a inclusion in the Science Citation Index Expanded database. While being in the ESCI, RCF is currently contributing to other journals' impact factor.

The visibility of the journal is now guaranteed as RCF migrated to the Open Journal System and every article is accessible online in final form with citable information (even when authors are not charged for publication). This is a step ahead in making sure that the content published is read and assessed upon publication and has a chance to be considered by authors in this or other journals.

Increasing the number of citations is crucial to increase every indicator of the journal, its CiteScore and potential future impact factor. The evolution of the citations since 2012 is presented in Fig. 2, with updated data from July 8th, 2019. The number of cited papers in the first half of 2019 seems to reach a similar tendency for a third consecutive year.
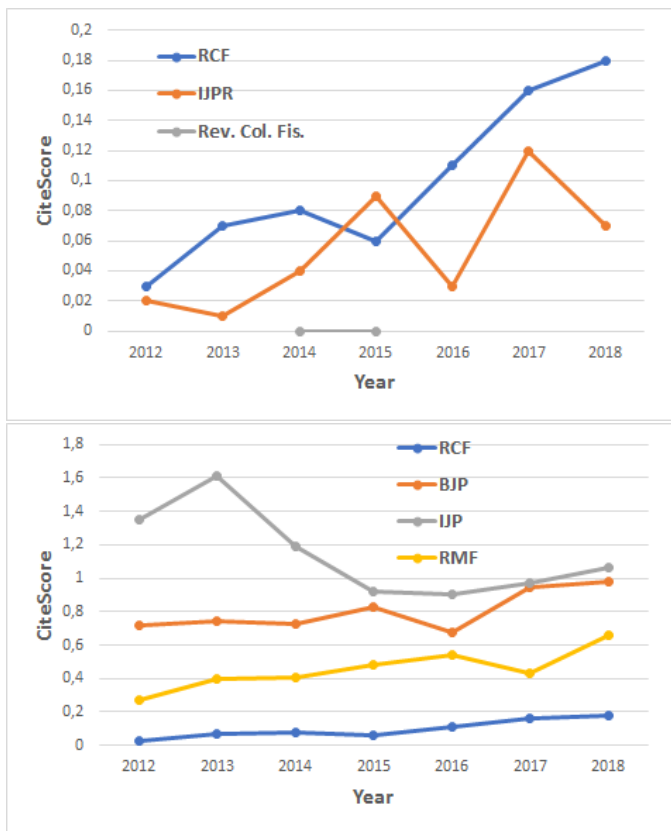
Figure 3. Comparison of CiteScore for multiple physics journals and their evolution from 2012 to 2018 (RCF, IJPR, Rev. Col. Fis, BJP, IJP and RMF stand for Revista Cubana de Física, Iranian Journal of Physics Research, Revista Colombiana de Física, Brazilian Journal of Physics, Indian Journal of Physics and Revista Mexicana de Física, respectively).

Compared to other physics-related journals, RCF outperforms the score of other "national" sister publications in terms of ranking provided by Scopus, including the Iranian Journal of Physics Research and the Revista Colombiana de Física, but still falls short in ranking as compared to the Brazilian Journal of Physics (BJP), the Revista Mexicana de Física (RMF) and the Indian Journal of Physics (IJP), which represent much larger physical societies. Figure 3 shows the evolution of a set of journals serving local and foreign physics communities around the world.

The editorial board has been diversified from 2011, with strong presence of international researchers. RCF's editorial team has taken measures to ensure that accepted papers hold sufficient novelty and significance in all domains. As reflected in Fig. 4, the rejection rate increased in 2018 markedly with respect to the previous five years. In addition, the number of articles published in English has a positive tendency and we expect to maintain this indicator with a continued presence in future volumes published by the journal. In addition, as a sign of diversification, we find more papers submitted and accepted from foreign contributors.
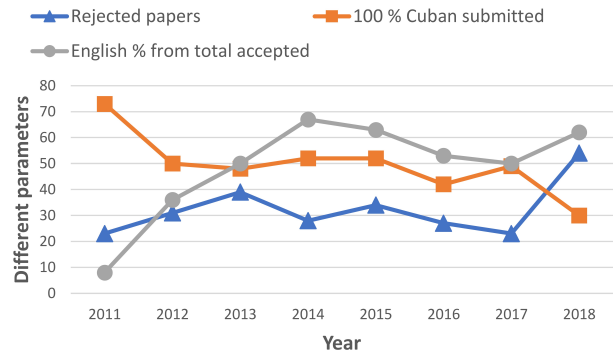
Figure 4. RCF operation statistics from 2011 to 2018. Note that 100 % refer to papers with authors belonging to Cuban institutions.

The editorial board finds imperative to increase the number of papers submitted in English, as they become relevant for the whole physics community –even when our bilingual policy is maintained. We encourage the authors to write and submit their manuscripts in professionally written English, regardless if they come from Spanish-speaking countries. In any case, the abstracts of the original articles will continue to appear in both languages.

In addition, the journal must get visibility in other media, always highlighting the impact of the most influent research presented in each published issue. Our science divulgation venues must also contribute to spreading the knowledge published in RCF.

We expect that in the years to come RCF will gain further impact, visibility and will become an archival journal for publishing relevant physics.

OPTICS UNDERGRADUATE EXPERIMENTS USING SMART (AND NOT SO SMART) PHONES

EXPERIMENTOS DE ÓPTICA EN PREGRADO USANDO TELÉFONOS INTELIGENTES (Y NO TAN INTELIGENTES)

V. L. Díaz-Melián[a], L. A. Rodríguez[b], F. Pedroso-Camejo[b], J. Mieres[b], Y. de Armas[c], A. J. Batista-Leyva[d] and E. Altshuler[a†]

a) Group of Complex Systems and Statistical Physics, University of Havana, 10400 La Habana, Cuba; ealtshuler@fisica.uh.cu[†]
b) Pedagogical Science University Enrique J. Varona, 11400 Havana, Cuba
c) Institute of Cybernetics, Mathematics and Physics (ICIMAF), 10400 Havana, Cuba
d) Instituto Superior de Ciencia y Tecnología Aplicadas (InSTEC), Universidad de la Habana, 10400 La Habana, Cuba
† corresponding author

Smartphones may be seen as miniature toolboxes to perform Physics experiments. In this paper, we present three different experimental optics designs mainly based on the light meter of a smartphone. One is aimed at the precise study of Malus law and other effects associated to linearly polarized light, the second allows quantifying the energy distribution of diffraction or interference patterns projected on a screen, and the third demonstrates the so-called inverse square law obeyed by the illumination from a point-like source. These experiments allow to quantitatively demonstrate three fundamental laws of optics using quite inexpensive equipment.

Los teléfonos inteligentes pueden verse como pequeñas "cajas de herramientas" para realizar experimentos de Física. En este artículo, presentamos tres "bancos ópticos" diferentes, basados fundamentalmente en el sensor de luz de los teléfonos inteligentes. Uno de ellos apunta hacia el estudio preciso de la ley de Malus y otros efectos asociados con la luz linealmente polarizada. El segundo permite cuantificar la distribución de energía en patrones de interferencia o difracción proyectados en una pantalla. El tercero demuestra la llamada ley del inverso del cuadrado, que obedece la iluminación asociada a una fuente puntiforme. Estos experimentos permiten demostrar cuantitativamente tres leyes fundamentales de la óptica usando equipamiento económico.

I. INTRODUCTION

Quite probably, the sensors typically found in smart-phones: light meters, proximity sensors, accelerometers, gyroscopes, magnetometers and even barometers were not included by their designers for educational or scientific purposes. But the fact is that thanks to their existence, smartphones constitute a truly portable toolbox for Physics experiments. In fact, they have been used to analyze free falling objects [1], oscillations of coupled springs [2], the magnetic field of small magnets [3], rolling motion [4], a simple pendulum [5] constant motion [6, 7] and optical phenomena [8, 9] among a number of other scenarios of interest for the Physics undergraduate lab. Furthermore, smartphones are also compact and relatively heavy-duty devices than could play a role in certain experiments beyond Physics teaching: from the measurement of effective gravities [10], to the characterization of coils and magnets used in materials science research at moderate magnetic fields [11].

In this contribution, we briefly introduce three different applications for Physics laboratories aimed at life science undergraduate students, based on the light meters of smart phones. The proposals can be expanded to advanced teaching, if more complex operations and data analysis are involved. The experiments shown here were conceived and tested as final projects of the one-semester course "Advanced Physics Experiments" (Experimentos Avanzados de Física, EXAV) offered at the Physics Faculty, University of Havana.

II. EXPERIMENTAL SETUPS AND RESULTS

II.1. *Workbench for polarized light studies*

The first proposal is a workbench for polarized light studies, depicted in Fig. 1(a). It consists in an inexpensive wooden "optical bench" with a 12V LED light source, two polarizers identified as "polarizer" and "analyzer" in the figure, and an adjustable holder to attach smart phone upside down, in such a way that the light meter sensor (typically near the "head" of the apparatus) faces the analyzer. The light meter of the smart phone can be easily accessed by using the Physics Toolbox Sensor Suite application [12], and the numerical values of the illuminance (in lux) can be read from the phone screen with relative easiness.

The non-polarized light produced by the LEDs is linearly polarized by the polarizer, then passes through the analyzer, and is detected by the lux-meter of the smart-phone. The analyzer can be rotated in order to change the angle Θ between its polarizing axis and that of the polarizer. The relation between the irradiance reaching the smartphone I

and that emerging from the polarizer, I_0 is supposed to follow Malus law [13]

$$I = I_0 cos^2\Theta. \tag{1}$$

Fig. 1(b) shows that equation (1) nicely follows the experimental points measured with the help of a Moto smartphone, thus demonstrating the validity of Malus law (the quality of the curve may suffer if very low-quality polaroids are used). It should be noticed that the smart phone's light sensor displays illuminance[1] (which is a subjective measure of irradiance hitting a unit surface), but its subjective nature does not influence our experiments, so we have written just "irradiance" in the formulas[2].
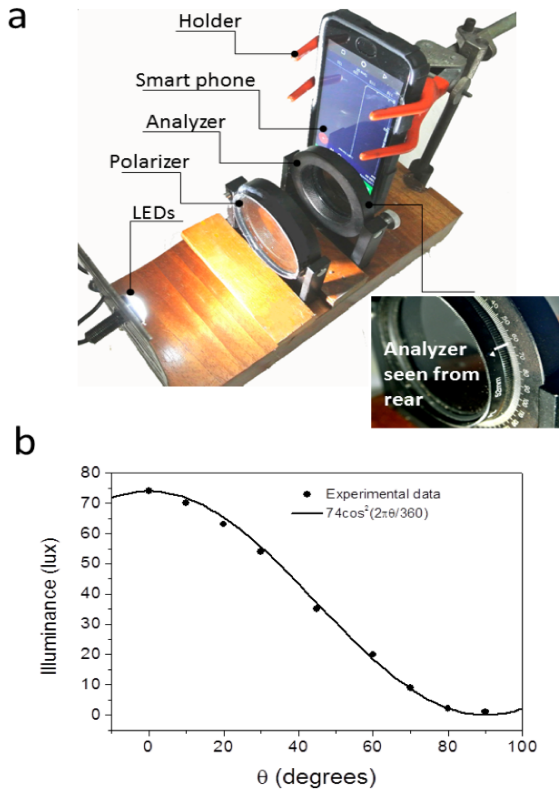
Figure 1. Quantifying Malus law. (a)A polarized light bench elaborated by the authors. In the picture, the smartphone is upside-down, since the light meter is typically at its head. (b) Fit of Malus law (continuous line) to the experimental data (circles).

The setup can be also used to perform other experiments, such as checking out that screens from older cell phones (i.e., those without a depolarizing sheet) produce linearly polarized light. This can be done by turning off the LEDs of our set up, and substituting the polarizer by the cell phone to be analyzed, with the screen facing the analyzer. Then, Malus law can be reproduced by rotating the analyzer, demonstrating that the light emitted by the phone screen is linearly polarized. This possibility has been previously reported by Monteiro and coworkers, in a paper we came across after writing the first version of this manuscript [8].

Taking that into account, it is possible to set up a truly "minimalistic" bench for polarized light experiments. It looks evident, for example, that the bench illustrated in Fig. 1 can be reduced by removing both the LEDs and the polarizer, and substituting it by a "not-so-smart" phone (or also by a screen of an old laptop, among other possibilities). Fig. 2, shows an example of an "extreme" minimalistic bench. There, we show a picture taken with a Moto smartphone of a photoeslastic disk sandwiched between an old Samsung "not-so-smart" phone, and a polarized sunglass. The Samsung phone provides linearly polarized light from the back, whose polarization direction is tilted by the optical activity associated to the local stresses "felt" by the photoelastic element due to compression: the resulting pattern is revealed by the sunglass playing the role of an analyzer, whose polarizing axis is almost at a right angle relative to that of the Samsung phone screen. This experiment can be taken as a motivational illustration at the introductory lab level, but, if the photoelastic effect is quantified and modeled, it can be moved to the advanced curriculum.
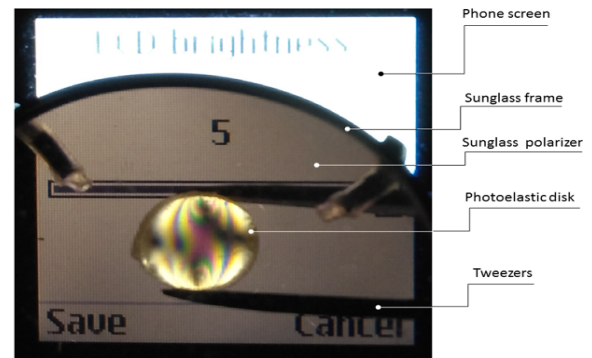
Figure 2. A minimalistic polarization workbench. From the back, an old cell phone illuminates with linearly polarized light a photoelastic disk compressed by tweezers. The disk is sandwiched between the cell phone and a sunglass with polarizing direction at a right angle relative to the phone's polarization direction. The light pattern on the photoelastic disk illustrates its stress distribution

II.2. Non-goniometric quantication of interference and diffraction

The second setup allows quantifying the interference or diffraction patterns resulting when laser light goes through different obstacles. We will illustrate here the diffraction pattern resulting from a green laser beam passing through a single vertical slit of horizontal width a. Differently from conventional "goniometric measurements", here we use the

---

[1]The illuminance is the luminous flux per unit surface perpendicular to the flux. The luminous flux is the flux of radiant energy (or radiant flux) weighted by the photopic spectral luminous efficiency [14]. So, different sources having equal radiant flux could have different luminous flux, provided they emit at different wavelengths.

[2]Let us suppose that a non-polarized polychromatic light beam passes through a polarizer-analyzer system. When passing through the polarizer, each wavelength diminishes its irradiance in a fixed percent (50 % for an ideal polarizer). When passing through the analyzer, a fixed amount, proportional to the square cosines of the angle is eliminated for each wavelength. So, from the analyzer exits an irradiance equal to the sum of its value for every wavelength. But the illuminance for each wavelength is proportional to its irradiance, so the overall illuminance will be proportional to the overall irradiance: all in all, Malus law also holds for polychromatic light beams

lux meter of a smartphone to determine the illuminance of the pattern projected on a screen attached to the phone, which is located at distance L ($L \gg a$) from the slit. The phone rests on a teaching-grade optical bench oriented perpendicularly to the laser beam, in such a way that it can be manually slid horizontally, as illustrated in Fig. 3(a). A clear cardboard screen is taped to the phone in such a way that a hole made with an office hole punch allows the light to enter the light sensor, while the pattern is displayed on the cardboard surface. Then, the intensity of the diffraction pattern can be measured every few millimeters (we notice that the horizontality of the phone path can be checked using other of its sensors: the g-force meter!). Fig. 3(a) shows that a diffraction pattern obtained with a green laser can be visualized easily up to second order. If we assume that the phone scans the pattern along the direction, the illuminance should follow the formula [13]

$$I = I_m \left(\frac{\sin \xi x}{\xi x} \right)^2 \tag{2}$$

where I_m is the maximum irradiance at the screen, and

$$\xi = \frac{\pi a}{\lambda L} \tag{3}$$
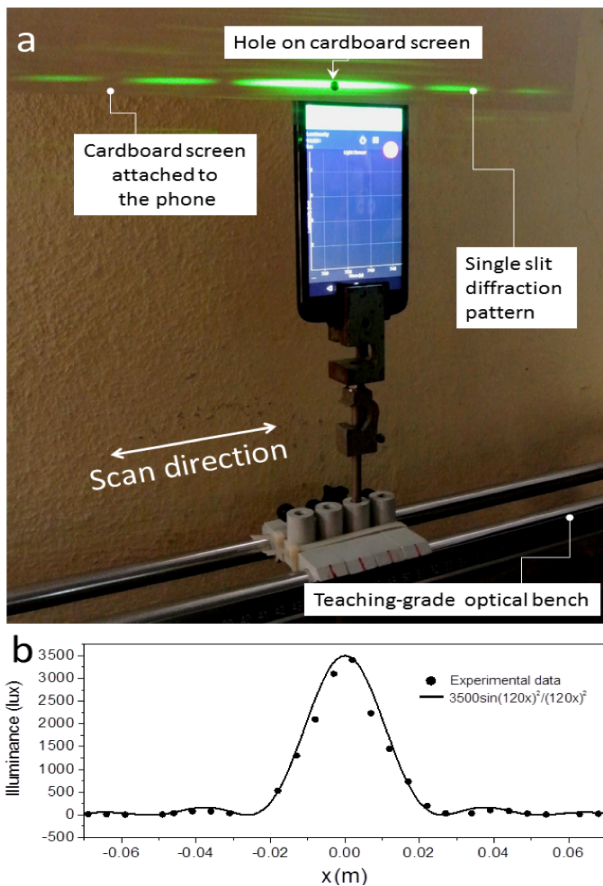
Figure 3. Scanning diffraction patterns with a setup elaborated by the authors (a) Diffraction pattern being scanned by a smart phone (b) Illuminance recorded along the diffraction pattern of a 140 μm slit located 7 m away from the phone, using a 532 nm green laser (the pattern in (a) was obtained with slightly different parameters).

Fig. 3(b) shows the good fit of the above formulas to the illuminance record of an actual diffraction experiment.

Notice that, as the light in mono chromatic, the illuminance is proportional to the irradiance.

II.3. The inverse-squared-distance law

On one extreme of a teaching-grade optical bench like the one shown in Fig. 3(a) we have fixed a white LED. A smart phone slides facing the LED along the optical bench, thanks to a holder similar to the one shown in Fig. 3(a), (but the phone has been rotated in such a way that it faces the LED source). Due to its simplicity, we are not showing a picture of the setup; we just illustrate one set of experimental data and its fit to the inverse-squared-distance law in Fig. 4. The fit clearly demonstrates the validity of the law. It is worth noticing that smart phones have been used very recently to characterize in a similar way linear light sources [9].
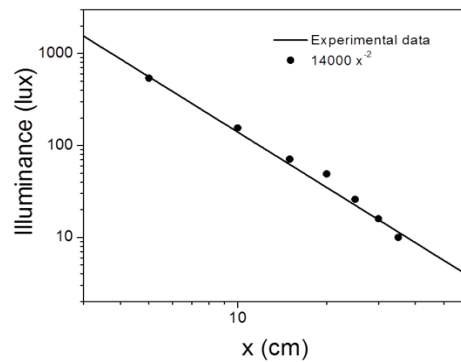
Figure 4. Fit of the inverse-squared-distance law (continuous line) to the experimental data (circles) measured using a setup elaborated by the authors.

III. CONCLUSIONS

Smartphones have been quite extensively used in introductory Mechanics experiments, involving not only the phone's accelerometer and gyroscope, but also its magnetometer and light sensor. In this paper we use smart-phones to tackle a different field of Physics, where much less work has been published: Optics.

We demonstrate that the light sensor of a smartphone can be used to design and construct very simple and inexpensive setups allowing the quantification of fundamental optical phenomena: the Malus formula, diffraction (and interference) through slits, and the inverse-squared-distance formula. In addition, we propose the use of the screen of a second phone or laptop as an inexpensive source of linearly polarized light, resulting in extremely inexpensive and simple setups. A key simplifying element of our setups is that they do not involve any goniometers.

Extending the span of experiments covered by our work benches is not difficult: the polarization setup can be used to measure the optical activity of certain solutions, while the inverse-squared-distance one can be used to quantify the absorption of light by a substance, to put two examples.

The third setup aims at the experimental confirmation of the inverse-square proportionality law followed by the irradiance (and related magnitudes) emitted by a pointlike light source with distance.

IV. ACKNOWLEDGEMENTS

REFERENCES

[1] J. Kuhn and P. Vogt, Phys. Teach. **50**, 182 (2012).

[2] J.A. Sans, F.J. Manjón, A.L. Pereira, J.A. Gómez-Tejedor and J.A. Monsoriu, Eur. J. Phys. **34**, 1349 (2013).

[3] E. Arribas , I. Escobar , C.P. Suárez, A. Nájera and A. Beléndez, Eur. J. Phys. **36**, 065002 (2015).

[4] P. Wattanayotin, C. Puttharugsa and S. Khemmani, Phys. Educ. **52**, 045009 (2017).

[5] T. Pierratos and H. M. Polatoglou, Phys. Educ. **53**, 015021 (2018).

[6] S. Kapucu, Phys. Educ. **52**, 045001 (2017).

[7] A.Y. Nuryantini, A. Sawitri and B.W. Nuryadin, Phys. Educ. **53**, 065021 (2018).

[8] M. Monteiro , C. Stari, C. Cabeza and A.C. Martí, The Physics Teacher **55m**, 264 (2017).

[9] I. Salinas , M.H. Giménez, J.A. Monsoriu and J.C. Castro-Palacio, The Physics Teacher **56**, 562 (2018).

[10] E. Altshuler, H. Torres , A. González-Pita, G. Sánchez-Colina, C. Pérez-Penichet, S. Waitukaitis and R. C. Hidalgo, Geophys. Res. Lett. **41**, 3032 (2014).

[11] A.J. Batista-Leyva, R. Cobas, M.T.D. Orlando and E. Altshuler, Supercond. Sci. Technol. **16**, 857 (2003).

[12] https://play.google.com/store/apps/details?id=com.chrystianvieyra.physicstoolboxsuite.

[13] E. Hetch, Optics, 5th Ed. Pearson, 2016.

[14] G.S. Landsberg, Óptica vol. I, Mir 1983.

ABOUT THE UPSTREAM CONTAMINATION
ACERCA DE LA CONTAMINACIÓN A CONTRACORRIENTE

D. Suárez Fontanella [a] and A. Cabo Montes de Oca [b†]

a) Facultad de Física, Universidad de La Habana, La Habana 10400, Cuba
b) Instituto Cibernética, Matemáticas y Física, La Habana 10400, Cuba; cabo@icimaf.cu[†]
† corresponding author

The effect through which water pollutants initially floating in a lower recipient, can appear at a higher vessel from which the liquid falls down, is investigated. While is effect has been previously studied experimentally for an inclined channel, here we develop a theoretical model for the case of a vertically falling water beam. Two cases are discussed, a simpler one, in which water flows vertically through a cylindrical tube, and a more complex one, in which water falls freely. For the first case, it is derived an expression for the water flux above which the upward flow of particles stops. For the second one, a relation between the water flux, the sizes of the particles and the height along the water beam is obtained which determines whether or not the particles can flow up to the higher recipient. In the case of the free fall it follows that the rising of the particles is only possible if the water surface tension is considered, and only happens below a maximal height difference between the two vessels.

Se investiga el efecto mediante el cual impurezas en agua flotando en un recipiente inferior pueden aparecer en otro situado más arriba y desde el cual el líquido cae hacia el primero. Un trabajo experimental previo reportó este efecto para el caso en que el agua fluye del recipiente superior al inferior a través de un canal abierto. Aquí se complementa la discusión teórica por medio del estudio de chorros de agua cayendo verticalmente. Se discuten dos casos, uno más simple en que el agua fluye a través de un tubo cilíndrico vertical, y otro más complejo en que el agua desciende en caída libre. Para el primer caso, se deriva una expresión para el flujo de agua que es capaz de detener el tránsito de partículas hacia arriba. En el segundo caso se obtiene una relación entre el flujo de agua, el tamaño de las partículas y la altura a lo largo del chorro, que determina si las partículas suben o no hacia el recipiente superior. Para la caída libre se concluye que la subida de las partículas es posible solo si se considera la existencia de la tensión superficial, y además por debajo de una diferencia de altura máxima entre las vasijas.

I. INTRODUCTION

The present work is devoted to discuss the so called *upstream contamination* effect. This phenomenon was detected when a jet of water fell into a recipient in which with *mate* particles were floating. Then, it was noticed that after a time lapse the particles also appeared at the higher recipient. This effect was observed in the year 2008 by a student at the Physics faculty, University of Havana, and was systematically studied and eventually published few years after in reference [1]. In that work, a water reservoir located at a certain height discharged clean water through an inclined channel on the surface of a second reservoir located approximately 1 cm below. If mate leaves or chalk particles were sprinkled in the surface of the lower container, eventually the particles would reach the upper container moving counter-stream along the channel. At the lower end of the channel there was also a free falling stream of water.

The experimental observations reported in that work, were mainly explained by invoking the so called Marangoni effect [2–7], which consists in the variation of the surface tension of substances when floating contaminants are present. Then, the gradient of the local density of surface contaminants was assumed to create a net force pushing the particles against the stream of water [1].

In this work we will present a complementary discussion of the contamination effect, limited to the simpler case of vertical falling beams of water. The objective is to consider the feasibility of the effect to occur without the additional influence of the Marangoni effect. That is, only the effects of viscosity and surface tension will be under consideration. Specifically, we will determine which conditions among the parameters should be obeyed in order that spherical particles can ascend through the water jet. The discussion will assume that the particles move through the interior of the water beam. The case in which the particle move through the surface will not be analyzed here.

Two different situations will be investigated. In the first one, the water falls down through a cylindrical tube of circular section. In the second case the water is assumed to fall freely under the action of gravity. In both cases the Stokes's frictional force associated to water viscosity plays a central role. However, while for the first case the surface tension plays no role, in the second one it becomes central.

In the first case, we are able to calculate the maximum flux of water above which the particles stop moving upstream. In the second case, we demonstrate that there is a maximum height difference between the recipients above which the particles are unable to flow upstream. This critical value grows with the increasing of the size of the particle and with

the reduction of the water flux. It follows that the numerical values predicted for the critical height values (associated to the water fluxes and sizes of the beam of free falling water at the end of the inclined channel) are in the range of the experimental estimates reported in reference [1].

The presentation of the work will be as follows. In Section 2 the relations among the parameters for the water to be stopped to contaminate the higher recipient for the case of water falling through a vertical tube, will be discussed. In Section 3, we will consider the derivation of the similar relation for the case of the free falling water beam. The determination of an approximate stationary form of the beam is also presented. Finally, the results are reviewed at the Summary.

II. WATER FALLING THROUGH A CYLINDRICAL PIPE

Let us consider that the reference frame for coordinates will be at the bottom of the upper recipient. The positive axis for the z coordinate will point downwards and along the symmetry axis of the water flow. Under this assumptions the Bernoulli theorem will be applied between two points a and b laying at different heights. Both points will be assumed to lay on a curve being tangent to the velocity field. Then, it is possible to write

$$\frac{1}{2}\rho\, v_a^2 - \rho\, g\, z_a + P_a = \frac{1}{2}\rho\, v_b^2 - \rho\, g\, z_b + P_b. \tag{1}$$

In the following this relation will be employed to discuss the two types of water flows under consideration. Assuming that the index $a = 0$ and the b is the z-coordinate, the Bernoulli Law can be written as

$$\frac{1}{2}\rho v_0^2 + P_0 = \frac{1}{2}\rho\, v(z)^2 - \rho g\, z + P(z),$$

$$\frac{1}{2}\rho v_0^2 = \frac{1}{2}\rho\, v(z)^2 - \rho\, g\, z + (P(z) - P_0),$$

where v_0, v_z are the flow velocities at the two points and P_0, P_z the corresponding pressures.

But, for the case under consideration in this section, the transversal area of the cylinder is constant at different heights. Therefore, the incompressibility of water determines that the velocity $v(z)$ is in fact not changing with z, i.e.

$$v(z) = v_0 \equiv v. \tag{2}$$

Thus, it also follows that the distribution of pressures along the vertical inside the tube is identical to the one in static water, thus

$$P(z) - P_0 = \rho\, g\, z. \tag{3}$$

Now, let us write the Newton equation of motion for a small spherical particle of radius R and density ρ_m located inside the water beam, as

$$\rho_m\, V\, \frac{dv_m(t)}{dt} = \rho_m V\, g + f_e - k\,(v_m(t) - v), \tag{4}$$

$$m = \rho_m\, V, \tag{5}$$

$$V = \frac{4}{3}\pi R^3, \tag{6}$$

which expresses that the acceleration is determined by the vector addition of the weight of the body, the floating forces produced by the pressure and the viscosity force defined by the Stoke's law. But, Archimedes Law turns out to be exactly valid for the floating force, due to the linear behavior of the pressure coinciding with the functional dependence of pressure with vertical distance for static water. Thus the floating force is given by

$$f_e = -V\frac{dP(z)}{dz} = -\rho\, g\, V, \tag{7}$$

where the negative sign is because the force tend to move the body in the negative direction of the height coordinate z. Then, the Newton equation can be rewritten in the form

$$\frac{dv_m(t)}{dt} = g\,(1 - \frac{\rho}{\rho_m}) - \frac{k}{m}(v_m(t) - v). \tag{8}$$

This equation includes the frictional Stokes force acting on a moving sphere in a fluid when the liquid movement is laminar

$$f_S = -k\,(v_m(t) - v), \tag{9}$$

where the constant k is given in terms of the viscosity constant μ and the radius of the sphere as

$$k = 6\,\pi\mu\, R. \tag{10}$$

This is a simple first order equation for the velocity of the particle in the observer's reference frame. Expressing it in the integral form, we can write

$$\int_0^{v(t)} \frac{dv_m}{(v_m(t) - v) + \frac{m\,g}{k}\,(\frac{\rho}{\rho_m} - 1)} = -\int_0^t \frac{k}{m}dt,$$

$$\log\,[\frac{v_m(t) - v + \frac{m\,g}{k}\,(\frac{\rho}{\rho_m} - 1)}{-v + \frac{m\,g}{k}\,(\frac{\rho}{\rho_m} - 1)}] = -\frac{k}{m}t. \tag{11}$$

This relation allows to write the following explicit solution for the velocity of the particle

$$v_m(t) = [v - \frac{m\,g}{k}\,(\frac{\rho}{\rho_m} - 1)](1 - \exp(-\frac{k}{m}t)), \tag{12}$$

which after being evaluated for large times, yields the following expression for the limit velocity of the particle with respect to the observer's frame

$$v_m(\infty) = [v - \frac{m\,g}{k}\,(\frac{\rho}{\rho_m} - 1)] \tag{13}$$

$$= v - \frac{2\pi R^2 g\, \rho_m}{9\,\pi\mu}\,(\frac{\rho}{\rho_m} - 1).$$

In the above relations it has been substituted

$$\frac{m}{k} = \frac{2\pi R^2 \rho_m}{9\,\pi\mu}. \tag{14}$$

Therefore, the single condition for the particles not to be allowed to climb to the upper reservoir is

$$v - \frac{2\pi R^2 g}{9\,\pi\mu}\,(\rho - \rho_m) > 0.$$

But, the velocity is defined in terms of the volume flux of water Q and the area A of the vertical cylinder as $v = \frac{Q}{A}$. Thus, the inequality becomes

$$Q > \frac{2\pi R^2 g A}{9\,\pi\mu}\,(\rho - \rho_m). \qquad (15)$$

This relation indicates that if Q stops all the particles regardless the value of their density ρ_m, the following modified relation should be satisfied

$$Q > \frac{2\pi R^2 g A \rho}{9\,\pi\mu}\,. \qquad (16)$$

Let us now assume that the fluid is water and that the experience is performed under normal gravity conditions. Then, the following set of parameters can be substituted $\rho = 1000$ Kg/m^3, $g = 9.8$ m/s^2, $\mu = 8.9 \times 10^{-4}$ Ns/m^2.

We now illustrate the resulting regions of values of the flux of water Q , the radius R of the spherical particles and the area A of the water conducting cylinder, for which the particles are not allowed (or allowed) to climb upstream along the cylinder. These regions are shown in figure 1. The surface shown defines the critical boundary in the space of parameters at which the particles are in the limit of being allowed and not being allowed to contaminate the upper recipient. The colored zone over the surface is the set of values of triplets of coordinates (Q, R, A) for which the particles can move against the flow up to the higher recipient. On the contrary, the white region below the surface represent the triplets of parameters for which the particles remain trapped in the lower vessel.
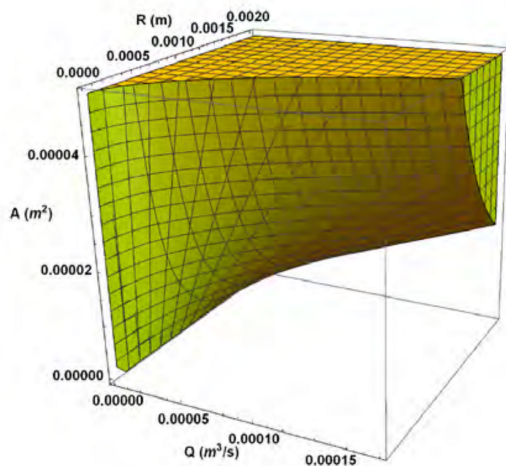
Figure 1. The plotted surface contains the set of points satisfying the equality in relation (16) as a function of R, A and Q. That is, at such points the velocity of the particles vanishes. Below the surface the particles have positive velocities and then do not contaminate the upper recipient. Above it, in the colored region, the particles tend to ascend against the flow.

Let us use the above derived relation to estimate the critical value of the flux for particles with size of the chalk powder used in reference [1]. Since the authors estimate it as of the order of hundreds of microns, we will assume a radius of the spherical particles of $R = 100$ $\mu m = 0.0001$ m. The flux of water falling from the upper to lower recipients was chosen as $Q = 16$ cm^3 /s$=0.000016$ m^3/s. For these values of the size of the particle and the flux of water, the point laying on the critical surface has a value of the sectional area of the cylinder given by $A = 0.000163469$ m$^2 = 1.63$ cm^2.

This result indicates that for the flux of water employed in the experiment in reference [1] and a size of the chalk particle powder of the estimated one in that reference, the area of the cylinder section considered in our model is of the order of a few cm^2. But, the sectional area of the waterfall at the end of the inclined channel employed in the experiments is expected to be of the same order. Therefore, it can be concluded that floating effects alone, without the consideration of the Marangoni effect can, partially justify the contamination against current effect through the waterfall at the end of the channel, at least for particles which are able to float.

We would like here to remark on a question that looks of interest in connection with the experiments reported in reference [1]. It should be underlined that the viscous character of water is expected to establish a zero velocity of the water relative to the channel when they meet. This situation suggests that the contact boundary of water with the walls of the channel should be expected to be a preferred path for the moving of the particles upwards. Therefore, it seem necessary to compare the dimensions of the particles with the sizes of the boundary layer in which the velocity varies from zero at the wall up to its maximum value at the center of the channel.

III. FREE FALLING WATER FLOW

Let us now consider the second situation in which the water free falls in a beam to the lower recipient. Firstly, we will determine the pressure difference between two points: one in the air just over the water surface, and one just underneath the surface. Then, we will consider the balance of momentum of the surface element illustrated in figure 2. The picture illustrates the two principal curvature radii R_{in} and R_{out} of the chosen symmetric surface element, and also the surface tension forces which are mainly exerted on the two arcs of circle corresponding to the respective two circumferences defining the curvature radii. The surface tension parameter is represented by γ. Therefore, considering that the two arc elements are infinitesimal with equal length dl, the momentum balance for the surface element gives

$$(P_{in} - P_{out})\,dl^2 = \gamma\,dl\,(d\theta_{in} - d\theta_{out}).$$
$$= \gamma\,dl^2\left(\frac{1}{R_{in}} - \frac{1}{R_{out}}\right), \qquad (17)$$
$$d\theta_{in} = \frac{dl}{R_{in}}, \quad d\theta_{out} = \frac{dl}{R_{out}}. \qquad (18)$$

Now, in order to simplify the discussion, let us assume that water beam shows curvature radii satisfying

$$R_{out} \gg R_{in}. \tag{19}$$

This relation indicates that the tangent vector to the water surface contained in a plane including the axis of the beam, becomes close in direction with the beam axis. But, this property in turns implies that the small radius is approximately given by the radius of the beam taken at the fixed height value defined by the z coordinate. This radius will be defined by $r(z)$. Thus,

$$P_{in} - P_{out} = \frac{\gamma}{r(z)}. \tag{20}$$
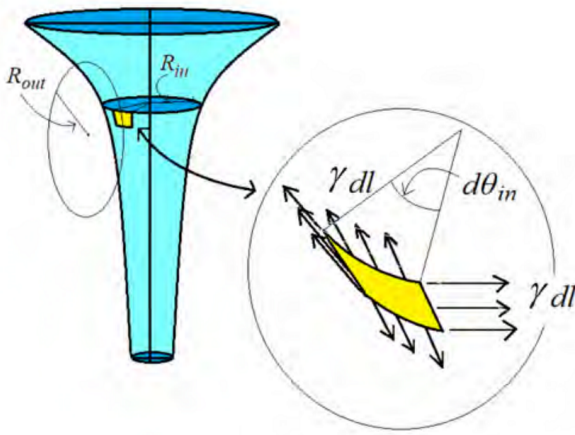
Figure 2. A model of the water beam that includes a surface element for which the momentum balance is worked out. The internal and external principal curvature radii are indicated. The surface element is colored in yellow and the surface tension forces acting on it are shown in the figure depicted at right.

But, the external pressure on the beam is given by the atmospheric one P_0, which implies the following relation between the internal pressure at any height z the formula

$$P(z) = P_0 + \frac{\gamma}{r(z)}. \tag{21}$$

Consider now at the origin of the height coordinates $z = 0$, the following initial conditions: the speed of the fluid when emerging form the upper recipient is $v(0) = v_0$ and the radius of the beam is $r(0) = a$. Then, substituting in the Bernoulli's equation, it follows

$$\frac{1}{2}\rho v_0^2 + P_0 + \frac{\gamma}{a} = \frac{1}{2}\rho\, v(z)^2 - \rho g\, z + P_0 + \frac{\gamma}{r(z)}, \tag{22}$$

$$\frac{1}{2}\rho v_0^2 + \frac{\gamma}{a} = \frac{1}{2}\rho\, v(z)^2 - \rho\, g\, z + \frac{\gamma}{r(z)}, \tag{23}$$

from which the velocity can be expressed in the form

$$v(z)^2 = v_0^2 + 2\, g\, z + \frac{2\,\gamma}{\rho\, a} - \frac{2\,\gamma}{\rho\, r(z)}. $$

Let us consider now a special origin for measuring the height coordinate z. Note first that if we assume the velocity v_0 of the flux is tending to zero in (23), the constancy of the total flux of water $Q = \pi a^2 v_0$ implies that the radius of the beam a should tend to infinity. Therefore, if we consider this point as the origin of coordinates $z = 0$, relation (23) becomes

$$\rho\, g\, z = \frac{1}{2}\frac{\rho\, Q^2}{\pi\, r(z)^4} + \frac{\gamma}{r(z)}. \tag{24}$$

But, the unique real and positive solution of this equation gives for $r(Q, z)$ (after fixing the density, surface tension and viscosity associated to water) is plotted in figure (3) as a function of the flux and the height z (as measured from the point at which the velocity of water vanishes). Note that this chosen origin of values of z is an unphysical point of the curve $r(z)$, since the section of a real beam never tends to infinity.
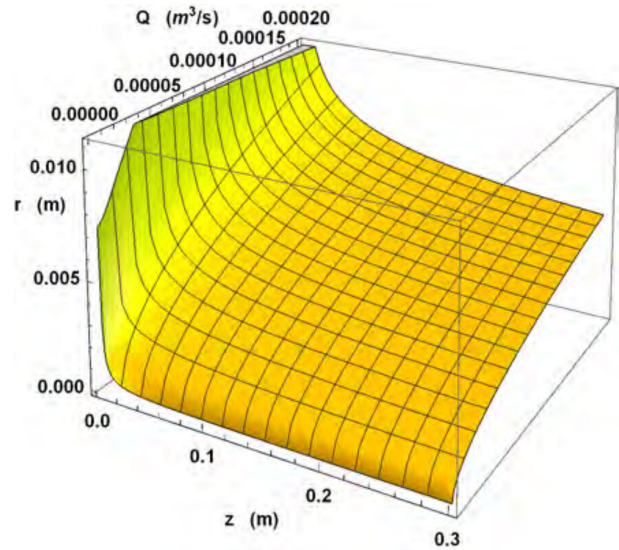
Figure 3. Radius of the free falling water beam as a function of the height coordinate z and the water flux Q passing through the beam.

The above discussion in this section, describing the flow of water regime in the falling beam, mainly follows the one given in reference [8]. It was presented for completeness.

Let us now consider how a particle situated in the water beam moves. The forces acting on this particle are determined by the variation of the pressure with the height, the weight of the particles and the viscosity. The viscosity force is proportional to the relative speed between the liquid and the particles (Stokes Law). Then, the Newton equation of motion takes the following form:

$$\rho_m V \frac{d^2z}{dt^2} = \rho_m V\, g - k\left(\frac{dz}{dt} - v(z)\right) - V\frac{dP(z)}{dz}, \tag{25}$$

$$m = \rho_m V, \tag{26}$$

which is very similar to relation (4) in the previous section with the only difference that the expression for the pressure as a function of the height z is different here. In this equation $\frac{dz}{dt} = v_m(t)$ is the speed of the particle relative to the observer and ρ, V (as in the previous subsection) the density and the volume of the floating particle, respectively. But, the

derivative of the pressure in (21) can be expressed in terms of $\frac{d\,r(z)}{dz}$, which in turns can be written as a function of $r(z)$ by taking the derivative of the relation (24). Using the result of this evaluation, the floating force (equal to minus the derivative of the pressure respect to the height z times the volume) can be calculated as

$$f_e = -V\frac{dP(z)}{dz}$$

$$= -m\,g\frac{\rho}{\rho_m}\frac{\gamma\,r(z)^3}{\frac{2\rho\,Q^2}{\pi} + \gamma\,r(z)^3}. \tag{27}$$

This result for the floating force deserves a comment. Note that by discarding the viscosity, the only force pointing in the -z (that is pushing the particle to the upper recipient) is this floating force that completely disappears if the surface tension vanishes. This allows to conclude that, in the here considered free falling case, the surface tension is a central element for the possibility of contamination of the upper recipient by particles coming from the lower one.

Then, by dividing the Newton equation by the mass of the particle $m = \rho_m\,V$, it is possible to write

$$\frac{d^2z}{dt^2} = (g - \frac{9\pi\mu}{2\pi\rho_m R^2}(\frac{dz}{dt} - v(z)) -$$

$$g\frac{\rho}{\rho_m}\frac{\gamma\,r(z)^3}{\frac{2\rho\,Q^2}{\pi} + \gamma\,r(z)^3}), \tag{28}$$

in which all the entering parameters are already well defined. We will consider now the restrictions implied by this equation on the values these parameters for allowing or not the transportation of particles from the lower recipient to the upper one. A drastic simplification for the derivation of these conditions follows after noting that the term in the equation pushing the particles down is a constant equal to g. Thus, when density ρ_m tends to zero we have the situation in which there is a maximal tendency to move up. That is the limit in which the particle is an empty bubble.

In this limit the equation reduces to the simpler form

$$0 = \frac{9\pi\mu}{2\pi R^2}(\frac{dz}{dt} - v(z)) + g\rho\frac{\gamma\,r(z)^3}{\frac{2\rho\,Q^2}{\pi} + \gamma\,r(z)^3}, \tag{29}$$

from which the velocity of the particle at any point can be expressed in terms of the already known magnitudes of the problem as

$$\frac{dz}{dt} = v(z) - \frac{2R^2 g\rho}{9\mu}\frac{\gamma\,r(z)^3}{\frac{2\rho\,Q^2}{\pi} + \gamma\,r(z)^3}. \tag{30}$$

Therefore, the condition for the particle to move up at a height value z can be written as

$$\frac{dz}{dt} = v(z) - \frac{2R^2 g\rho}{9\mu}\frac{\gamma\,r(z)^3}{\frac{2\rho\,Q^2}{\pi} + \gamma\,r(z)^3}$$

$$= \frac{Q}{\pi r(z)^2} - \frac{2R^2 g\rho}{9\mu}\frac{\gamma\,r(z)^3}{\frac{2\rho\,Q^2}{\pi} + \gamma\,r(z)^3} < 0. \tag{31}$$

Assuming that the fluid under consideration is water, the above conditions are equivalent to

$$C(Q, R, z) = Q - \frac{2\pi R^2 g\rho}{9\mu}\frac{\gamma\,r(z)^5}{\frac{2\rho\,Q^2}{\pi} + \gamma\,r(z)^3} < 0. \tag{32}$$
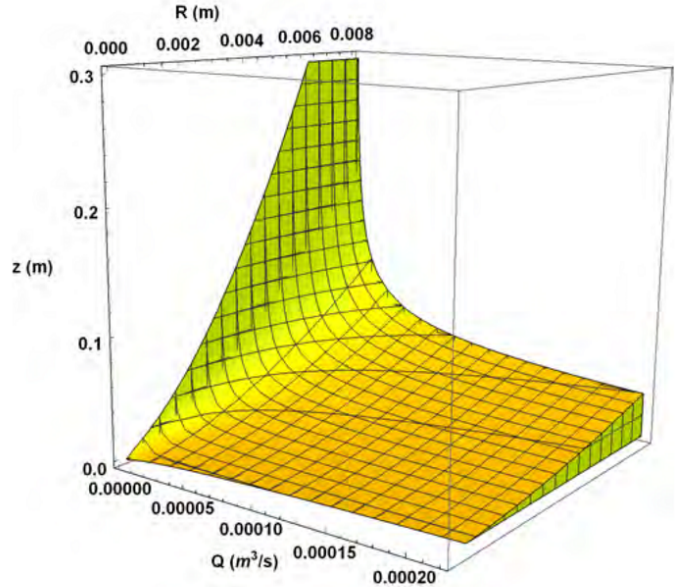
Figure 4. The plotted surfa9ce is formed by the set of points satisfying the equality in relation (32). That is, at such points the velocity of the bubble particles vanishes when the triplet of parameters take the plotted values. Above the surface the particles have positive velocities and then do not contaminate the upper recipient. Below it, in the colored region, the particles have negative velocities and then, tend to ascend against the flow.
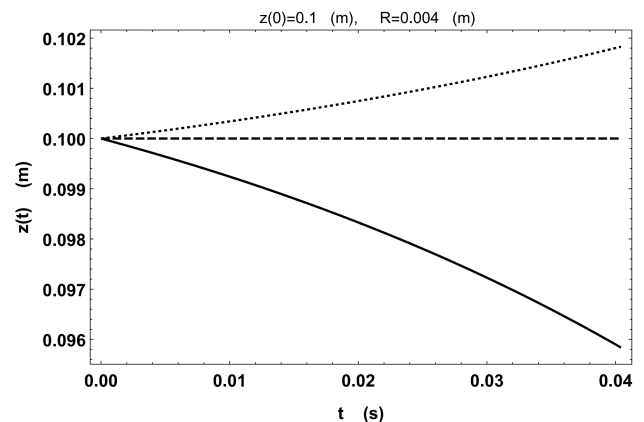
Figure 5. The plotted curves illustrate that when the flux is smaller, and such that the triplet of parameters (Q, z, R) is below the critical surface, the motion of the particle is towards negative values of z. That is, the particle ascends to the upper reservoir. For higher values of flux (for which the triplet of parameters is over the critical surface) the particle moves in the direction of the positive values of z. Thus, in this case the particle moves down and does not tend to contaminate the upper container.

The satisfaction of the relation (32) in the space of the three still free parameters: the flux Q, the radius of the particles R and the height coordinate z (measured from the point of

zero velocity) is illustrated in figure 4. The shown surface describes the triplets of values of the parameters (Q, R, z) at which the velocity of the particle becomes equal to zero. For all the points being over this surface the particle shows a positive value of its velocity and then it is not able to climb to the upper reservoir (remember that the increments of the height z are defined as positive ones if the point moves down). Correspondingly, the points being below the surface correspond to particles that will contaminate the upper vessel. That is, having a negative velocity value. In this way, given the parameters of the system, the conditions for the particle to appear in the upper recipient have been identified also for this free falling water situation. In the next subsection we will check how the direct solution of the exact system of equations reproduces the same conclusions extracted from the simplified analysis for a spherical bubble of the same radius as a particle with density ρ_m.

III.1. Direct solution of the full Newton equation around the critical surface

Let us consider the Newton equation

$$\frac{d^2z}{dt^2} = g - \frac{9\pi\mu}{2\pi\rho_m R^2}\left(\frac{dz}{dt} - v(z)\right) - g\frac{\rho}{\rho_m}\frac{\gamma\, r(z)^3}{\frac{2\rho\, Q^2}{\pi} + \gamma\, r(z)^3}, \tag{33}$$

for values of the triplet of parameters (Q, R, z) being close to the critical surface in figure 4. For concreteness, it will be assumed the following specific values for the height position and the radius of the particle

$$z(0) = 0.1 \text{ m}, \qquad R = 0.004 \text{ m}, \tag{34}$$

by also selecting two values of the flux

$$Q_1 = 1.4 \times 10^{-6} \text{ m}^3/s \qquad Q_2 = 1.6 \times 10^{-6} \text{ m}^3/s, \tag{35}$$

being close to an specific value $Q^* = 1,53 \times 10^{-6}$. This value Q^* is chosen for making sure that the triplet $(Q^*, R, z(0))$ is exactly on the critical surface. Then, the two triplets associated to the fluxes Q_1 and Q_2 are situated, one of them over and the other below, the critical surface.

Now, it will be considered the solution of the equations (33) by assuming that the density of the particle is very small, by example satisfying

$$\frac{\rho_m}{\rho} = 10^{-9}.$$

In addition, we will assume two independent boundary condition for the velocity of the particles as coinciding at the initial time $t = 0$ with the velocities of the water flow in the form

$$\frac{d}{dt}z(t)_{t=0} = \dot{z}(0) = \frac{Q}{\pi r(z(0))^2},$$

as calculated for the two specified values of the flux: one of them associated to a higher value and defining a point over the critical surface and the other one with a smaller flux,

which is linked with a point being below the critical surface. The specific values of the two fluxes were defined in (35).

The solutions of the equation of motion for the height coordinate z of the particle are shown in figure 5. The curves clearly show that when the flux is the smaller one, and such that the triplet of parameters is below the critical surface, the movement of the particle is tending to the negative values of z. That is, the motion is ascending to the upper reservoir. However, for the higher flux, when the triplet of parameters is over the critical surface, the particle moves in the direction of the positive values of z. Thus, in this case it does not tend to contaminate the upper vessel.

IV. SUMMARY

We have theoretically modeled the effect associated to the rising of particles from a lower recipient to a higher one, through a water flux falling from the higher one [1]. Conditions for the occurrence of the effect for two types of mechanisms for the water falling were established. It follows that for water going down through a cylindrical tube of constant cross section, there is a critical value of the flux were above which the particles are not allowed to rise up to the upper recipient. For the case in which the water is free falling, it firstly became clear that the possibility of the particles to climb up exists only under the presence of surface tension in water. If the surface forces are assumed to be absent, the particles can not flow up, at least for the discussed case of particle motion through the volume. In this case, it also follows that there is a critical value of the difference of height between the vessels, above which the particles are not allowed to climb the water flow. These critical values rise with the increasing size of the particles and decrease as the amount of water flux through the falling beam is reduced. The discussion results in a simple criterion for the occurrence of the effect which is based on a simplified equation of motion for empty bubbles of the same sizes as the particles. The almost vanishing of the density of the bubbles permits to reduce the equation of motion to a first order in the time derivative one, in the limit of zero density. The satisfaction of the criterion for the occurrence of the effect obtained for bubbles is checked by solving the full Newton equations of motion for particles near the critical surface, under simplified conditions.

BIBLIOGRAPHY

[1] S. Bianchini, A. Lage, T. Siu, T. Shinbrot and E. Altshuler, Proc. Roy. Soc. A **469**, 20130067 (2013).
[2] O. Reynolds, Proc. MA Lit. Phil. Soc. **21**, 1 (1881).
[3] C. Marangoni, Il Nuovo Cimento **3**, 50 (1870).

[4] V. G. Levich, Physicochemical hydrodynamics, p. 754, New York, NY: Advance Publications (1977).

[5] L. E. Scriven, C. V. Sternling, Nature **187**, 186 (1960).

[6] P. Singh, D. D. Joseph, S. K. Gurupatham , B. Dalal, S. Nudurupati, Proc. Natl Acad. Sci. USA **106**, 19761 (2009).

[7] P. L. du Nouy, J. Gen. Physiol. **7**, 625 (1925).

[8] M. Hancock, J.W.M. Bush, J. Fluid Mech. **466**, 285 (2002).

ENERGY SENSITIVITY OF THE LOW-ENERGY PARAMETERS OF NEUTRON-PROTON SCATTERING FOR VARIOUS NUCLEON-NUCLEON POTENTIALS

SENSIBILIDAD A LA ENERGÍA DE PARÁMETROS DE BAJA ENERGÍA EN EL SCATTERING NEUTRÓN-PROTÓN PARA VARIOS POTENCIALES NUCLEÓN-NUCLEÓN

M. Abusini[†] and A. Ahbika

Department of Physics, Al al-Bayt University, Al-Mafraq - 130040, Jordan; abusini@aabu.edu.jo[†]
† corresponding author

The triplet and singlet low-energy parameters in the effective-range expansion for neutron–proton scattering were determined with the aid of the most popular modern realistic nucleon–nucleon potentials (Nijm I), (Nijm II) and (Reid93). We compared our results with the latest partial wave analysis experimental data from the SAID nucleon–nucleon database and newest values a_t, a_s, r_t and r_s parameters were presented. Our calculations based on these three potentials at incident neutron energy less than 60 KeV show that there are some discrepancies with experimental data. In order to decrease the discrepancy between our results and the experimental ones at very low energy, we suggest to include coupling terms $^3S_1 + {}^3D_1$ for constructing various realistic nuclear-force models. Furthermore, the calculated effective range expansions in this work are not very accurate for very low energy unless considering into account many terms v_n in the expansions.

Se determinaron los parámetros de singlete y triplete de baja energía en la expansión de rango efectivo para el scattering neutrón-protón, con la ayuda de los potenciales nucleón-nucleón realistas más populares (Nijm I), (Nijm II) y (Reid93). Comparamos nuestros resultados con la data experimental más avanzada basada en análisis parcial de ondas de la base de datos SAID nucleón-nucleón y se rpresentaron los valores más actuales de los parámetros a_t, a_s, r_t y r_s. Nuestros cálculos basados en estos tres potenciales con energía de neutrones incidentes menores de 60 kEV muestran que hay algunas discrepancias con la data experimental. Para disminuir la discrepancia a muy bajas energías, sugerimos incluir los términos de acoplamiento $^3S_1 + {}^3D_1$ para construir varios modelos de fuerza nuclear realistas. Las expansiones de rango calculadas en este trabajo no son muy precisas oara muy bajas energías, excepto si se considera muchos términos vn en las expansiones.

I. INTRODUCTION

In the past years, researchers were focused on the subtleties and various extensions of the nuclear force leading to setting up more sophisticated two and few-nucleon potentials. Therefore, various high-quality models and forms for Nucleon-Nucleon interaction has been presented nowadays [1–7]. One way to study the nuclear two-body interactions is to use a two-nucleon system namely, the deuteron that has two nucleons ($n + p$).

The primary goals of this article is to use a model-independent analysis, to extract the best possible values of the effective range theory (ERT) parameters for np elastic scattering, the spin-triplet and spin-singlet scattering lengths a_r and a_s, and their effective ranges r_t and r_s, and the zero-energy free neutron cross section. The secondary goal is to check the accuracy of effective range expansion method for various modern realistic nucleon–nucleon potentials, namely, Nijm I, Nijm II and Reid93 [8, 9] at very low energy of incident neutron.

Along with the deuteron parameters, the low-energy parameters in the effective-range expansion for neutron–proton scattering were given by:

$$k \cot \delta = -\frac{1}{a} + \frac{1}{2} r k^2 + v_2 k^4 + v_3 k^6 + v_4 k^8 + \dots, \qquad (1)$$

where $k^2 = 2\mu E/\hbar^2$ and δ-the phase shift.

The effective-range expansion, including the scattering length a, the effective range r, the shape parameter v_2, and the higher order parameters v_n for neutron–proton scattering are fundamental quantities that play a key role in studying strong nucleon–nucleon interaction [10]. These parameters are of great importance not only to construct various realistic nuclear-force models, but also to form a basis for studying the structure of nuclei and various nuclear processes. The theoretical value of these parameters greatly depends on the used nuclear-force model. As we go over from one model to another, it follows that the shape parameter is very sensitive to nucleon–nucleon interaction.

We would like to note that the shape parameter v_2 depends not only on the form of interaction, but depends on the scattering length a, and the effective range r. In particular, a change of only a few tenths of a percent in the scattering length may lead to a several fold change in the shape parameter.

Starting with Schrodinger equation:

$$\left[\frac{d}{dr^2} + k^2 - U(r)\right]u_k(r) = 0, \tag{2}$$

where $U(r) = (2\mu/\hbar^2)V(r)$. The boundary conditions of $u_k(r)$ are given in terms of phase shift δ:

$$u_k(0) = 0; \qquad u_k(r \to \infty) \to \frac{\sin(kr + \delta)}{\sin \delta}.$$

Whereas, the wave function $u_k(0)$ was taken when the incident energy is zero, $k = 0$. The equation 2 for this case is given as follows:

$$\left[\frac{d}{dr^2} - U(r)\right]u_0(r) = 0. \tag{3}$$

The above equation holds even when $U(r) = 0$. Thus, we can have the same discussion with the following Schrodinger equation with different wave function:

$$\left[\frac{d}{dr^2} + k^2\right]\omega_k(r) = 0. \tag{4}$$

Along with the boundary condition, $\omega_k(r \to \infty) \to u_k(r \to \infty)$.

$$\omega_0 \frac{d^2\omega_k}{dr^2} - \omega_k \frac{d^2\omega_0}{dr^2} = -k^2\omega_0\omega_k \tag{5}$$

According to the boundary conditions, $[u_0 u_k' - u_k u_0']_0^\infty$ will cancel out and only when $r = 0$, we can have the following:

$$[\omega_0\omega_k' - \omega_k v_0']_{r=0} = k^2 \int_0^\infty (\omega_0\omega_k - u_0 u_k)dr. \tag{6}$$

Where

$$\omega_k = \cos kr + \cot \delta \sin kr. \tag{7}$$

From this, we can derive $\omega_0(r)$ which is the asymptotic function when $k \to 0$,

$$\omega_0 \equiv \lim_{k \to 0} \omega_k(r) = 1 + r \lim_{k \to 0} k \cot \delta. \tag{8}$$

We also perform an expansion with k^2; then, we have for the scattering length a and the effective range r

$$k \cot \delta = -\frac{1}{a} + \frac{1}{2}rk^2 + O(k^4). \tag{9}$$

Where the parameter r is the usual effective range at zero energy, which is a good approximation in studying nucleon–nucleon (NN) scattering at low energies.

II.   RESULTS AND DISCUSSIONS

The total scattering cross-section of two nucleonic systems for different singlet and triplet states is written as:

$$\sigma = \frac{3}{4}\sigma_t + \frac{1}{4}\sigma_s. \tag{10}$$

Where σ_t and σ_s are the cross-sections for scattering in the triplet and singlet states, respectively. The scattering length a is defined in such a way the low-energy cross-section is equal to $4\pi a^2$, where

$$\lim_{k \to 0} \sigma = 4\pi a^2, \tag{11}$$

with

$$a = \pm \lim_{k \to 0} \frac{\sin \delta_0}{k}. \tag{12}$$

Where δ_0 is the zero-energy phase shift.

In order to determine the triplet and singlet scattering lengths (a_t and a_s, respectively), we employ equations that relate to the above quantities with the total cross-section for zero-energy scattering of neutrons by protons,

$$\sigma_0 = \pi(3a_t^2 + a_s^2). \tag{13}$$

The coherent scattering length then is defined as:

$$f = \frac{1}{2}(3a_t + a_s). \tag{14}$$

The values of the triplet effective range r_t were determined primarily in an approximation that does not depend on the form of interaction that is,

$$r_t \equiv \delta(-\varepsilon_d, 0) = 2R(1 - \frac{R}{a_t}). \tag{15}$$

Where $\delta(-\varepsilon_d, 0)$ is the mixed effective radius of the deuteron.

$$R = \frac{1}{\alpha}, \tag{16}$$

R is a parameter that characterizes the spatial dimensions of the deuteron; and α is the deuteron wave number, which is directly related to the deuteron binding energy ε_d by the equation $\varepsilon_d = (\hbar^2\alpha^2)/m_N$.

The singlet effective range r_s is usually determined on the basis of the analysis of the total cross-section for neutron–proton scattering σ_0 in the low-energy region at fixed values of the parameters a_t, a_s, and r_t. To determine the other parameters, we fitted the total cross section for various realistic nucleon-nucleon potentials, namely the most popular modern realistic nucleon–nucleon potentials (Nijm I, Nijm II and Reid93) using the equation 13 for zero-cross section σ_0 and the equation 14 for the coherent scattering length f. We chose the values of experimental data for the total cross section σ_0 from SAID nucleon–nucleon database [11]. Here we determined the values of the triplet effective range r_t using the equations 15 and 16, then we compared our results for all low energy parameters a_t, a_s, r_t and r_s by using the value of coherent scattering length $f = -3.756$ fm from previous experimental data [12–14]. The chosen experimental data along with our results for various realistic potential (Nijm I, Nijm II and Reid93) were summarized in Table .

Table 1. Low-energy parameters of neutron–proton scattering from various experimental studies compared with our results based on potentials Nijm I, Nijm II and Ried 93. References were provided next to each experimental study.

Model	$a_t(fm)$	$a_s(fm)$	$r_t(fm)$	$r_s(fm)$
(Exp.data) Dilg [12]	5.423(21)	-23.749(54)	1.740(28)	2.772(11)
(Exp.data) Houlk. [13]	5.405(11)	-23.728(28)	1.738(12)	2.56(9)
(Exp.data) Noyes [14]	5.396(4)	-23.678(13)	1.727(4)	2.51(10)
Nijm I (Our Calculations)	5.08236	-22.7371	1.315	2.445
Nijm II. (Our Calculations)	5.08343	-22.7603	1.316	2.455
Ried 93. (Our Calculations)	5.08388	-22.7616	1.317	2.51
Babenko and Petrov (theory) [15]. < 150 keV .	5.411(27)	-23.7155 (8)	1.7601(27)	2.706(21)

As we can see from Table our calculated results using Nijm I, Nijm II and Ried 93 potentials for parameters a_t, a_s, r_t and r_s, are in a good agreement with each other. However, some discrepancies were observed between the obtained data and the experimental data. In particular for the effective range in the triplet state r_t, the discrepancies are about 25 %. In addition we also compared our obtained results with other theoretical calculations at energies below 150 keV, (Babenko and Petrov [15]) for the total cross sections of neutron–proton scattering at zero energy.n We noticed that Babenko and Petrov results below 150 keV also were at odds with Dilg's experimental cross section as ours. According to Babenko and Petrov, the discrepancies with Dilg's experimental cross section is indicates that Dilg's cross section is in a glaring contradiction with experimental data in the energy region of several keV units and is likely to be erroneous.

This fact deserves special attention because all modern realistic nucleon–nucleon potentials (Nijm-I, Nijm-II,Reid93); Argonne [16]; and CD-Bonn [17, 18] are based on a fit to the Nijmegen nucleon–nucleon database, which includes Dilg's cross section as an input parameter, and therefore lead to an insufficiently accurate description of the present-day experimental data at low energies.

Table 2. A comparison between experimental data of total cross-section for neutron scattering on a proton (σ_0) at low energies ($l = 0$) [11] with the obtained data of total cross-section for the three potentials (Nijm I, Nijm II and Reid93).

Energy (MeV)	Experimental data (σ_0), barn	Nijm I potential (σ_0), barn	Nijm II potential (σ_0), barn	Reid93 Potential (σ_0), barn
00.000132	20.491∓ 0.014 [39]	0.040852467(13)	0.038483489(22)	0.038528427(43)
00.000300	20.436∓0.023 [42]	0.097287109(27)	0.097382615(44)	0.097382615(33)
00.001970	20.130∓0.030 [43]	02.04260796(34)	02.04330996(19)	02.04392938(28)
00.060000	15.400∓0.462 [44]	14.90949419(11)	14.91276065(43)	14.90874451(37)
00.075000	14.200∓0.426 [44]	14.01762298(19)	14.02030094(11)	14.01455952(41)
00.090000	13.000∓0.390 [44]	13.24459177(22)	13.24681517(14)	13.23983230(39)
00.120000	12.050∓0.121 [44]	11.99111572(29)	11.99270806(13)	11.98420184(33)
00.143000	11.210∓0.030 [43]	11.20928574(28)	11.21055428(23)	11.20141927(26)
00.492600	06.202∓0.011 [45]	06.20429833(38)	06.20397122(22)	06.19607508(27)
00.555000	06.041∓0.103 [46]	05.82498798(19)	05.82531337(44)	05.81289620(19)
00.600780	05.557∓0.088 [46]	05.58979939(45)	05.59012464(46)	05.58292632(44)
00.702690	05.173∓0.052 [46]	05.14674364(47)	05.14629833(41)	05.13965183(41)
00.803430	04.817∓0.043 [46]	04.79434200(38)	04.79404296(29)	04.78785422(17)
00.902520	04.472∓0.036 [46]	04.50706514(11)	04.50687126(39)	04.50106316(11)
01.053000	04.274∓0.001 [47]	04.15012476(33)	04.15046381(33)	04.14512978(10)
02.082000	02.819∓0.003 [47]	02.85372251(45)	02.85398756(28)	02.85021791(22)
03.069000	02.246∓0.004 [47]	02.26502099(29)	02.26517930(12)	02.26194264(41)
03.986000	01.889∓0.004 [47]	01.91441046(11)	01.91447913(11)	01.91150386(19)
05.115000	01.608∓0.005 [47]	01.61142047(14)	01.61139859(10)	01.60863412(11)
06.032000	01.411∓0.004 [47]	01.42759440(19)	01.42751368(16)	01.42488243(18)
07.222000	01.219∓0.004 [47]	01.24191462(23)	01.24177352(17)	01.23929313(27)
08.363000	01.092∓0.005 [47]	01.10230937(18)	01.10212380(18)	01.09977674(22)
09.281000	01.000∓0.007 [47]	01.00955693(21)	01.00934309(38)	01.00709898(18)
10.360000	00.903∓0.008 [47]	00.91734345(19)	00.91710324(33)	00.91497690(13)
10.972000	00.861∓0.009 [47]	00.87154787(27)	00.87129543(26)	00.86923464(19)

In the present work to explain the discrepancies of our obtained results for low energy parameters with the experimental data, we collected a set of experimental values of the total cross-section of neutron-proton scattering at specific low energies from the SAID nucleon–nucleon database, then compared the calculated values of the total np scattering cross-section based on the three potentials (Nijm I, Nijm II and Reid93) at the same energies range [0.0002 − 10 MeV]. In Table we summarized the obtained results based in our studied potentials with experimental total cross section from the SAID nucleon–nucleon database at the interval of energies [0.0002 − 10 MeV].

As we can see from Table , there is a huge discrepancy between the values of total cross-section of neutron-proton scattering σ_0 for three potentials Nijm I, Nijm II and Reid93 with experimental data at energy of incident neutron less than 0.06 MeV. However, as the incident neutron goes above the value 0.06 MeV, a good agreement with experimental data was observed.

Table 3. The contributions of expansion terms v_n (v_2, v_3 and v_4) in the low-energy scattering potentials Nijm I, Nijm II and Reid93 in energy interval [0.0002 − 10 MeV].

Potentials	v_2	v_3	v_4
NijmI	0.046	0.675	−3.97
NijmII	0.044	0.672	−3.95
Reid93	0.045	0.676	−3.90

Figures 1, 2 and 3 show the total cross section at zero energy (σ_0) vs. energy of incident neutron for all studied potentials (Nijm I, Nijm II and Reid93), compared with experimental data. These data were taken from the SAID nucleon–nucleon database. Figures show a good agreement between our calculations and experimental data above the incident neutron energy of 0.06 Mev; as energy decreases we see the discrepancies with experimental data increases.
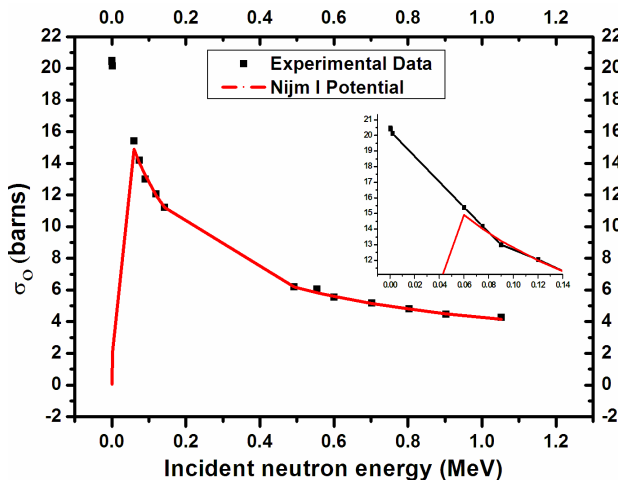
Figure 1. The total cross-section for neutron scattering by a proton for the potential Nijm I as function incident neutron energy, the experimental data were obtained from [11]. The inset represents a zoom for the cross section at low energy from (0.0–0.06) Mev.

The insets of Figs. 1, 2 and 3 represent a zoom for the total cross section at interval energy from (0.0 − 0.06). This observation leads us to an important conclusion: the three

potentials have an obvious defect when the incident neutron energy is less than 0.06 MeV. In Table we presented the contributions of the higher order expansion terms v_2, v_3 and v_4 in the effective range expansions at very low energies for all studied potentials (Nijm I, Nijm II and Reid93). The higher order terms have an important contribution in the total cross section, constituting about 10-15 %; it follows that the shape parameter is very sensitive to nucleon–nucleon interaction at very low energies. Moreover, in Table we presented some of the effective ranges for various potentials and the contributions of terms v_n in the expansions of effective range theory in energy interval [0.0002 − 10] MeV. In a future paper we intend to show the contributions of all expansion terms v_2, v_3 and v_4 separately in our calculations for the cross section at very low incident energies.
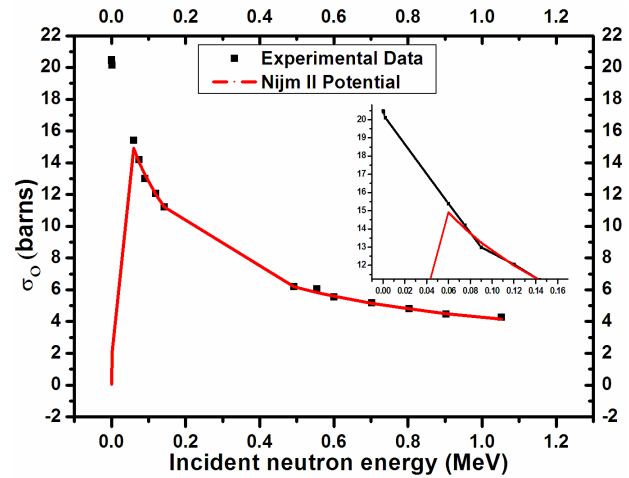
Figure 2. The total cross-section for neutron scattering by a proton for the potential Nijm II as a function incident neutron energy, the experimental data were obtained from [11] the inset represent a zoom for the cross section at low energy from (0.0–0.06) Mev.
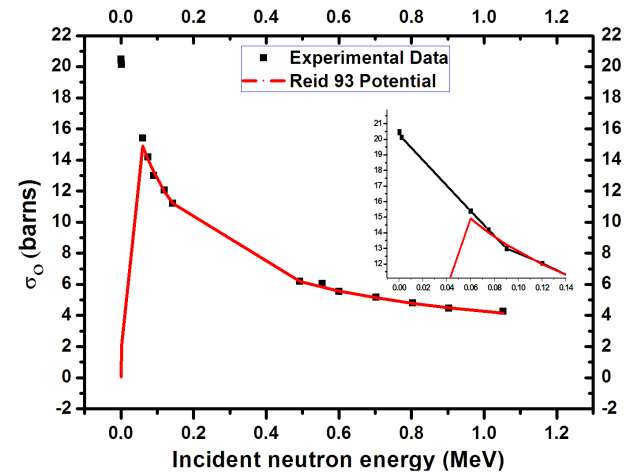
Figure 3. The total cross-section for neutron scattering by a proton for the potential Reid93 as function incident neutron energy, the experimental data were obtained from [11]. The inset represents a zoom for the cross section at low energy from (0.0–0.06) Mev.

So we may conclude that the obtained results for various nucleon- nucleon potentials such Nijm I, Nijm II and Reid93 show that the construction of these potentials are incomplete at zero-energy specially at incident energy less

than 60 keV. To eliminate the discrepancy between our results and the experimental one at very low energy, we may suggest including coupling terms in addition to the term $^1S_0$ for constructing various realistic nuclear-force models. Furthermore, to achieve a good agreement for the low energy parameters, one should take into account many terms v_n in the expansions of effective range theory.

III. CONCLUSIONS

We determined the four low energy parameters: singlet scattering length a_s, triplet scattering length a_t, singlet effective range r_s and triplet effective range r_t of low-energy neutron-proton scattering using three neutron-neutron potentials: Nijm I, Nijm II and Reid93. Compared to experimental data, some discrepancies were observed. We mentioned here that the calculated effective range expansions in this work are not very accurate for very low energy unless one takes into account many terms v_n in the expansions. Besides, our calculations lead us to an important conclusion that the three potentials, Nijm I, Nijm II and Reid93 have obvious defect to calculate the values of total cross-section of neutron-proton scattering when the incident neutron energy is less than 60 KeV. As the energy of incident neutrons increases, the calculated results become in a good agreement with the experimental data for all three potentials. This is a good indication that the methodology adopted for constructing these potentials follows the same logic. To improve the consistency between our results and the experimental results at very low energy we suggest to include coupling terms $^3S_1 + ^3D_1$ in addition to the term $^1S_0$ for constructing various realistic nuclear-force models. Finally, we found that a reliable experimental determination of the total cross section for neutron–proton scattering at zero energy, σ_0, and of the coherent scattering length, f, is now quite a pressing problem. Precise values of these quantities would make it possible to determine unambiguously the triplet and singlet scattering lengths and to solve the problem of choosing a correct set of the low-energy parameters and phase shifts among currently recommended experimental values.

REFERENCES

[1] E. Epelbaum, H.W. Hammer, and U.G. Meissner, Rev. Mod. Phys. **81**, 1773 (2009).

[2] F. Gross, T.D. Cohen, E. Epelbaum, and R. Machleidt, Few-Body Syst., **50**, 31, (2011).

[3] R. Machleidt, Q. MacPherson, E. Marji, R. Winzer, Ch. Zeoli, and D.R. Entem, Few-Body Syst . **54**, 821 (2013)

[4] M. Taketani, S. Nakamura, and M. Sasaki, Prog. Theor. Phys. **6**, 581 (1951).

[5] M. Naghdi, Phys. Part. Nucl., **45**, 924 (2014).

[6] A. Al-Jamel, M. Serhan, M. Abusini., J. Theor. Appl. Phys. (Iranian Phys. J.) **5**, 47 (2011)

[7] N. Al-Bouzieh, and M. Abusini, J. Theor. Appl. Phys. (Iranian Phys. J.) **5**, 39 (2010)

[8] V.G.J. Stoks, R.A.M. Klomp, M.C.M. Rentmeester, and J.J. de Swart, Phys. Rev. C **48**, 792 (1993).

[9] C. Van der Leun and C. Anderliesten, Nucl. Phys. A **380**, 261 (1982).

[10] G.L. Squires and A.T. Stewart, Proceedings of the Royal Society of London A: Mathematical, Physical and Engineering Sciences **230**, 19550110 (1955).

[11] R.A. Arndt, I.I. Strakovsky, and R.L. Workman, Phys. Rev. C. 62, 034005 (2000).

[12] W. Dilg, Phys. Rev. C **11**, 103 (1975).

[13] T.L. Houk and R. Wilson, Rev. Mod. Phys. **40**, 672 (1968).

[14] H. Pierre Noyes, Phys. Rev. 130, 2025 (1963).

[15] V.A. Babenko and N.M. Petrov, Phys. At. Nucl. **73**, 1499 (2010).

[16] R.B. Wiringa, V.G.J. Stoks, and R. Schiavilla, Phys. Rev. C **51**, 38 (1995).

[17] R. Machleidt, Phys. Rev. C **63**, 024001 (2001).

[18] R. Machleidt, F. Sammarruca, and Y. Song, Phys. Rev. C **53**, R1483 (1996).

CLUSTER VARIATION METHOD FOR FRUSTRATED MAGNETS
MÉTODO DE VARIACIÓN DE CLUSTERS EN MATERIALES MAGNÉTICOS FRUSTRADOS

E. Domínguez[†], A. Lage-Castellanos, C.E. Lopetegui and R. Mulet

Facultad de Física, Universidad de La Habana, 10400 La Habana, Cuba; edv2rd0@gmail.com[†]
† corresponding author

The model J_1-J_2 has provided a good theoretical benchmark for the study of frustrated magnets. This model is studied from the perspective of the Cluster Variation Method (CVM). In a first moment, Bethe approximation is considered. In this context it is possible to obtain a phase diagram where a stripes phase and a paramagnetic phase are observed, though separated by a non convergence zone. Secondly, plaquette approximation is considered and a complete phase diagram is obtained. In the latter it is observed an additional nematic phase with orientational but not positional order, which was not possible to observe using the Bethe approximation.

El modelo J_1-J_2 ha servido como base para el estudio teórico de materiales magnéticos frustrados. Este modelo es estudiado desde la perspectiva del Método de Variación de Clusters (CVM). En un primer momento se estudia utilizando la aproximación de Bethe. En este contexto se obtiene un diagrama de fases en el que es posible observar una fase de franjas y una fase paramagnética, separadas por una zona de no convergencia. Posteriormente se emplea la aproximación de plaquetas, lo cual permite obtener un diagrama de fases completo. En este último es posible observar la fase nemática, que no se observa al utilizar la aproximación de Bethe.

I. INTRODUCTION

Competing interactions are a common feature of many natural and artificial systems. Examples can be found in very different scenarios like solid state physics, mathematical optimization or quantum systems. In particular, ultra-thin magnetic films [2,3], spin glasses [4], high T_c superconductors [5–9], colloidal suspensions [10], and strongly correlated electron systems [11, 12], are some of the many examples where competing interactions are present. An interesting aspect when dealing with competing interactions is the arising of frustration, that is the inability of the system to satisfy all the interactions at the same time. High frustration gives place to very interesting and complex landscapes in the equilibrium (stripes, bubbles, clusters, spin liquid, disordered phases, etc). Also, to the occurrence of very complex phenomena such as slow relaxation to equilibrium and strong metastability [1].

One of the simplest models with competing interactions is the well known J_1-J_2 model. In a square lattice it is a simple extension of the Ising Model where, besides of the nearest neighbor (NN) ferromagnetic interaction characterized by the coupling factor J_1, one adds an antiferromagnetic interaction between next nearest neighbors (NNN) characterized by the parameter J_2.

The Hamiltonian describing the model is

$$H = -\sum_{\langle ij \rangle} J_1 s_i s_j - \sum_{\langle\langle ij \rangle\rangle} J_2 s_i s_j - \sum_i h_i s_i, \tag{1}$$

where $\langle ij \rangle$ stands for the NN and $\langle\langle ij \rangle\rangle$ for the NNN.

This model has served as a paradigm for the study of frustrated magnets and a renewed attention has been put into it during the last decades [13–20]. The interest on the model is motivated by many factors.

In the very first place it is a simple model with a rich phase diagram [14, 20–22]. Depending on the adjustable parameter $k = |J_2/J_1|$ and the relative signs of the exchange interaction parameters, it offers the chance to describe Néel antiferromagnetic order (NAF), columnar antiferromagnetic order (CAF), or spin liquid and nematic phases.

It is precisely the evidence of the presence of the spin liquid phase [20, 21, 23], one of the reasons for the renaissance of the interest in the model. It is a fact that it provides a good opportunity to understand the spin liquid properties or even to obtain a realization of this type of order that conserves its properties near the absolute zero.

Besides, it is relevant for the understanding of high T_c superconductivity of cuprates and iron based superconductors such as LaFeAsO, that have shown superconductivity at temperatures up to 50 K [7–9, 24].

The recent experimental realization of "J_1-J_2 materials", such as $VOMoO_4$ [25], $Pb_2VO(PO_4)_2$ [21], Li_2VOSiO_4 and Li_2VOGeO_4 [26, 27], has open the gate for the necessity of a deep theoretical understanding of the model in order to compare with experimental results and make predictions.

Most of the theoretical work on the model has been devoted to the zero external field scenario [28–33], where a good understanding of the equilibrium properties has been reached already. In the case of the Ising J_1-J_2 in the zero field case for $k > 1/2$ a stripes phase of alternating up and down

spins is the ground state at low temperatures. The stripes phase is characterized by the presence of both orientational and positional order in the lattice.

On the other hand, nematic phases related to the stripe-like order are present in many quasi two dimensional systems like ultra-thin magnetic films and electronic liquids [34–38]. These nematic phases are characterized by the presence of orientational, but no positional order. In this sense there is an intermediate degree of symmetry between the disorder phase and the stripes (See Fig. 1 for an intuitive comprehension).
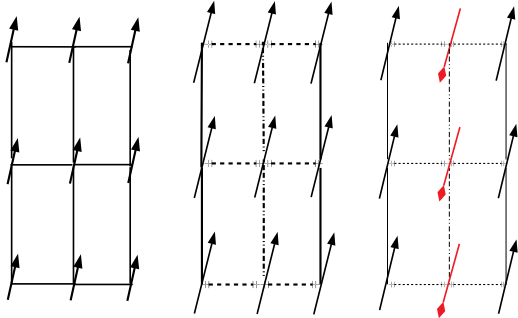

Figure 1. Schematic representation of order in the equilibrium state of the model. From left to right, paramagnetic (under homogeneous field), nematic and stripes order. Arrows stand for the mean local magnetization and lines for site to site correlations. **Left Paramagnetic**: All sites are equally tagged. There is no order at all, but a high symmetry. **Center Nematic**: Magnetizations are the same. However the correlation between horizontal neighbors is different from the correlation between vertical neighbors. There is orientational order characterized by non isotropic correlations. **Right Ferromagnetic**: Magnetization in the middle column point in an opposite direction to that of the rest of the sites. Correlations are just as in the nematic phase, so there is nor positional neither orientational order in the stripes phase.

A natural question arises: whether J_1-J_2 model would be able or not, to sustain such a nematic phase, as an intermediate phase in the breaking of the Z_4 symmetry of the disordered phase to the Z_2 symmetry of the stripes. The difficulty on the study of such anisotropic phases arises from the necessity of computing correlations in different directions.

In [22], Stariolo et al. answered the previous question by constructing an H-T phase diagram of the model. In this phase diagram it can be observed a region where nematic order arises. The phase diagram was built by using the well known Cluster Variational Method (CVM) approximation, which showed to be very appropriate for the study of anisotropic correlations. These authors point out that it is necessary to go beyond naive mean field (MF) and Bethe, in order to compute anisotropy in correlations. They asseverate that the minimal approximation suitable for detecting the stripes phase is the plaquette or Kikuchi approximation.

In the present paper we show that it is possible to observe the stripes phase in the context of the Bethe approximation, provided the regions and the symmetries of the problem are considered in a proper way. We will show the phase diagram of the problem, using both Bethe and the Kikuchi approximation, the latter resulting similar to the one reported in [22].

In order to differentiate the phases to which the model converges in equilibrium, two order parameters are used,

one measuring the positional order and one measuring the orientational order. The orientational order parameter defined as

$$Q = \frac{1}{4} \left(l_{34} + l_{12} - l_{23} - l_{14} \right), \tag{2}$$

and the positional order parameter as

$$M = \frac{1}{2} \left(m_1 - m_4 \right), \tag{3}$$

where $l_{ij} = \langle s_i s_j \rangle$ stands for the correlation between spins j and i, and m_i for the local magnetization at site i. The numeration follows Fig. 2
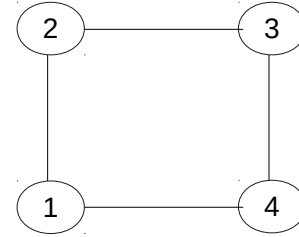
Figure 2. Sketch of the typical structure considered to compute the order parameters.

When the system is in the stripes phase both the order parameters are finite. The transition to disorder, where they are both zero, can occur in two ways. There can be a slow transition, characterized by a nematic intermediate order, or a discontinuous transition when both abruptly go to zero. Orientational order parameter plays the leading role when nematic order is present, and in fact, after leaving the stripes phase, there is no need to follow the behavior of the positional order.

As the largest correlations to be considered in order to compute these order parameters are links, it seems appropriate to consider at first instance the Bethe Approximation. This approximation considers links as largest regions in the Region Based Free Energy [39]. This will gives us the opportunity to consider different kind of interactions, which is not possible using Mean Field. In a second moment we consider the Kikuchy approximation which consider four site plaquettes as largest regions. This allows to take into account correlations among all four spins in the basic cell of the lattice, which improves the quality of the results.

II. BETHE APPROXIMATION

We study the equilibrium of the model using the CVM formalism [39]. The simplest approximation in this context is the Bethe-Peierls one, in which the largest regions considered in the variational free energy to minimize are links. It has been widely established that the constrained minimization of the Bethe free energy leads to a set of self-consistent equations in the Lagrange multipliers. Carefully treated, these equations result to map into the standard *Belief*

Propagation Algorithm (BP) equations [39]. In BP, Lagrange multipliers are understood as messages from links to sites. This algorithm is known to be exact in tree like graphs, and even when in structures with loops it does not give the exact results, it provides a simple and good insight into the equilibrium properties of a system.

The self-consistent equations for the messages have the form [39]

$$m_{j\to i}(s_i) = k_i \sum_{s_j} f(s_i, s_j) \prod_{k\in N(j)\backslash i} m_{k\to j}(s_j),$$ (4)

where the message $m_{j\to i}(s_i)$ can be thought as the probability, as seen by the spin j that spin i has value s_i. The form of the functions $f(s_i, s_j)$ depends on whether spins i and j are NN or NNN. For NN it has the form

$$f(s_i, s_j) = \exp\left[\beta\left(J_1 s_i s_j + h_j s_j\right)\right],$$ (5)

and for NNN

$$f(s_i, s_j) = \exp\left[\beta\left(J_2 s_i s_j + h_j s_j\right)\right].$$ (6)

It is usual to parametrize the messages as functions of cavity fields [40]

$$m_{j\to i}(s_i) = \exp\left[\beta u_{j\to i} s_i\right],$$ (7)

where $u_{j\to i}$ has the form of a cavity field representing the influence of spin j over spin i.

It is useful to do so both because it improves the efficiency of the implementation and because it provides a very intuitive way to understand the messages.

The algorithm consists in solving the set of self-consistent equations by the fixed point iteration of the equations over the full lattice considering random initial values for the cavity fields. At every step new values are computed for the fields by taking the previous step ones, by means of the equation

$$u_{j\to i} = \frac{1}{\beta}\tanh^{-1}\left[\tanh\left(\beta J_{ij}\right)\tanh\left(\beta \sum_{k\in N(j)\backslash i} u_{k\to j}\right)\right],$$ (8)

which is derived from equation 4.

All the important information of the system is finally obtained from the *beliefs* of each region. They represent the marginal distributions obtained for each region in the CVM framework. These beliefs approximate the exact Boltzmann marginals. If we moved in the CVM context to consider incrementally size regions the beliefs values should converge to that of the exact Boltzmann marginals.

Beliefs can be obtained in terms of the effective fields as

$$b_{ij}(s_i, s_j) = \frac{f(s_i, s_j)}{Z_{ij}}\exp\left(\sum_{k\in N(i)\backslash j} u_{k\to i} s_i + \sum_{k\in N(j)\backslash i} u_{k\to j} s_j\right)$$ (9)

$$b_i(s_i) = \frac{1}{Z_i}\exp\left(h_i s_i + \sum_{k\in N(j)} u_{j\to i} s_i\right)$$ (10)

At the time of the implementation it is possible to take advantage from the symmetry of the interactions. Supposing the whole lattice to be a repetition of a basic structure in the equilibrium, we can study the whole system by just considering some important links. In a way it is like removing the rest of the lattice without removing its influence. The important links are shown in Fig. 3. Not all the effective fields are represented there and the reason is that we make some considerations based on the symmetry of the interactions. In Fig. 3 a distinction is made between the sites of different columns. There are two reasons for this. The first one is that NN interactions are all defined by the same exchange parameter J_1 and the same for NNN interactions (J_2). Based on this, we are aware that the symmetry of the order phase should somehow be related to this fact. The form in which the order appears depends on the relation between J_1 and J_2. If $J_1 < J_2/2$, J_2 domains, otherwise J_1 does. The later is the case we are considering, so it is obvious to expect the symmetry of the stripes phase previously described. Considering this, we can reduce the amount of degrees of freedom (*d.o.f*) of the system to six effective fields, that are the ones in Fig. 3. So, the implementation we make is not the standard BP algorithm for lattices, but actually a fixed point calculation on the set of BP self-consistent equations for these six degrees of freedom.
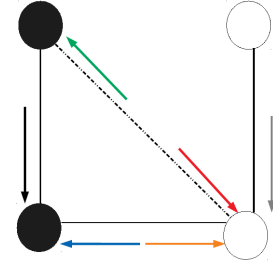
Figure 3. Representation of the relevant links in Bethe approximation.

In order to make it clear, for example, let's look at a horizontal link, it is the one between the sites represented black and white. The fields that enter into the update equations of the cavity fields between the two sites are represented in Fig. 4. The ones acting on the black spin enters into the update equation for the cavity field from the black site to the white one, and vice versa.
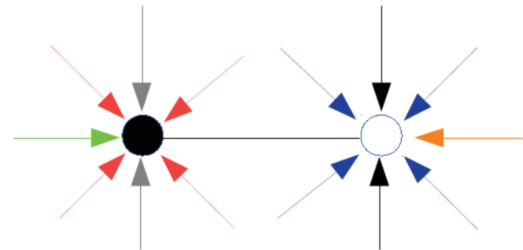
Figure 4. Fields that enter into the update equation for the effective fields in the link.

As a result of the Fixed Point study on this system it was possible to obtain an approximate phase diagram for the model (Fig. 5).

There are some important points to discuss about the phase diagram. First, it was possible to observe the stripes phase for low external magnetic fields and temperatures, which is in agreement with the results reported in [22]. On the other hand, the presence in this phase of anisotropic correlations seems to contradict their statement that the minimal approximation in which such a behavior could be observed is the Kikuchy one. The fact is that it is true only if you do not include in the Bethe region graphs the NNN links. So what we did was to include the diagonal links in the set of regions and consider the messages between NNN in the BP formulation.
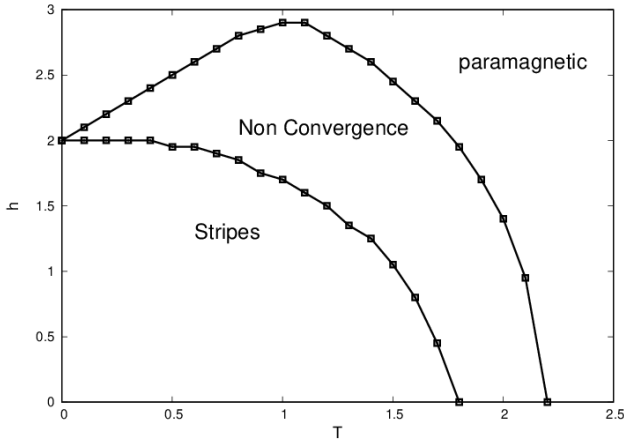
Figure 5. Phase diagram for J_1-J_2 model in the context of the Bethe Approximation.

For high temperatures and fields, it is predicted the existence of a paramagnetic phase, where nor orientational neither positional order are observed, and the average magnetization is only due to the presence of an external field.

On the other hand, a region of the diagram could not be described, as the algorithm did not converge. The reason why nematic phase could not be observed within this approximation is not completely clear to us, neither the reason of the non convergence. However, we will see below that it could be well connected with the appearence of the nematic phase.

Still, we want to emphasize that even when a complete characterization of the phase diagram is not possible at the Bethe level it proved again to be a useful tool in a fast exploration of the model.

III. PLAQUETTE APPROXIMATION

In order to obtain a more complete and accurate phase diagram for the model we go a step further in the CVM formalism and consider Kikuchi approximation. In this framework the largest regions to be taken into account in the construction of the variational free energy are the plaquettes of four sites. It is widely established that the constrained minimization of the Kikuchi free energy leads to a set of equations that are equivalent to those of the algorithm *Generalized Belief Propagation* [39]. In the *Parent to Child* formulation of the algorithm, messages go from parent

regions to children only, that is, from plaquettes to links, and from links to sites.

The objective is again to determine the marginal distributions for each region, which in this context are called *beliefs*. These beliefs are obtained from the equilibrium values of the messages by [40]

$$
b_R(s_R) \, \alpha \prod_{a \in A_R} f_a(s_a) \left(\prod_{P \in \mathcal{P}(R)} m_{P \to R}(s_R) \right) \\
\prod_{D \in \mathcal{D}(R)} \prod_{P' \in \mathcal{P}(D) \setminus \varepsilon(R)} m_{P' \to D}(s_D) ,
$$

(11)

where $f_a(s_a)$ has a similar meaning to that of $f(s_i, s_j)$, with the difference that for plaquettes, the expression includes all the pair interactions between the sites that conform it; $\mathcal{P}(R)$ stands for the parent regions of region R; $\mathcal{D}(R)$ for the regions descending from R; and $\varepsilon(R)$ represents the set formed by R and its descendants.

It is important to notice that at the time of constructing the region based free energy, links between NNN sites are not included as they have counting number zero, which is logical if we realize that they are not part of any intersection of larger regions.

Again it is appropriate to parametrize the messages in terms of cavity fields [40]. The messages from links to spin have the form stated in (7). On the other side, the parametrization of plaquette to link messages is more subtle. This is

$$
M_{\mathcal{P} \to \mathcal{L}}(s_i, s_j) = \exp \left[\beta \left(U_{\mathcal{P} \to \mathcal{L}} \right) s_i s_j + u_{\mathcal{P} \to i} s_i + u_{\mathcal{P} \to j} s_j \right],
$$

(12)

where $U_{\mathcal{P} \to \mathcal{L}}$ has the form of an effective interaction term like J_{ij} and the other terms have a similar meaning to that of the cavity fields that parametrize link to spin messages.

Some symmetry considerations were made before the implementation. In the first place, as it can be predicted from the results in the Bethe context, and as it is known from [22], the higher possible degree of order for the model is that of the stripes phase. Based on that, it is possible to impose some constrains over the values of the messages. This idea is shown in Fig. 6 where we show that some messages are taken to be the same, in the way it should be in the stripes phase. In this figure messages from the plaquette P to its children are not represented, but they are to be considered equivalent to the ones coming from neighbor plaquettes. Notice that doing this represents a great simplification of the computational requirements as we reduce the problem to a set of eleven selfconsistent equations.

We consider a characteristic plaquette to reproduce the behavior of the entire lattice, considering the effect of the rest of the system through the messages or in our case the cavity fields from nearby regions (Fig. 6). In this way our computation translates into a *Fixed Point* calculation on the set of GBP self-consistent equations for the fields remaining

in the structure.
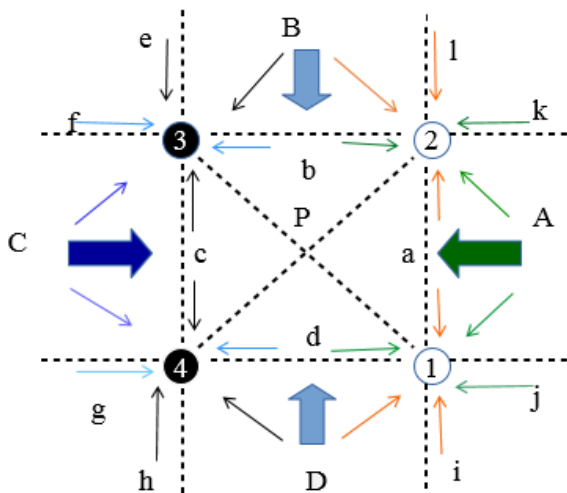
Figure 6. Structure over which the algorithm is run and the constrains over the messages.

Following the ideas outlined in [40], we can remove the *gauge* invariance in the cavity field equations. The standard parent-to-child implementation of the GBP method introduces more parameters than actually needed [40, 41] to characterize the local beliefs distributions. The redundant parameters do not alter the fixed point solution, but could affect the convergence of the fixed point algorithm. So, based on the recommendation in the previous reference, we set two of the field variables to be zero. In Fig. 7 we omit the fields that we force to be zero.
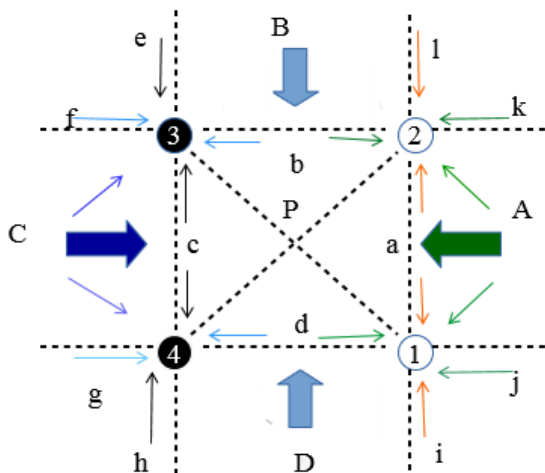
Figure 7. Structure over which the *Fixed Point* calculation is done, and constrains over the fields. The ones forced to be zero are omitted in this sketch.

On the other hand, there is a set of fields which enter into the update equation of each other partly linearly, which usually slows down the convergence. It can be avoided by solving the linear system they form, in function of the non linear parts of the update equations. Doing this drastically improves the convergence of the algorithm.

In this context it was obtained a complete phase diagram (Fig. 8), similar to that in [22].
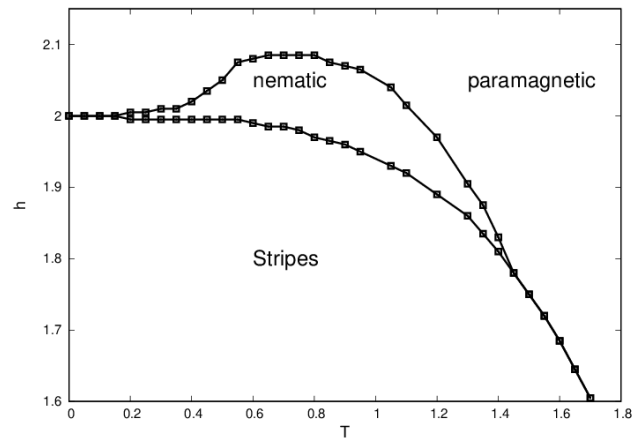
Figure 8. Phase Diagram using GBP.
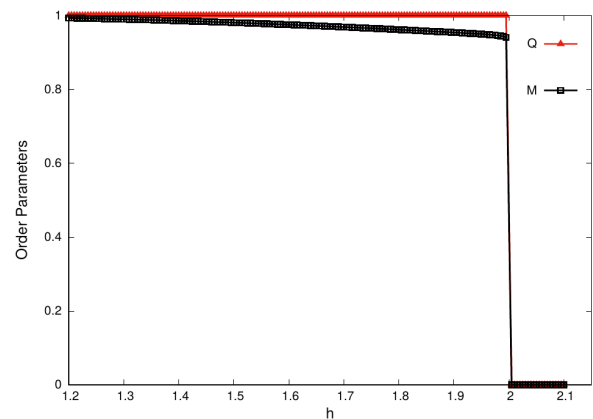
Figure 9. Order parameters as a function of h for $T = 0.05$. A discontinuous transition is observed for both of the parameters. So, the transition from stripes to paramagnetic phase is direct.
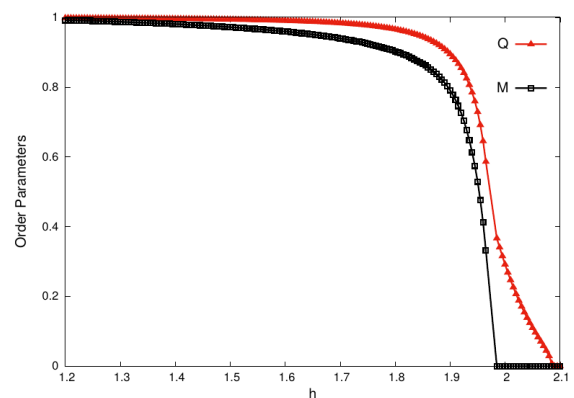
Figure 10. Order parameters as a function of h for $T = 0.8$. It can be observed a first transition in which positional order goes to zero while there is still orientational order. This is the signature of the nematic phase. A second transition occurs in which orientational order goes continuously to zero, so that paramagnetic phase is reached. At this temperature, transition from order phase (that is, from stripes), to disorder, occurs by passing through an intermediate nematic type order, rather than directly as at $T = 0.05$.

It is important to notice that at very low temperatures the transition from the stripes ordered phase to the paramagnetic

one seems to occur directly without passing through the nematic order, which is the main difference with the results published in [22]. In order to make it clear we show the behavior of the order parameters as a function of the external field for $T = 0.05$ (Fig. 9).

On the other hand we can look at the behavior of these parameters for $T = 0.8$, where the nematic phase is clearly observed (Fig. 10).

IV. CONCLUSIONS

In this work we studied the J_1-J_2 using the Cluster Variational Method. By considering the proper symmetries of the model, it was possible for the first time in the literature, to describe the presence of stripes in the Bethe approximation. Unfortunately the Bethe approximation does not converge for all the parameters of the model.

We improved over Bethe by studying also the model in the plaquette or Kikuchi approximation. In this case, the full phase diagram is accessible without convergence issues, and in addition to the stripes and the paramagnetic phases, we show the existence of a nematic phase. Our results are mostly consistent to the ones in [22]. However the phase diagram in [22] was computed through a numerical minimization of the Kikuchi free energy, while our results come from the exact solution of the fixed point equations obtained after the analytical minimization of an equivalent free energy. Both methods have advantages and disadvantages of their own, but certainly fixed point equations usually provides faster convergence (if they converge).

We are able to show a finer description of the low temperature extreme of the transition curves. In [22] it is suggested that the nematic phase is stable for any $T > 0$. Our results, on the contrary, point to the presence of a minimum $T_c(h_c) \simeq 0.2$. Below this temperature the nematic phase does not exist and the transition occurs directly between the paramagnetic to the stripe phase.

REFERENCES

[1] D. Wales, Cambridge University Press, Cambridge, 2003.

[2] K. De'Bell, A.B. MacIsaac and J.P. Whitehead, Rev. Mod. Phys. **72**, 225, (2000).

[3] A. Vaterlaus, C. Stamm, U. Maier, M.G. Pini, P. Politi and D. Pescia, Phys. Rev. Lett. **84**, 2247, (2000).

[4] K.H. Fischer and J.A. Hertz, Cambridge University Press, Cambridge, 1991.

[5] E. Fradkin, S.A. Kivelson, M.J. Lawler, J.P. Eisenstein and A.P. Mackenzie, Annu. Rev. Condens. Matter Phys. **1**, 153, (2010).

[6] E. Berg, E. Fradkin, S.A. Kivelson and J.M. Tranquada, New Journal of Physics **11**, 115004, (2009).

[7] Q. Si and E. Abrahams, Phys. Rev. Lett. **101**, 076401, (2008).

[8] C. Fang, H. Yao, W.F. Tsai, J.P. Hu and S.A. Kivelson, Phys. Rev. B **77**, 224509, (2008).

[9] T. Yildirim, Phys. Rev. Lett. **101**, 057010, (2008).

[10] D. Coslovich, M. Bernabei and A.J. Moreno, J. Chem. Phys. **137**, 184904, (2012).

[11] V.J. Emery, S.A. Kivelson and E. Fradkin, Nature **393**, 550, (1998).

[12] E. Fradkin and S.A. Kivelson, Phys. Rev. B **59**, 8065, (1999).

[13] T. Aoki, J. Phys. Soc. Jpn. **73**, 599, (2004).

[14] E. Dagotto and A. Moreo, Phys. Rev. Lett. **63**, 2148, (1989).

[15] M. Mambrini, A. Láuchli, D. Poilblanc and F. Mila, Phys. Rev. B **74**, 144422, (2006).

[16] X.G. Wen, Phys. Rev. B **44**, 2664, (1991).

[17] R. Darradi, O. Derzhko, R. Zinke, J. Schulenburg, S.E. Krúger and J. Richter, Phys. Rev. B **78**, 214415, (2008).

[18] M.E. Zhitomirsky and K. Ueda, Phys. Rev. B **54**, 9007, (1996).

[19] N. Read and S. Sachdev, Phys. Rev. Lett. **62**, 1694, (1989).

[20] H.C. Jiang, H. Yao and L. Balents, Phys. Rev. B **86**, 024424, (2012).

[21] N. Shannon, B. Schmidt, K. Penc and P. Thalmeier, Eur. Phys. J. B **38**(4), 599, (2004).

[22] A.I. Guerrero, D.A. Stariolo and N.G. Almarza, Phys. Rev. E **91**, 052123, (2015).

[23] P.W. Anderson, Materials Research Bulletin **8**(2), 153, (1973).

[24] K. Seo, B.A. Bernevig and J. Hu, Phys. Rev. Lett. **101**, 206404, (2008).

[25] P. Carretta, N. Papinutto, C.B. Azzoni, M.C. Mozzati, E. Pavarini, S. Gonthier and P. Millet, Phys. Rev. B **66**, 094420, (2002).

[26] H. Rosner, R.R.P. Singh, W.H. Zheng, J. Oitmaa and W.E. Pickett, Phys. Rev. B **67**, 014416, (2003).

[27] R. Melzi, S. Aldrovandi, F. Tedoldi, P. Carretta, P. Millet and F. Mila, Phys. Rev. B **64**, 024409, (2001).

[28] S. Jin, A. Sen and A.W. Sandvik, Phys. Rev. Lett. **108**, 045702, (2012).

[29] A. Kalz, A. Honecker, S. Fuchs and T. Pruschke, J. Phys.: Conf. Ser. **145**(1), 012051, (2009).

[30] A. Kalz, A. Honecker and M. Moliner, Phys. Rev. B **84**, 174407, (2011).

[31] J.L. Morán-López, F. Aguilera-Granja and J.M. Sanchez, Phys. Rev. B **48**, 3519, (1993).

[32] J.L. Moran-Lopez, F. Aguilera-Granja and J.M. Sanchez, J. Phys.: Condens. Matter **6**(45), 9759, (1994).

[33] R.A. dos Anjos, J.R. Viana and J.R. de Sousa, Phys. Lett. A **372**(8), 1180, (2008).

[34] D.G. Barci, A. Mendoza-Coto and D.A. Stariolo, Phys. Rev. E **88**, 062140, (2013).

[35] S.A. Cannas, M.F. Michelon, D.A. Stariolo and F.A. Tamarit, Phys. Rev. B **73**, 184425, (2006).

[36] N.G. Almarza, J. Pekalski and A. Ciach, J. Chem. Phys. **140**(16), 164708, (2014).

[37] L. Nicolao and D.A. Stariolo, Phys. Rev. B **76**, 054453, (2007).

[38] Ar. Abanov, V. Kalatsky, V.L. Pokrovsky and W.M. Saslow, Phys. Rev. B **51**, 1023, (1995).

[39] W.T. Freeman, J.S. Yedidia and Y. Weiss, TR2004-040, (2004).

[40] E. Domínguez, A. Lage-Castellanos, R. Mulet, F. Ricci-Tersenghi and T. Rizzo, Journal of Statistical Mechanics: Theory and Experiment **2011**(12), 12007, (2011).

[41] E. Domínguez, A. Lage-Castellanos, R. Mulet and F. Ricci-Tersenghi, Phys Rev E **95**, 043308, (2017).

OPTICAL PROPERTIES OF DEFECTIVE SILICON CARBIDE NANOTUBES: THEORETICAL STUDY
PROPIEDADES ÓPTICAS DE NANOTUBOS DE CARBURO DE SILICIO DEFECTUOSOS: ESTUDIO TEÓRICO

A. A. Ghozlan and J. A. Talla[†]

Department of Physics, Al al-Bayt University, Al-Mafraq - 130040, Jordan; jtalla@aabu.edu.jo[†]

The optical properties of silicon carbide nanotubes with different orientations of Stone Wales defects were investigated for polarized light, unpolarized light and light incident through polycrystalline media. Density functional theory were used to study the effect of different orientations of Stone Wales defects on the optical properties of chiral (8, 4) silicon carbide nanotube. We monitored the corresponding changes in dielectric function, optical conductivity, absorption, reflection spectra, refractive index, and loss function. We found that introducing different orientations of Stone Wales defects to silicon carbide structure modified yet improved the optical properties of the nanotubes.

Se investigaron las propiedades ópticas de nanotubos de carburo de silicio con diferentes orientaciones de defectos de Stone Wales para luz polarizada, no polarizada, y luz incidente a través de medios policristalinos. Se usó la teoría del funcional de densidad para estudiar el efecto de diferentes orientaciones de los defectos de Stone Wales sobre las propiedades ópticas del nanotubo quiral (8,4) de carburo de silicio. Monitoreamos los cambios correspondientes en la función dieléctrica, conductividad óptica, absorción, espectro de reflexión, índice de refracción y función de pérdidas. Encontramos que el introducir diferentes orientaciones de defectos de Stone Wales en la estructura modificada de carburo de silicio logró mejorar las propiedades ópticas de los nanotubos.

I. INTRODUCTION

The successes in synthesizing carbon nanotubes prompted experimental and theoretical efforts on producing other types of nanostructured material [1–6]. For instance, silicon nanostructures, especially silicon carbide nanotubes have been theoretically predicted and experimentally produced [7, 8]. Currently, silicon carbide nanotubes are the focus of intense theoretical and experimental research [5, 8, 9]. For example, silicon carbide nanostructures have been recently produced by numerous experimental works. Furthermore, theoretical studies based on density functional theory are known to be more reliable method to predict the properties of nanostructure material [7, 10–14]. The interest in silicon carbide nanostructures emerges primarily from their extraordinary properties including; high reactivity of the internal/ external surface, chemical inertness, high thermal conductivity, thermal stability, and much more [15–18]. Furthermore, silicon carbide nanotubes are one ofthe hardest materials which suites applications designed for operations at high temperature and radiation environments [16, 19, 20]. This could be attributed to their semiconducting nature, radiation resistance and high thermal conductivity [16, 19]. Besides, the polar nature of silicon carbide nanotubes can intrinsically be excellent sensors for detecting some toxic gases, including; HCN, HCOH, CO, and NO [10, 21, 23]. Moreover, theoretical calculations proved an increase in the binding energy of H_2 around 20 % with silicon carbide nanotube compared with pure carbon nanotubes [24, 25]. This increase in the binding energy could be attributed to the partially hetero-polar binding nature of the Si−C bonds [24]. Therefore, silicon carbide nanotubes could be considered as the most suitable candidate for hydrogen storage [4, 26, 27]. Furthermore, previous theoretical calculations prove that silicon carbide nanotubes are stable structures, with the most stability predicted for silicon-carbon ratio 1:1 [8]. Moreover, these calculations prove that these silicon carbide nanotubes are always semiconducting in nature.

Unlike carbon nanotubes, the band gap energy of silicon carbide nanotubes is weakly dependent on the tube chirality with direct band gaps for zigzag tubes and indirect gaps for chiral and armchair nanotubes [28, 29]. Besides, compared to carbon nanotubes, silicon carbide nanotubes are polar materials which exhibit some unusual physical properties(11). For example, zigzag silicon carbide nanotubes become piezoelectric material and exhibits second order nonlinear optical response [10, 30].

Stone Wales defect is a typical defect in silicon carbide nanotubes [1, 6, 13, 31]. Wang's et al in their investigations indicates that Stone Wales defects in silicon carbide nanotubes can be created by irradiation technique [17]. However, not many studies conducted on chiral silicon carbide; this could be ascribed to the complexity in modeling the structure and the calculations accompany it [30].

To the best of our knowledge, there are no theoretical and experimental studies addressing the optical properties of chiral silicon carbide nanotubes with different orientations of Stone Wales defects. Furthermore, no first principal studies

of the dielectric response as well as other optical properties of silicon carbide nanotubes have been reported. This might be attributed to the heavy demand on computer resources. Therefore, predictions of the effect of introducing different orientations of Stone Wales defects on the optical proprieties of silicon carbide nanotubes are strongly desirable. Besides, studying the optical properties of silicon carbide nanotubes is important for electro optical applications. The main objective of this work is to study optical characteristics of silicon carbide nanotubes and silicon carbide nanotubes with Stone Wales defects by first-principles calculations. Whereas, tuning the optical properties of silicon carbide nanotube will open a wide range of applications including; solar energy, Anti-reflection coatings, self-cleaning systems, ultraviolet light-emitting diodes, photo-catalysis and flat panel displays [1,13,31].

II. COMPUTATIONAL METHOD

In this theoretical work, we aim to study the optical properties of silicon carbide nanotubes that contain different orientations of Stone Wales defects. To achieve our goal, we simulated different orientations of Stone Wales defects on a chiral (8, 4) silicon carbide nanotube. Stone Wales defects could be created when Si−C bond rotated by 90 deg [1], whereas, for chiral silicon carbide nanotubes, there are three possible Si−C bonds that more likely to be rotated by 90 deg, (Figure 1). Consequently, three types with three different orientations of Stone Wales defects were created. The chiral angle (χ) were identified in such a way $0 \leq \chi \leq \pi/6$. Therefore, three different possible angles were identified, i.e. $\pi/3 - \chi$, χ and $\pi/3 + \chi$, with 19.11deg. Therefore, the angles of Stone Wales defects are 19.11deg (Type I), 40.89deg (Type II) and 79.11deg (Type III), refer to Figure 1. The results obtained from silicon carbide nanotubes that contain the three types of Stone Wales defects were compared with the results obtained with pristine silicon carbide nanotubes. We set the lattice constant "a" and "b" for all simulated structures to be large enough to eliminate any possible interaction with the tube and its image.However, the third lattice direction "c" was set to be exactly the same as the nanotube length in order to keep the tube periodicity. Density functional theory was performed with the aid of CASTEP code, whereas, all simulated structures were relaxed using geometry optimization calculations. Eigen functions were also calculated using self-consistent Kohn Sham equation. Furthermore, the revised Perdewe Burkee Ernzerhof (RPBE) sub-functional was used with generalized gradient approximation. While, the norm-conserving pseudo-potential was employed in reciprocal space, and an extended electronic wave functions into plane wave basis set with finite basis set correction were used. A 600 eV cutoff energy was assigned for the grid integration $1 \times 1 \times 18$ kpoints from Monkhorst-Pack scheme. To improve the calculation's accuracy, energy convergence tolerance was set to 5×10^{-5} eV. Moreover, we set the maximum force convergence tolerance and the maximum displacement was set to 0.01 eV/å and 0.002 å, respectively. To reduce the computational time,

we implemented DFT Semi-core Pseudopotential core treatment. We performed our optical calculations on chiral(8, 4) silicon carbide nanotube with three different orientations of Stone Wales defects. Finally, energy calculations were performed for all geometry optimized structures. We monitored the corresponding changes in dielectric function, optical conductivity, absorption, reflection spectra, refractive index, and loss function. We analyzed the obtained results to figure out the effect of introducing different orientations of Stone Wales defects on the optical properties of silicon carbide nanotubes [6,31].
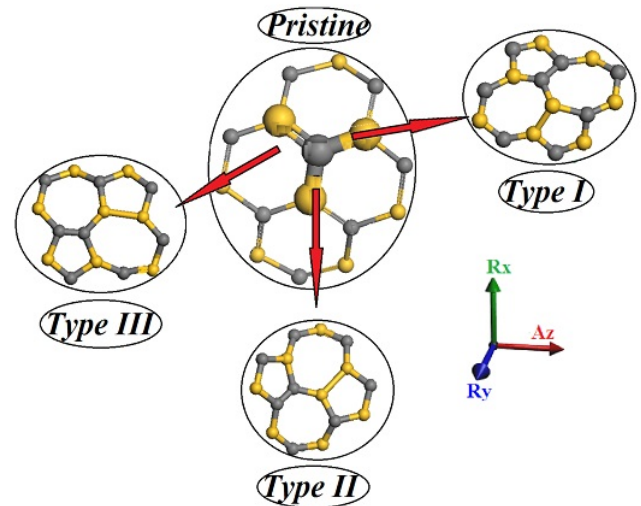
Figure 1. Schematic diagram represents differenttypes of Stone Wales defects as well as the bonds that create the three types of Stone Wales defects.

III. RESULTS AND DISCUSSION

We studied the optical properties of silicon carbide nanotubes with different orientations of Stone Wales defects. To study all possible cases, three types of incident lights were used i.e. polarized and unpolarized light, as well as light incident through polycrystalline media. Three different orientations of Stone Wales defects were simulated on the surface of chiral (8, 4) silicon carbide nanotubes. To have a complete insight, six optical properties were extensively studied: dielectric function, optical conductivity, absorption, reflection spectra, refractive index, and loss function.

III.1. Dielectric function

Dielectric function ($\varepsilon(\omega)$) could be used to characterize not only the optical properties of materials but also the materials electrical properties. Dielectric function can be calculated with the aid of the following equation:

$$\varepsilon(\omega) = \varepsilon_1(\omega) + \varepsilon_2(\omega) \tag{1}$$

Where $\varepsilon_1(\omega)$ is the dielectric function real part and $\varepsilon_2(\omega)$ is the dielectric function imaginary part [13,31].

III.2. Dielectric function real part

Figure 2. Real part of dielectric function for the three types of Stone Wales defects upon applying polarized light, unpolarized light and light incident through polycrystalline media.

We theoretically investigated the effect of different directions of Stone Wales defects on the dielectric function for silicon carbide nanotubes, by applying three different cases of incident light: polarized and unpolarized as well as light incident through polycrystalline media. The discrepancy in the dielectric function for all silicon carbide nanotubes

under investigation is a good indication that these silicon carbide nanotubes are anisotropic in nature (Figure 2 (a, b, c)). Whereas, the most obvious anisotropicity occurs for unpolarized incident light and incident light through polycrystalline media cases, refer to Figure 2 (a, b, c). The maximum peak observed around 3-3.5 eV. Whereas, the most declared peak for pristine silicon carbide nanotubes observed when the incident light is unpolarized and the incident light through polycrystalline media. However these peaks are not clearly distinguished from each other upon applying polarized light. Furthermore, introducing different orientations of Stone Wales defects has direct impact on the dielectric function static value, whereas, this clear discrepancy in the dielectric function static value could attributed to the type of defects created by Stone Wales defects, refer to inset in Figure 2 (a, b, c). Moreover, some intermediate peaks observed at low frequency region. Whereas, this peak intensity decrease/increase depending on the incident light nature, refer to Figure 2 (a, b, c).

The dielectric function peaks originated from electron transitions between carbon $2p$ statesand silicon $3p$ states in the π^* bond of silicon carbide nanotube. However, in higher energy range, no clear dielectric peaks were found. Compared with dielectric functions for the pristine silicon carbide nanotube, the mainlydielectric peak for different orientations of Stone Wales defects is suppressed, which has a direct relationship with the depression in the density peaks at high frequency range (Figure 2 (a, b, c)).

III.3. Dielectric function imaginary part

Although the dielectric functions real part oscillates between negative and positive values (Figure 3 (a, b, c)), the dielectric function imaginary part is positive throughout the whole range of frequency, refer to Figure 3 (a, b, c). Besides, the dielectric function imaginary part static value for all silicon carbide nanotubes under study is also positive which consistent with the continuous media theory. Furthermore, the imaginary part static value of dielectric function is always zero regardless the incident light nature and the type of Stone Wales defects, refer to Figure 2 (a, b, c). For polarized incident light, the maximum peak occurs for type III Stone Wales defects followed by type II. This peak originated around 3.25 (1/fs) and red shifts upon applying unpolarized incident light and light incident through polycrystalline media. Furthermore, upon applying unpolarized light and the incident light through polycrystalline media, the maximum values of the dielectric function imaginary part for all silicon carbide nanotubes under study occur around2.75 (1/fs) at 4.5 eV and 3.75 eV, 1.75 eV, and 3.5 eV for pristine silicon carbide nanotubes and silicon carbide nanotubes with type I and type II and type III Stone Wales defects, respectively (Figure 3 (a, b, c)). Dielectric function peaks ε_2 can be divided into three parts; first part of dielectric peaks located at low frequency range. These peaks originated from transitions in the π^* bond. Second part of dielectric peaks originated from electron transitions from π bond to π^* bond which play a crucial role in the formation of dielectric peaks. The third part

of dielectric peaks located at higher frequency range. These peaks mainly originated from the electronic transitions from σ bond to σ^* bond.
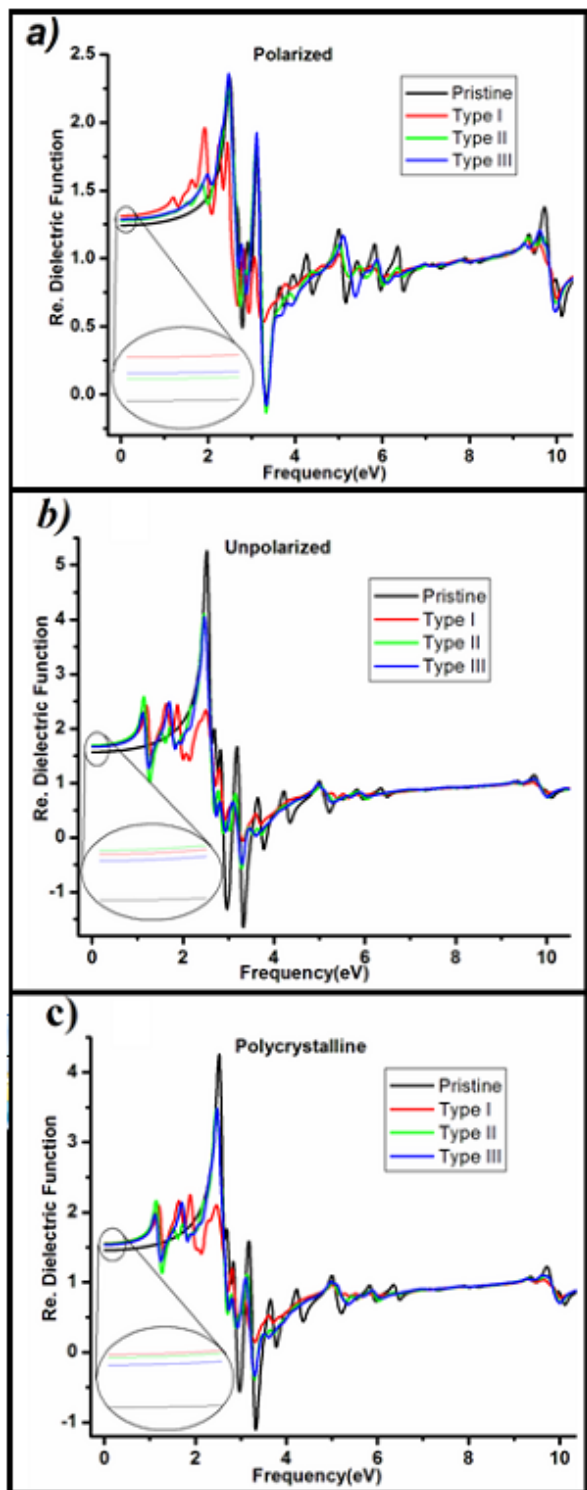

Figure 3. Imaginary part of dielectric function for the three types of Stone Wales defects upon applying polarized light, unpolarized light and light incident through polycrystalline media.

From the above, at different incident light nature, introducing different orientations of Stone Wales defects to pristine silicon carbide nanotube significantly modify the peaks intensity of the dielectric functions imaginary part.

III.4. Optical conductivity

Optical conductivity is defined when a material becomes more conductive as a result of absorption of electromagnetic waves. Figure 3 (a, b, c) represent the optical conductivity ($\sigma(\omega)$) for pristine silicon carbide nanotubes and silicon carbide nanotubes with Stone Wales defects at three different incident light nature i.e (polarized light, unpolarized light, and light incident through polycrystalline media). The optical conductivity ($\sigma(\omega)$) can be calculated using the following equation, whereas ε is the dielectric function,

$$\sigma(\omega) = i\omega 4\pi(1 - \varepsilon) \qquad (2)$$

Optical conductivity real part

Neither the type of the incident light nature nor the orientations of Stone Wales defects have any impact on the static value of the optical conductivity of silicon carbide nanotubes, refer to Figure 4 (a, b, c). This might be correlated to overlapping between valence and conduction bands at the Fermi level. Furthermore, it is clearly observed from Figure 4 (a, b, c) that the real part of the optical conductivity for all simulated silicon carbide nanotubes is strongest in the low frequency region, whereas, the maximum peak observed around 2.5-3.0 eV, with the highest peak related to pristine silicon carbide nanotubes for unpolarized incident light and light incident through polycrystalline media. In case of polarized incident light, the maximum peak observed in type III Stone Wales defects. Furthermore, in all cases of incident light, an intermediate peaks originated at lower frequency region, however, the optical conductivity of pristine silicon carbide nanotubes does not show up. For polarized incident light, the main peak ofoptical conductivity for pristine silicon carbide nanotube located around 3.25 eV with 0.7 (1/fs). However, upon applying unpolarized light, not only the main peak red shifts, but also a clear increase in optical conductivity value. Almost the same behavior observed upon introducing light incident through polycrystalline media with less increase in optical conductivity values compared to unpolarized case.

While type I Stone Wales defects behave differently, same behavior observed in other types of Stone Wales defects. For instance, in case of type I Stone Wales defects, blue shift observed in the main peak with slight increase in the optical conductivity values, refer to Figure 3 (a, b, c). From Figure 4 (a, b, c), it is clearly seen that, regardless the nature of the incident lights, the optical conductivity real part is positive. In addition, for polarized incident light, introducing type I Stone Wales defects to pristine silicon carbide nanotubes completely increase the optical conductivity real part, however, for unpolarized incident light and light incident through polycrystalline media, a clear decrease in the optical conductivity values. This could be attributed to the deformation occurs upon introducing Stone Wales defects. While introducing different orientations of Stone Wales defects create defects in the nanotube surface, a clear deformation observed in case of type I Stone Wales
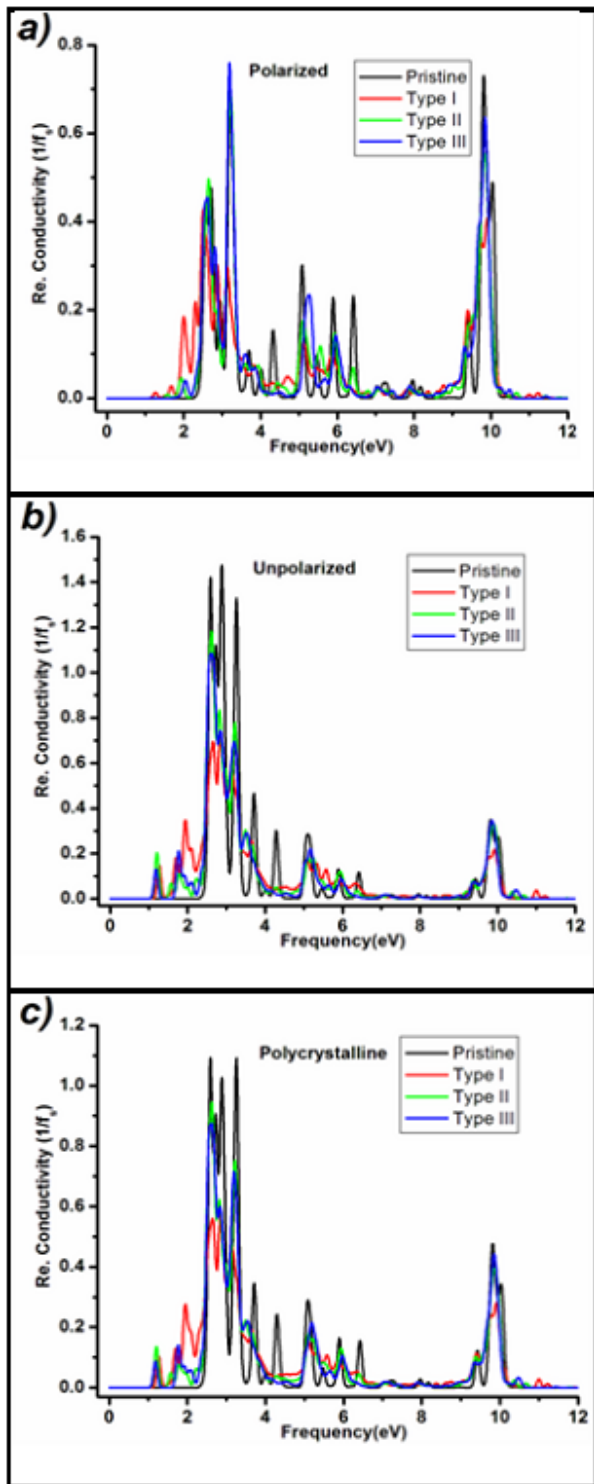
defects.

Figure 4. Real part of optical conductivity for the three types of Stone Wales defects upon applying polarized light, unpolarized light and light incident through polycrystalline media.

Optical conductivity imaginary part

The optical conductivity imaginary part has the highest peak intensity for type II Stone Wales defects nanotubes followed by type III Stone Wales defects when light is polarized. The minimum peak observed for type I of Stone Wales defects when light is polarized. In other words, when incident light is polarized, introducing type II and type III of Stone

Wales defects to pristine silicon carbide nanotube increase the optical conductivity imaginary part peak intensity.
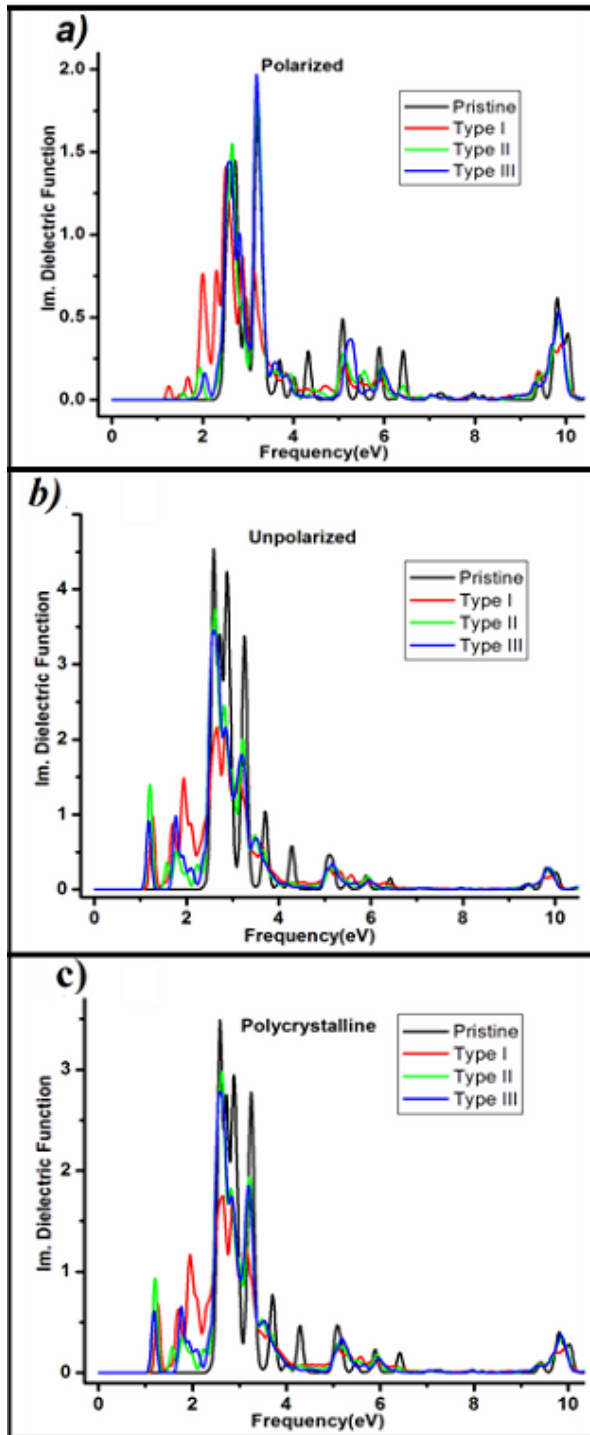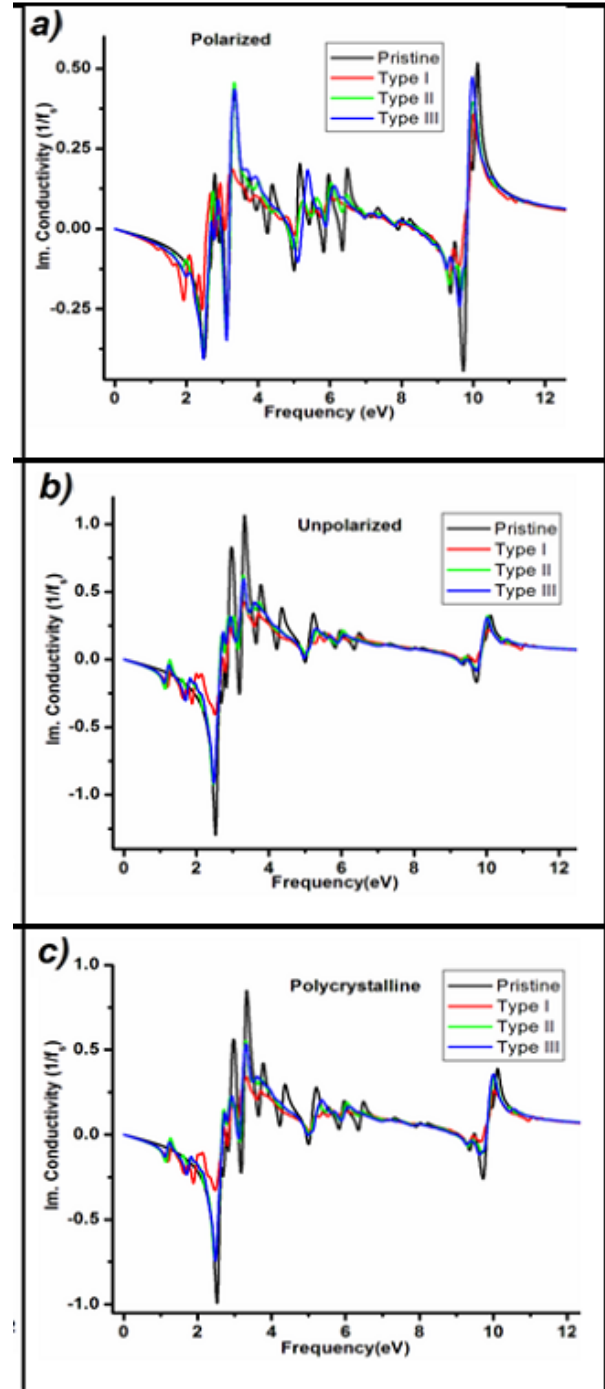

Figure 5. Imaginary part of optical conductivity for the three types of Stone Wales defects upon applying polarized light, unpolarized light and light incident through polycrystalline media.

For the same incident light, introducing type I Stone Wales defects to pristine silicon carbide nanotubes decrease the optical conductivity imaginary part peak intensity, refer to Figure 5 (a, b, c). This discrepancy in the three types could be attributed the orientation of Stone Wales defects and also to the amount of deformation occurred upon introducing Stone Wales defects, refer to Figure 5 (a, b, c). In case of unpolarized incident light and light incident through polycrystalline

media, pristine silicon carbide nanotube has the maximum values of optical conductivity imaginary part compared to other three types of Stone Wales defect. Besides, a clear increase in the pristine nanotube peak intensity compared to polarized incident light. For instance, the peak intensity for pristine silicon carbide nanotubes for polarized incident light is around 0.50 (1/fs). Upon applying unpolarized incident light and light incident through polycrystalline media, the peak intensity increased to 1.00 (1/fs) and 0.85 (1/fs) respectively. Moreover, some intermediate peaks appear at low frequency region like in case of polarized incident light. These peaks start to distinguish from each other when the incident light is unpolarized and incident light through polycrystalline media (5 (a, b, c).

III.5.   Absorption

Figure 6 (a, b, c) represents the absorption spectra for pristine silicon carbide nanotubes and silicon carbide nanotubes with Stone Wales defects for different incident light nature. The absorption spectra show anisotropicity behavior in the optical properties in all silicon carbide nanotubes under study. For example, when the incident light is polarized, the strongest absorption peak located around the frequency 3.25 eV. These maximum peaks belong to type II and type III Stone Wales defects. The absorption peak significantly decreases upon introducing Stone Wales defects, refer to Figure 6 (a, b, c). Besides, the strong absorption peak appears in an ultraviolet region. Upon introducing different orientations of Stone Wales defects, and for the case of polarized light, the absorption peak was significantly increased. This could be ascribed to intrinsic indirect inter-band transitions along the band gap. Furthermore, regardless the incident light nature and in all silicon carbide nanotubes under study, the highest absorption peak occurs in the frequency range of about 3.0 - 3.5 eV. However, upon applying unpolarized and polycrystalline incident light, the behavior is quite different as the maximum absorption spectra observed for pristine silicon carbide nanotube. However, introducing different orientations of Stone Wales defects to the nanotube surface will significantly decrease the absorption spectra. Furthermore, for all incident light nature, type I of Stone Wales defect has the minimum absorption spectra. This could be directly correlated to the orientation of Stone Wales defects. The heptagon and pentagon rings created in the nanotube surface create special kind of deformation with protrude and intrude in the structure, this protrude and intrude significantly depends on the orientation of the heptagon and pentagon rings. Moreover, at low frequency region, no absorption spectra were observed for pristine silicon carbide nanotubes. However, for the same low frequency region, absorption starts to show up as a result of introducing different types of Stone Wales defects. This could be attributed to defects created at the surface of silicon carbide nanotubes, refer to Figure 6 (a, b, c). For all silicon carbide nanotubes, the absorption spectra display a significant anisotropicity in wide range of ultraviolet region. Besides, the observed peaks in the absorption spectra is a

good indication that maximum absorption occurs at that specific energy; however, introducing different orientation of Stone Wales defect to silicon carbide nanotube surface significantly modify the absorption peak.

Figure 6. Absorption spectra for the three types of Stone Wales defects upon the applying: a) polarized light, b) unpolarized light and c) light incident through polycrystalline media.

The modification in the peak frequency and peak intensity could be attributed to semiconducting-metal phase transition as previously reported. Naturally, incident light peaks energies occur around 3.25 eV which attributed to inter πband transitions. Whereas, depending on the incident light nature, some peaks emerge while other peaks disappear,

refer to Figure 6 (a, b, c). For instance, in pristine silicon carbide nanotube when incident light is polarized a clear peak located around 3.0 eV. This peak completely disappear when the incident light is unpolarized and incident light through polycrystalline media. After all,and regardless the incident light nature, introducing different orientations of Stone Wales defects have a direct impact on the absorption spectra.

Figure 7. Reflectivity spectra for the three types of Stone Wales defects upon the applying: a) polarized light, b) unpolarized light and c) light incident through polycrystalline media.

III.6. Reflection spectra

Anti-reflection coatings were not only used for self-cleaning systems but also used to damp the transparent substrates reflectivity. Figure 7 (a, b, c) represents the reflectivity spectra for pristine silicon carbide nanotubes and silicon carbide nanotubes with different orientations of Stone Wales defects. Regardless the incident light nature, introducing different orientations of Stone Wales defects to pristine silicon carbide nanotubes structure have a significant impact to the reflectivity static value, refer to Figure 7 (a, b, c). For unpolarized light and incident light through polycrystalline media, introducing different orientations of Stone Wales defects significantly decreases the reflectivity main peaks. However, when light is polarized, the reflectivity main peak increases upon introducing different orientations of Stone Wales defects. Regardless the incident light natures, the main reflectivity peaks for all silicon carbide nanotubes under study occur around 3.25 eV, refer to Figure 7 (a, b, c). Besides, for all incident light nature, the reflectivity spectra are red shifted upon introducing Stone Wales defects to pristine silicon carbide nanotubes (Figure 7 (a, b, c)). Unlike pristine, type I, type II, and type III behaves differently when light is polarized as the reflectivity is significantly increased.

Furthermore, the static reflectivity value for pristine silicon carbide nanotubes significantly increased upon introducing Stone Wales defects to silicon carbide surface. The above behavior could be ascribed to anisotropicity in reflection which becomes more declared upon introducing different orientations of Stone Wales defects.

III.7. Refractive-index

The refractive index can be calculated using the following equation:

$$n(x) = \sqrt{\frac{(\varepsilon_1^2 + \varepsilon_2^2)^{1/2} + \varepsilon_1^2}{2}} \qquad (3)$$

Whereas, Figure 8 (a, b, c) represents the optical refractive indices for pristine silicon carbide nanotubes and silicon carbide nanotubes with different orientations of Stone Wales defects when light is polarized, unpolarized and light incident through the polycrystalline media. Clearly from Figure 8 (a, b, c) and regardless the incident light nature, the static refractive indices significantly increased upon introducing different orientations of Stone Wales defects to the nanotubes structure. The most pronounced increase occurs upon introducing type I to pristine silicon carbide nanotube. This increase in the static refractive index is a good indication that introducing different orientations of Stone Wales defects to pristine silicon carbide nanotubes has a direct impact in improving the optical properties anisotropicity. Besides, for all incident light nature, introducing different orientations of Stone Wales defects to the nanotubes surface red shifts the refractive indices spectra, refer to Figure 8 (a, b, c).

The loss function spectra for pristine silicon carbide nanotube and silicon carbide nanotube with different orientations of Stone Wales defects were illustrated for polarized incident light, unpolarized incident light and light incident through polycrystalline media, refer to Figure 9 (a, b, c).
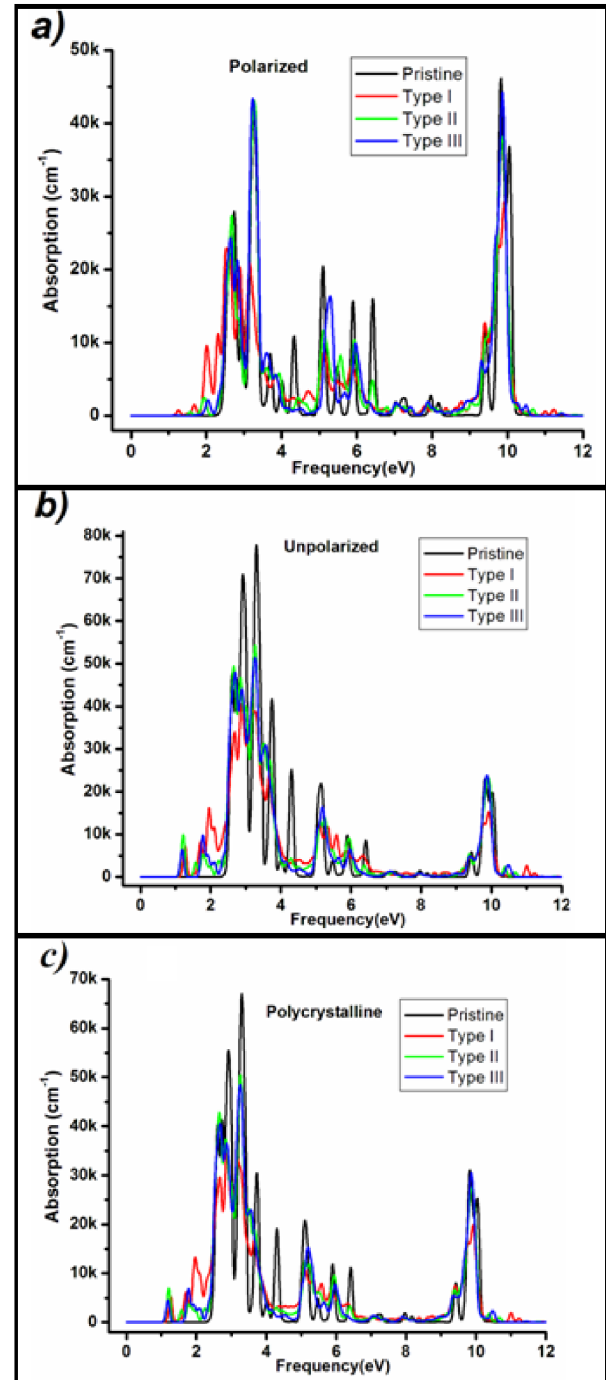

Figure 8. Refractive index for the three types of Stone Wales defects upon applying: a) polarized light, b) unpolarized light and c) light incident through polycrystalline media.

III.8. Loss function spectra

The loss function peak position represents the typical energy of the Plasmon's in the nanotubes under study. It can be calculated using the following equation:

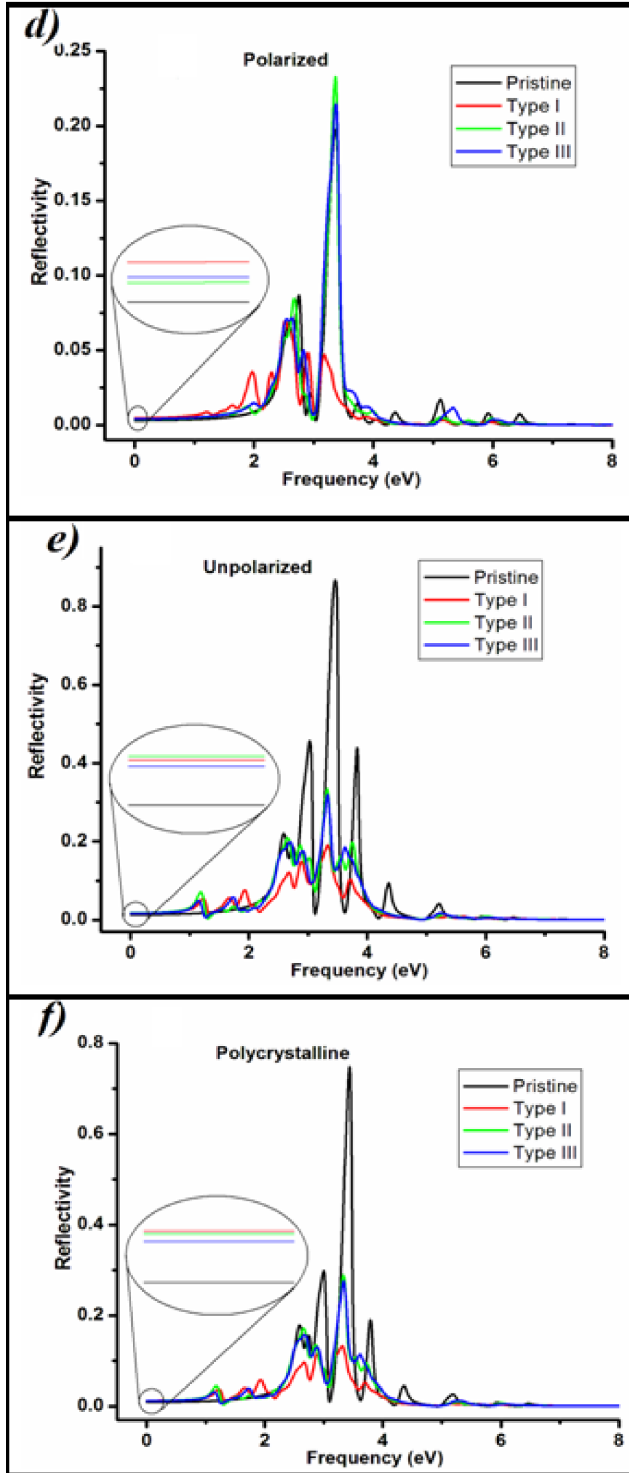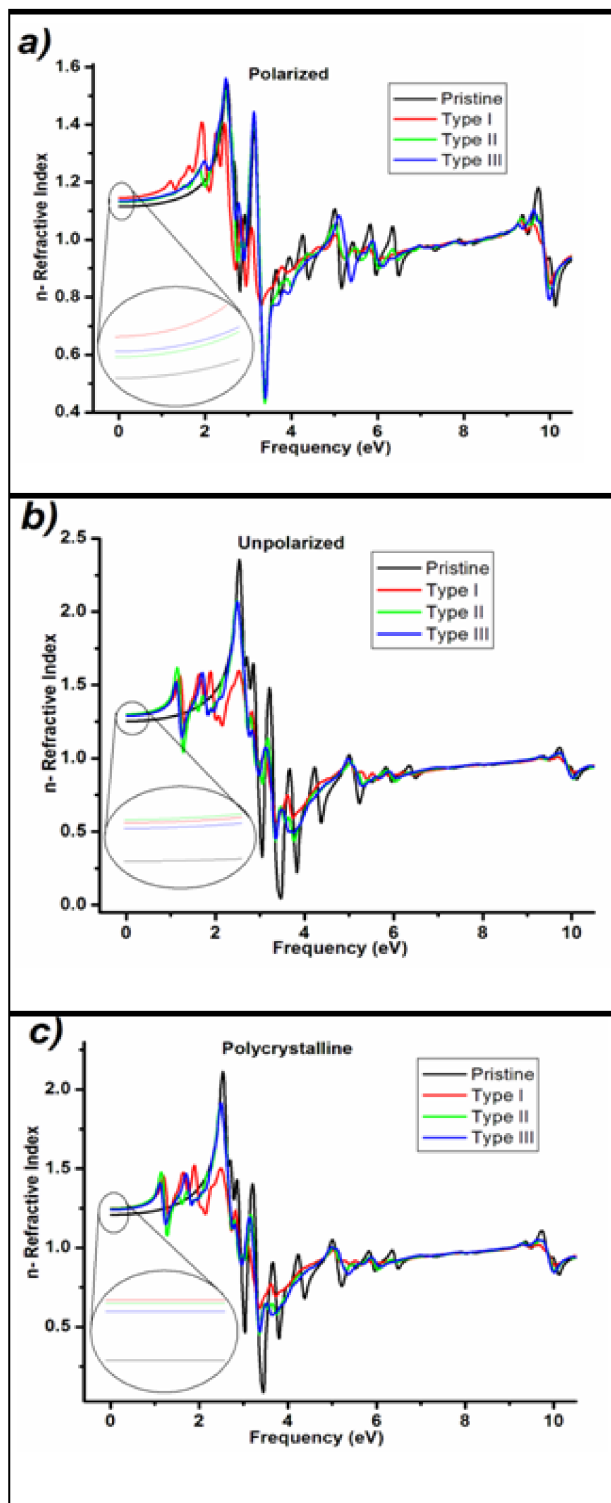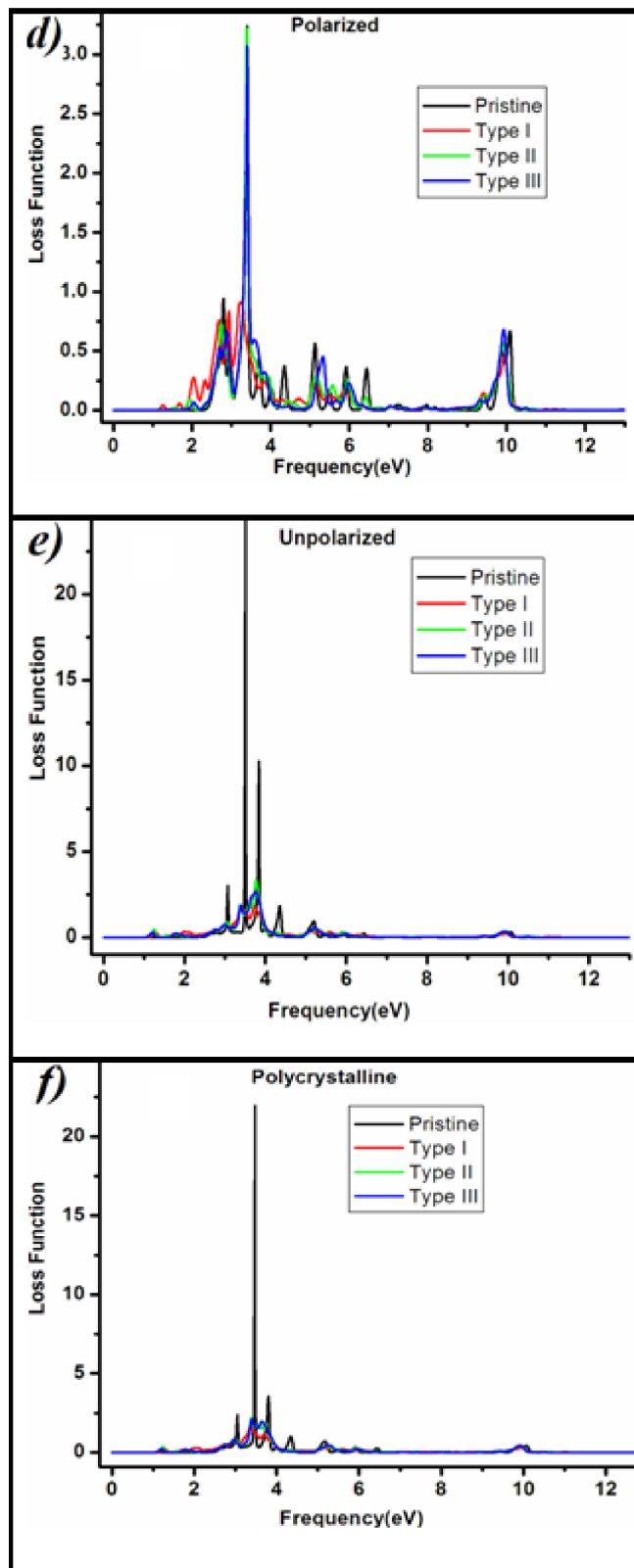$$Im = \left[\frac{1}{\varepsilon(q, \omega)} \right]. \qquad (4)$$

Figure 9. Loss function for the three types of Stone Wales defects upon applying: a) polarized light, b) unpolarized light and c) light incident through polycrystalline media.

When polarized light is used, the loss function magnitude for pristine silicon carbide nanotube is significantly decreased upon introducing three types of Stone Wales defects. This significant reduction in the loss function magnitude might be attributed to decrease in free charge carriers. In addition, the loss function spectra red shifted upon introducing different orientation of Stone Wales defects, refer to Figure 9 (a, b, c). This could be attributed not only to decrease in the Fermi energy but also to decrease in the total number of electrons.

IV. CONCLUSIONS

The optical properties of pristine silicon carbide nanotube and silicon carbide nanotube with different orientations of Stone Wales defects were studied for polarized and unpolarized light as well as light incident through polycrystalline media. With the aid of density functional theory, different optical properties were investigated, including; dielectric function, optical conductivity, absorption, reflection spectra, refractive index, and loss function.We have noticed that introducing Stone Wales defects plays a crucial rule on tuning the optical properties of silicon carbide nanotubes. Besides, introducing different orientations of Stone Wales defects to pristine silicon carbide nanotubes has a direct impact on dielectric function frequency. Therefore, depending on the nature of incident light, the peak intensity of the dielectric spectra real part has shown a clear decrease/increase upon introducing different orientations of Stone Wales defects. The discrepancy in the dielectric function for all silicon carbide nanotubes under investigation is a good indication that these silicon carbide nanotubes are anisotropic in nature. Furthermore, introducing different orientations of Stone Wales defects has direct impact on the dielectric function static value, whereas, this clear discrepancy in the static dielectric function value could attributed to the type of defects created by Stone Wales defects. Whereas, the most obvious anisotropicity occurs for unpolarized incident light and incident light through polycrystalline media cases. In addition, and regardless the nature of the incident lights,the optical conductivity real part is all the way positive. Besides, for polarized incident light, introducing type I Stone Wales defects to pristine silicon carbide nanotubes completely increases the optical conductivity real part. However, for unpolarized incident light and light incident through polycrystalline media, a clear decrease in the optical conductivity values. For all silicon carbide nanotubes, the absorption spectra display a significant anisotropicity in wide range of ultraviolet region.

Furthermore, introducing different orientations of Stone Wales defects to pristine silicon carbide nanotubes have a significant impact on the reflectivity static value. Moreover, the static reflectivity value for pristine silicon carbide nanotubes significantly increased upon introducing different orientations of Stone Wales defects to silicon carbide surface. Regardless the incident light nature, the static refractive indices significantly increased upon introducing different orientations of Stone Wales defects to the nanotubes structure. This increase in the static refractive index is a good indication that introducing different orientations of Stone Wales defects to pristine silicon carbide nanotubes has a direct impact in improving the optical properties anisotropicity. Finally, the loss function magnitude for pristine silicon carbide nanotube is significantly decreased upon introducing Stone Wales defects. In addition, the loss function spectra red shifted upon introducing different orientation of Stone Wales defects.

REFERENCES

[1] J.A. Talla, Advanced Science, Engineering and Medicine **19**, e00378 (2019)..
[2] B. Xu, J. Ouyang, Y. Xu, M.S. Wu, G. Liu, and C.Y. Ouyang, Comput. Mater. Sci. **68**, 367 (2013).
[3] A. Wu, Q. Song, L. Yang, and Q. Hao, Comput. Theor. Chem. **977**, 92(2011).
[4] J. Zhou, M. Zhou, Z. Chen, Z. Zhang, C. Chen, R. Li, X. Gao, and E. Xie, Surf. Coat. Technol. **203**, 3219 (2009).
[5] Phys. Lett. A **383**, 2076 (2019).
[6] J.A. Talla, Computational Condensed Matter **15**, 25 (2018).
[7] H. Dong, Z. Guo, K. Gilmore, C. Du, T. Hou, S.T. Lee and Y. Li, Nanotechnology **26**, 275201 (2015).
[8] R.J. Baierle, P. Piquini, L.P. Neves, and R.H. Miwa, Phys. Rev. B **74**, 155425 (2006).
[9] J.A. Talla, Computational Condensed Matter **19**, e00378 (2019).
[10] S. Behzad, R. Chegel, R. Moradian, and M. Shahrokhi, Superlattices Microstruct. **73**, 185 (2014).
[11] J.A. Talla and A.F. Alsalieby, Chin. J. Phys. **59**, 418 (2019).
[12] J.A. Talla, K.A. Al-Khaza'leh, and A.A. Ghozlan, Adv. Sci., Eng. Med. **11**, 1 (2019).
[13] J.A. Talla and A.A. Ghozlan, J. Adv. Phys. **7**, 33 (2018).
[14] J. Talla, M. Abusini, K. Khazaeleh, R. Omari, M. Serhan, and H. El-Nasser, Mater. Express **7**, 516 (2017).
[15] P. Partovi-Azar and A. Namiranian, J. Phys.: Condens. Matter **24**, 035301 (2012).
[16] K. Adhikari and A.K. Ray, Solid State Commun. **151**, 430 (2011).
[17] S.-J. Wang, C.-L. Zhang, and Z.-G. Wang, Chin. Phys. Lett. **27**, 106101 (2010).
[18] K.M. Alam and A.K. Ray, Phys. Rev. B **77**, 035436 (2008).
[19] Z. Wang, F. Gao, J. Li, X. Zu, and W.J. Weber, J. Appl. Phys. **106**, 084305 (2009).
[20] H. El-Nasser and O. D. Ali, Iran. Polym. J. **19**, 57 (2010).
[21] J.A. Talla, Chem. Phys. **392**, 71 (2012).
[22] T. Jamal A, Phys. B **407**, 966 (2012).
[23] A.A. Ahmad, A.M. Alsaad, B.A. Albiss, M.A. Al-Akhras, H.M. El-Nasser, and I.A. Qattan, Phys. B **470-471**, 21 (2015).
[24] X. Wang and K.M. Liew, The Journal of Physical Chemistry C **116**, 26888(2012).
[25] S. Karatas, H. El-Nasser, A. Al-Ghamdi, and F. Yakuphanolu, Silicon **10**, 651 (2018).
[26] G. Alfieri and T. Kimoto, Nanotechnology **20**, 285703 (2009).
[27] H. El-Nasser, Appl. Phys. Res. **9**, 5 (2017).

[28] R.J. Baierle and R.H. Miwa, Phys. Rev. B **76**, 20 (2007).

[29] M. Yu, C.S. Jayanthi, and S.Y. Wu, Phys. Rev. B **82**, 075407 (2010).

[30] R. Ansari, M. Mirnezhad, and H. Rouhi, Nano **9**, 1450043 (2014).

[31] J.A. Talla, M. Nairat, K. Khazaeleh, A.A. Ghozlan, and S.A. Salman, Computational Condensed Matter **16**, e00311 (2018).

THE ONSET OF ELECTROHYDRODYNAMIC INSTABILITY IN A COUPLE-STRESS NANOFLUID SATURATING A POROUS MEDIUM: BRINKMAN MODEL

EL UMBRAL DE LA INESTABILIDAD ELECTROHIDRODINÁMICA EN UN NANO-FLUÍDO ACOPLADO POR STRESS QUE SATURA UN MEDIO POROSO: MODELO DE BRINKMAN

G. C. Rana[a†], H. Saxena[b] and P. K. Gautam[b]

a) Department of Mathematics, NSCBM Govt. College, Hamirpur-177 005, Himachal Pradesh, India; drgcrana15@gmail.com
b) Department of Mathematics, Career Point University, Kota - 325003, Rajasthan, India

Electrohydrodynamic thermal instability of an elastic-viscous nanofluid saturating a porous in the presence of vertical AC electric field is investigated analytically and numerically. For porous medium, Brinkman model is employed and couple-stress fluid model is used to describe rheological behavior of a nanofluid. On the boundary of fluid layer nanoparticle the flux is assumed to be zero. The problem is solved by applying linear stability analysis based upon perturbation theory and normal mode analysis for isothermal free-free boundaries. The effects of couple-stress parameter, Brinkman-Darcy number, AC electric field, Lewis number, modified diffusivity ratio, nanoparticle Rayleigh number and medium porosity are presented for the case of stationary convection. Under the considered boundary conditions, the oscillatory convection does not exist.

La inestabilidad térmica electro-hidrodinámica de un nanofluido elástico-viscoso que satura un poro en presencia de un campo eléctrico vertical de AC se investiga analíticamente y numéricamente. Para el medio poroso, se emplea el modelo de Brinkman y el modelo de fluido par- estrés se utiliza para describir el comportamiento reológico de un nanofluido. En el límite del flujo de nanopartículas de la capa de fluido el flujo se supone que es cero. El problema se resuelve aplicando un análisis de estabilidad lineal basado en la teoría de perturbaciones y el análisis de modo normal para los límites isotérmicos libre-libre. Los efectos del parámetro de par-estrés, número de Brinkman-Darcy, campo eléctrico en AC, número de Lewis, relación de difusividad modificada, número de Rayleigh de nanopartículas y porosidad media se presentan para el caso de convección estacionaria. Bajo las condiciones de contorno consideradas, la convección oscilatoria no existe.

I. NOMENCLATURE

a wave number

c specific heat

d thickness of the horizontal layer

D_B diffusion coefficient (m²/s)

D_T thermophoretic diffusion coefficient

F Couple-stress parameter

g acceleration due to gravity

$\mathbf{g}$ gravitational acceleration vector

$\mathbf{E}$ root mean square value of the electric field

k Thermal conductivity

L_e Lewis number

N_A modified diffusivity ratio

p pressure (Pa)

$\mathbf{q}$ Darcy velocity vector (m/s)

R_a thermal Rayleigh number

R_n concentration Rayleigh number

R_{ea} AC electric Rayleigh number

t time (s)

T temperature (K)

(u, v, w) Darcy velocity components

(x, y, z) space co-ordinates (m)

Greek symbols

α coefficient of thermal expansion

φ noparticles volume fraction

κ thermal diffusivity

κ_m effective thermal diffusivity of porous medium

μ viscosity of the fluid

μ_c Couple-stress viscosity

ρ density of fluid

ρ_p nanoparticle mass density (kg/m3)

ω growth rate of disturbances

∇_H^2 horizontal Laplacian operator

∇ Laplacian operator

ε medium porosity

K dielectric constant

$\tilde{D}_a$ Brinkman-Darcy number

Superscripts

' non-dimensional variables

'' perturbed quantity

Subscripts

p particle

f fluid

b basic state

0 lower boundary

1 upper boundary

II. INTRODUCCIÓN

The problem of thermal instability in fluid in a porous medium has many practical applications in physical and industrial processes. It has importance in geophysics, soil sciences, thermal insulation of buildings, winding structures for high power density electric machines, food processing and storage, underground disposal of heavy water ground water hydrology and astrophysics.

Thermal instability of non-Newtonian fluids becomes an important field of research for the last few decades. There are many elastico-viscous fluids which cannot be characterized by linear relationship between stress and rate of strain components. One such type of fluid is couple-stress fluid. The theory of couple-stress fluid was first coined by Stokes [1]. Inertia effect in the squeeze film of a couple-stress fluid in biological bearings was studied by Walicki and Walicka [2] and found that the effects of couple-stress and inertia provide an enhancement in the pressure distribution and in the load-carrying capacity. The application of couple-stress fluid is in the study of the mechanism of lubrication of synovial joints, which has become the main objective of scientific research and found that the synovial fluid in human joints behaves like a couple-stress fluid. The stability of a Boussinesq couple-stress horizontal fluid layer, when the boundaries are subjected to time periodic temperature modulation or in the presence of time periodic body force has been studied by Malashetty and Basavaraja [3] using linear stability theory and found that the effect of couple-stress parameter is to advance the onset of convection whereas Bishnoi et al. [4] studied thermal convection in a couple-stress fluid in the presence of horizontal magnetic field with hall currents and found that couple-stress has destabilizing or stabilizing effect on the thermal convection under certain conditions. Rana [5] has studied thermal convection in

couple-stress fluid in hydromagnetics saturating a porous medium and found that couple-stress parameter stabilizes the system.

In the past few years, thermal convection in a nanofluid saturating a porous medium became an important field of research. Nanofluid is a fluid mixture of nano-sized metallic particles immersed in common fluids such as water, ethanol or engine oils are typically used as base fluids in nanofluids and the nanoparticles may be taken as oxide ceramics such as Al_2O_3 or CuO, nitride ceramics such as AlN or SiN and several metals such as Al or Cu. Nanofluid has various applications in automotive industries, energy saving etc. Further, suspensions of nanoparticles are being developed medical applications including cancer therapy. Different authors [6–14] have studied thermal convection in a layer of nanofluid in a porous medium based upon Buongiorno [15] model. They found that nanofluid has enhancing property of heat transfer.

Recently, considerable interest has been evinced in the study of electrohydrodynamic thermal instability in a viscous and viscoelastic fluid. Takashima [16] discussed the effect of uniform rotation on the onset of convective instability in a dielectric fluid under the simultaneous action of AC electric field. It has various applications in different areas such as EHD enhanced thermal transfer, EHD pumps, EHD in microgravity, micromechanic systems, drug delivery, micro-cooling system, nanotechnology, oil reservoir modeling, petroleum industry, building of thermal insulation, biomechanics, engineering [17–25]. Couple-stress fluid under rotation in electrohydrodynamics has been studied by Shivakumara et al. [26] and found that the couple-stress fluid under rotation has destabilizing effect on the system. The instability of a viscoelastic fluid saturating a porous medium in electrohydrodynamics has been studied by Rana et al. [27–29] whereas Chand et al. [30] studied electrothermo convection in a porous medium saturated by a nanofluid and found that AC electric field has destabilizing effect on the system.

The growing number of applications of electrohydrodynamic thermal instability in an elastico-viscous nanofluid fluid in a porous medium which include several engineering and medical fields, such as automotive industries, energy saving and cancer therapy, motivated the current study. In the present paper, we analyze thermal instability problem in a horizontal layer of an elastico-viscous couple-stress nanofluid in a Darcy-Brinkman porous medium in the presence of AC electric field.

III. FORMULATION OF THE PROBLEM AND MATHEMATICAL MODEL

Here we consider an infinite horizontal porous layer of a couple-stress elastico-viscous nanofluid of thickness d saturating a porous medium, bounded by the planes $z = 0$ and $z = d$ under the action of a uniform vertical AC electric field applied across the layer; the lower surface is grounded and the upper surface is kept at an alternating (60 Hz)

potential whose root mean square value is V_1 (see Figure 1). The layer is acted upon by a gravity force $\mathbf{g} = (0, 0, -g)$ aligned in the z direction which is heated from below. The temperature, T, and the volumetric fraction of nanoparticles, φ, at the lower (upper) boundary is assumed to take constant values T_0, and φ_0 (T_1, and φ_0), respectively.
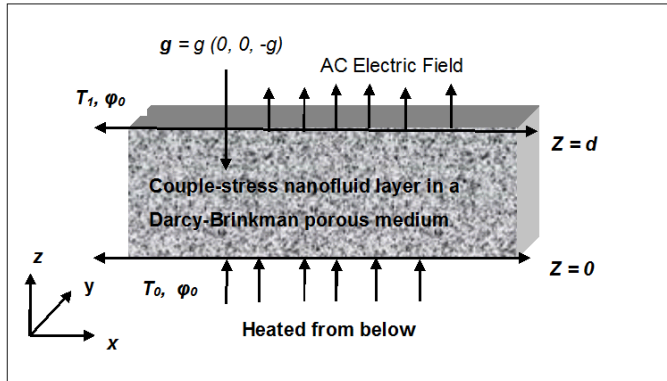
Figure 1. Physical Configuration

III.1. GOVERNING EQUATIONS

Let ρ, μ, μ_c, $\tilde{\mu}$, p, ε, α, φ, ρ_p, k_1, $\mathbf{E}$, K, T and $\mathbf{q}(u, v, w)$, denote, respectively, density, viscosity, couple-stress viscosity, effective viscosity, pressure, medium porosity, coefficient of thermal expansion, volume fraction of nanoparticles, density of nanoparticles, medium permeability, root mean square value of the electric field, temperature and Darcy velocity vector. The equations of mass-balance and momentum-balance for couple-stress nanofluid in the presence of vertical AC electric field saturating a Darcy-Brinkman porous medium by applying oberbeck-Boussines approximation [1,3,4,8,10,11,16] are,

$$\nabla \mathbf{q} = 0, \tag{1}$$

$$0 = -\nabla P - \frac{1}{k_1}(\mu - \mu_c \nabla^2)\mathbf{q} + \tilde{\mu}\nabla^2\mathbf{q} -$$
$$- \frac{1}{2}(\mathbf{E} \cdot \mathbf{E}\nabla K + \mathbf{g}(\varphi\rho_p + \rho_0(1 - \varphi)(1 - \alpha(T - T_0)))), \tag{2}$$

where $P = p - \frac{\rho}{2}\frac{\partial K}{\partial \rho}(\mathbf{E} \cdot \mathbf{E})$ is the modified pressure.

The mass-balance equation for the nanoparticles (Buongiorno [15]) and thermal energy equation for a nanofluid are given by,

$$\frac{\partial \varphi}{\partial t} + \frac{1}{\varepsilon}\mathbf{q} \cdot \nabla^2\varphi = D_B\nabla^2\varphi + \frac{D_T}{T_1}\nabla^2 T, \tag{3}$$

$$(\rho c)_m\left(\frac{\partial T}{\partial t} + \mathbf{q} \cdot \nabla\varphi\right) = k_m\nabla^2 T$$
$$+ \varepsilon(\rho c)_p\left[D_B\nabla\varphi \cdot \nabla T + \frac{D_T}{T_1}\nabla T \cdot \nabla T\right]. \tag{4}$$

where $(\rho c)_m$ is heat capacity of fluid in porous medium, $(\rho c)_p$ is heat capacity of nanoparticles and k_m is thermal conductivity.

The Maxwell equations are:

$$\nabla \times \mathbf{E} = 0, \tag{5}$$

$$\nabla \cdot (K\mathbf{E}) = 0, \tag{6}$$

Let V be root mean square value of electric potential, the electric potential can be expressed as,

$$\mathbf{E} = -\nabla V \tag{7}$$

The dielectric constant is assumed to be linear function of temperature and is of the form,

$$K = K_0[1 - \gamma(T - T_0)], \tag{8}$$

where γ, is the thermal coefficient of expansion of dielectric constant and is assumed to be small.

We assume that the temperature is constant and nanoparticles flux is zero on the boundaries. The appropriate boundary conditions [3,11] are

$$w = 0, \ T = T_0 \ D_B\frac{\partial \varphi}{\partial z} + \frac{D_T}{T_1}\frac{\partial T}{\partial z} = 0 \text{ at } z = 0 \tag{9a}$$

and

$$w = 0, \ T = T_1 \ D_B\frac{\partial \varphi}{\partial z} + \frac{D_T}{T_1}\frac{\partial T}{\partial z} = 0 \text{ at } z = d. \tag{9b}$$

Introducing non-dimensional variables as

$$(x', y', z') = \left(\frac{x, y, z}{d}\right), \ (u', v', w') = \left(\frac{u, v, w}{\kappa_d}\right) \ t' = \frac{t\kappa_m}{\sigma d^2},$$

$$P' = \frac{Pk_1}{\mu\kappa_m}, \ \varphi' = \frac{\varphi - \varphi_0}{\varphi_0}, \ T' = \frac{T}{\Delta T}, \ K' = \frac{K}{\gamma E_0\Delta Td},$$

where $\kappa_m = \frac{k_m}{(\rho c_p)_f}$ is thermal diffusivity of the fluid and $\sigma = \frac{(\rho c_p)_m}{(\rho c_p)_f}$ is the thermal capacity ratio. Eliminating the modified pressure from the momentum-balance equation 8 by operating twice curl and retaining the vertical component, we obtain the following equations in non-dimensional form (after dropping the dashes (') for convenience) as

$$\nabla \mathbf{q} = 0, \tag{10}$$

$$0 = -(1 - \eta\nabla^2 - \tilde{\mu}\nabla^2)\nabla^2 w + R_a\nabla_H^2 T$$
$$- Rn\nabla_H^2\varphi + R_{ea}\nabla_H^2\left(T - \frac{\partial K}{\partial z}\right), \tag{11}$$

$$\frac{1}{\sigma}\frac{\partial \varphi}{\partial t} + \frac{1}{\varepsilon}\mathbf{q}\nabla\varphi = \frac{1}{Le}\nabla^2 T, \tag{12}$$

$$\frac{\partial \varphi}{\partial t} + \mathbf{q} \cdot \nabla T = \nabla^2 T + \frac{N_a}{Le}\nabla\varphi\nabla T + \frac{N_A N_B}{Le}\nabla T \cdot \nabla T, \tag{13}$$

$$\nabla^2 V = \frac{\partial T}{\partial z}. \tag{14}$$

Here $Le = \frac{\kappa_m}{D_B}$ is the thermal Lewis number,

$\eta = \frac{\mu_c}{\mu d^2}$ is the couple-stress parameter,

$R_a = \frac{\rho g \alpha d k_1 (T_0 - T_1)}{\mu \kappa_m}$ is the thermal Rayleigh number,

$R_n = \frac{(\rho_g - \rho)\varphi_0 g k_1 d}{\mu \kappa_m}$ is the nanoparticle Rayleigh number,

$N_A = \frac{D_T (T_0 - T_1)}{D_B T_1 \varphi_0}$ is the modified diffusivity ratio,

$N_B = \frac{\varepsilon(\rho c)_p \varphi_0}{(\rho c)_f}$ is the modified particle-density ratio,

$R_{ea} = \frac{\gamma^2 K E_0^2 d^2 (\Delta T^2)}{\mu \kappa_m}$ is the AC electric Rayleigh number,

$\tilde{D}a = \frac{\tilde{\mu} k_1}{\mu d^2}$, is the Brinkman-Darcy number and ∇_H^2 is the two-dimensional Laplace operator on the horizontal plane, that is $\nabla_H^2 = \frac{\partial}{\partial x^2} + \frac{\partial}{\partial y^2}$.

The dimensionless boundary conditions are

$$w = \frac{\partial^2 w}{\partial z^2} = \frac{\partial K}{\partial z} = 0, \; T = 1, \; \frac{\partial \varphi}{\partial z} + N_A \frac{\partial T}{\partial z} = 0 \text{ at } z = 0, \quad (15a)$$

and

$$w = \frac{\partial^2 w}{\partial z^2} = \frac{\partial K}{\partial z} = 0, \; T = 0, \; \frac{\partial \varphi}{\partial z} + N_A \frac{\partial T}{\partial z} = 0 \text{ at } z = 1, \quad (15b)$$

III.2. BASIC SOLUTIONS

We assume that the basic state is quiescent [3, 8–11] and is given by

$$u = v = w = 0, \; p = p(z), \; K = K_b(z), \; T = T_b(z), \; \varphi = \varphi_b(z),$$
$$E = E_b(z), \; \psi = \psi_b(z). \quad (16)$$

$$T_b = T_0 - \frac{\Delta T}{dz}, \; \varphi_b = \varphi_0 + \left(\frac{D_T \Delta T}{D_b T_1 d}\right) z,$$

$$K_b = K_0 \left(1 + \frac{\gamma \Delta T}{d} z\right)\hat{k}, \; E_b = \frac{E_0}{1 + \frac{\gamma \Delta T}{d} z}\hat{k}.$$

Also, we have

$$v_b = -\frac{E_0 d}{\gamma \Delta T} \log\left(1 + \frac{\gamma \Delta T}{d} z\right)\hat{k},$$

where $E_0 = -\frac{V_1 \gamma \Delta T}{d \log(1 + \gamma DeltaT)}$ is the root mean square value of the electric field at $z = 0$.

The basic state defined in 16 is substituted into equations 12 and 13, these equations reduce to

$$\frac{d^2 \varphi_b(z)}{dz^2} + N_A \frac{d^2 T_b(z)}{dz^2} = 0, \quad (17)$$

$$\frac{d^2 \varphi_b(z)}{dz^2} + \frac{N_b}{Le} \frac{d\varphi_b(z)}{dz} \frac{dT_b(z)}{dz} + \frac{N_A N_B}{Le}\left(\frac{dT_b(z)}{dz}\right)^2 = 0, \quad (18)$$

Using boundary conditions 15b in equations 17 and 18, on integration equation 17 gives

$$\frac{d\varphi_b(z)}{dz} + N_A \frac{dT_b(z)}{dz} = 0. \quad (19)$$

Using equation 19 in equation 18, we obtain

$$\frac{d^2 T_b(z)}{dz^2} = 0. \quad (20)$$

Applying the boundary conditions 15b, the solution of equation 20 is given by

$$T_b(z) = 1 - z. \quad (21)$$

Integrating equation 19 by applying the boundary conditions 15b, we get

$$\varphi_b(z) = \varphi_0 + N_A z. \quad (22)$$

These results are identical with the results obtained by Sheu [10] and Nield and Kuznetsov [9–11].

III.3. PERTURBATION SOLUTIONS

To study the stability of the system, we superimposed infinitesimal perturbations on the basic state, so that

$$\mathbf{q}(w, v, w) = q''(u, v, w), \; T = T_b + T'', \; p = p_b + p'', \quad (9)$$
$$E = E_b + E'', \; V = V_b + V''. \quad (23)$$

Introducing equation 9 along with equations 21 and 22 into equations 10 – 14, linearizing the resulting equations by neglecting nonlinear terms that are product of prime quantities and dropping the primes ('') for convenience, we obtain the following equations

$$\nabla \cdot \mathbf{q} = 0, \quad (24)$$

$$0 = -\nabla P - \frac{1}{k_1}(\mu - \mu_c \nabla^2) + \tilde{\mu}\nabla^2)\nabla^2 w + Ra\nabla_H^2 T$$
$$- R\nabla_H^2 \varphi + R_{ea}\nabla_H^2\left(T - \frac{\partial K}{\partial z}\right), \quad (25)$$

$$\frac{1}{\sigma}\frac{\partial \varphi}{\partial t} + \frac{1}{\varepsilon}w = \frac{1}{Le}\nabla^2\varphi + \frac{N_A}{Le}\nabla^2 T, \quad (26)$$

$$\frac{\partial T}{\partial t} - w = \nabla^2 T + \frac{N_B}{Le}\left(\frac{\partial T}{\partial z} - \frac{\partial \varphi}{\partial z}\right) - \frac{2N_A N_B}{Le}\frac{\partial T}{\partial z}, \quad (27)$$

$$\nabla^2 V = \frac{\partial T}{\partial z}, \quad (28)$$

Boundary conditions for equations 24-28 are

$$w = \frac{\partial^2 w}{\partial z^2} = \frac{\partial K}{\partial z} = 0, \; T = 0, \; \frac{\partial \varphi}{\partial z} + N_A \frac{\partial T}{\partial z} = 0 \quad (29)$$

at $z = 0$ and at $z = 1$.

IV. NORMAL MODE ANALYSIS

We express the disturbances into normal modes of the form

$$[w, T, \varphi, V] = [W(z), \Theta(z), \Phi(z), \Psi(z)]exp[i(lx + my + \omega t)] \quad (30)$$

where l, m are the wave numbers in the x and y direction, respectively, and ω is the growth rate of the disturbances.

Substituting equation 30 into equations 24-30, we obtain the following eigenvalue problem

$$(1 - \eta(D^2 - a^2) - \tilde{D}a(D^2 - a^2))(D^2 - a^2)W+$$
$$+ a^2 Ra\Theta - a^2 Rn\Phi + a^2 R_{ea}(\Theta - D\Psi) = 0 \quad (31)$$

$$W + \left(D^2 + \frac{N_A}{Le}D - \frac{2N_A N_B}{Le}D - d^2 - \omega\right)\Theta - \frac{N_B}{Le}D\Phi = 0 \quad (32)$$

$$\frac{1}{\varepsilon}W - \frac{N_A}{Le}(D^2 - a^2)\Theta - \left(\frac{1}{Le}(D^2 - a^2) - \frac{\omega}{\sigma}\right) = 0, \quad (33)$$

$$(D^2 - a^2)\Psi = D\Theta, \quad (34)$$

where $D = d/dz$ and $a^2 = l^2 + m^2$ is the dimensionless resultant wave number.

The boundary conditions of the problem in view of normal mode analysis are

$$W = 0, \ D^2 W = 0, \ \Theta = 0, \ D\Psi = 0, \ D\Phi + N_A D\Theta = 0 \quad (35)$$

at $z = 0$ and $z = 1$.

V. LINEAR STABILITY ANALYSIS AND DISPERSION RELATION

The case of two free boundaries, though a little artificial is the most appropriate for stellar atmospheres. Using the boundary conditions 35, the proper solution of equations 31–34 is given by,

$$W = W_0 \sin \pi z, \quad (36a)$$

$$\Theta = \Theta_0 \sin \pi z, \quad (36b)$$

$$\Phi = \Phi_0 \cos \pi z, \quad (36c)$$

$$\Psi = \Psi_0 \cos \pi z, \quad (36d)$$

where W_0, Θ_0, Φ_0 and Ψ_0 are constants.

Substituting equation 36a into the eigen-value problem given by equations 31–34 we obtain,

$$\begin{bmatrix} (\pi^2 + a^2)(1 + \eta(\pi^2 + a^2)) + \tilde{D}a(\pi^2 + a^2) & -a^2(Ra + R_{ea}) & -a^2 N_A Rn & -a\pi R_{ea} \\ 1 & -(\pi^2 + a^2 + \omega) & 0 & 0 \\ \frac{1}{\varepsilon} & \frac{1}{Le}(\pi^2 + a^2) & -\left(\frac{1}{Le}(\pi^2 + a^2) + \frac{\omega}{\sigma}\right) & 0 \\ 0 & -\pi & 0 & -(\pi^2 + a^2) \end{bmatrix} \begin{bmatrix} W \\ \Theta \\ \Phi \\ \Psi \end{bmatrix} = \begin{bmatrix} 0 \\ 0 \\ 0 \\ 0 \end{bmatrix}. \quad (37)$$

The above system of matrix equations has non-trivial solution if

$$\begin{vmatrix} (\pi^2 + a^2)(1 + \eta(\pi^2 + a^2)) + \tilde{D}a(\pi^2 + a^2) & -a^2(Ra + R_{ea}) & -a^2 N_A Rn & -a\pi R_{ea} \\ 1 & -(\pi^2 + a^2 + \omega) & 0 & 0 \\ \frac{1}{\varepsilon} & \frac{1}{Le}(\pi^2 + a^2) & -\left(\frac{1}{Le}(\pi^2 + a^2) + \frac{\omega}{\sigma}\right) & 0 \\ 0 & -\pi & 0 & -(\pi^2 + a^2) \end{vmatrix} = 0. \quad (38)$$

which gives an expression for Rayleigh number Ra as

$$Ra = \frac{(1 + \eta(\pi^2 + a^2) + \tilde{D}a(\pi^2 + a^2))(\pi^2 + a^2)(\pi^2 + a^2 + \omega^2)}{a^2} - \frac{a^2}{\pi^2 + a^2}R_{ea} - \frac{\varepsilon N_A(\pi^2 + a^2) + Le(\pi^2 + a^2 + \omega^2)}{(\pi^2 + a^2)\sigma + \omega Le}\frac{\sigma}{\varepsilon}Rn \quad (39)$$

Equation 39 is the required dispersion relation accounting for the effect of Lewis number, couple-stress parameter, AC electric Rayleigh number, nanoparticle Rayleigh number, modified diffusivity ratio and medium porosity on thermal instability in a layer of couple-stress elastico-viscous nanofluid saturating a porous medium under the influence of vertical AC electric field.

STATIONARY CONVECTION

The growth rate ω is, in general, a complex quantity such that $\omega = \omega_r + i\omega_i$. The system with $\omega_r < 0$ is always stable, for $\omega_r > 0$, it will become unstable (neutral stability $\omega_r = 0$).

For the case of steady state (i. e., principle of exchange of stability), we put $\omega = 0$ in equation 39, we obtain

$$Ra = \frac{(1 + \eta(\pi^2 + a^2) + \tilde{D}a(\pi^2 + a^2))(\pi^2 + a^2)^2}{a^2}$$
$$- \frac{a^2}{\pi^2 + a^2}R_{ea} - \left(N_A + \frac{Le}{\varepsilon}\right)Rn \quad (40)$$

Equation 40 expresses the Rayleigh number as a function of the dimensionless resultant wave number a, the couple-stress parameters η, the Brinkman-Darcy number the AC electric Rayleigh number R_{ea}, the medium porosity ε,

the nanoparticle Rayleigh number Rn, the Lewis number Le, modified-diffusivity ratio N_A. Equation 40 is identical to that obtained by Kuznetsov and Nield [8], and Rana et al. [27–29] in the absence of the couple-stress parameters η, the Brinkman-Darcy number and the AC electric Rayleigh number R_{ea}. Since equation 51 does not contain the particle increment parameter N_B but contains the diffusivity ratio parameter N_A in corporation with the nanoparticle Rayleigh number Rn. This shows that the nanofluid cross-diffusion terms approach to be dominated by the regular cross-diffusion term.

In the absence of Brinkman-Darcy number $\tilde{D}a$, equation 40 becomes,

$$Ra = \frac{(1 + \eta(\pi^2 + a^2))(\pi^2 + a^2)^2}{a^2} - \frac{a^2}{\pi^2 + a^2}R_{ea} - \left(N_A + \frac{Le}{\varepsilon}\right)Rn \tag{41}$$

In the absence of AC electric field R_{ea}, equation 41 reduces to

$$Ra = \frac{(1 + \eta(\pi^2 + a^2) + \tilde{D}a(\pi^2 + a^2))(\pi^2 + a^2)^2}{a^2} - \left(N_A + \frac{Le}{\varepsilon}\right)Rn, \tag{42}$$

which is identical with the result derived by Kuznetsov and Nield [8], Rana et al. [27–29].

In the absence of couple-stress parameter, equation (42) reduces to

$$Ra = \frac{(\pi^2 + a^2)^2}{a^2} - \left(N_A + \frac{Le}{\varepsilon}\right)Rn, \tag{43}$$

which is identical with result derived by Kuznetsov and Nield [8].

Thus, the presence of nanoparticles and vertical AC electric field lower the value of the critical Rayleigh number by usually by substantial amount. Also parameter N_B does not appear in the Eq. 40, thus instability is purely phenomena due to buoyancy coupled with conservation of nanoparticles. Thus average contribution of nanoparticles flux in the thermal energy equation is zero with one-term Galerkin approximation.

VI.   OSCILLATORY CONVECTION

For the marginally oscillatory state, we put $\omega = i\omega$ in equation 39, we obtain

$$Ra = \Delta_1 + i\omega\Delta_2, \tag{44}$$

where

$$\Delta_1 = \frac{(1 + \eta(\pi^2 + a^2) + \tilde{D}a(\pi^2 + a^2))(\pi^2 + a^2)^2}{a^2}$$
$$- \frac{a^2}{\pi^2 + a^2}R_{ea} - \frac{(\pi^2 + a^2)^2\left(N_A + \frac{Le}{\varepsilon}\right) + \frac{\omega^2}{\sigma\varepsilon}}{(\pi^2 + a^2)^2 + \left(\frac{\omega Le}{\sigma}\right)^2}Rn, \tag{45}$$

and

$$\Delta_2 = \frac{(1 + \eta(\pi^2 + a^2) + \tilde{D}a(\pi^2 + a^2))(\pi^2 + a^2)^2}{a^2}$$
$$+ \frac{(\pi^2 + a^2)\left(\frac{Le}{\sigma}\left(N_A + \frac{Le}{\varepsilon}\right) - \frac{Le}{\varepsilon}\right) + \frac{\omega^2}{\sigma\varepsilon}}{(\pi^2 + a^2)^2 + \left(\frac{\omega Le}{\sigma}\right)^2}Rn, \tag{46}$$

Since Ra is a physical quantity, so it must be real. Thus, it follows from the Eq. 44 that either $\omega = 0$(exchange of stability, steady state) or $\Delta 2 = 0$ ($\omega \neq 0$ overstability or oscillatory onset) which gives an expression for the frequency of oscillations in the form ω^2. But $\omega^2 < 0$ when $10^2 \leq Le \leq 10^4$ (Lewis number), $-1 \leq Rn \leq 10$ (nanoparticles Rayleigh number), $0.1 \leq \varepsilon 1$ (porosity parameter) (Rana et al. [27–29]) and $10 \leq R_{ea} \leq 10^4$ (AC electric Rayleigh number) (Shivakumara et al. [26]). Hence, oscillatory convection does not exist under the considered boundary conditions.

VII.   RESULTS AND DISCUSSIONS

To study the effect of couple-stress parameter, AC electric Rayleigh number, Lewis number, nanoparticle Rayleigh number, modified diffusivity ration nanoparticle Rayleigh number, medium porosity and Brinkman-Darcy number, we examine the behavior of $\frac{\partial Ra}{\partial \eta}$, $\frac{\partial Ra}{\partial R_{ea}}$, $\frac{\partial Ra}{\partial Le}$, $\frac{\partial Ra}{\partial N_A}$, $\frac{\partial Ra}{\partial N_A}$, $\frac{\partial Ra}{\partial Rn}$, $\frac{\partial Ra}{\partial \varepsilon}$ and $\frac{\partial Ra}{\partial \tilde{D}a}$ analytically.

From equation (40), we obtain

$$\frac{\partial Ra}{\partial \eta} = \frac{(\pi^2 + a^2)^3}{a^2}, \tag{47}$$

$$\frac{\partial Ra}{\partial R_{ea}} = -\frac{a^2}{\pi^2 + a^2}, \tag{48}$$

$$\frac{\partial Ra}{\partial Le} = -\frac{Rn}{\varepsilon}, \tag{49}$$

$$\frac{\partial Ra}{\partial N_A} = -Rn, \tag{50}$$

$$\frac{\partial Ra}{\partial Rn} = -N_A + \frac{Le}{\varepsilon}, \tag{51}$$

$$\frac{\partial Ra}{\partial \varepsilon} = \frac{LeRn}{\varepsilon^2}, \tag{52}$$

$$\frac{\partial Ra}{\partial \tilde{D}a} = \frac{(\pi^2 + a^2)^3}{a^2}, \tag{53}$$

From equations 47, 52 and 53, we see that the partial derivative of Rayleigh number Ra with respect to couple-stress parameter η, medium porosity ε and Brinkman-Darcy number $\tilde{D}a$ is positive implying implying thereby couple-stress, medium porosity and Brinkman-Darcy number stimulate the stationary convection. Thus, couple-stress parameter, medium porosity and Brinkman-Darcy number has stabilizing effect on the

which is in an agreement with the result derived by Shivakumara [25], Rana et al. [26–28] and Chand et al. [29].
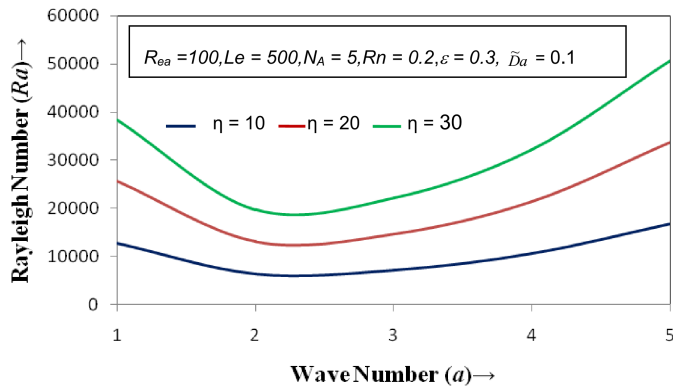
Figure 2. The variations of thermal Rayleigh number Ra with the wave number a for different values of the couple-stress parameter $\eta = 10$, $\eta = 20$ and $\eta = 30$.

The right hand sides of equations 48-51 are negative implying thereby the AC electric Rayleigh number R_{ea}, Lewis number Le, modified diffusivity ratio NA and nanoparticle Rayleigh number Rn inhibit the stationary convection. Thus, the AC electric Rayleigh number, Lewis number, modified diffusivity ratio and nanoparticle Rayleigh number have destabilizing effects on the system which is in an agreement with the results derived by Sheu [10], Nield and Kuznetsov [16], Takashima [22] and Shivakumara [25], Rana et al. [26–28] and Chand et al. [29].
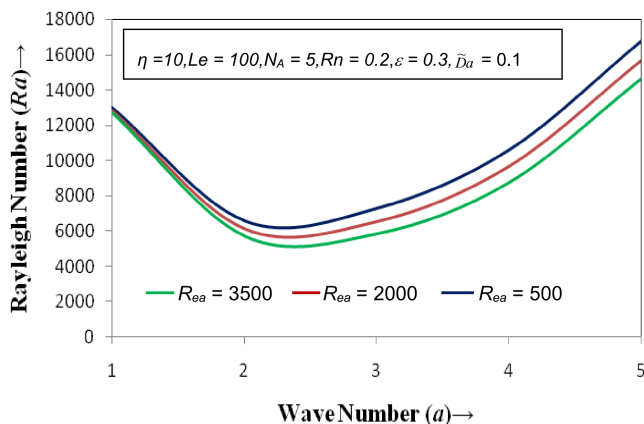
Figure 3. The variations of thermal Rayleigh number Ra with the wave number a for different values of the AC electric Rayleigh number $R_{ea} = 500$, $R_{ea} = 2000$ and $R_{ea} = 3500$.

The dispersion relation 40 is also analyzed numerically. Graphs have been plotted by giving some numerical values to the parameters to depict the stability characteristics, e. g., Lewis number ($10^2 \leq Le \leq 10^4$), nanoparticles Rayleigh number ($-1 \leq Rn \leq 10$), porosity parameter ($0.1 \leq \varepsilon 1$) (Rana et al. [27–29]) and AC electric Rayleigh number ($10 \leq Re \leq 10^4$) (Shivakumara et al. [26]). Stability curves for couple-stress parameter η, AC electric Rayleigh number R_{ea}, Lewis number Le, nanoparticles Rayleigh number Rn, modified diffusivity ratio N_A and porosity parameter ε are shown in figures 2-8.

The variations of thermal Rayleigh number Ra with the wave number a for three different values of couple-stress

parameter, namely, $\eta = 10, 20, 30$ is plotted in Fig. 2 and it is observed that the thermal Rayleigh number increases with the increase in couple-stress parameter which shows that couple-stress parameter stabilizes the system.
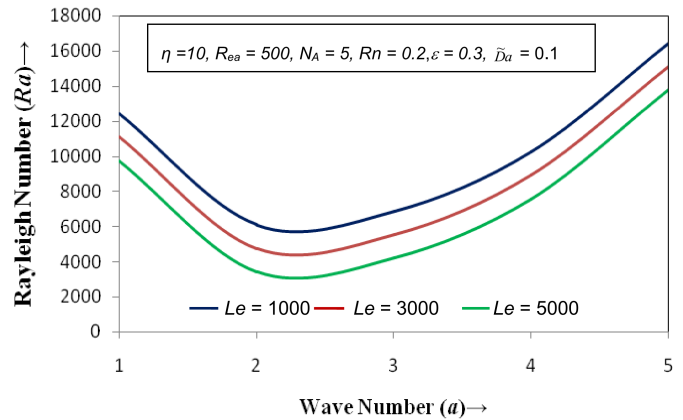
Figure 4. The variations of thermal Rayleigh number Ra with the wave number a for different values of the Lewis number $Le = 500$, $Le = 2000$, $Le = 3500$.

In Fig. 3, the variations of thermal Rayleigh number Ra with the wave number a for three different values the AC electric Rayleigh number, namely, $R_{ea} = 500, 2000$ and 3500 is plotted and it is observed that the thermal Rayleigh number decreases with the increase in AC electric Rayleigh number implying there by AC electric Rayleigh number destabilizes the system.

In Fig. 4, the variations of thermal Rayleigh number Ra with the wave number a for three different values of the Lewis number, namely, $Le = 1000, 3000$ and 5000 which shows that thermal Rayleigh number increases with the increase in Lewis number. Thus, Lewis number has stabilizing effect on the system.
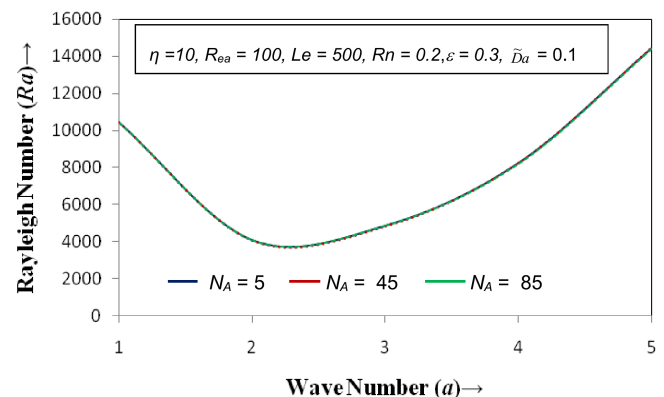
Figure 5. The variations of thermal Rayleigh number Ra with the wave number a for different values of the modified diffusivity ratio $N_A = 5$, $N_A = 45$ and $N_A = 85$.

The variations of thermal Rayleigh number Ra with the wave number a for three different values of the modified diffusivity ratio, namely, $NA = 5, 45, 85$ is plotted in Fig. 5 and it is found that thermal Rayleigh number decreases very slightly with the increase in modified diffusivity ratio implying thereby modified diffusivity ratio has slightly destabilizing effect on

the system.
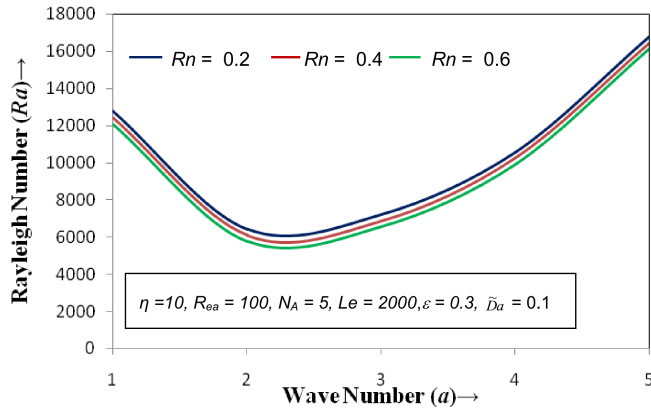
Figure 6. The variations of thermal Rayleigh number Ra with the wave number a for different values of the nanoparticle Rayleigh number $Rn = -0.2$, $Rn = 0.4$ and $Rn = 0.6$.
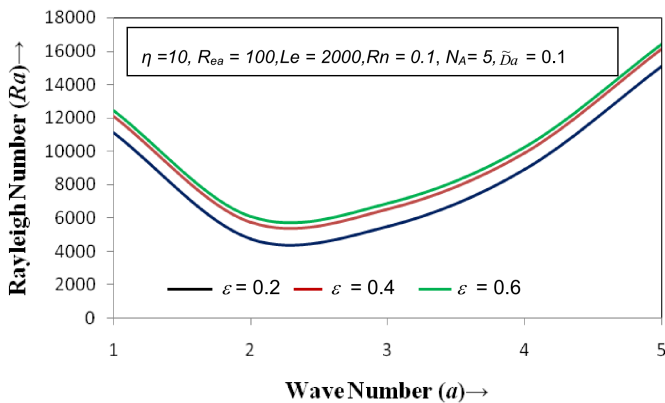
Figure 7. The variations of thermal Rayleigh number Ra with the wave number a for different values of the medium porosity $\varepsilon = 0.2$, $\varepsilon = 0.4$ and $\varepsilon = 0.6$.
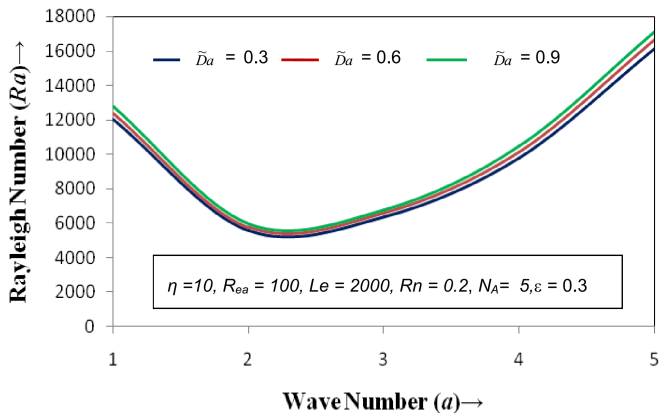
Figure 8. The variations of thermal Rayleigh number Ra with the wave number a for different values of the Brinkman-Darcy number $\tilde{D}a = 0.3$, $\tilde{D}a = 0.6$ and $\tilde{D}a = 0.9$.

In Fig. 6, the variations of thermal Rayleigh number Ra with the wave number a for three different values of the nanoparticle Rayleigh number, namely $Rn = 0.2$, 0.4, 0.6 which shows that thermal Rayleigh number increases with the decrease in nanoparticle Rayleigh number. Thus, nanoparticle Rayleigh number has destabilizing effect on the system. The variations of thermal Rayleigh number

Ra with the wave number a for three different values of medium porosity, namely $\varepsilon = 0.2$, 0.4 and 0.6 is plotted in Fig. 7 and it is found that thermal Rayleigh number increases with the increase in medium porosity implying thereby medium porosity has stabilizing effect on the onset of stationary convection in a layer of couple-stress elastico-viscous nanofluid saturating a porous medium. In Fig. 8, the variations of thermal Rayleigh number Ra with the wave number a for three different values of the Brinkman-Darcy number $\tilde{D}a = 0.3$, $\tilde{D}a = 0.6$ and $\tilde{D}a = 0.9$ which shows that thermal Rayleigh number increases with the increase in nanoparticle Rayleigh number. Thus, Brinkman-Darcy number has stabilizing effect on the system.

VIII. CONCLUSIONS

The onset of electrohydrodynamic thermal instability in an elastico-viscous couple-stress nanofluid saturating a Darcy-Brinkman porous medium has been investigated analytically and numerically for free-free boundaries by applying a linear stability analysis. Dispersion relation for Rayleigh number accounting for the effect of Lewis number, couple-stress parameter, AC electric Rayleigh number, nanoparticle Rayleigh number, modified diffusivity ratio, medium porosity and Brinkman-Darcy number has been derived. Analytical expression for the occurrence of steady and oscillatory convection has been obtained for isothermal free-free boundaries. For the case of stationary convection, it is found that couple-stress parameter, médium porosity and Brinkman-Darcy number have stabilizing effect whereas AC electric Raleigh number, Lewis number and modified diffusivity ratio and nanoparticle Rayleigh number have destabilizing effect on the system. Oscillatory convection has been ruled out under the considered boundary conditions (see, Nield and Kuznetsov [11]).

ACKNOWLEDGEMENTS

BIBLIOGRAPHY

[1] V.K. Stokes, Phys. Fluids. **9**, 1709 (1966).
[2] E. Walicki and A. Walicka, Appl. Mech. Eng. **4**, 363 (1999).
[3] M.S. Malashetty and D. Basavaraja, Int. J. Trans. Phenom. **7**, 31 (2005).
[4] J. Vikrant., Kumar, V., Applications and Applied Mathematics **8**, 161 (2013).
[5] G.C. Rana, Bull. Polish Academy of Sc.-Tech. Sc. **62**, 357 (2014).
[6] S. Choi, Enhancing thermal conductivity of fluids with nanoparticles. In: Siginer D.A., Wang, H.P. (eds.) Developments and Applications of Non-Newtonian Flows, ASME FED-Vol. 231/MD-66, 1995 99.

[7] D.Y. Tzou, Int. J. of Heat and Mass Transfer **51**, 2967 (2008).

[8] A.V. Kuznetsov and D.A. Nield, Transp. Porous Medium **81**, 409 (2009).

[9] D.A. Nield and A.V. Kuznetsov, Int. J. Heat Mass Transfer **52**, 5796, (2009).

[10] L.J. Sheu, Transp. Porous Med. **88**, 461 (2011).

[11] D.A. Nield and A.V. Kuznetsov, Int. J. Heat Mass Transf., **68**, 211 (2014).

[12] D. Yadav and M.C. Kim, J. Porous Media, **18**, 369 (2015).

[13] G.C. Rana, R. Chand and D. Yadav, J. Theor. Appl. Mech., Sofia **47**, 69 (2017)

[14] R. Chand and G.C. Rana, Structural Integrity and Life **17**, 113 (2017).

[15] J. Buongiorno, ASME Journal of Heat Transfer **128**, 240 (2006).

[16] M. Takashima, Canadian J. Phys. **54**, 342 (1976).

[17] M. Takashima and A.K. Ghosh, J. Phys. Soc. Jpn. **47**, 1717 (1979).

[18] M. Takashima and H. Hamabata, J. Phys. Soc. Jpn. **53**, 1728 (1984).

[19] L.D. Landau, Electrodynamics of Continuous Media, (New York: Oxford, 1960).

[20] P.H. Roberts, Quarterly J. Mech. Appl. Math. **22**, 211 (1969).

[21] A. Castellanos, Electrohydrodynmics, New York: Springer-Verlag Wien New York, (1998).

[22] J.R. Melcher and G.I. Taylor, Annu. Rev. Fluid Mech. **1**, 11 (1969).

[23] T.B. Jones, Electrohydrodynamically enhanced heat transfer in liquids-A review, In T.F. Irvine Jr. & J.P. Hartnett (Eds.), Advances in Heat Transfer, Academic Press, pp. 107 (1978).

[24] M.I. Othman, Z. Angew. Math. Phys. **55**, 468 (2004).

[25] I.S. Shivakumara, M.S. Nagashree and K. Hemalatha, Int. Commun. Heat Mass Transfer **34**, 1041, (2007).

[26] I.S. Shivakumara, M. Akkanagamma and Chiu-On Ng, Electrohydrodynamic instability of a rotating couple-stress dielectric fluid layer, Int. J. Heat Mass Transfer **62**, 761 (2013).

[27] G.C. Rana, R. Chand, and D. Yadav, FME Transactions **43**, 154 (2015).

[28] G.C. Rana, R. Chand, and V. Sharma, Acta Technica **61**, 31 (2016).

[29] G.C. Rana, R. Chand, and V. Sharma, Rev. Cub. Fis. **33**, 89 (2016).

[30] R. Chand, G.C. Rana, and D. Yadav, J. Appl. Fluid Mech. **9**, 1081 (2016).

MEASURING THE PERFORMANCE OF A ROVER WHEEL IN MARTIAN GRAVITY

MIDIENDO EL COMPORTAMIENTO DE UNA RUEDA DE ROVER A LA GRAVEDAD DE MARTE

J. Amigó-Vega[a†], G. Viera-López[a], A. Serrano-Muñoz[a] and E. Altshuler[a]

Group of Complex Systems and Statistical Physics, University of Havana, 10400 La Habana, Cuba; joaquin.amigov@gmail.com[†]
† corresponding author

With the increase of planetary exploration missions and thereby the resultant increase of extraterrestrial rovers deployed, their mobility performance meets new challenges. Wheel-soil interaction plays an important role in the movement of these rovers. Our research addresses the study of this interactions in the first moments of the trajectory. The investigations reported so far, focus on long-distance motion (approx. 20-30 cm). However, the authors believe that the firsts interactions are crucial for the future performance of the motion. Here, by means of a device that allows multiple and precise repetitions of a wheel rolling experiment at controlled gravities, we characterize the movement of a wheel on sandy soil, in the gravity of Mars. Our study reveals that gravity influences the performance of the wheel, under these conditions. The experiments show that, as the gravity decreases, the rolling efficiency also decreases.

Con el incremento de las misiones de exploración espacial y por tanto el incremento resultante en la cantidad de rovers desplegados, su eficiencia de desplazamiento se enfrenta a nuevos retos. La interacción rueda-suelo juega un papel importante en el movimiento de estos rovers. Nuestra investigación está dirigida al estudio de esta interacción en los primeros instantes de la trayectoria. Los trabajos reportados hasta la actualidad, se enfocan en desplazamientos de largas distancias (aprox. 20-30 cm). Sin embargo, los autores creen que los primeros instantes son cruciales en el futuro desempeño del movimiento. En este trabajo, usando un dispositivo que permite múltiples y precisas repeticiones de un experimento de rodadura a gravedades controladas, se realiza una caracterización del movimiento de la rueda sobre suelo arenoso a la gravedad de Marte. Nuestro estudio revela que la gravedad influye en la eficiencia de rodadura. En los experimentos realizados a medida que disminuye la gravedad, la eficiencia del movimiento de la rueda empeora.

I. INTRODUCTION

Walking or rolling on a sandy soil involves a delicate balance between mechanically stable and flowing states: an excess of the latter can easily prevent any further motion of a wheeled vehicle. That is perhaps what happened with the Mars *rover Spirit* as it sank into and tried to escape from a shallow sand dune in 2009, after 5 years of fulfilling an extremely successful mission [1]. At the In Situ Instrument Laboratory at NASA's Jet Propulsion Laboratory (Pasadena, California), scientists maneuvered with a clone of Spirit in a sandbox designed to imitate the soil conditions in the Martian environment. While the compositional and grain size distribution of the Martian soil were accurately imitated on Earth, other peculiarities associated to the reduced Martian gravity were impossible to reproduce. The team used a lighter version of the clone to imitate smaller weight in Mars but the method could not account for the possible changes in the behavior of the soil itself due to smaller-than-Earth gravity, which could be an important factor on this interaction.

Due to the enormous practical importance of the performance of wheels in granular soils there is a relatively large amount of literature on the subject, which concentrates on parameters of direct engineering impact such as the nature of the soil, the weight, size and surface design of the wheel, and the imposed velocity or torque [2–9]. The performance of granular materials in such conditions is key for space exploration and eventual colonization of space bodies such as the Moon and Mars: in those cases, our relatively poor understanding of the statics and dynamics of sand [10–14] is aggravated by lower values of *g*, which substantially complicates experimental efforts [15]. Reproduction of lower than Earth gravities requires complex experimental facilities [16–21], which has hindered the research efforts in the subject.

However, pioneering experiments to examine the performance of wheels at low gravities in a controlled environment have been performed recently. The first was reported by Kobayashi *et al.* in 2010 [22]: based on parabolic flight maneuvers, they studied the performance of a cylindrical wheel in "variable gravity conditions", where plateaus at gravities near that of Mars were achieved. The typical experiment lasted from 15 to 30 seconds, depending of the gravity, at a constant 0.314 rad/s velocity. The authors drive two main conclusions. Firstly, that the wheel's sinkage is independent from gravity, a result later explained in 2014 by Altshuler *et al.* through low gravity experiments on an spherical intruder [23]. Secondly, that the increase of soil "flowability" at small gravities lessens the shear resistance of the wheel rotation, so it is unable to hold sufficient traction, and slips more, as compared to ground experiments.

Curiously enough, the same group has suggested that conducting Earth experiments on wheels with the same mass of those intended to roll on a lower gravity environment, allows the prediction of performance in the extraterrestrial environment [24, 25]. Other low-gravity experiment was reported as recently as 2017 by Viera-López *et al.* [26]: they set up a large Atwood machine capable of achieving very stable and repeatable Martian gravities, while a miniature reproduction of NASA's Mars rover wheel rolls on sand into an accelerated laboratory. Preliminary results indicated a larger slip ratio of the wheel at Martian gravity, in agreement with Kobayashi *et al.* [22].

In this paper, we benefit from the precision and experimental reproducibility of the setup reported in [26] to study systematically the performance of a realistic scaled-down model of NASA's Mars rover wheel under different experimental parameters, at the gravity of Mars ($g_{Mars} \approx 0.4$ g_{Earth}) and the gravity of Earth.

II. EXPERIMENTAL WORK

In Fig. 1, one of the main components of the experimental setup reported by Viera-López *et al.* [26] is shown, which has been used in the present report.

Figure 1. Lab-in-a-bucket: photograph of the accelerated laboratory. When attached to a 15-m long Atwood machine, the wheel can "feel" an effective gravity equivalent to that on the surface of Mars.

The most important measured variables are the actual linear displacement and the angular displacement. The efficiency and slippage are inferred from other measurements. Below we describe how we quantify these parameters.

The wheel is attached to a DC motor with a 270.9 steps-per-revolution pulse encoder used to measure the rotation of the wheel while rolling on sand inside the instrument. This measured angular velocity is used to

calculate the linear displacement along the perimeter of the circular trajectory following the formula

$$x_{calculated}(t) = \int_0^t r\omega(t)\,dt, \tag{1}$$

where r is the radius of the wheel. The function $\omega(t)$ can be obtained by a numerical integration of the encoder pulses in time. This calculated linear displacement assumes no slippage and can be used as a reference to estimate the efficiency if we were able to measure the actual linear displacement.

We can also directly obtain the actual linear displacement of the wheel, based on the motion of its center of mass, by processing the images taken with the camera on top of the instrument. Consider the initial position of the wheel, described as a vector in polar coordinates, where R_0 is the initial distance between the center of the wheel and the central pivot placed in the instrument, and the angle α_0 is the initial angle referred to the positive x axis, in the coordinate system placed in the central pivot.

The wheel describes a circumferential trajectory due to the holonomic restriction imposed by the central pivot. To obtain the displacement up to a certain time, we can use the following expression

$$x_{measured}(t) = R_0[\alpha(t) - \alpha_0], \tag{2}$$

where $\alpha(t)$ and α_0 are the angles defined in Fig. 2.

Using the calculated and measured values of linear displacement, we are able to quantify the instantaneous slippage of the wheel for a given value of gravity, angular velocity, mass and granular matter properties.
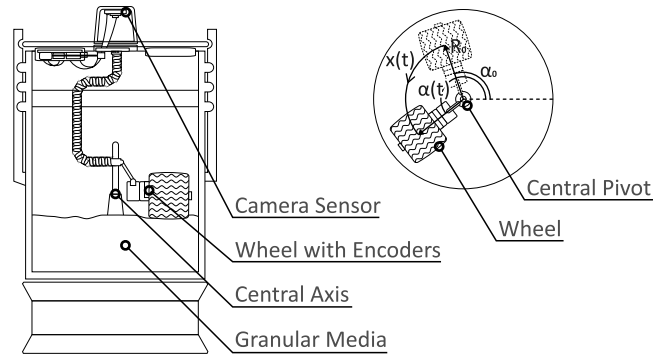
Figure 2. Motion of the rover wheel into the accelerated lab. The wheel moves on the sand describing a circumference around the vertical symmetry axis of the instrument. The inset shows some basic parameters characterizing the motion.

The data of g_{eff} was obtained directly through an inertial accelerometer.

The instantaneous efficiency is calculated as the ratio between the time derivatives of *x calculated* and *x measured*, using the following formula

$$\text{efficiency} = \frac{\dot{x}_{measured}}{\dot{x}_{calculated}}. \tag{3}$$

We designed a set of experiments in order to understand how the differences of gravity between Earth and Mars could

affect the wheel's performance while it is rolling on sandy soil. First, we performed experiments on Earth and Mars gravities and evaluated the total slippage after the same amount of time in both conditions. Next, in order to quantify the role of the weight's difference, we increased the mass of the wheel before performing the Mars gravity experiments, in a factor that compensates the gravity decrease. With this "normalized mass" we were able to quantify the slippage with the same weight at both gravities.

We used, for this experiments, a scaled-down 3D printed wheel similar to the ones used by the Mars *rover Curiosity* [27]. The radius and width of the 'replica' were reduced relative to the original rover wheel. In order to reproduce as good as possible the behavior of the wheel on Mars conditions and validate the results, considering the size differences, a mass scaling was made.

The wheel was scaled assuming that the density is conserved, and that all other dimensions scale as the size of the wheel. Assuming that m, r and w are the mass, radius and width of the 'replica' and M, R and W are their analogues for the original wheel, it is possible to estimate the mass of the 'replica' according to

$$\frac{M}{R^2 W} = \frac{m}{r^2 w}. \tag{4}$$

Substituting M = 900/6 kg/wheel, R = 0.25 m and W = 0.4 m from a realistic Mars rover [27] and r = 0.07 m, w = 0.049 m for our replica, we get a normalized mass of 1.44 kg.

To measure the mass of the wheel, we attached the wheel to the DC motor and placed it inside the instrument on its final position. In the bottom of the instrument, instead of the granular media, we placed a small high-resolution weighing scale. We called the value obtained "effective mass", because this is the mass of the wheel+motor system that is in direct contact with the granular media. This "effective mass" value (1.05 kg) is the one used for calculations on the next section.

III. RESULTS

In the first experiment, the wheel was configured to roll over sand at Mars gravity. The angular velocity used was of 4 rad/s and the mass of the wheels was 1.05 kg, which is of the order of magnitude of the mass calculated with the scaling (we did not use the calculated value of 1.44 kg due to technical reasons). The actuator, a motor attached to the wheel, was configured to receive the start signal when detecting the system's stabilization at the effective gravity (g_{eff}).

The second experimental configuration consisted in using the same values of mass and angular velocity, but this time at Earth's gravity. This configuration was designed to determine if the gravity plays an important role on the wheel's performance on sand. The average results, after concluded both set of experiments, are shown in Fig. 3. It should be noted that in both configurations the angular velocity and mass were exactly the same, the only experimental parameter that changed was gravity.

Fig. 4 shows the average efficiency and maximum dispersion after 10 repetitions in the Earth and Mars configurations using the same wheel mass. Notice that the average and maximum dispersion values follow the same general shape, which corroborates that the peak in the efficiency reported for the Earth environment is experimentally sound.
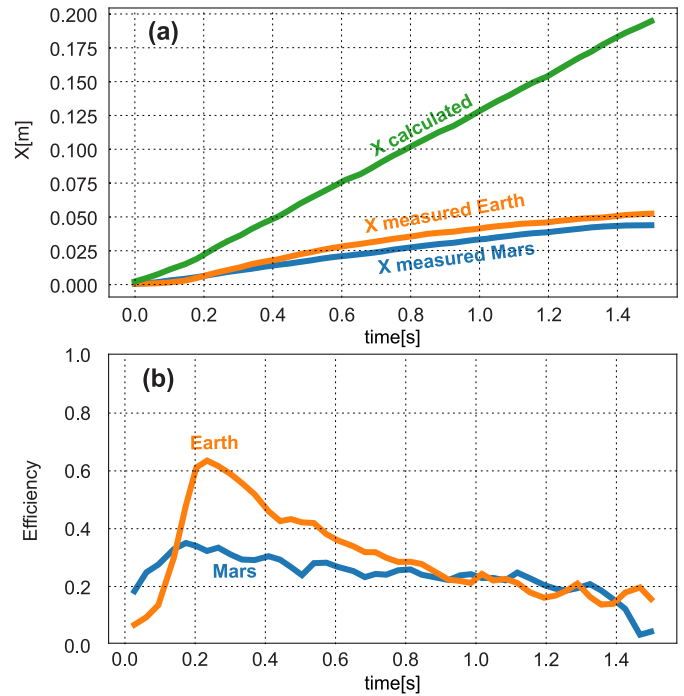
Figure 3. Rolling in Mars and in Earth (ω = 4 rad/s, m = 1.05 kg). (a) Temporal evolution of the averaged linear position, obtained by direct measurements processing the images (*x measured*) and by calculating using angular displacement (*x calculated*). (b) Temporal evolution of the averaged instantaneous efficiency (averages after 10 repetitions).

In Fig. 3, relevant changes are not observed in the wheel's general behavior. The biggest difference lies on the temporal evolution during the first 0.6 - 0.8 seconds of the motion. This departure between the two records may suggest that gravity plays some role when rolling over sandy soil. However, the observed differences might be caused by the trivial effect of the weight loss related to the gravitational difference. In order to determine if the differences observed in the experiments are truly related to different "intrinsic" behaviors in the granular media related to gravity, it is reasonable to compensate the mass difference causing the weight to be the same under both conditions.

If the wheel's mass on Mars is 1.05 kg, causing a 3.89 N weight, and we want the wheel to produce this same weight on Earth, its necessary to multiply the Mars's mass by the ratio between the gravities's accelerations of both planets. We obtain that the mass necessary for the Earth's experiments is of 0.4 kg.

Consequently, the mass of the wheel was reconfigured to be the one calculated before, guaranteeing constant weight for both experimental configurations. All other parameters were kept constant. Once more, 10 iterations (on Earth's gravity) were performed. The average results are shown in Fig. 5.
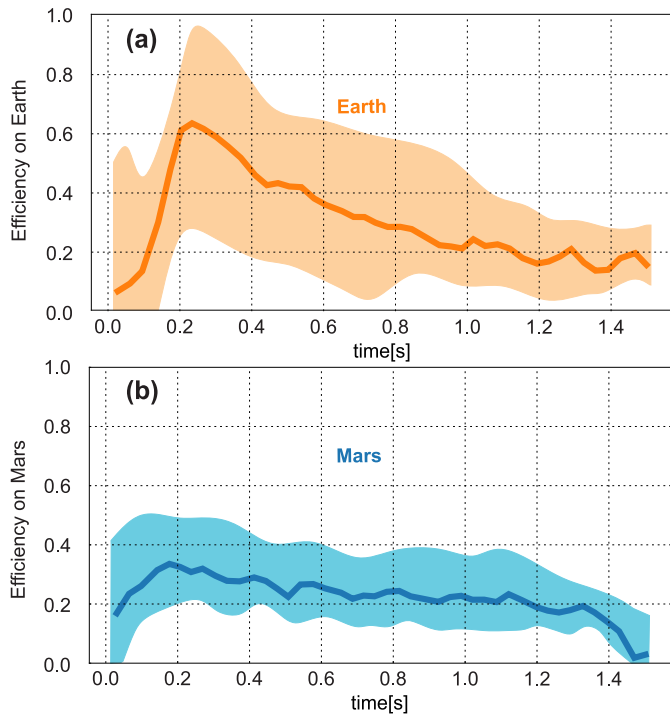
Figure 4. Rolling in Mars and in Earth (ω = 4 rad/s, m = 1.05 kg). In each case the average after 10 iterations is shown as a thin and darker curve. The clearer regions indicates the maximum dispersion found on the experiment's data. (a) Earth experiments, temporal evolution of the instantaneous efficiency. (b) Mars experiments, temporal evolution of the instantaneous efficiency.

Based on the data displayed in Fig. 5, we are able to conclude that the mobility performance of a wheel at different gravities is not a trivial consequence of the weight variation experienced due to gravitational reduction: there is a modification in the behavior of the granular medium associated to gravity that influences the rolling efficiency of the wheel, which confirms the findings of Kobayashi *et al.* [22]. A possible hypothesis to explain the similarities of the results found on the same mass experiments at different gravities, is that the modification of the interactions on the granular media gets compensated with the weight loss of the wheel. If the vertical penetration of the wheel during rolling is a key parameter to understand the motion, then these results are consistent with the observation of Altshuler *et al.* [23], who demonstrated that the maximum penetration depth of a sphere into granular media is independent of gravity, if the sphere conserved its mass in all gravities.

The Earth curves of Fig. 3 and 5 also reveal several interesting behaviors. Apparently there is a reduction of the rolling efficiency on Earth over time, that could be due to an increase of the wheel's burrowing on the granular media.

The Earth efficiency curves (orange line in Fig. 3b and 5b) are calculated using the data plotted on the green and orange curves of Fig. 3a and 5a respectively. In both cases, the measured linear displacement on Earth shown a non-linear behavior within the 0.1-0.3 s time interval. The peak found on the Earth efficiency curves, in a similar interval of time, is an unexplained effect.

When comparing the Mars and Earth efficiency curves, we

appreciate that the Mars rolling efficiency behavior is much smoother, and despite it decreases slowly, the curve does not present any relevant irregularities.
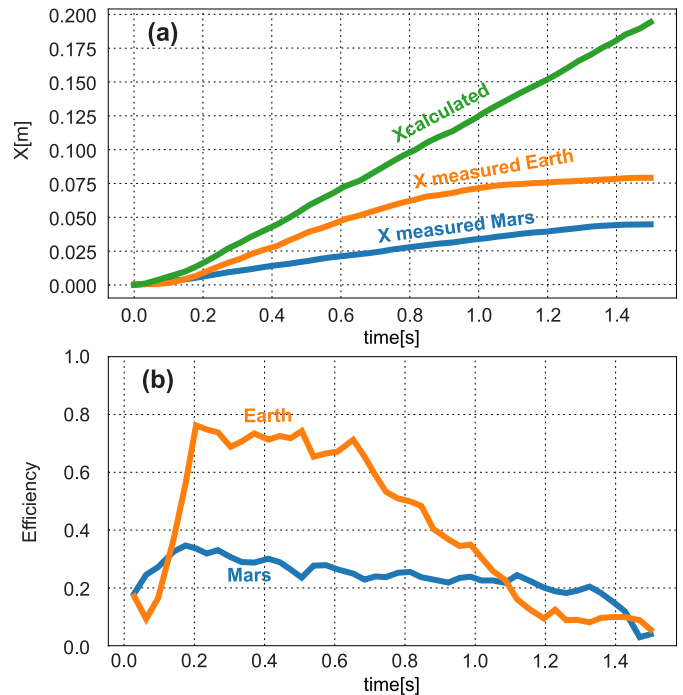
Figure 5. Rolling in Mars and in Earth (ω = 4 rad/s, w = 3.889 N). (a) Temporal evolution of the actual averaged linear position (10 iterations). (b) Temporal evolution of the averaged instantaneous efficiency (averages after 10 repetitions).

IV. CONCLUSIONS

The rolling performance of a scaled-down Mars rover wheel on a granular bed was studied. Experiments were performed at two different gravitational conditions, Mars and Earth's. Two sets of experiments, performed at both gravitational conditions, were designed: equal angular velocity and mass of the wheel; equal angular velocity and weight of the wheel.

No substantial differences in the rolling efficiency were observed between both gravities if the wheel's mass is kept constant (except within the interval from 0.2 to 0.6 seconds). It can be qualitatively explained by the fact that the change of weight experienced by the wheel due to the lowering of gravity gets compensated with the loosening of the granular media.

A larger efficiency difference over a larger time is observed between Earth and Mars experiments when the wheel's mass is adjusted to compensate weight variations. It shows that the rolling performance does not depend on the change of weight of a vehicle. There may also be a modification on the particles interactions inside the granular media that may be causing a modification of the wheel's rolling efficiency. Further experimentation for quantifying other parameters that may be relevant, as the impact of changing the moment of inertia (separately from the role of gravity), are necessary to get more accurate conclusions.

In all experiments on Earth, a peak in the efficiency during the first moments of the motion was found. That is an unexpected behavior that we will study in more detail elsewhere. We also plan to perform future studies in a wider range of gravities, masses and angular velocities in order to see if the general tendencies in the efficiency reported here are maintained.

REFERENCES

[1] Mars Exploration Rovers (2016). http://www.planetary.org/multimedia/space-images/spacecraft/diagram-of-a-curiosity-wheel.html. [Accessed March 12, 2019]

[2] I. Littleton and J. Hetherington, J. Terramechanics **15**, 95 (1978).

[3] A. Oida, A. Satoh, H. Itoh and K. Triratanasirichai, J. Terramechanics **28**, 319 (1991).

[4] B. Coutermarsh, J. Terramechanics **44**, 275 (2007).

[5] N. Taberlet, S.W. Morris and J.N. McElwaine, Phys. Rev. Lett. **99**, 68003 (2007).

[6] F.V. De Blasio and M.B. Saeter, Phys. Rev. E **79**, 22301 (2009).

[7] M. Gutierrez and A. Mohamed, Springer Ser. Geomech. Geoengin. **12**, 243 (2011).

[8] L. Ding, H. Gao, Z. Deng, K. Nagatani and K. Yoshida, J. Terramechanics **48**, 27 (2011).

[9] K.J. Burns, N.J. Balmforth and I.J. Hewitt, Proc. R. Soc. A Math. Phys. Eng. Sci. **473**, 20170375 (2017).

[10] P.A. Lemieux and D.J. Durian, Phys. Rev. Lett. **85**, 4273 (2000).

[11] P. By, J. Fluid Mech. **541**, 167 (2016).

[12] A. Rivera, K.E. Bassler, O. Ramos, A.J. Batista-Leyva, E.Altshuler and E. Martínez, Phys. Rev. Lett. **91**, 014501 (2003).

[13] E. Martínez, C. Pérez-Penichet, O. Sotolongo-Costa, O. Ramos, K.J. Måløy, S. Douady and E. Altshuler, Phys. Rev. E **75**, 31303 (2007).

[14] E. Altshuler, R. Toussaint, E. Martínez, O. Sotolongo-Costa, J. Schmittbuhl and K.J. Måløy, Phys. Rev. E **77**, 31305 (2008).

[15] R.A. Wilkinson, R.P. Behringer, J.T. Jenkins and M.Y. Louge, AIP Conf. Proc. **746**, 1216 (2005).

[16] V. Pletser, Acta Astronaut. **55**, 829 (2004).

[17] N. Callens, J. Ventura-Traveset, T.fL. De Lophem, C. Lopez De Echazarreta, V. Pletser and J.J. Van Loon, Microgravity Sci. Technol. **23**, 181 (2011).

[18] N. Murdoch, B. Rozitis, S.F. Green, T.L. De Lophem, P. Michel and W. Losert, Granul. Matter **15**, 129 (2013).

[19] U. Kaczmarczik, H.J. Rath and P. von Kampen, Acta Astronaut. **59**, 278 (2006).

[20] D.I. Goldman and P. Umbanhowar, Phys. Rev. E **77**, 21308 (2008).

[21] C. Sunday, N. Murdoch, O. Cherrier, S. Morales Serrano, C. Valeria Nardi, T. Janin, I. Avila Martinez, Y. Gourinat and D. Mimoun, Rev. Sci. Instrum. **87**, 84504 (2016).

[22] T. Kobayashi, Y. Fujiwara, J. Yamakawa, N. Yasufuku and K. Omine, J. Terramechanics **47**, 261 (2010).

[23] E. Altshuler, H. Torres, A. González-Pita, G. Sánchez-Colina, C. Pérez-Penichet, S. Waitukaitis and R.C. Hidalgo, Geophys. Res. Lett. **41**, 3032 (2014).

[24] J.Y. Wong and T. Kobayashi, J. Terramechanics **49**, 349 (2012).

[25] H. Nakashima and T. Kobayashi, J. Terramechanics **53**, 37 (2014).

[26] G. Viera-López, A. Serrano-Muñoz, J. Amigó-Vega, O. Cruzata and E. Altshuler, Rev. Sci. Instrum. **88**, 86107 (2017).

[27] Diagram of a Curiosity wheel. http://www.planetary.org/multimedia/space-images/spacecraft/diagram-of-a-curiosity-wheel.html. [Accessed March 12, 2019]

MOVIMIENTO ARMÓNICO SIMPLE: DETERMINANDO LA CONSTANTE DE FASE
SIMPLE HARMONIC MOTION: FINDING THE PHASE CONSTANT

C. Osaba-Rodríguez

Departamento de Física, Universidad Tecnológica de La Habana, "José Antonio Echeverría" (CUJAE), 19390 La Habana, Marianao, La Habana, Cuba; carloso@automatica.cujae.edu.cu

El tratamiento de las oscilaciones mecánicas en los cursos de Física General suele iniciarse con el estudio del Movimiento Armónico Simple en un sistema compuesto de un cuerpo y un resorte. En la obtención de la ley de movimiento en tales sistemas la determinación de la constante de fase resulta particularmente trabajosa entre los estudiantes. Para la determinación de dicha constante algunos textos presentan una relación matemática que simplifica el procedimiento al punto de conducir a errores. Por ello se discute la determinación de la constante de fase para este tipo de movimiento.

The treatment of mechanical oscillations in General Physics courses usually begins with the study of Simple Harmonic Motion in a system composed of a block attached to the end of a spring. To obtain the law of motion for such system involves finding the phase constant as a difficult step for students. To determine the phase constant requires operating with two independent equations related with the particle's initial speed and position. Some textbooks oversimplify the procedure and obtain the phase constant using only one equation related to the initial conditions of the motion. How to determine the phase constant for such oscillatory systems is discussed.

I. INTRODUCCIÓN

El movimiento oscilatorio reviste gran importancia para la Física y aparece en diversas escalas, desde las oscilaciones de moléculas hasta las de una viga empotrada o un cuerpo celeste.

Si bien en muchos casos lo esencial en tal movimiento radica en la frecuencia o la amplitud de las oscilaciones, en los cursos de Física General están presentes los ejercicios en que disponiendo de los parámetros de un sistema oscilatorio y las condiciones iniciales del movimiento, se solicita obtener la correspondiente ley de movimiento lo que entraña, entre otros asuntos, determinar la constante de fase.
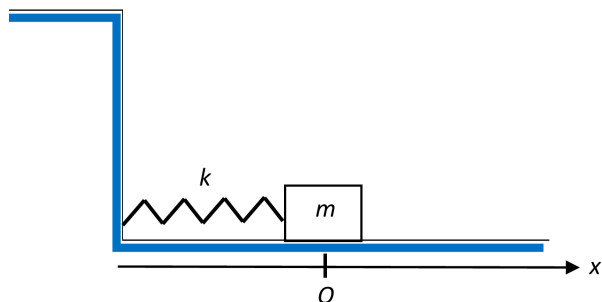
Figura 1. Sistema cuerpo-resorte.

De los diversos sistemas físicos con oscilaciones que corresponden al Movimiento Armónico Simple (MAS), el Sistema Cuerpo – Resorte mostrado en la Figura 1 es frecuentemente tomado como punto de partida pues su análisis dinámico resulta relativamente sencillo en pos de obtener la ecuación de movimiento.

El modelo correspondiente a un sistema cuerpo – resorte se apoya en las siguientes suposiciones:

1. Un cuerpo de masa m, sujeto a un resorte de constante elástica k que tiene su otro extremo empotrado en una pared, se desliza sobre una superficie horizontal.

2. Se desprecia la fricción entre el cuerpo y la superficie.

3. El cuerpo se considera como un cuerpo rígido y la masa del resorte es despreciable en comparación con la del cuerpo.

4. El resorte obedece a la Ley de Hooke

Si bien la suposición 2 apunta a la fricción seca entre el cuerpo y la superficie, también ha de despreciarse el efecto de fuerzas disipativas, como las viscosas.

La suposición 3 expresa que las propiedades elásticas radican en el resorte y las inerciales en el cuerpo, por lo que el sistema posee parámetros concentrados.

De la suposición 4 se desprende que el resorte admite tanto extensiones como compresiones sin que sus espiras se toquen entre sí.

En un montaje experimental de este sistema, los resortes helicoidales habitualmente empleados se mantendrían rectos bajo tracción pero se doblarían en compresión. Por ello un montaje experimental práctico podría lograrse con un resorte a cada lado del cuerpo, ambos ligeramente estirados. En el

modelo teórico, en cambio, el resorte se mantiene recto en todos los casos.

La aplicación de la segunda ley de Newton para el cuerpo en su movimiento a lo largo de la superficie conduce a,

$$m\frac{d^2x}{dt^2} + kx = 0. \tag{1}$$

Si bien esta ecuación diferencial, caracterizada por los parámetros m y k, rige el movimiento abordado, el planteamiento completo del problema ha de acompañarse de las condiciones iniciales. Tratándose de una ecuación de segundo orden, dichas condiciones han de contener el valor de la función incógnita –la ecuación de movimiento $x(t)$– y de su primera derivada, que evaluadas en el instante inicial $t = 0$ corresponden respectivamente a la posición inicial y la velocidad inicial:

$$x(t = 0) = x_0, \tag{2}$$

$$\frac{dx}{dt}(t = 0) = v_0. \tag{3}$$

De tal modo el conjunto de ecuaciones 1 a 3 constituye el planteamiento completo del problema que permitiría obtener la ecuación de movimiento con sus parámetros evaluados para un caso dado.

La solución general de este problema admite la forma,

$$x(t) = B \sin(\omega t) + C \cos(\omega t), \tag{4}$$

aunque suele resultar más conveniente,

$$x(t) = A \cos(\omega t + \varphi). \tag{5}$$

En la ecuación 5 A es la amplitud, ω la frecuencia angular y φ la constante de fase.

La frecuencia angular está dada por:

$$\omega = \sqrt{\frac{k}{m}} \tag{6}$$

De 5 puede obtenerse la expresión de la velocidad,

$$v(t) = -\omega A \sin(\omega t + \varphi). \tag{7}$$

A partir de 5 y 7, las expresiones para la posición y la velocidad iniciales son respectivamente:

$$x_0 = A \cos\varphi, \tag{8}$$

$$v_0 = -\omega A \sin\varphi. \tag{9}$$

Operando con las ecuaciones 8 y 9 puede obtenerse la expresión de la amplitud,

$$A = \sqrt{x_0^2 + \frac{v_0^2}{\omega^2}}. \tag{10}$$

Con el objeto de obtener una expresión para determinar la constante de fase φ, algunos textos optan por formar un cociente con las expresiones 8 y 9 para eliminar la amplitud,

$$\frac{x_0}{v_0} = \frac{-\omega A \sin\varphi}{A \cos\varphi} = -\omega \tan\varphi. \tag{11}$$

y obtener:

$$\varphi = \arctan -\frac{v_0}{\omega x_0}. \tag{12}$$

Si bien la ecuación 12 es cierta, su presentación en un texto inducirá a algunos estudiantes a emplearla para hallar el valor de la constante de fase, aceptando el resultado de la arcofunción que brinda la calculadora empleada.

Mas resulta que 12 por sí sola no resulta suficiente para obtener de manera unívoca y correcta el valor de la constante de fase, ya que a un valor dado de $\tan\varphi$ corresponden dos valores del argumento φ en el intervalo de 0 a 2π radianes. Del mismo modo disponiendo de los valores de x_0 y A, de 8 puede obtenerse el valor de $\cos\varphi$, lo que en general conduce a dos valores posibles para φ; y análogamente a partir de los valores de v_0, ω y A, de 9 puede obtenerse el valor de $\sin\varphi$, lo que también conduce a dos valores posibles para φ en el intervalo citado. Es la consideración conjunta de los posibles valores de φ provenientes de al menos dos ecuaciones independientes lo que permite hallar el valor correcto de la constante de fase.

La operación efectuada con las ecuaciones 8 y 9 para obtener 11 o 12 si bien elimina la presencia de la amplitud, conlleva una pérdida de información para la determinación de la constante de fase.

Vale resaltar que si una pareja de valores de posición y velocidad iniciales x_0 y v_0 corresponden a un valor de φ y por tanto a una ecuación de movimiento, tomar otra pareja con los mismos valores absolutos pero con los signos opuestos conduciría a otro valor de φ y con ello a otra ecuación de movimiento, mientras que en ambos casos la ecuación 12 proporciona el mismo resultado para $-v_0/\omega x_0$, y aparentemente igual valor de φ.

II. DETERMINACIÓN DE LA CONSTANTE DE FASE EN DIVERSOS TEXTOS

Textos de diversas épocas, tras exponer la teoría del MAS, se refieren a la determinación de los parámetros del sistema oscilatorio, entre ellos la constante de fase.

En [1] tras haberse planteado la solución de la ecuación de movimiento como $x = A \sin(\omega_0 t + \varphi)$ se declara que a partir de $x_0 = A \sin\varphi$ y $v_0 = \omega A \cos\varphi$ pueden determinarse A y φ, mas no se explica el procedimiento. Posteriormente, operando con una solución en la forma $\theta = \theta_0 \sin(\omega_0 t + \phi)$ correspondiente a un movimiento pendular, se plantea que $\phi = \sin^{-1}(\theta_1/\theta_0)$, donde θ_1 es el valor de θ para $t = 0$, igualmente sin exponer un algoritmo de trabajo.

En [2] no se proporciona un método general para la determinación de la constante de fase. La exposición contiene un ejemplo en el que a partir de los valores de frecuencia angular y de posición y velocidad iniciales ($\omega = 5,00$ rad/s, $x_0 = 5,00$ cm, $v_0 = -0,100$ m/s) se determina de [11] $\tan\varphi$ ($\tan\varphi = 0,400$), y de ahí $\varphi = 0,121\pi$ rad. Si bien este valor de φ es correcto, constituye un caso que podría calificarse de feliz, pues a partir de un valor positivo de $\tan\varphi$ se brinda como respuesta y única alternativa el valor de φ ubicado en el primer cuadrante, sin considerar la posibilidad de que φ esté ubicado en el tercer cuadrante.

En [3] se halla un valor de φ y se sugiere una forma de verificar si el mismo es correcto. En concreto, se presenta un sistema cuerpo – resorte con sus valores de masa, constante elástica, así como de posición y velocidad iniciales. Los valores de ω, x_0 y v_0 conducen a un valor negativo de $\tan\varphi$ y de [12] se obtiene un valor de φ que resulta correcto, el cual se emplea junto a otros resultados para obtener la ecuación de movimiento $x(t)$. El ejemplo concluye invitando al lector a comprobar si la ecuación de movimiento obtenida satisface las condiciones iniciales, lo que pudiera indicar que el valor seleccionado de φ no es correcto y debe explorarse el otro valor que proporciona $\tan\varphi$.

En [4] mediante un ejemplo se muestra un método correcto para la determinación de la constante de fase. Dicho ejemplo considera un sistema del que se conocen su frecuencia angular así como la posición y velocidad iniciales. Con empleo de [8] se halla $\cos\varphi$ y los dos posibles valores de φ en el intervalo de 0 a 2π, los que son sustituidos en [9] para hallar la velocidad inicial, seleccionándose el que brinda el valor correcto de v_0

Si bien este procedimiento es irreprochable, un ejercicio al final del capítulo pide demostrar que la relación general entre los valores de posición inicial, velocidad inicial y constante de fase es

$$\tan\varphi = -\frac{v_0}{\omega x_0}, \tag{13}$$

lo que puede conducir a algunos estudiantes a suponer que tal ecuación es suficiente para la determinación de φ, cuando es solo una condición necesaria que conduce a dos valores posibles de la constante de fase los que han de someterse a una comprobación adicional, tal como ilustró el ejemplo del texto.

En [5] no se brinda un método para hallar la constante de fase. Mediante un ejemplo a partir de los valores de frecuencia angular y de posición y velocidad iniciales, se obtiene mediante [11] el valor de $\tan\varphi$ y de ahí el valor correcto de la constante de fase para el ejemplo, mas no se considera otra posibilidad para su valor en el intervalo de 0 a 2π.

En [6] se formula la ecuación de movimiento como $x = A\cos(\omega_0 t + \theta)$, planteándose que la solución se obtiene tras determinarse A mediante [10] y θ mediante [13].

En [7] se brindan indicaciones correctas para obtener la constante de fase a partir de [13], aclarándose que dicha ecuación se satisface para dos valores del argumento entre $-\pi$ y π, y que ha de tomarse el que brinda los signos

correctos para el seno y el coseno en las condiciones iniciales. Si bien dicho texto no incluye un ejemplo numérico, las indicaciones que brinda son suficientes para determinar de forma adecuada la constante de fase.

En [8] mediante un ejemplo en el que se dispone de los valores de amplitud y de posición y velocidad iniciales, se obtienen de la expresión para la posición inicial dos posibles valores de la constante de fase, y de la correspondiente a la velocidad inicial otros dos valores de dicha constante, tomándose el valor coincidente. Así este texto ilustra una forma correcta para la determinación de la constante de fase, y lo logra sin emplear una ecuación que vincule la constante de fase con la frecuencia angular y la posición y velocidad iniciales. Si en ese texto tal ecuación se obtuviera, no sería como [12], pues la ecuación de movimiento es formulada como,

$$x(t) = A\sin(\omega t + \varphi), \tag{14}$$

por lo que la expresión de la velocidad de oscilación es,

$$v(t) = \omega A\cos(\omega t + \varphi), \tag{15}$$

y se obtendría, a diferencia de [12], el resultado,

$$\varphi = \arctan\frac{\omega\omega x_0}{v_0}. \tag{16}$$

III. DETERMINACIÓN DE LA CONSTANTE DE FASE COMO UNA ARCOFUNCIÓN

Si bien el procedimiento expuesto en [8] es correcto, una variante consiste en comenzar determinando solo el cuadrante en que se localiza la constante de fase.

Un problema frecuente en el estudio del MAS consiste en partir de un sistema cuerpo – resorte del que se conocen la masa del cuerpo, la constante elástica del resorte, así como la posición y velocidad iniciales del cuerpo, y se pide determinar la ecuación de movimiento [5] con sus parámetros evaluados. Para ello calcular mediante [6] la frecuencia angular y mediante [10] la amplitud no presenta dificultades.

Luego a partir del valor de la posición inicial se determina de [8] el signo de $\cos\varphi$ y para el intervalo entre 0 y 2π, los dos cuadrantes en que puede situarse el valor de φ. De modo similar a partir del valor de la velocidad inicial se determina de [9] el signo de $\sin\varphi$ y los dos cuadrantes en que puede localizarse φ. Obviamente la constante de fase se ubica en el cuadrante coincidente en las dos determinaciones anteriores.

Conocido el cuadrante en que se ubica φ, basta emplear una de las ecuaciones [8] o [9] o [12] para hallar el valor de la constante de fase.

La determinación de la constante de fase se simplifica cuando $\cos\varphi$ adopta valores como 1 o -1, o si de [9] se obtienen esos valores para $\sin\varphi$, pues cada uno de tales casos conduce a una sola opción para la constante de fase en el intervalo de 0 a 2π.

Determinar ϕ mediante una calculadora a partir de una de las expresiones [8], [9] o [12] operando con la arcofunción

correspondiente requiere el cuidado de verificar si el resultado que brinda la calculadora se encuentra en el cuadrante correcto. De lo contrario es necesario obtener el otro resultado de la arcofunción mediante las relaciones trigonométricas necesarias.

IV. CONCLUSIONES

Si bien en el tratamiento del MAS la habilidad de determinar la constante de fase no ha de sobreestimarse, capacitar a los que estudian tal movimiento en su obtención correcta puede reportar utilidad. Una constante de fase también aparece en el movimiento oscilatorio infra-amortiguado, así como en la formulación de las ondas viajeras armónicas unidimensionales.

La determinación de los coeficientes de la solución de una ecuación diferencial a partir de condiciones iniciales (o de frontera en otros casos) es una habilidad importante en el estudio de la Física, y hallar la constante de fase para un MAS puede ser una pequeña contribución a tan importante objetivo.

BIBLIOGRAFÍA

[1] C. Kittel, W. D. Knight, M, A. Ruderman, Mecánica, Berkeley Physics Course, volumen 1, Segunda edición, Editorial Reverté, S. A. 1989, pp. 212-215.

[2] R. A. Serway, J. W. Jewett Jr, Physics for Scientists and Engineering with Modern Physics, Brooks/Cole Cencage Learning. 2014, p. 457.

[3] F. W. Sears, M. Zemansky, H. D. Young, R. A. Freedman, Física Universitaria, Décimo segunda edición, Volumen 1, Pearson Educación, México, 2013, p. 428.

[4] R. Resnick, D. Halliday, K. Krane, Física Vol. 1, Cuarta edición, Compañía Editorial Continental S. A. de C. V., México, 1996, pp. 360-361.

[5] P. A. Tipler, G. Mosca, Physics for Scientist and Engineers, Fifth edition, Extended version, Worth and W. H. Freeman, 1997, p. 407.

[6] K. R. Symon, Mechanics, Third edition, Addison Wesley Publishing Company, 1971 p. 45.

[7] I. V. Saveliev, Curso de Física General, volumen 1, Editorial Mir, Moscú, 1984, p. 204.

[8] F. W. Sears, Mecánica, movimiento ondulatorio y calor, Edición Revolucionaria, La Habana, 1968, pp. 305-306.

ALUMINIUM MATRIX COMPOSITE WITH SUGARCANE BAGASSE ASH AS REINFORCEMENT MATERIAL

COMPÓSITO DE MATRIZ DE ALUMINIO CON CENIZA DE BAGAZO DE CAÑA DE AZÚCAR COMO MATERIAL DE REFUERZO

J.E. Hernández-Ruiz[a†], L. Pino-Rivero[b] and E. Villar-Cociña[a]

a) Physic Department, Central University of Las Villas, 50100 Santa Clara, Cuba; jesusehr@uclv.edu.cu[†]
b) West Coast University, Miami, Florida, USA

The results of the characterization of the Sugarcane Bagasse Ash from the co-generator boiler (SCBAB) of a Cuban sugar mill, obtained in previous works are offered. Aluminum Matrix composites (AMCs) samples were fabricated employing powder metallurgy technique.

The comparative study of the Al-SCBAB composite with respect to the non-reinforced matrix showed an increment in the hardness of the AMCs reinforced with SCBAB as compared with the non-reinforced matrix. Finally, it was concluded that the SCBAB has good properties for its use as reinforcing material in AMCs.

Se ofrecen los resultados de la caracterización de la ceniza de bagazo de caña de azúcar procedente de la caldera del turbogenerador de un central azucarero obtenidos en trabajos precedentes. Empleando la técnica de pulvimetalurgia se fabricaron las muestras del composite.

El estudio comparativo del compuesto con respecto a la matriz no reforzada mostró un incremento en la dureza del composite reforzado con la ceniza con respecto a la matriz no reforzada. Finalmente, se concluyó que la ceniza tiene buenas propiedades para su uso como material de refuerzo en composite de matriz de aluminio.

I. INTRODUCTION

A composite is defined as the material which has two or more distinct constituents: the matrix and the reinforcement materials. The composite is distinguished by its bulk properties, which are significantly different from those of any of the constituents present in this system [1, 2]. The reinforcement is a discrete constituent distributed into the continuous matrix. However, as described by Sharanabasappa and Motgi [1], many common materials also have a small amount of a dispersed constituent in their structure and they are not considered as composite materials because their properties are similar to those of their base constituents. In previous definitions and analysis, the term "phase"has been replaced by "component" or "constituent" due to a recent point of view expressed by Fakirov [3], whom has indicated the incorrect practice in the composite community of using the term "phase" instead of "component" when dealing with composite materials.

The composite materials are usually classified based on the physical or chemical nature of the matrix [2], e.g., polymer-matrix, metal-matrix and ceramic composites. There are some reports [2, 4–8] that described both, the emergence and present time of the Metal Matrix Composite (MMCs). The MMCs hold significantly higher properties when compared to non-reinforced same materials, and can be widely applied in various industrial sectors. However, as explained [6, 7, 9] their current usage apparently have been limited due to their relatively high production cost.

According to Alaneme [10], the Aluminium Matrix Composite (AMCs) are the most versatile of the MMCs because of a number of factors, whose advantages include ease of processing, relatively low cost of Al matrices in comparison with other competing metal matrices (Cu, Ti, Mg), good combination of physical and mechanical properties, good properties at high temperature and thermal management capability, excellent tribological properties, and reasonable corrosion resistance [4, 9–14]. This same author, referring to Miracle [4] explains that it is for these reasons that AMCs have found application in diverse technological areas and their influence as an engineering material is expected to continue to rise in the years ahead. Of course, in the base of this is found, as described by Kumar and Purohit [15] the fact that Aluminium is the most abundant metal and the third most abundant chemical element in the earth's crust. In addition, Aluminium and Aluminium alloys have lightweight and a very desirable combination of properties, along with the ease with which of the most pieces of a great variety shapes and dimensions can be manufactured.

In previous investigations, it was shown that there is a growing interest in exploring low-cost options for the development of AMCs with the hope of still maintaining their high performance levels in service applications [2, 4, 10, 12] and [16]. At the same time, according with Lancaster, Lung and Sunjan [17] at present the application of agro-industrial wastes in AMCs has been getting more attention because of that the ashes of this wastes can be used as reinforce particles in metal matrices to enhance their strength properties. In

addition, by applying these agro-industrial wastes in useful ways not only save the manufacturing cost of products but also reduce pollution on the environment [17, 18]. In recent years, several studies have been made [10,16,22] about AMCs that use Rice husk ash, Bamboo leaf ash, Coconut shell ash, Palm oil fuel ash or Bagasse ash among other agro-industrial waste materials as reinforcements. In Cuba, big amounts of sugar cane are processed, generating high volumes of solid waste. A part of these wastes are employed in animal feeding and other parts are disposed and burnt in open landfills, with its negative impact on the environment. Bagasse is an important by-product of the sugar cane industry and most of it is burned to produce steam and generate electricity in co-generators at sugar factories. Sugar cane bagasse ash is the result from the bagasse combustion in the boiler, and is a solid waste too. However, although there are international reports of the successful use of different cellulose materials ashes and particularly of sugar cane bagasse ash like reinforcement materials in MMCs (cited above); it was not found any report that refers to the employment of the Cuban sugar cane bagasse ash with this end.

The present work is an effort in considering the potentials of sugar cane bagasse ash from boiler of co-generation plant at the sugar factories (SCBAB) for development of low-cost AMCs. In addition, the morphology and hardness of AMCs reinforced with a level of 4 % in weigh of SCBAB was studied.

II. MATERIALS AND METHODS

II.1. Ash Characterization

The sugar cane bagasse ash (SCBA) used was collected directly from the boiler of the co-generator plant (turbo generator) at the "Luis Arcos Bergnes" sugar factory in Camajuani city, province of Villa Clara, Cuba. In the turbo generator boiler, the combustion process is not controlled. The obtained ash has a gray color. The SCBAB was milled in a ceramic ball mill during 60 minutes at rotational speed of 150 rpm and sieved below 150 μm. The particle size distribution was determined using a laser diffraction particle size analyzer (Malvern Mastersizer Particle Size Analyzer and Mastersizer Software long bed Version 2.19) in liquid mode with deionizer water as dispersant and ultrasound agitation for 60 s.

The chemical compositions of the obtained SCBAB was determined by X-Ray Fluorescence Spectrometry (XRF), using Phillips PW1400 (tube of Rh, 30 kV, 60 mA) Axios XRF spectrometer.

The mineralogical composition of the SCBAB was studied by X-Ray Diffraction (XRD), employing Phillips MPD 1880 spectrometer made in Holland. The radiation used was Cu Kα. The identification of the crystalline phases was carried out by comparison of the experimental data with the database PAN-ICSD (PANanalytical Inorganic Crystal Structure Database).

The morphological study of this ash was carried out by SEM, using a FEI Quanta 600 FEG scanning electron microscope.

II.2. Specimen preparation

The composite specimens have been prepared employing the powder metallurgy technique. Two kinds of samples were manufactured. The first class of samples corresponds to the Aluminum matrix composite reinforced with SCBAB (Al-SCBAB Composite) and the second kind to a non-reinforced Aluminum matrix.

A powder form 99.5 % reagent grade Aluminium was selected as the metal matrix. The Aluminium powder was preconditioned prior to adding the SCBAB and mixing powders. This preconditioning procedure involves drying the Aluminium powder in a furnace with atmospheric nitrogen and temperature of 450degC. The drying took place until no further change in mass was observed. The procedure normally required around 4 hours to remove the associated water molecules present in the hydrated oxide film of the Aluminium powder particles to avoid subsequent gas porosity into the composite. The Aluminium powder was then cooled at room temperature in desiccators with activated zeolite.

In the same way, the SCBAB was preconditioned prior to mixture with the Aluminium powder. The SCBAB was dried in a furnace at 250degC of temperature and cooled at room temperature in desiccators with activated zeolite.

The SCBAB was added to the Aluminium powder up to a level of 4 % in weight and then the powders were mixed in a stirring- mixer during one hour until a homogeneous mixture of powders was achieved.

The mixed powders were compacted axially at cold state in stainless steel cylindrical dies of (19.60±0.01) mm and (46.91±0.01) mm of diameter and length respectively in the laboratory vertical unidirectional mechanic press. The obtained compact specimens have similar dimensions and density. The same way it proceeded with non-reinforced matrix (comparative sample test). In both cases, the applied pressure was 10 tn.

The compact specimens were subjected to the sintered process in a furnace at 600degC. The sintering process was carried out under constant flow of nitrogen. The heating of the furnace was started after that the samples have been place inside it. The temperature of 600degC was reached at about 60 minutes. Later, once the sintering process is completed, the compact specimens were removed from the furnace and allowed to cool in desiccators with activated zeolite.

Finally, the compact specimens was extruded and cylindrical bars with diameter of (10±0.01) mm and length of (20±0.01) mm were obtained as the end composite sample.

Five groups of ten specimens of each type were submitted to the Vickers hardness test and, one of each type was allocated for morphological study by optic microscopy.

Hardness is a measure of how the solid matter can withstand pressures with objects of various shapes when acting on it with a permanent force for a given time. There are three types of tests used for hardness measurement. However,

in the present work only the Vickers hardness test was considered. Vickers hardness measurements were carried out in order to investigate the influence of SCBAB on the matrix hardness. Hardness measurement was carried out using a Microhardness tester Shimadzu Corporation made in Japan with a measurement uncertainty of 3 %. The load applied was 25 g for 10 seconds.

Before testing, specimen surfaces were polished using emery papers of 1000 mesh. Finally, the trials were made on five specimens of each type (five Al-SCBAB composite and five comparative sample tests.

The morphological study of both, the Al-SCBAB composite and the non-reinforced Aluminium matrix was made using a Novel optic microscope from Nanjing Jiangnan NOVEL Optics Co., Ltd. The microstructure images were acquired by a camera, high-sensitivity Yuva mark of 1.3 MPixel. The camera was coupled to both the ocular of the microscope and a computer with specialized software for both the images acquisition. Image digital processing was made with the software ImageJ version 1.43 cite[25].

Before testing, specimen flat surfaces were polished. First, the flat surfaces of the cylindrical discs were devastated using a series of abrasive papers of different mesh and then polished with diamond paste.

III. RESULTS AND DISCUSSION

III.1. Ash characterization results

Ash characterization was made in previous work and its results reported by Villar-Cociña et al. [23] and Pino-Rivero et al. [24]. The fundamental results obtained from these previous works can be summarized below:

(a) The SCBA particles have irregular shape and varying size distribution. The higher percentage have an diameter size between 10 and 100 microns, with an average diameter size of 34.97 μm.

(b) The SCBAB is basically formed by silica in concentrations of about 80 %.

(c) The Cristobalite and tridymite are the principal crystalline phases present in the SCBAB. These results makes the ash studied an excellent candidate as reinforcement material in metal matrix composites.

III.2. Comparative study of morphology and hardness of Al-SCBAB composite and its non-reinforced matrix

Morphological aspect of Al-SCBAB composite and its non-reinforced matrix

Typical AMC microstructures are represented in Figure 1. In the microphotographs a change of appearance of the composite with respect to the unreinforced matrix can be appreciated.

The above microphotograph shows that the SCBAB is near uniformly distributed in the metal matrix and good bonding between Aluminium matrix and this reinforcement are achieved. Most notably, SCBAB and Aluminium are practically uniformly distributed along the specimen, i.e., the negligible variations of local fractions that can be appreciated, perhaps due to the inhomogeneity of the preform, which can be avoided by sufficient mixing of the Aluminium powder and SCBAB.
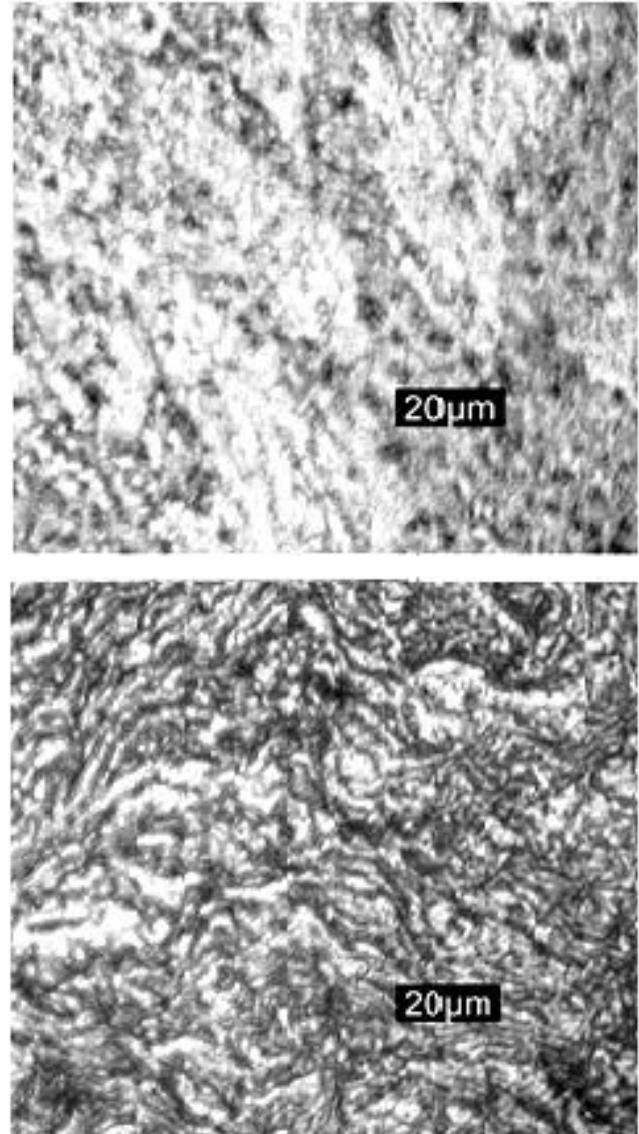
Figure 1. Optic microphotograph of Al-SCBAB composite specimen (above) and the non-reinforced matrix sample (down).

Both images were analyzed using image digital processing techniques with the software ImageJ version 1.43. This analysis allowed not only to improve the quality of the original images, but also to determine the fraction of grain area corresponding to each sample, which was 4.9 and 6.7 for the composite and the non-reinforced matrix, respectively. This is an indication that the grains of the composite have a lower Feret diameter [26], and at the same time, according to the Hall-Petch equation's, a higher hardness of the composite [27]. Then, during the composite conforming process and its

sintering at 600degC of temperature, the hardening of the material was produced by reduction of the grain size.

Hardness of Al/SCBAB composite and its unreinforced matrix

Table II shows the results of the Vickers hardness test.

Table 1. Hardness of the different groups of Al-SCBAB composite and its non-reinforced matrix.

Groups	Un-reinforced Matrix	Al-SCBAB Composite
1	86.5	92.3
2	87.5	93.5
3	89.0	93.5
4	89.0	93.9
5	92.5	96.5
Mean	88.9	93.94

It can be appreciated that the mean hardness increases from 88.9 HV for non-reinforced matrix to 93.94 HV for the Al-SCBAB composite, i.e., for the Aluminium with addition of sugarcane bagasse ash from boiler of the co-generator of the Cuban sugar factory. This hardness increment is in the order of that reported by other researchers [10,17,18,28,29] for composites of similar nature. However, the relative increase in hardness of the composite compared with its similar non-reinforced is relatively low, only of at 5.67 percent. At the same time, as mentioned before, the uncertainty in the measurement of this property was 3 %, so that the quantity measured is in the same order of the instrument uncertainty and only 2.67 units above it.

Through statistical tests (Pair Simple t test, ANOVA and others) it can be verified that the mean hardness of the composite significantly increased compared to the non-reinforced matrix. The SPSS software and the Pair Simple t test were employed for statistical analysis. As the null hypothesis it was established that the difference between the mean hardness for the non-reinforced matrix and Al-SCBAB composite is equal or greater than zero, and as alternative hypothesis that this difference is less than zero. It was obtained that for a confidence level of 0.05, difference between means is significant.

The hardness values increased possibly due to the presence of the hard ceramic phase of the bagasse ash (cristobalite and tridymite) and its interaction with the ductile matrix. As explained by Aigbodion and co-workers [22] referred by Lancaster, Lung and Sujan [17] as far as hardening behavior of the composites is concerned, the particle addition in the matrix alloy increases the strain energy in the periphery of the particles in the matrix, and these tendencies may be due to the formation of dislocations at the boundary of the ceramic particles by the difference in the thermo-expansion coefficient between the matrix and ceramic particles.

For AMCs that employ different agro-industrial wastes as reinforcement materials, it has been reported that hardness increases until certain limit when ash weight ratios with a silica high content increases [10, 17, 18, 20, 28, 29]. Thus, it is valid to assume that in this case the same can be observed. The hardness behavior together with other mechanical properties

and the wear with SCBAB percentage increase is a research aim for the future.

IV.   CONCLUSIONS

The basic conclusions that can be drawn through this research work are summarized below:

- A level of 4 % in weight of SCBAB in AMCs acts favorably as reinforcing material. In particular, it produces a significant increase of the hardness from 88.9 HV for the non-reinforced matrix to 93.94 HV for the matrix with addition of this ash.
- To sum up, the SCBAB studied shows good properties (ceramic materials-like), which makes them a good reinforcement material for AMCs.

Future studies will include both, the mechanical properties and wear behavior of AMCs reinforced with varied weight ratios of SCBAB.

BIBLIOGRAPHY

[1] R. P. Sharanabasappa and B.S. Motgi, IOSR J. Mech. Civ. Eng. **7**, 6 (2013).
[2] M. K. Surappa, Sadhana-Acad. Proc. Eng. Sci. **28**, 1 (2003).
[3] S. Fakirov, Mater. Todays. **18**, 10 (2015).
[4] D. B. Miracle, Compos. Sci. Technol. **65**, 15 (2005).
[5] A. Włodarczyk-Fligier, L.A. Dobrzański, M. Kremzer and M. Adamiak, J. Achieve. Mater. Manuf. Eng. **27**, 1 (2008).
[6] M. B. N. Shaikh, S. Arif and M. A. Siddiqui, Mater. Res. Exp. **5**, 4 (2018).
[7] G. Itskos, A. Moutsautsou, P. K. Rohatgi, N. Koukouzas, C. Vasilatos and E. Katsika, Coal Combust. Gasify. Prod. **3** (2011).
[8] R. Dasgupta, Int. Sch. Res. Newt. (ISRN Metall.), (2012).
[9] S. Haque, P. Kumar Bharti and A. Hussain Ansari, J. Min. Mater. Charact. Eng. **2014**, 2 (2014).
[10] K. K. Alaneme and E. O. Adewuyi, Metall. Mater. Eng. **19**, 3 (2013).
[11] H. Zuhailawati, P. Samayamutthirian, and C. H. Mohd Haizu, J. Phys. Sci. **18**, 1 (2007).
[12] T. V. Christy, N. Murugan and S. Kumar, J. Min. Mater. Charact. Eng. **9**, 1 (2010).
[13] K. K. Alaneme and A. O. Aluko, Scientia Iranica. Trans. A: Civ. Eng. **19**, 4 (2012).
[14] M.A. Hassan, T.C. Ofor, A.M. Usman and N.Y. Godi, Int. J. Eng. Sci. **3**, 8 (2014).
[15] P. Kumar Suragimath and G. K. Purohit, IOSR J. Mech. Civ. Eng. **8**, 5 (2013).
[16] H. Zuhailawati, M. N. Halmy, I. P. Almanar, A. A. Seman and B. K. Dhindaw, Int. J. Metall. Mater. Eng. **2**, 120 (2016).
[17] L.M. Lancaster, H. Lung, and D. Sujan, Int. J. Environ., Chem., Ecol., Geol., Geophys. Eng. **7**, 1 (2013).

[18] M. Anas, M. Zafaruddin Khan, Int. J. Sci. Adv. Res. Technol. **1**, 7 (2015).

[19] S. O. Adeosun, L. O. Osoba, and O. O. Taiwo, J. Chem., Mol., Nucl., Mater. Metall., Eng. **8**, 7, (2014).

[20] A. M. Usman, A. Raji, N. H. Waziri and M. A. Hassan, IOSR J. Mech. Civ. Eng. **11**, 4, (2014).

[21] A. Bahrami, M.I. Pech-Canul, C.A. Gutierrez and N. Soltani, J. Alloys. Compd. **644**, (2015).

[22] V.S. Aigbodion, S.B. Hassan, G.B. Nyior and T. Ause, Acta Metall. Sin. **23**, 2 (2010).

[23] E., Villar-Cociña, M. Frías, J.E. Hernández-Ruiz and H. Savastano Jr, Adv. Cem. Res. **25**, 3 (2013).

[24] L. Pino-Rivero, J.E. Hernández-Ruiz, E. Villar-Cociña and A. Alujas Díaz, Acad. J. Env. Sci. **6**, 8 (2018).

[25] T. A. Ferreira and W. Rasband, ImageJ User Guide. 1.43, 2010. In: https://www.iib.uam.es/portal/.../75233/.../2ef41251-249e-4f86-a8c7-bfd-1792988d3 Consulted in April 11, 2019.

[26] S. Al-Thyabat, N. J. Miles and T. S. Koh, Min. Eng. **20**, 1 (2007).

[27] J. R. Weertman, Mat. Sci. Ing.: A. **166**, 1-2 (1993).

[28] P. N. Jyothi and B. S. Bharath Kumar, Int. J. Lat. Res. Eng. Technol. **1**, 4 (2015).

[29] S.D. Saravanan, and M. Senthilkumar, Int. J. Eng. Technol. **5**, 6 (2014).

STUDY OF "DOCTOR BLADE" NANO-CuO PHOTOELECTRODE FOR PERSPECTIVE WATER SPLITTING

ESTUDIO DE FOTOELECTRODO DE CuO NANOESTRUCTURADO OBTENIDO POR "DOCTOR BLADE" PARA "WATER SPLITTING" PERSPECTIVO

A. Benedit-Cárdenas[a], R. Cabrera[a], A. Fundora[b], B. González[b], C. Laza[b] and E. Vigil[a,b†]

a) Facultad de Física, Universidad de La Habana, 10400 La Habana, Cuba; evigil@fisica.cu[†]
b) Instituto de Ciencia y Tecnología de Materiales (IMRE), Universidad de La Habana, 10400 La Habana, Cuba

In this paper, nano-CuO films, fabricated using the simple "doctor blade" technique, are studied as photoelectrodes in a two-electrode PEC cell for water photolysis. SEM analysis confirm the nanometric size of film grains and the photoelectrode porosity. The photocurrent behavior is studied, particularly, photocurrent transients for non-assisted and assisted water photolysis. Existing defects acting as carrier traps explain the different transient behaviors found. The existence of defects is explored using X-ray diffraction technique and the Williamson-Hall method.

En el presente trabajo, capas de CuO nanoestructurado, fabricadas utilizando la técnica simple de "doctor blade", se estudian como fotoelectrodos en una celda fotoelectroquímica de dos electrodos para la fotolisis del agua. Los análisis utilizando SEM confirman la dimensión nanométrica de los granos y la porosidad de los fotoelectrodos. Se estudia el comportamiento de la fotocorriente, en particular, sus transitorios, tanto para la fotolisis asistida como la no asistida. Los defectos existentes actuando como trampas de portadores explican los diferentes comportamientos encontrados. La existencia de defectos se analiza utilizando la técnica de difracción de rayos X y el método de Williamson-Hall.

I. INTRODUCTION

Cupric oxide (CuO) is a p-type semiconductor with a monoclinic crystal structure [1] and a direct bandgap of 1.2 eV [2]; for nanostructured CuO direct bandgaps values in the range of 1,4 eV – 1,9 eV have been reported [3–8]. Nevertheless, some researchers have reported indirect bandgaps in the same range [9–11]. All these reported values imply that CuO can convert solar radiation to photocurrent with a good efficiency [12]. Also, for practical use, an inexpensive technique is needed for photoelectrode fabrication because water splitting with solar light requires very large areas. On the other hand, larger CuO gap values have motivated the study of its nanostructured morphologies to split the water molecule (cohesion energy E_c = 1.23 eV) [4–7, 9–11]; since the smaller the nanocrystals, the larger the bandgap due to quantum effects [8, 13].

Photoelectrochemical cells (PEC) with a semiconductor acting as photoelectrode are used for water photolysis or "water splitting" [14–16]. The possibility to split the water molecule depends on the position of the band edges of the semiconductor with respect to water redox levels. The overall band edge positions must straddle the redox potentials of water. This means that the band edge of the conduction band must be above the redox potential of the Hydrogen Energy Reaction (HER) for water splitting without bias. This process is called non-assisted photoelectrolysis or photolysis. If the previous condition is not fulfilled, a bias will be needed for water splitting; in this case, the process is called assisted photoelectrolysis. For CuO,

Chauhan et. al. [17] have reported that a bias is necessary to carry out the photoelectrolysis. But, more recently; other authors have reported that water splitting is possible for nano-CuO photoelectrodes without any bias [4–7, 9–11]. Besides, porous nanostructured photoelectrodes allow a contact area between the semiconductor and the electrolyte larger than the visible flat area. This tridimensional interface improves PEC performance [3, 18, 19].

In the present work nanostructured CuO photoelectrodes are fabricated using the simple "doctor blade" technique [20–22] and their possible use for water photoelectrolysis is analyzed. To the best of our knowledge, this inexpensive technique has not been reported previously to obtain nano-CuO films. The photocurrent behavior for nano-CuO photoelectrodes is analyzed, particularly, photocurrent transients for non-assisted and assisted water photolysis. It is known that defects acting as carrier traps decrease the process efficiency in assisted and non-assisted water splitting [23]. The existence of defects is explored further processing X-ray diffraction patterns with the Williamson-Hall method [24,25].

II. MATERIALS AND METHODS

II.1. CuO films fabrication

CuO films were prepared using Aldrich nano-powder (particle diameter < 50 nm). First, the nanopowder was mortar disaggregated. Then, 2 mL of a 40 % distilled water and 60 % ethylene glycol solution per gram of CuO were used to prepare a nano-CuO colloidal suspension. This suspension

was deposited on optical glass, as well as, on conducting glass FTO Tec-15 by "doctor blading". Air drying of the CuO layer was followed by a heat treatment in air for an hour at T = 80°C to avoid brisk water evaporation. Afterwards, temperature was raised to 500°C for another hour to eliminate organics and to produce nanocrystals necking. This is a usual procedure in DSSC to favor charge conduction between nanocrystals [26]. Three samples were fabricated with this technique: NP 1, NP 2 and NP 3.

II.2. PEC cell photocurrent measurements

CuO films were evaluated as photoelectrodes inside a two-electrode photoelectrochemical cell (PEC) system (dimensions $2.5 \times 3.3 \times 4.0$ cm^3) as described elsewhere [27]. The CuO/FTO film acted as photoelectrode, a platinum wire as counter-electrode and distilled water as electrolyte. Photocurrent was measured in a lab-developed set-up with an Agilent 34410A multimeter attached to a PC. A 100 mW/cm^2 light intensity on the photoelectrode was established employing a halogen lamp, focusing lenses and a calibrated photodiode. The PEC and its electrical contacts were placed inside a Faraday box. Measurements were taken automatically using a Labview program which allows: to control the amperemeter, to plot photocurrent values in real time and to save all the data. Photocurrent behavior for light-on and off cycles was registered with and without an applied voltage of 1.2 V.

II.3. Morphological and structural analysis

Scanning electron microscopy (SEM) was performed with a JEOL 7600 instrument and 10kV acceleration voltage. Secondary electrons were used for surface imaging. The nano-powder and the prepared films were analyzed to detect the existence of defects using X-ray diffraction (XRD). Experiments were performed with an Empyrean Panalytical diffractometer, X' Pert3 Powder. XRD patterns cover the range $10° < 2\theta < 90°$, where θ is the Bragg reflection angle. Cu K_α radiation, $\lambda = 1.5406$ Å, was used for all XRD experiments.

III. RESULTS AND DISCUSSIONS

III.1. Scanning electron microscopy

The SEM image in Fig. 1 shows that the film is porous and formed by nanograins. This is advantageous because porosity gives rise to a tridimensional semiconductor/electrolyte interface with an area much larger than the visible photoelectrode area. This favors photocurrent increase. On the other hand, carriers must follow a tortuous path to the external contact and they must cross multiple interfaces between nanograins where recombination losses occur.

III.2. Photocurrent measurements

It is important that energy levels requirements for water splitting are fulfilled for "doctor bladed" films since when illuminated a current always exists without any bias. Fig. 2 shows an example of photocurrent versus time for zero bias; transients are observed when light is turned on and also when it is turned off. The behavior of these transients is analyzed and related to recombination centers.
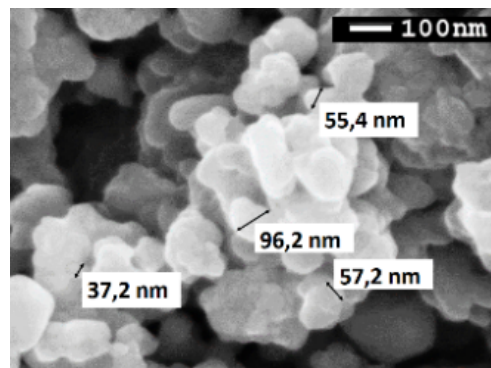
Figure 1. SEM image of a fabricated films.
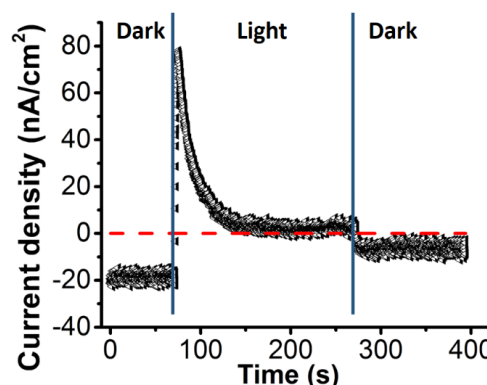
Figure 2. Photocurrent density vs time at zero bias. Transients for light-on and light-off conditions are observed.

Fig. 3 shows photocurrent transients for samples NP 1, NP 2 and NP 3, for bias voltage V = 0 V and V = 1,2 V. Figs. 3a and 3c allow to compare photocurrent values for these bias voltages during light-on periods. Photocurrent values are higher than one order of magnitude when voltage is applied. This indicates that bias favors the relative positions of CuO bands with respect to the electrolyte redox levels. One can observe in Fig. 3b that without an applied voltage and without light a negative current exists in all samples. Therefore, in the dark, the porous-nanostructured CuO photoelectrodes under study show a small electromotive force effect. This behavior has been previously reported for CuO [4,5,7,28]. It has been associated with weak chemical stability or charge accumulation in trap centers located at CuO interphases. No change was observed or registered for samples after repeated measurements, so, weak stability was discarded as the reason for negative dark current. The dark current must be due to accumulated charge release.

For both, non-assisted and assisted photoelectrolysis, photocurrent light-on and light-off transients were fitted with (1) and (2), respectively.

$$I(t) = I_{dark} + A\left(1 - e^{-\frac{1}{T_1}}\right) + B\left(1 - e^{-\frac{1}{T_2}}\right) + Q\left(1 - e^{-\frac{1}{T_3}}\right), \qquad (1)$$

$$I(t) = I'_{dark} + Ae^{-\frac{1}{T_1}} + Be^{-\frac{1}{T_2}} + Qe^{-\frac{1}{T_3}}. \qquad (2)$$

These linear combinations of exponentials have coefficients A, B and Q and characteristic times T_1, T_2 and T_3. I_{dark} and I'_{dark} are the current values in the dark. The second, third and fourth term in equations 1 and 2 have the sign of the coefficients A, B and Q, respectively. A negative coefficient means that the photocurrent decreases and viceversa.

Table 1 shows parameter values obtained by fitting (1) (light-on) for samples NP 1, NP 2 and NP 3. The values of are always positive; i.e., the photocurrent increases. The values of and change from negative to positive when the bias changes from 0 V to 1.2 V. Therefore, the effect associated

with T_2 and T_3 causes a photocurrent decrease when no bias is applied and an increase when a bias of 1.2 V is applied.

Figs. 3b and 3d show current transients when light is turned off. These figures show experimental values, as well as, those that result from fitting them with (refeq2). In this case, the values for the characteristic time are: $0.5\,s < T_1 < 0.6\,s$; $8,0\,s < T_2 < 8,5\,s$ and $24,5\,s < T_3 < 25,0\,s$. These values are similar to those that correspond to T_1, T_2 and T_3 for light-on transients (see Table 1). Similar values indicate that the same processes are involved during light-on and light-off transients.

The A coefficient term can be assigned to light-generated free carriers initially reaching the FTO contact. The delayed increase, shown in Fig. 3a and 3c and characterized by T_1, indicates that carriers do not reach the FTO contact inmediately. Most probably, transport occurs by trapping and detrapping as has been already reported in nanostructured solar cells [29, 30].

Table 1. Parameters in (1) for light-on photocurrent transients.

Samples	Bias	I_{dark} (nÅ/cm^2)	T_1 (s)	A (nÅ/cm^2)	T_2 (s)	B (nÅ/cm^2)	T_3 (s)	Q (nÅ/cm^2)
NP 1	0 V	-89	0.4	240	8.0	-91	25.2	-91
	12 V	495	0.6	291	8.0	96	25.0	27
NP 2	0 V	-9	0.7	51	8.0	-3	25.0	-40
	12 V	425	0.5	454	8.0	72	25.0	6
NP 3	0 V	-19	0.7	115	8.2	-44	25.0	-51
	12 V	442	0.5	564	8.2	88	25.0	18

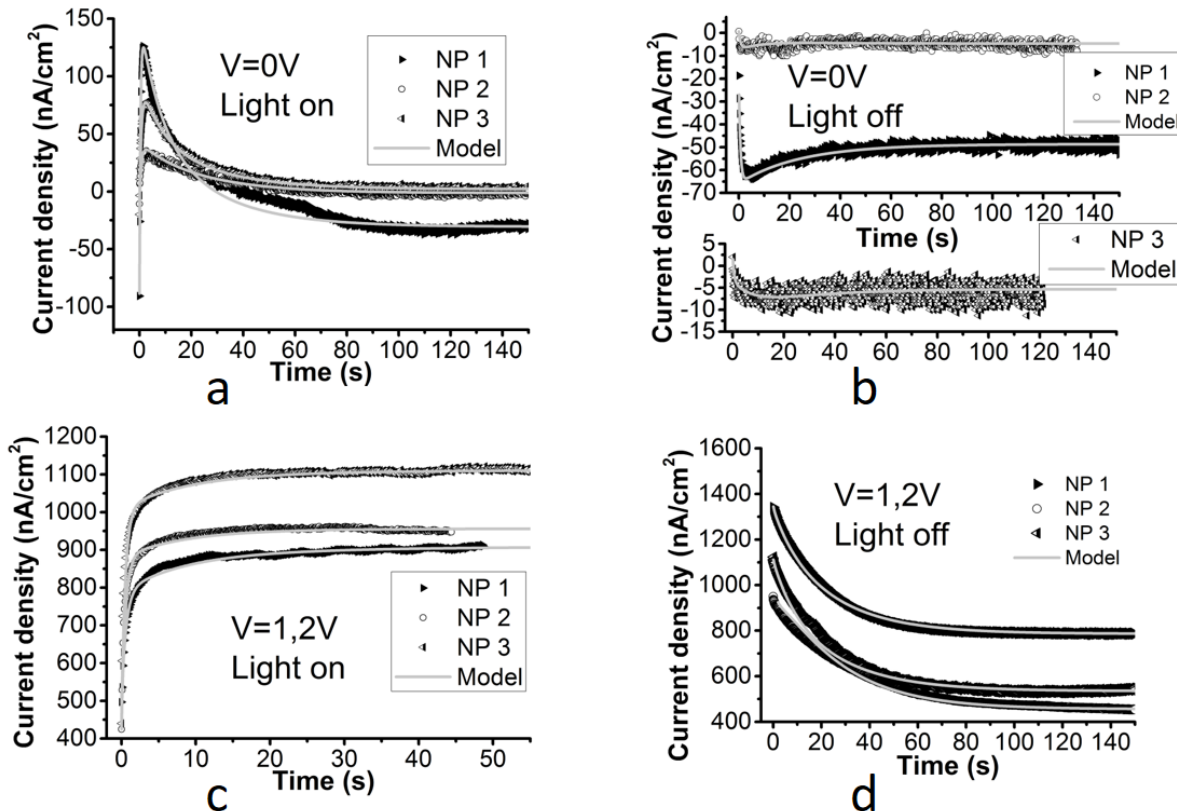Figure 3. Photocurrent transients for samples NP 1, NP 2 and NP 3. Experimental values are shown together with continuous line corresponding to (1) and (2). a) light-on, zero applied bias (V= 0 V) b) light-off, zero applied bias (V= 0 V). c) light-on, applied bias, V=1.2 V d) light-off, applied bias, V=1.2 V.

The values of coefficient and shown in Table 1 can be explained through the existence of traps with energy values in the bandgap of the semiconductor. Fig. 4a shows a band scheme with one trap level and it applies to "light-off" condition without bias. In this situation the electron trap (above the Fermi level) is mostly empty. When the photoelectrode is illuminated and free electrons generated (Fig. 4b) the electron trap captures them from the conduction band. Therefore, when the photoelectrode is illuminated with no voltage applied, the electron trap causes photocurrent to decrease, because some electrons are trapped and cannot behave as free carriers.
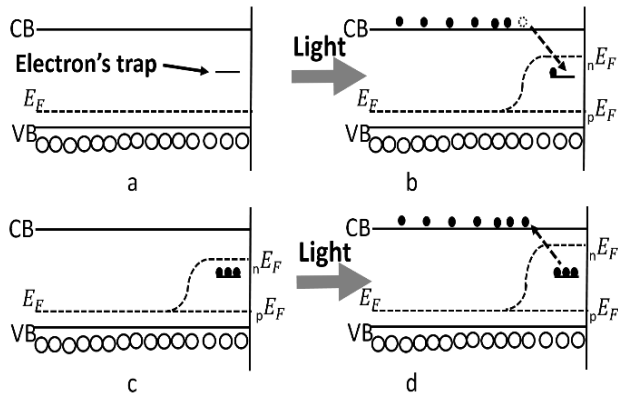

Figure 4. Band diagrams showing trap levels a) dark condition without an applied bias b) light- on condition without an applied bias c) dark condition with an applied bias d) light-on condition with an applied bias.

When a high enough bias is applied, the quasi-Fermi level can be above the electron trap level; therefore, this level will be mostly filled in the dark (see Fig. 4c). When the photoelectrode is illuminated (Fig. 4d), since traps are mostly filled, they are limited in capturing electrons and may inject electrons to the conduction band. (contrary to the non-assisted photoelectrolysis situation). Accordingly, an electron trap can decrease the photocurrent in non-assisted photoelectrolysis and increase the photocurrent in assisted photoelectrolysis.

Therefore, existing electron traps in the sample can be associated with the terms having the B and Q coefficients; i.e. to the processes characterized by T_2 and T_3. When no bias is applied, the values of the coefficients B and Q are negative (see Table 1), which means that there is a photocurrent decay (see Fig. 3a), in agreement with the behavior of the electron trap in Fig. 4b. When a bias is applied the values of the coefficients B and Q are positive (see Table 1), which means that the photocurrent increases (see Fig. 3c), in agreement with the behavior of the electron trap in Fig. 4d. It was impossible to fit the experimental curves to a sum of only two exponentials; three terms were necessary. This means that there are two trap levels with characteristic times T_2 and T_3, respectively. Therefore, photocurrent transients show the existence of more than one trap level and their deleterious effect on photocurrent. It is known that structural volume defects could create strains and they could act as carrier traps.

III.3. XRD analysis

The previous photocurrent analysis shows the existence of traps in the samples [31]. These can be due to volume or surface defects. Surface defects cause carrier losses at the surface of the nano-crystal where they are created but also during their transport to the contact. This is due to the barriers existing between crystallites and between nanograins; even though, usual heat treatment decreases the last ones by producing "necking" between nanocrystals. Strain-defects in the samples were analyzed applying the Williamson-Hall method to XRD patterns [32–34]. Fig. 5a shows CuO line pattern (from the version of 2011 of ICSD, collection code: 628616). Figs. 5b and 5c show nanopowder and films XRD patterns, respectively. For Williamson-Hall analysis, the diffraction peaks were fitted with a PseudoVoigt function in order to find the FWHM (full width at half maximum) of each one.

The crystallite size L, and the coefficient characterizing strain distribution ϵ, were calculated using Williamson-Hall method. This takes into account the contribution of both, the crystallite size and the strain distribution, to the peak width at half the maximum intensity (FWHM) [35], which is equal to

$$FWHM(2\theta) = 4\epsilon \frac{\sin\theta}{\cos\theta} + \frac{k\lambda}{L\cos\theta}, \qquad (3)$$

where θ is the Bragg angle, the peak width at half the maximum intensity ($FWHM$) is obtained from diffraction peaks in an intensity vs 2θ plot, λ is the wavelength and k is the Scherrer's constant ($k = 0.90$). For the Williamson-Hall plots shown in Figs. 5d and 5e, small peaks with poor fitting parameters according to PseudoVoigt analysis were discarded, as well as, two pairs of unresolved peaks: (111) with (200) plus (-222) with (004). Figs. 5d and 5e show the Williamson-Hall plots for the nano-powder and films, respectively. Values for the crystallite size and the coefficient characterizing strain distribution obtained from them are shown in Table III.3.

Table 2. Parameters obtained with the Williamson-Hall method.

	Powder	Film
Crystallite size (nm)	12.6 ± 0.4	20 ± 4
strain coefficient	$-(7 \pm 2) \times 10^{-4}$	$(1.0 \pm 0.8) \times 10^{-3}$

Comparison of crystallite value in Table III.3 with grain dimensions in Fig. 1 indicate that there are very few crystallites in a nanograin. According to values in Table III.3, crystallite size in the film increases with respect to its nanopowder size. This change can be associated with the heat treatment at 500°C during one hour. Heat treatment originates necking between nanograins [26] which increases their sizes.

Besides, according to (3), the slope of the line in Fig. 5e for the nano-CuO film is equal to four times the strain coefficient ϵ. Its value (m = 0.00384) is very close to zero; i.e. to no strain at all. Therefore, strain distribution contributes little to FWHM value. This points to a small number of strain-defects in the nanocrystal volume.

Considering this and that there are very few crystallites in a nanograin, a high number of defects in the disordered surfaces of nanograins must be the origin of the large number of traps responsible for low photocurrent values obtained. A low number of defects in the film nanocrystals supports Dimopoulos et. al. [36] who reports a carrier diffusion length of 40 nm in nanostructured CuO. This value is high enough so as to limit recombinations inside the nanocrystals.
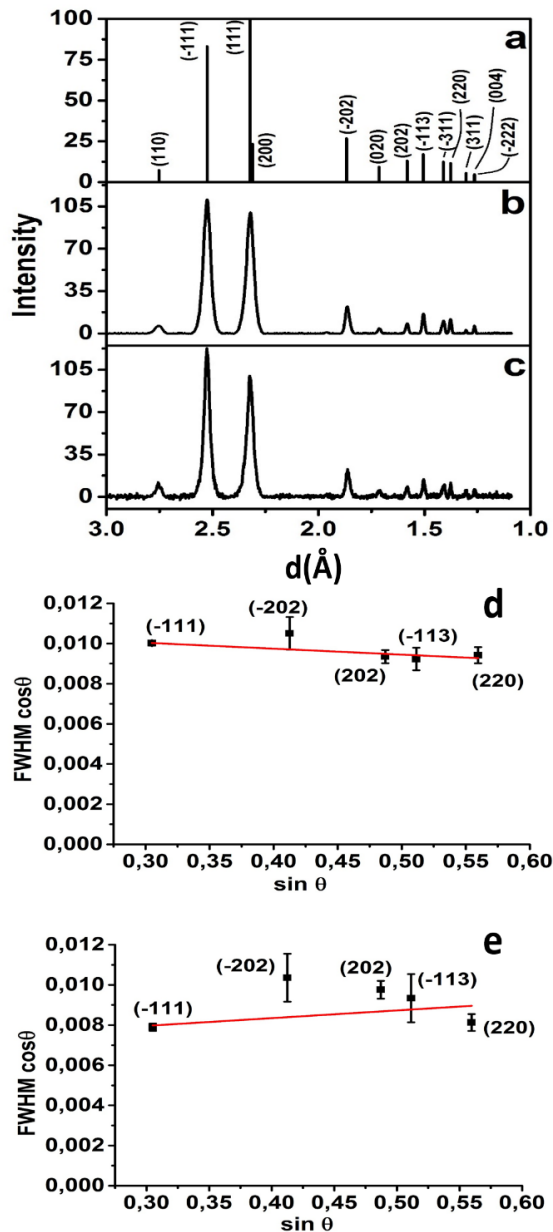
Figure 5. XRD analysis a) CuO line pattern (ICSD 628616) b) nanopowder XRD pattern c) film XRD pattern d) Williamson-Hall plot for nanopowder e) Williamson-Hall plot for films.

IV. CONCLUSIONS

CuO nanostructured photoelectrodes were fabricated using the inexpensive and simple "doctor blade" technique. SEM analysis showed the nanostructure morphology and porosity of deposited films. These are important characteristics to create a semiconductor-electrolyte tridimensional interface with an area much larger than the visible photoelectrode area. Photocurrent registered with zero bias corroborates that the non-assisted photoelectrolysis of water is possible with the "doctor blade" fabricated CuO films. Photocurrent values for voltage bias V = 1.2 V are one order of magnitude higher. This indicates that voltage bias favors the relative position of the CuO bands with respect to the electrolyte redox levels.

Photocurrent transients were fitted with a linear combination of three exponentials plus a dark current term. Three characteristic times were found for light-on, as well as, light-off transients; which are explained by the same mechanisms: carrier transport to the FTO contact and electron capture by two different trap centers.

Williamson-Hall analysis of XRD patterns indicate that strain defects practically do not exist in the nanocrystal volume. Therefore, the trap centers that affect photocurrent behavior must be surface and interface defects.

REFERENCES

[1] J.B. Forsyth and S. Hull, J. Phys.: Condens. Matter **3**, 5257, (1991).
[2] Handbook of Chemistry & Physics 71st Edition. Michigan: CRC Press; (1990).
[3] X.D. Wang, Y.F. Xu, B.X. Chen, N. Zhou, H.Y. Chen, D.B. Kuang and C.Y. Su, ChemSusChem **9**(20), 3012 (2016).
[4] A. Ray, I. Mukhopadhyay, R. Pati, Y. Hattori, U. Prakash and Y. Ishii, J. Alloys Compd. **695**, 3655 (2017).
[5] M. Patel, H.S. Kim, D.B Patel and J. Kim, J. Mater. Res. **31**, 3205 (2016).
[6] J.G. Lee, D.Y. Kim, J.H. Lee, M.W. Kim, S. An and H.S. Jo, ACS Appl. Mater. Interfaces **8**, 15406 (2016).
[7] W. Septina, R.R. Prabhakar, R. Wick, T. Moehl and S.D. Tilley, Chem. Mater. **29**, 1735 (2017).
[8] O. Langmar, C.R. Ganivet, P. Schol, T. Scharl, G. de la Torre and T. Torres, J. Mater. Chem. C **6**, 5176 (2018).
[9] A. Mahmood, F. Tezcan and G. Kardas, Int. J. Hydrogen Energy **42**, 23268 (2017).
[10] A. Kushwaha, R.S. Moakhar, G.K.L. Goh and G.K. Dalapati, J. Photochem. Photobiol., A **337**, 54 (2017).
[11] M. Einert, T. Weller, T. Leichtweis, B.M. Smarsly and R. Marschall, ChemPhotoChem **1**, 326 (2017).
[12] W. Shockley and H.J. Queisser, J. Appl. Phys. **32**, 510 (1961).
[13] Q. Zhang, K. Zhang, D. Xu, G. Yang, H. Huang and F. Nie, Prog. Mater Sci. **60**, 208 (2014).
[14] I. Roger, M.A. Shipman and M.D. Symes, Nat. Rev. Chem. **1**, 0003 (2017).
[15] C. Jiang, S.J.A. Moniz, A. Wang, T. Zhang and J. Tang, Chem. Soc. Rev. **46**, 4645 (2017).

[16] J. Joy, J. Mathew and S.C. George, Int. J. Hydrogen Energy **43**, 4804 (2018).

[17] D. Chauhan, V.R. Satsangi, S. Dass and R. Shrivastav, Bull. Mater. Sci. **29**, 709 (2006).

[18] Y.J. Jang, J.W. Jang, S.H. Choi, J.Y. Kim, J.H. Kim and D.H. Youn, Nanoscale, **7**, 7624 (2015).

[19] H.B. Oh, H. Ryu and W.J. Lee, J. Alloys Compd. **620**, 55 (2015).

[20] M.K. Nazeeruddin, A. Kay, I. Rodicio, R. Humphry-Baker, E. Mueller and P. Liska, J. Amer. Chem. Soc. **115**, 6382 (1993).

[21] K. Kalyanasundaram and M. Grätzel, Coord. Chem. Rev. **177**, 347 (1998).

[22] M.H. Habibi and M.H. Rahmati, Spectrochim. Acta, Part A **137**, 160 (2015).

[23] L. Zhang, H.H. Mohamed, R. Dillert and D. Bahnemann, J. Photochem. Photobiol., C **13**, 263 (2012).

[24] A.A. Akl, S.A. Mahmoud, S.M. Al-Shomar and A.S. Hassanien, Mater. Sci. Semicond. Process., **74**, 183 (2018).

[25] P.M. Shafi and A.C. Bose, AIP Adv. **5**, 057137 (2015).

[26] S. Nakade, M. Matsuda, S.Kambe, Y. Saito, T. Kitamura and T. Sakata, J. Phys. Chem. B **106**, 10004 (2002).

[27] I. Zumeta, R. Espinosa, J.A. Ayllón, X. Domènech and X. Rodri, Sol. Energy Mater. Sol. Cells **76**, 15, (2003).

[28] J. Oh, H. Ryu, W.J. Lee and J.S. Bae, Ceram. Int. **44**, 89 (2018).

[29] G. Schlichthörl, N.G. Park and A.J. Frank, J. Phys. Chem. B **103**, 782 (1999).

[30] C.R. McNeill, I. Hwang and N.C. Greenham, J. Appl. Phys. **106**, 024507 (2009).

[31] R. van de Krol, Principles of Photoelectrochemical Cells. Photoelectrochemical Hydrogen Production (Boston, Springer, 2012).

[32] V.P. Singh, D. Das and C. Rath, Mater. Res. Bull. **48**, 682 (2013).

[33] B. Choudhury, P. Chetri and A. Choudhury, J. Exp. Nanoscience **10**, 103 (2015).

[34] G.K. Williamson and W.H. Hall, Acta Metall. **1**, 22 (1953).

[35] E.J. Mittemeijer and U. Welzel, Modern Diffraction Methods (John Wiley & Sons, New York, 2013).

[36] T. Dimopoulos, A. Peić, P. Müllner, M. Neuschitzer, R. Resel and S. Abermann, J. Renew. Sustain. Energia **5**, 011205 (2013).

RADIOMETRY AND PHOTOMETRY: TWO VISIONS OF ONE PHENOMENON

RADIOMETRÍA Y FOTOMETRÍA: DOS VISIONES DE UN FENÓMENO

A.J. Batista-Leyva[†]

Instituto Superior de Tecnologías y Ciencias Aplicadas, Universidad de La Habana, 10400 Habana, Cuba; abatista@instec.cu

Radiometry, the measurement of the energy of electromagnetic waves (EMW) is one of the most important fields of experimental physics, reaching all Natural Sciences. Photobiology, for instance, is based in the quantification of the action of light on biological systems. The interaction of EMW with photosensitive cells (an eye in a mammalian, for instance) is key in the understanding of the interaction of living beings with their environment. A human eye is sensitive only to a fraction of the EM spectrum, ranging approximately from 400 to 760 nm. Eye's sensitivity varies with wavelength, growing from 400 to 555 nm, where it reaches a maximum, then monotonically decreasing up to 760 nm, where it reaches a value of zero. That is the reason of the existence of two different (though related) system of units. In one hand the radiometric or energetic units, characterizing the energy of a light beam and, on the other, the photometric units, characterizing the action of EMW upon a human eye. Both systems are often confused, and the extent and exact definition of their magnitudes misinterpreted, without a precise relation among related units of both systems. This is so even in some textbooks. In the present contribution we will try to clarify all these topics. This paper could be useful in courses of Optics, Ophthalmic Optics, Metrology and design of illuminating systems.

La medición de la energía de las ondas electromagnéticas (OEM), la radiometría, es uno de los campos de la física experimental con más aplicaciones prácticas. Cuantificar la acción de las radiaciones sobre los sistemas biológicos, es central para la fotobiología. La acción de las OEM sobre las células fotosensibles (los ojos de los mamíferos, por ejemplo) es de singular importancia para la comprensión de la interacción de los organismos con el ambiente que les rodea. Los ojos son sensibles solo a un rango limitado de frecuencias de las OEM que sobre ellos influyen. El ojo humano es sensible a radiaciones entre 400 y 760 nm aproximadamente, rango que se conoce como luz visible. En ese rango la sensibilidad cambia con la longitud de onda, creciendo con esta a partir de 400 nm, alcanzando un máximo a los 555 nm para decrecer monótonamente hasta hacerse cero a los 760 nm. Además de las unidades que caracterizan energéticamente la luz (llamadas radiométricas), se ha introducido otro sistema de unidades para caracterizar la respuesta del ojo humano a la luz (las magnitudes fotométricas). Ambos sistemas son a menudo confundidos, incluso en los libros de texto, mezclándose sus unidades. De igual forma sus nombres y definiciones se dan incorrectamente, sin precisarse la relación entre ambos sistemas. En la presente contribución trataremos de esclarecer estos aspectos. El artículo puede ser útil en la enseñanza de la Óptica, la Óptica Oftalmológica, la Metrología y el diseño de la iluminación.

I. INTRODUCTION

The study of the interaction of electromagnetic waves (EMW) with matter is a major branch in physics. The incidence of electromagnetic energy on different systems provokes a plethora of phenomena having both theoretical an experimental importance. In order to quantify the action of EMW upon a system, a group of physical magnitudes has been developed, which has a common ground: measuring the power of the electromagnetic radiation that interacts with the system. But measuring only the power is not always enough: the effects depend also on the angle of incidence of the radiation upon a surface, the solid angle that form the rays exciting from a source and other elements. Some times it also depends on the wavelength of the radiation. It implies that is necessary to introduce a set of physical magnitudes that are used to characterize the light - matter interaction in different physical situations. All these magnitudes are grouped under the global term of radiometric magnitudes''. Radiometry is, according to this, the measurement of the energy content of electromagnetic fields propagating through a region, and the determination of how this energy is transferred from a source, through a medium, and to a detector [1]. Normally radiometry is restricted to the range of infrared, visible and ultraviolet radiation, but it could also reach the microwave spectrum. The reader must be aware that in some areas of Astronomy they call photometry to what is called radiometry in Optics.

Radiometry has several branches, depending on the wavelength range of the EMW. Infrared radiometry is mainly (but not only) used in astronomy, due to the lower absorption of infrared radiation by the atmosphere, when compared to visible and ultraviolet radiation [2]. Another use is in the measurement of the temperature of objects and gases. Microwave radiometry is used in the measurement of EMW with frequencies (wavelengths) from 300 MHz (1 m) to 300 GHz (1 mm) [3]. It has applications in many different areas, from temperature measurement to radio broadcasting [4]. Ultraviolet radiometry measures EMW with wavelengths

from 10 nm to 400 nm [5] and has among it main purposes the determination of the doses absorbed due to sun light and clinical procedures [6].

Visible and near-visible radiometry measures the power (and related quantities) of light in a range of wavelength for which a human eye could develop visual sensations. Though the spectral range of visibility changes from person to person, it approximately reaches wavelengths from 400 nm to 760 nm, while the near visible range spans approximately from 360 - 830 nm [1, 7]. The objective measurement of these EMW is the same in all range of wavelengths and consists in determining the output of a detector, calibrated previously at different energies and wavelengths. But the human eye has different physiological responses to different wavelengths. Its sensitivity reaches a maximum at 555 nm and decreases to zero for wavelengths bellow 400 nm and above 760 nm, approximately. Though this effect is subjective, because is related with human perception, it has a great importance for color industry, Ophthalmology, illumination design, art and other areas where the visual sensation is central. Due to this reason, a separated set of physical magnitudes has been developed to deal with the measurement of light, considering its action upon a human eye. This set is known as "photometric system of units".

As important as this subject is, in physics textbooks it is most of times poorly treated, varying the name and definition of the units from one book to another. It is also omitted the way to calculate or measure the photometric quantities starting from the radiometric ones. The aim of the present contribution is to define precisely both systems of units, emphasizing on their relation and practical applications. To facilitate its use in different countries, the names of different units when defined will be given in English and in Spanish (in brackets). This paper could be useful in courses of Optics, Ophthalmic Optics, Metrology and design of illuminating systems.

II. RADIOMETRIC MAGNITUDES

There exist two kind of radiometric magnitudes. The first one does not take into account the spectral composition of the light, measuring only its overall power or related units. By this reason these are called integral magnitudes. The second set expresses the power and related units for a narrow interval of wavelengths and are termed spectral magnitudes. We will use in what follows the recommendations of the International Standard Office of using the suffix e (for energetic) to distinguish the radiometric units. Also the spectral units are distinguished by a suffix λ, though sometimes the dependence with the wavelength could be specified putting λ into brackets. Another specification that is rarely used is the suffix Ω for directional units. Readers must be aware of the fact that all the formulae developed below are valid in the approximation of geometrical optics.

Integral Radiometric Magnitudes: The fundamental radiometric magnitude is the radiant energy (energía radiante) and is defined as the energy of the EMW. In the International System of Units is measured in Joules (J). The common symbol is Q_e, though other symbols (as W_e or E_e)

are also used in the literature. Derived from this magnitude are defined:

- *Radiant Flux* Φ_e (Flujo de energía radiante o flujo radiante): Radiant energy emitted, reflected, transmitted or received per unit time, and is measured in watt (W). This is the power transported by the EMW. If we are dealing with an isotropic source (emitting equal amounts of energy per second in all directions) it is possible to determine the radiant flux measuring the energy arriving to an unit area perpendicular to the flux, and dividing this amount by the time the process takes. If, on the contrary, the flux is anisotropic it is necessary to divide the illuminated field in areas small enough to consider the radiant flux $d\Phi_e$ as uniform, being the total flux the sum of its value over all the differential areas: $\Phi_e = \int_S d\Phi_e$.

- *Radiant intensity* $E_{e,\Omega}$ (Intensidad radiante): Is the radiant flux emitted, reflected, transmitted or received, per unit solid angle. As the suffix indicates, it is a directional quantity. Is measured in watt per steradian (W·sr^{-1}). This unit is of paramount importance for defining the photometric units. Remember, the suffix Ω could be omitted. The luminous flux of a source is a magnitude that characterizes it, though it could be increased or decreased by optical means: focusing the light of the source with convergent lenses will increase E_e. An HeNe laser, for instance, has a small radiant flux (is a low power light source), but has a huge radiant intensity, due to its extremely focused beam.

- *Irradiance* I_e (Irradiancia) Radiant flux received by a surface per unit area. Its unit is watt per square meter (W·m^{-2}). In Optics, this is the fundamental observable, and is calculated as the average value of the modulus of the Poynting vector in a time lapse much larger than the period of the EMW: $I_e = \langle |\vec{S}| \rangle_\tau$, $\tau \ll T$. In some textbooks is erroneously termed intensity. For a point like source, the irradiance decreases with the square of the distance between the source and the point where it is measured.

- *Radiance* $L_{e,\Omega}$ (Radiancia) Radiant flux emitted, reflected, transmitted by a surface, per unit solid angle per unit projected area. Measured in watt per steradian per square meter (W·sr^{-1}·m^{-2}). If the source is not isotropic, the radiation field most be divided in differential solid angles, small enough to consider the radiance constant, and then integrate over all the illuminated region.

- *Radiosity* J_e (Radiancia emitida) Radiant flux leaving a surface per unit area. It includes the emitted, reflected and transmitted electromagnetic radiation. Its unit is watt per square meter (W·m^{-2}).

- *Radiant exitance* M_e (Excitancia radiante o luminosidad) Radiant flux emitted by a surface, being the emitted component of the radiosity. Is obviously measured in W·m^{-2}.

These are the most frequently used magnitudes. For a complete list of radiometric units, the reader is invited to check reference [8,9].

Spectral radiometric magnitudes: This set of magnitudes is related with the distribution of the energy transported by the EMW along the wavelength (or frequency) spectrum spanned by it, the so called spectral distribution. In order to characterize this distribution, a density function has to be defined. There are two possibilities, the first one is to determine the density for an infinitesimal interval of wavelengths ($d\lambda$), the second for an infinitesimal interval of frequencies ($d\nu$). As $\lambda \cdot \nu = c$ both magnitudes are related by the expression

$$d\lambda = \frac{c}{\nu^2}d\nu, \tag{1}$$

where a minus sign has been ignored; it only indicates that λ increases when ν diminishes.

The first spectral magnitude is the *spectral flux* (densidad espectral de flujo) defined as the radiant flux per unit frequency or wavelength. The first is defined as

$$\Phi_{e,\nu} = \Phi_e(\nu) = \frac{d\Phi_e}{d\nu}, \tag{2}$$

measured in W·Hz^{-1}.

The radiant flux per unit wavelength is defined as:

$$\Phi_{e,\lambda} = \Phi_e(\lambda) = \frac{d\Phi_e}{d\lambda}, \tag{3}$$

measured in W·m^{-1}. In some books it is often used the (incorrect) form W/nm. Note that this last form, though expresses correctly the definition, is not correct from the point of view of the standard organizations, as expressed in Ref. [10].

Other spectral magnitudes are:

- *Spectral intensity* $E_{e,\Omega,\nu}$ or $E_{e,\Omega,\lambda}$ (Intensidad radiante espectral) is the radiant intensity per unit frequency or wavelength. The first one is measured in W·sr^{-1}·Hz^{-1}. The latter is commonly measured in W·sr^{-1}·m^{-1} or (incorrectly) W·sr^{-1}·nm^{-1}.

- *Spectral irradiance* $I_{e,\nu}$ or $I_{e,\lambda}$ (Irradiancia espectral) Irradiance of a surface per unit frequency or wavelength. The units are W·m^{-2}·Hz^{-1} and W·m^{-3}, which means watt per unit area per unit wavelength, not watt per unit volume.

- *Spectral radiance* $L_{e,\Omega,\nu}$ or $L_{e,\Omega,\lambda}$ (Radiancia espectral) Radiance of a surface per unit frequency or wavelength. The latter is commonly measured in W·sr^{-1}·m^{-2}·nm^{-1} or in the more appropriate form W·sr^{-1}·m^{-3}. In terms of frequency the units are W·sr^{-1}·m^{-2}·Hz^{-1}.

- *Spectral radiosity* $J_{e,\nu}$ or $J_{e,\lambda}$ (Radiancia emitida espectral) Is the radiosity of a surface per unit frequency or wavelength. Units are W·m^{-2}·Hz^{-1} or W·m^{-3}.

The reader could derive other spectral quantities following the definitions above. It is important to recall that the suffix should be used only to avoid confusions. If the context is clear, suffix could be eliminated. It is usually preferred to write the wavelength or the frequency dependence of the magnitude as a function instead of a suffix ($I_e(\lambda)$ instead of $I_{e,\lambda}$, for instance).

II.1. Relation between integral and spectral radiometric magnitudes

As far as the spectral quantities are the value of the quantity in a narrow (infinitesimal) range of frequencies or wavelengths, they act as a density function, so the relation (using as an example the irradiance) is

$$I_e(\lambda) = \frac{dI_e}{d\lambda}. \tag{4}$$

Due to the above mentioned relation $\lambda \cdot \nu = c$, it is easy to obtain that

$$I_e(\lambda) = \frac{\nu^2}{c}I_e(\nu), \tag{5}$$

which is equivalent to

$$\lambda I_e(\lambda) = \nu I_e(\nu). \tag{6}$$

Starting from the above equations, the following useful relations are easily obtained

$$I_e = \int_0^\infty I_e(\lambda)d\lambda = \int_0^\infty I_e(\nu)d\nu, \tag{7}$$

or

$$I_e = \int_0^\infty \lambda I_e(\lambda)d\ln\lambda = \int_0^\infty \nu I_e(\nu)d\ln\nu. \tag{8}$$

Similar procedure could be applied to all the radiometric units. Eqs. (4-8) were derived for vacuum. In another medium with refraction index n, (1) changes to

$$d\nu = \frac{c}{n\lambda^2}d\lambda, \tag{9}$$

This correction must be introduced to other relations.

III. HUMAN VISION

The process of human vision is very complex, and includes physical, physiological and psychological phenomena. The physical part is the path of light rays through the cornea, a limiting aperture (iris), the lens or crystalline and the vitreous humor, to be ideally focused on the retina. There, the light energy is transformed by a complex system of biochemical reactions, occurring in the sensitive cells, into a nervous signal that travels to the brain by the optical nerve.

In the visual cortex of the brain, the signals are interpreted according to the previous experience of the subject, to understand the forms of the objects as well as the contexts where they are.

A human eye does not perceive equally all the wavelengths contained in a light beam arriving to retina. A normal eye has its maximum sensibility for monochromatic light with wavelength $\lambda_m = 555$ nm ($\nu_m = 5.401 \cdot 10^14$ Hz). It means that two monochromatic beams having equal radiant flux, one of them with $\lambda_1 = \lambda_m$ and the other with $\lambda_2 \neq \lambda_m$ would be perceived differently by a normal eye, in such a way that the beam with λ_m would be seen as more bright. The larger the difference between λ_m and λ_2, the fainter is seen the later beam, until for a limiting value of wavelength the eye looses its sensitivity: the light does not provoke a visual sensation. These limits are different from person to person and change with age, but conventionally are located at 400 nm (below which is the ultraviolet zone) and 760 nm (above which is infrared). The so called enhanced visual zone is located between 360 and 830 nm [1].

An experiment to quantify this effect could be schematically described as follows: the person subject of the experiment sees with only one eye the beams λ_1 and λ_m alternatively. Let us suppose that initially the radiant flux of both beams is equal, $\Phi_{e,i}(\lambda_1) = \Phi_e(\lambda_m)$. It is obvious that the first beam is perceived fainter by the eye. Then, its radiant flux is increased until (for a given value $\Phi_{e,f}(\lambda_1)$)the subject finally declares that sees both beams equally intense. The value of $\Phi_{e,f}(\lambda_1)$ is registered, and the experiment is repeated for another wavelength. At the end of the experiment there is a table of values of radiant flux for different λ at which these radiations are seen equally intense when compared with λ_m. The eye sensitivity function (función visibilidad), also known as luminous efficiency function is defined as

$$V(\lambda) = \frac{\Phi_e(\lambda_m)}{\Phi_{e,f}(\lambda)}. \tag{10}$$

It is obvious from the definition that $V(\lambda) \leq 1$, being equal for $\lambda = \lambda_m$. The actual procedure to construct $V(\lambda)$ includes the repetition of this experiment for a great number of young healthy eyes. The average values has been declared by agreement as the photopic spectral luminous efficiency function by the International Committee of Illumination (or CIE, the French acronym of Commission Internationale de l'Eclairage). These values are periodically rectified to include new experimental data.

The word photopic indicates vision in bright light, as opposed to scotopic, related with vision in dim light. The cells of the retina responsible for this photopic response are called cones. There are three different types of cones, having maximum sensitivity in the range of red, green and blue, respectively. From the combined response of the three types of cells, the brain determines the color of incident light.

The retina also contains another type of photosensitive cells, the rods. Under low light, cones are almost blind and only rods are responsible of vision. The curve constructed in

this illumination condition is known as scotopic efficiency function. The maximum of this curve is shifted to lower wavelengths (approximately 507 nm). In an intermediate range of irradiances (the so called mesopic vision) does not exists an accepted standard.
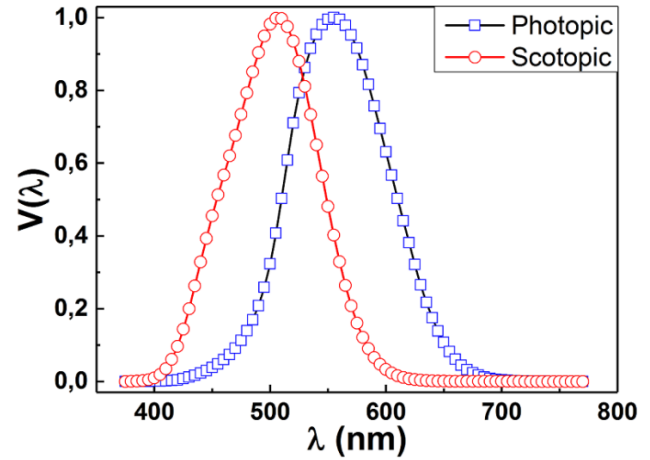
Figure 1. Photopic and scotopic eye sensitivity curves for a young healthy eye (CIE standard observer, see text).

In Fig. 1 the photopic and scotopic average response curves of a normal eye (the so called CIE standard observer) are represented. It is important to remember that it is not an analytic elementary function; the continuous line is only a spline connecting the isolated measured points. In the appendix the reader could find a Table of both photopic and scotopic eye efficiency functions.

IV. PHOTOMETRIC SYSTEM OF UNITS AND THEIR MEASUREMENT

When the measurements of light beams is focused in their visual effect, it is obvious that their energetic description is not enough. New magnitudes have to be introduced in order to correctly describe the interaction light - eye. The set of units are analogous to energetic ones, only are weighted by the wavelength dependence of eye response $V(\lambda)$.

IV.1. Photometric magnitudes

The fundamental magnitude in photometry is the *luminous intensity* $I_v(\lambda)$ (intensidad luminosa). It is defined as the radiant intensity emitted by a light source, weighted according to the visual sensation it provokes. Its unit is named candela (also candela in Spanish, it is a fundamental unit of the International System), being one candela (not candle, the name of the unit has changed) the luminous intensity in a given direction of a source emitting monochromatic radiation of 540 THz (555.016 nm) having a radiant intensity of 1/683.002 W/sr.

Note that the definition does not use the maximum of $V(\lambda)$, but a very close wavelength. The suffix v is used for all photometric units to avoid confusion. The candela is abbreviated as cd. Usually the constant in the definition is rounded to 683.

The second photometric magnitude is the *luminous flux* $\Phi_v(\lambda)$ (flujo luminoso). This is the radiant flux weighted according to its visual sensation. It is the product of the luminous intensity by the solid angle it is emitted. Its unit is named lumen (lm), which relates to candela as

$$\Phi_v(\lambda) = I_v(\lambda) \cdot \Omega, \qquad \rightarrow \qquad 1\text{lm} = 1\text{cd} \cdot \text{sr}. \tag{11}$$

Comparing the definitions of luminous intensity and luminous flux, it is easy to see that a light beam with $\nu = 540$ THz having a luminous flux of 1 lm has a radiant flux $\Phi_e = 1/683$ W. It means that one Watt of this light creates a luminous flux of 683 lm. As far as the luminous flux is easier to measure than the luminous intensity, (11) is used to define the standard of the unit candela, as will be seen below.

What if the wavelength is another, say $\lambda \neq \lambda_m$? In this case the visual sensation will be lower, by a factor determined by the sensitivity function. From Eq. (10)

$$\Phi_v(\lambda) = V(\lambda) \cdot \Phi_e(\lambda_m) = 683 \cdot V(\lambda) \cdot \Phi_e(\lambda). \tag{12}$$

Note that the constant 683 in (12) has dimensions of lm·W^{-1}. It is called the maximum spectral luminous efficacy (eficacia luminosa espectral máxima) of radiation for photopic vision, Km;ph = 683 lm·W^{-1}. In situations of low illumination, the scotopic constant $K_{m,sc} = 1700$ lm·W^{-1} has to be used. For the intermediate or mesopic regime no standard value has been defined.

Other photometric magnitudes are:

- *Illuminance E_v* (Iluminación) Luminous flux per unit area arriving at a surface perpendicular to it.

$$E_v = \frac{\Phi_v}{S}. \tag{13}$$

  The unit is named lux (lx). 1 lx = 1 lm·m^{-2}. This is the photometric equivalent of irradiance.

- *Luminance L_v* (Luminancia) Is the luminous intensity per unit area emitted by a source perpendicular to its surface.

$$L_v = \frac{I_v}{S}. \tag{14}$$

  Its unit is some times named nitio (nt), 1 nt = 1 cd·m^{-2}, though the name has fallen in disuse. This magnitude is related with the photometric magnitude radiance.

- *Luminous exitance M_v* (Emitancia luminosa) Luminous flux emitted per unit area of a surface perpendicular to it.

$$M_v = \frac{\Phi_v}{S}. \tag{15}$$

  the unit is also the lux (lx). Photometric equivalent of radiant exitance.

- *Luminous exposure H_v* (exposición luminosa) Is the time integral of illumination, measured in lx·s.

The general relation between radiometric (Rad) and photometric (Phot) magnitudes, for monochromatic light of wavelength λ is

$$\text{Phot} = 683 \cdot V(\lambda) \cdot \text{Rad}. \tag{16}$$

In case we are dealing with polychromatic radiation it is necessary to integrate the contribution of each interval of wavelengths of the spectral distribution spanned by the radiometric quantity, to obtain the photometric one.

For instance, a luminous beam with an spectral irradiance $I_e(\lambda)$ illuminates a surface with an illuminance

$$E_v = K_m \int_{\lambda_{min}}^{\lambda_{max}} I_e(\lambda)V(\lambda)\mathrm{d}\lambda. \tag{17}$$

In (17) the integration interval extends to all the wavelengths included in the visible range $\lambda_{min} = 400$ nm, $\lambda_{max} = 760$ nm. Of course, the actual range could be a subset of the visible, and the limits could be narrower. There exists situations where the extended visible range should be used.

To calculate the integral of (17) it is important to remember that $V(\lambda)$ does not have an analytic expression, so the integral must be calculated numerically, using the equation

$$E_v = K_m \sum_{i=1}^{n} I_e(\lambda_i)V(\lambda_i)\Delta\lambda. \tag{18}$$

If Table IV.1 is used to calculate the corresponding photometric magnitude via Eq. (18), i goes from 1 to 80, and the $V(\lambda_i)$ are taken from the photopic or scotopic column, depending on the conditions and $\Delta\lambda = 5$ nm. The tabulated values of $V(\lambda_i)$ has been determined by CIE at 1 nm increments. An interpolation process must be used if a finer mesh is needed.

The relation between irradiance and illumination is particularly important, because some times you have an instrument to measure illuminance and need the value of irradiance or vice versa as in Ref. [12], where a cellphone is used to test Mallus law and to record the diffraction pattern of a green laser monochromatic light through a thin long slit. In the second case it is easy to test, applying (16) that $I_e(\lambda_{laser}) \propto E_e(\lambda_{laser})$. As long as the equation that describes the irradiance distribution could be written in terms of the irradiance of the light diffracted according to a given angle φ divided by the irradiance of the central maximum, is simple to find that $I_e(\varphi)/I_0 \propto E_e(\varphi)/E_0$.

In case of a polychromatic source, there are two possibilities, firstly, the light emitted by the source is a superposition of some discrete spectral lines, a lamp of sodium or mercury, for instance. For each of the discrete wavelengths the irradiance is proportional to the illuminance, being the integral quantities also proportional.

The second possibility occurs when the light source emits a continuous spectrum, and the light does not travel through a dispersing system, as in Ref. [12] when studying Malus

law. Even in this case, considering that $I_e(\lambda)$ is a continuous function we could apply the mean value theorem to (17) and obtain

$$I_e(\lambda_{av}) = \frac{E_v}{K_m \int_{\lambda_{min}}^{\lambda_{max}} V(\lambda)\mathrm{d}\lambda}, \qquad (19)$$

where $\lambda_{av} \in (\lambda_{min}, \lambda_{max})$. This means that the action of the polychromatic source creates an illumination equal to that of a monochromatic source of wavelength λ_{av} and irradiance given by (19). Again the irradiance is proportional to illumination.

Table 1. Photopic and Scotopic Spectral Luminous Efficiency Functions.

λ (nm)	Phot	Scot	λ (nm)	Phot	Scot
375	0.00002		575	0.91540	0.16020
380	0.00004	0.00059	580	0.87000	0.11212
385	0.00006	0.00111	585	0.81630	0.08990
390	0.00012	0.00221	590	0.75700	0.06550
395	0.00022	0.00453	595	0.69490	0.04690
400	0.00040	0.00929	600	0.63100	0.03315
405	0.00064	0.01852	605	0.56680	0.02312
410	0.00121	0.03484	610	0.50300	0.01593
415	0.00218	0.06040	615	0.44120	0.01088
420	0.00400	0.09660	620	0.38100	0.00737
425	0.00730	0.14360	625	0.32100	0.00497
430	0.01160	0.19980	630	0.26500	0.00334
435	0.01684	0.26250	635	0.21700	0.00224
440	0.02300	0.32810	640	0.17500	0.00150
445	0.02980	0.39310	645	0.13820	0.00101
450	0.03800	0.45500	650	0.10700	0.00068
455	0.04800	0.51300	655	0.08160	0.00046
460	0.06000	0.56700	660	0.06100	0.00031
465	0.07390	0.62000	665	0.04458	0.00021
470	0.09098	0.67600	670	0.03200	0.00015
475	0.11260	0.73400	675	0.02320	0.00010
480	0.13902	0.79300	680	0.01700	0.00007
485	0.16930	0.85100	685	0.01192	0.00005
490	0.20802	0.90400	690	0.00821	0.00004
495	0.25860	0.94900	695	0.00572	0.00003
500	0.32300	0.98200	700	0.00410	0.00002
505	0.40730	0.99800	705	0.00293	0.00001
510	0.50300	0.99700	710	0.00209	0.00001
515	0.60820	0.97500	715	0.00148	0.00001
520	0.71000	0.93500	720	0.00105	0.00000
525	0.79320	0.88000	725	0.00074	0.00000
530	0.86200	0.81100	730	0.00052	0.00000
535	0.91485	0.73300	735	0.00036	0.00000
540	0.95400	0.65000	740	0.00025	0.00000
545	0.98030	0.56400	745	0.00017	0.00000
550	0.99495	0.48100	750	0.00012	0.00000
555	1.00000	0.40200	755	0.00008	0.00000
560	0.99500	0.32880	760	0.00006	0.00000
565	0.97860	0.26390	765	0.00004	0.00000
570	0.95200	0.20760	770	0.00003	0.00000

IV.2. Realization of the photometric units

In order to experimentally define the photometric units, it is important to construct a standard. This is of paramount importance for the candela, which is a fundamental unit of the International System. There are two paths, one is

to construct a source which emits radiation with a fixed luminous intensity (a source standard) and the other is to construct a calibrated measurement system (a detectorbased standard).

The first method construct a luminous source in the following way. A cylinder filled with platinum (Pt) is heated using high frequency electric currents, until it reaches the fusion temperature of Pt, 2046.6 K. This temperature is kept constant along the cylinder. In this conditions, and with the geometry of the installation, each square centimeter of the cylinder emits 60 cd in the perpendicular direction. For a detailed description the reader is invited to see Ref. [11], epigraph 8.

The second method consist in the construction of a calibrated sensor. The sensor is illuminated by a point-like source with a known relative spectral power distribution $S(\lambda)$, usually one of the CIE Standard Illuminants, formed by a black body at a given temperature; illuminant A, for instance, is a black body at 2856 K.

The light of the source passes through a filter which mimics $V(\lambda)$. The action of the filter is to subtract for each range of wavelengths $\Delta\lambda$ centered at λ_i the amount of power determined by $V(\lambda_i)$, calculated by (10).

The absolute spectral power responsivity $s(\lambda)$ (defined as the intensity of the electric current produced in the sensor per watt of incoming radiation, and measured in A/W) of the entire photometer is calibrated using a very precise light source; with these elements, the illuminance responsivity (in A/lx) of the detector is

$$s_v = \frac{A \int_{\lambda_{min}}^{\lambda_{max}} S(\lambda)s(\lambda)\mathrm{d}\lambda}{K_m \int_{\lambda_{min}}^{\lambda_{max}} S(\lambda)V(\lambda)\mathrm{d}\lambda}. \qquad (20)$$

In (20) A is the area of a window in front of the detector that limits the amount of light arriving to it; this area is measured with a calibrated instrument. The distance between the light source and the aperture is fixed taking into account that the solid angle subtended from the source to the aperture should have a known value. In this way the responsivity in Ampere per lux could be converted to A/cd.

For a more detailed description of the detector standard of cd, visit the web page at the National Institute of Standards and Technology NIST, Ref. [13]. NIST has also developed a standard for the lumen [14] as well as for other photometric units [15].

V. CONCLUSIONS

In every experimental or theoretical situation in Optics it is important to understand the type of magnitude (radiometric or photometric) you are interested in, and the aim of the measurement or the calculation. The lack of precision leads to misunderstandings and ambiguities or, in worst cases, errors. Textbooks should be analyzed searching for this kind on errors before using them in a course.

It is important to note that the name of the different magnitudes some times differ from book to book, being necessary to consult the names approved by the standard organizations.

BIBLIOGRAPHY

[1] Michael Bass (ed.), Handbook of Optics Volume II - Devices, Measurements and Properties, 2nd Ed., McGraw-Hill (1995).

[2] F.J. Low, G.H. Rieke, The Instrumentation and Techniques of Infrared Photometry, Editor: N. Carleton, Methods in Experimental Physics, Academic Press, Volume 12, Part A, 415-462 (1974).

[3] https://en.wikipedia.org/wiki/Microwave, Accessed 01/07/2019.

[4] J. Polívka, Int. J. of Infrared and Millimeter Waves, 16, 1593-1672 (1995).

[5] https://en.wikipedia.org/wiki/Ultraviolet, Accessed 01/07/2019.

[6] D. R. Grimes, Adv Exp Med Biol. 996,349-360 (2017).

[7] https://www.nist.gov/programs-projects/photometry, Accessed 07/01/2019.

[8] https://en.wikipedia.org/wiki/Radiometry, Accessed 01/07/2019.

[9] E. Gómez-González. Guía básica de conceptos de radiometría y fotometría. http://laplace.us.es/campos/optica/general/opt-guia2.pdf, Accessed 04/30/2019.

[10] B.N.Taylor,Guide for the use of the International System of Units (SI), NIST Special Publication 811,U.S.Government Printing Office, Washington, DC 20402-9325,1995.

[11] G. S. Landsberg, Optics, Mir Ed. Moscow (1983).

[12] V. L. Díaz-Melian, L. A. Rodríguez, F. Pedroso-Camejo , J. Mieres , Y. de Armas, A. J. Batista-Leyva, E. Altshuler. Accepted for publication, Rev. Cub. Fis. 36, xxx (2019).

[13] https://www.nist.gov/pml/sensor-science/opticalradiation/ realization-candela, Accessed 02/20/2019.

[14] https://www.nist.gov/pml/sensor-science/opticalradiation/ realization-lumen, Accessed 02/20/2019.

[15] https://www.nist.gov/pml/sensor-science/opticalradiation/ realization-related-photometric-units, Accessed 02/20/2019.

SENSITIVITY TO CONTACT GEOMETRY OF THE TRANSVERSE CURRENT DISTRIBUTION INTO A BSCCO TAPE: A COMPUTATIONAL STUDY

SENSIBILIDAD A LA GEOMETRÍA DE LOS CONTACTOS DE LA DISTRIBUCIÓN DE CORRIENTE TRANSVERSAL EN CINTAS DE BSCCO: UN ESTUDIO COMPUTACIONAL

A. S. García-Gordillo[a†], A. Reyes[a] and E. Altshuler[a]

Superconductivity Laboratory, Physics Faculty-IMRE, University of Havana, 10400 Havana, Cuba. andy.garcia@fisica.uh.cu[†]

The four-probe technique is a standard way for measuring transport properties in samples with low output voltage. The use of this technique to study inhomogeneities of superconducting properties of ceramic superconductors [1–6], coated superconductors [7,8], films [9,10] and tapes [11,12] has been well established. A less common practice in the study of these materials is to change the positions of the voltage probes in order to explore local properties. A study of the local transport properties in the transverse direction of $Bi_2Sr_2Ca_2Cu_3O_{10+x}$ tapes [13] and some studies related to the anisotropy in the dissipation associated to transport currents in the longitudinal and transverse directions on multi-filamentary $Bi_2Sr_2Ca_2Cu_3O_{10+x}$ tapes [14, 15] were accomplished by changing the position of the voltage probes in the four-probes set-up. However, very small attention has been put in studying the effects of the positions of the *current* leads on the transport measurements and sample performance. Particularly, it is interesting to know how the current injection geometry may influence the formation of hot spots [16] and the shape of the I - V curves.

Understanding the onset of hot spots under different experimental conditions is very relevant, since local overheating has always been an important issue in the behavior of superconducting magnets and power transmission lines. The transverse direction in the presence of transverse cracks [17,18] constitutes "an escape way" for the current. To study the transport properties of the tape when current meets one of these cracks it is required to inject current in the transverse direction.

In the present paper we study by means of numerical simulations the sensitivity of the current distribution inside a $Bi_2Sr_2Ca_2Cu_3O_{10+x}$/Ag multi-filamentary superconducting tape when an external current flows transverse to the superconducting filaments. It is possible by using a transverse bridge, i.e., a slice of a superconducting tape cut perpendicular to the filaments [13–15,19].
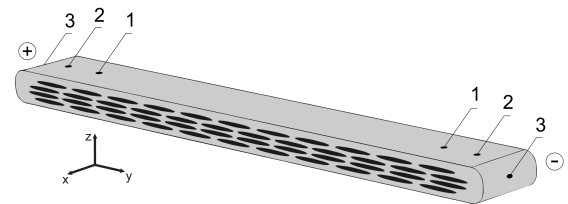
Figure 1. Sketch of a transverse bridge on a multi-filamentary tape. The pairs of current probes labelled as "1", "2" and "3" correspond to Configurations 1, 2 and 3, respectively, and the current flows in the direction from "+" to "-". The dimensions along x, y and z of the bridge in a real sample are of 0.5 mm, 4.32 mm and 0.23 mm, respectively.

The transverse bridge used in the simulations replicated quite precisely the cross-section of the BSCCO tape used by us in previous experiments [19]. It was 4.32 mm wide and 0.23 mm thick, and contained 46 elliptical cross-sectioned filaments. All the filaments were identical, each one 0.3 mm wide and 25 microns thick, giving a filling factor of $S_{BSCCO}/S_0 = 0.27$, where S_{BSCCO} is the cross-section area of the superconductor and S_0 is the whole cross-section of the tape. The width of the bridge (i.e., its size parallel to the main direction of the tape) was 0.5 mm.

COMSOL Multiphysics was used to run the simulations. It uses the FEM (Finite Elements Method) to solve the stationary electrical problem we are aiming at. Three different current probes configurations were set in order to explore the current distribution inside the bridge.

Figure 1 shows a sketch of the transverse bridge where the current probes configurations are depicted. In 'Configuration 1' the probes are located on top of the tape, close to the edges of the transverse bridge, directly over the gap of the two closest filaments. 'Configuration 2' is quite similar to the first one: the probes are also on top of the tape. However, they are closer to the edges of the transverse bridge in such a way that each probe has only one filament directly underneath it. In 'Configuration 3', the probes are located at the center of the sides of the transverse bridge.
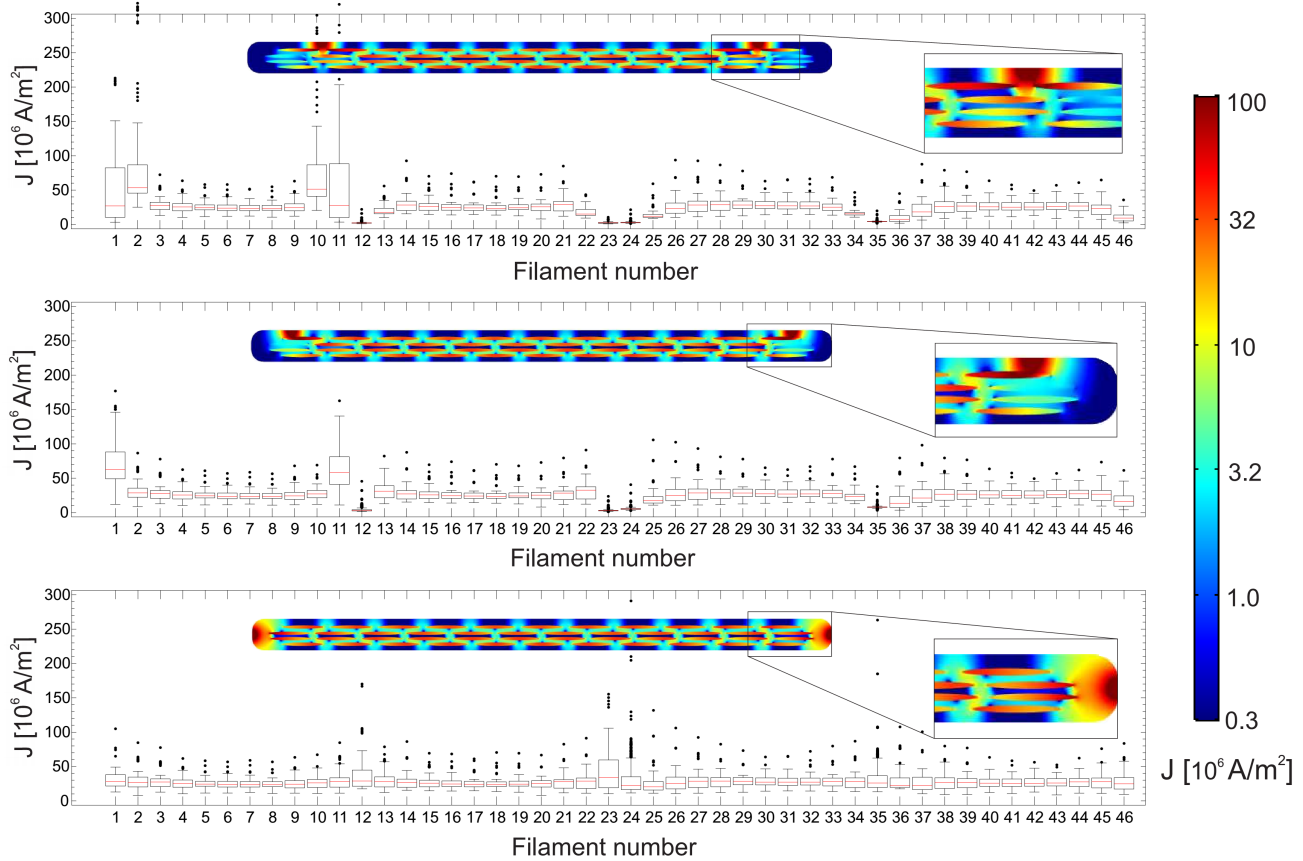
Figure 2. Detailed current density distributions for configurations 1, 2 and 3, from top to bottom. Each graph consists in a box diagram showing the current densities circulating through each filament (boxes from 1 to 11 correspond to the first 11 filaments of the top row, counting from left to right; boxes from 12 to 23 correspond to the second row of 12 filaments, counting from left to right, and so on). The central insets show a transversal cut of the bridge, where the current density module follows the color code indicated by the bar at the far right. The right insets are zooms of the current density distribution near the right contacts.

The superconducting filaments were modeled as normal conductors with high conductivity values, and the material surrounding was modeled as silver with a $\sigma = 3.44 \times 10^8$ S/m (at liquid nitrogen temperature [20]). The conductivity values of the filaments exceeded in six orders the ones of the silver. The bias current was set to 1 A in the three configurations. That value is supposed to be lower than the value of the critical current, so that the filaments remain in the superconducting state. Silver was chosen in order to reproduce the original tape, but different values of the superconductor and metal conductivities could have been used instead. However, the results are robust if the two conductivities differ by five orders of magnitude or more.

The current density through the filaments and the silver matrix was calculated for the three configurations. Aimed at decreasing the calculation time, all data was calculated exclusively within the plane including the current probes. Due to the geometry partition into small domains made by the program to solve the continuity equation in a discrete way using the FEM, a mean of 650 values of current density can be extracted from each filament in that slice. Filaments are numbered in the computational model for a better understanding of the spatial current density distribution. If we imagine the cross-section of the tape, as seen in the transverse bridge of figure 1, filaments are numbered from left to right and from top to bottom. The top row of filaments

goes from 1 to 11, second one goes from 12 to 23, third from 24 to 35, and the bottom row goes from filament 36 to 46.

Figure 2 shows, for the three configurations, box whisker charts with the distributions of the current density values inside each filament. 'Configuration 1', '2' and '3' are shown in the top, middle and bottom panels respectively. Each chart has an inset containing a color graph with a map of the current density distribution inside the whole transverse bridge center slice. A global legend at the right of the graphs illustrates the color scale of the insets current density distribution. The convention used for whiskers and outliers was taken according to Tukey's method [21], in which if Q_1 and Q_3 are the lower and upper quartiles of the data set respectively, then one could define an outlier to be any observation outside the range: $[Q_1 - k(Q_3 - Q_1), Q_3 + k(Q_3 - Q_1)]$ where $k = 1.5$ defines the points that will be considered outliers and $k = 3$ those classified as "far out".

In 'Configuration 1' current distributes all over the transverse bridge with a visible increase of the current density values inside four filaments at the top row, as seen from the medians and the tails of the current density distributions shown in the box whisker chart. The filaments with high current density values are the ones located immediately underneath the current probes, indicating that current flows almost entirely through them, and then redistributes among the rest of the filaments. We can confirm this by analysing the centered

slice color graph in the inset. In 'Configuration 2' the current density distribution exhibits a similar behavior resulting in a pair of filaments with high current density values. The medians of the distributions inside these filaments are larger than in 'Configuration 1', which seems obvious if we take into account that the current is sustained almost entirely by two filaments instead of four, as can be seen from the inset. These values are not substantially different from each other since the current density median of filament 2 in 'Configuration 1' is approximately $53.6 \times 10^6 A/m^2$ and the current density median of filament 1 in 'Configuration 2' is approximately $63 \times 10^6 A/m^2$; but the slightest difference may start the transition. 'Configuration 3', on the other hand, does not show a high concentration of current in very few filaments: they have current density distributions with almost the same median and, in general, they show short tails. The difference with previous configurations can be explained by the fact that the contacts are located at the center of the sides of the transverse bridge -relatively far from any particular group of filaments- which allows the current to flow a certain distance inside the silver and reach, in a more homogenized way, a larger number of filaments.

Thus, filaments below current probes in configurations 1 and 2 constitute regions of local overheating -hot spots- which may compromise the conduction in the transverse direction of the tape. If we look closely at the color graphs in the insets of Figure 2 we can see that inside these filaments there are regions with very high current density values corresponding to these hot spots but also there are regions of silver and filaments with substantially lower current density values. These "cold" regions that can be viewed as "reservoirs" of conductive paths, have an effect in the velocity of the transition to the normal state. So, in principle, they can prevent a "fatal rupture" of the tapes when transversal cracks are present.
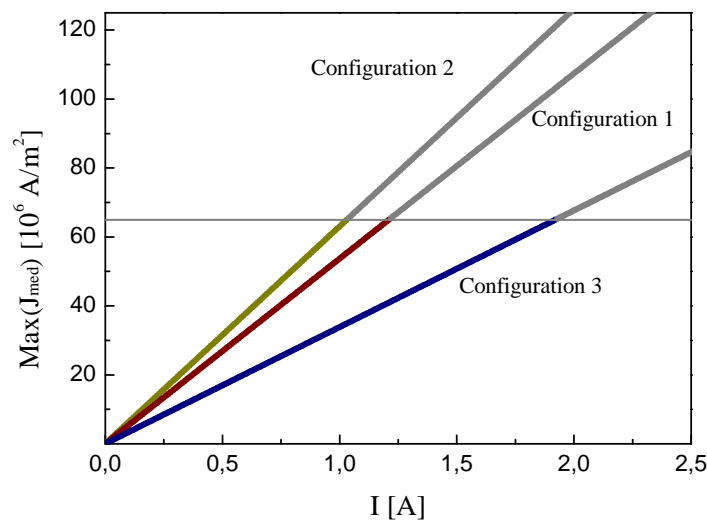

Figure 3. Dependence of the maximum of the current density distributions medians with the applied current. The red curve corresponds to 'Configuration 1', the yellow one corresponds to 'Configuration 2' and the blue one belongs to 'Configuration 3'. J_c is marked with a gray horizontal line. The inset shows the behavior of the maximum of the current density distributions upper fences.

A parametric study related to the medians of the current density distributions inside the filaments endorse the fact that the characterization curves are strongly conditioned by the position of the current probes. Applied current was varied from 0 to 2.5 A in order to find out which of these configurations allow us to reach the critical current density 'earlier', under realistic experimental parameters [13–15, 19].

Figure 3 shows the behavior of the maximum of the current density distributions medians among all filaments (Max(J_{med}) with the applied current (I). The curves for the different configurations are labeled in the graph, showing that the red curve corresponds to 'Configuration 1', the yellow one corresponds to 'Configuration 2' and the blue one belongs to 'Configuration 3'. The maxima of the current density distributions medians were always found in the same filament according to the corresponding configuration. In 'Configuration 1' the maximum was found in filament number 2, 'Configuration 2' presented its maximum in filament 1 and in 'Configuration 3' the maximum was on filament 23. These are the filaments which have the highest median values in each configuration. It is important to mention that despite of the symmetry in the position of the current probes, filaments below the right and the left probes do not hold exactly the same current density because we realistically reproduced the filament distribution of a real tape, which includes a slight asymmetry in the filament distribution. Hence, in configurations 1 and 2 the important filaments are bellow the left current probe, and, in 'Configuration 3', the filament with the highest median is placed at the left of the right probe.

If we assume the critical current density (J_c) of the filaments equals to $239.8 \times 10^6 A/m^2$ (calculated from the S_{BSCCO}/S_0 ratio and the engineering critical current of the BSCCO multi-filamentary superconducting tape at liquid nitrogen temperature [15] -marked in the graph as a gray horizontal line-) we can see from Figure 3 that J_c is reached first in 'Configuration 2'. This will switch at least one filament out of the superconducting state, redistributing the current density to neighboring filaments. As the applied current increases this redistribution involves more filaments, giving rise to a gradual transition of the full bridge to the normal state. This is in accordance with the box whisker charts of Figure 2 where the highest value of the medians corresponds to 'Configuration 2', followed by 'Configuration 1' and then 'Configuration 3', which needs a much larger current value to reach the critical current density. The difference can be unexpectedly large: Fig. 3 shows that the horizontal line intercepts 'Configuration 3' at approximately twice the current at which it intercepts 'Configuration 2'.

Although taking the medians of the distributions as reference parameters to compare the different configurations seems to be a reasonable decision because of the complexity of the transition to the normal state, the maximum deviation above medians might constitute a more suitable and interesting magnitude to evaluate this difference as well. The inset in Fig. 3 shows the dependence of the maximum of the current density distributions upper fences with the applied current, defining the upper fences as the values of current density at

the end of the upper whisker (maximum deviation above medians not including the outliers). The maxima of the upper fences [Max(J_{max})] were always found in the same filament according to the corresponding configuration as in the medians study. However, relevant filaments were not the same. In configurations 2 and 3 the maximum was found in filaments number 1 and 23 respectively, but in 'Configuration 1', instead of in filament number 2, the maximum was found in filament number 11 (clearly visible from the box diagrams of Figure 2). The values of the maxima of the upper fences in 'Configuration 1' are larger than those of 'Configuration 2' changing the order in which the transitions out of the superconducting state occur in the different configurations. Additionally, the values of the intersections with the J_c horizontal line are way smaller if the upper fences are taken into account. It is quite difficult to tell which of these statistical magnitudes best describes the transition: while the study of the upper fences seems to give an onset of the transition, the medians offers a more "averaged out" data.

In summary, the sensitivity of the transverse current to different configurations of current probes in $Bi_2Sr_2Ca_2Cu_3O_{10+x}$/Ag multi-filamentary superconducting tapes was studied. Simulations strongly suggest that a configuration where the current probes are far from a particular group of filaments does not create hot spots; a desirable scenario for applications. In addition, the different values of applied current needed to reach the critical current density in the different configurations, as well as the different current distributions inside the transverse bridge of the tape suggest that the transverse transport characterization of a multi-filamentary tape is unexpectedly dependent on the detailed positioning of the current probes.

REFERENCES

[1] J. R. Clem, Physica C **153-155 (part1)**, 50 (1988).
[2] E. Altshuler, R. Cobas, A. J. Batista-Leyva, C. Noda, L. E. Flores, C. Martínez and M. T. D. Orlando, Phys. Rev. B **60**, 3673 (1999).
[3] A. J. Batista-Leyva, R. Cobas, E. Estévez-Rams, M. T. D. Orlando, C. Noda and E. Altshuler, Physica C **331**, 57 (2000).
[4] A. J. Batista-Leyva, R. Cobas, M. T. D. Orlando and E. Altshuler, Supercond. Sci. Tecnol. **16**, 857 (2003).
[5] S. Recuero, N. Andrés, J. Lobera, M. P. Arroyo, L. A. Angurel, and F. Lera, Meas. Sci. Technol. **16**, 1030 (2005).
[6] W. Treimer, O. Ebrahimi and N. Karakas, Appl. Phys. Lett. **101**, 162603 (2012).
[7] S. Trommler, R. Hühne, E. Reich, K. Ida, S. Haidndl, V. Matias, L. Schultz and B. Holzapfel, Appl. Phys. Lett. **100**, 1226602 (2012).
[8] D. Colangelo and B. Dutoit, Supercond. Sci. Technol. **25**, 1 (2012).
[9] J. Hua, Z. L. Xiao, D. Rosenmann, I. Beloborodov, U. Welp, W. K. Kwok and G. W. Crabtree, Appl. Phys. Lett. **90**, 072507 (2007).
[10] T. Horide and K. Matsumoto, Appl. Phys. Lett. **101**, 112604 (2012).
[11] K. Ogawa and K. Osamura, Phys. Rev. B **67**, 184509 (2003).
[12] M. Zhang, J. Kvitkovic, J. H. Kim, C. H. Kim, S. V. Pamidi and T. A. Coombs, Appl. Phys. Lett. **101**, 102602 (2012).
[13] A. Borroto, L. Del Río, E. Altshuler, M. Arronte, P. Mikheenko, A. Qviller and T. H. Johansen, Supercond. Sci. Technol. **26**, 115004 (2013).
[14] A. Borroto, L. Del Río, M. Arronte, T. H. Johansen and E. Altshuler, Appl. Phys. Lett. **105**, 202604 (2014).
[15] A. Borroto, A. S. García-Gordillo, L. Del Río, M. Arronte, and E. Altshuler, Supercond. Sci. Technol. **28**, 075008 (2015).
[16] L. Del Río, E. Altshuler, S. Niratisairak, Ø. Haugen, T. H. Johansen, B. A. Davidson, G. Testa and E. Sarnelli, Supercond. Sci. Technol. **23**, 085005 (2010).
[17] X. Y. Cai, A. Polyanskii, Q. Li, G. N. Riley Jr and D. C. Larbalestier, Nature **392**, 906 (1998).
[18] H. Akiyama, Y. Tsuchiya, S. Pyon and T. Tamegai, Physica C **504**, 65 (2014).
[19] A. S. García-Gordillo, A. Borroto and E. Altshuler, Rev. Cubana Fis. **31**, 96 (2014).
[20] D. R. Smith and F. R. Fickett, J. Res. Natl. Inst. Stand. Technol. **100**, 119 (1995).
[21] J. W. Tukey, *Exploratory Data Analysis*, 1st Ed. (Addison-Wesley, 1977)

ALTERNATIVA METODOLÓGICA PARA EL USO DEL MÉTODO CIENTÍFICO EXPERIMENTAL EN LAS CLASES DE LABORATORIO DE FÍSICA

METHODOLOGICAL ALTERNATIVE FOR USING THE EXPERIMENTAL SCIENTIFIC METHOD IN PHYSICS LABORATORY LESSONS

L. Landa[a][†] y C. Morales[a].

Facultad de Informática y Ciencias Exactas, Universidad de Camagüey, 70100 Camagüey, Cuba; luis.landa@reduc.edu.cu[†]
† autor para la correspondencia

Los insuficientes resultados de aprendizaje obtenidos durante las últimas décadas en la enseñanza de la Física, han traído como consecuencia un inusitado interés por transformar la educación científica de los estudiantes.

Estos resultados explican el porqué de la necesidad de prestar atención al trabajo experimental en la enseñanza de la Física. A juicio de los autores, es necesario revolucionar el método empleado para el desarrollo de este tipo de clases, de modo que se logre un mayor nivel de implicación del estudiante en este proceso [1].

Es propósito de los autores ofrecer una alternativa metodológica para los docentes que propicie el tránsito de los estudiantes por los procedimientos del método científico experimental, como acercamiento de las clases de laboratorio de Física a los métodos de la ciencia.

En los trabajos referidos a esta temática abordados hasta ahora se ha alcanzado la operacionalización del método científico, sin embargo, la metodología a seguir por los docentes en función de lograr la apropiación del método continúa siendo una cuestión no resuelta totalmente.

Para introducir el método experimental en las clases de laboratorio de Física y hacer que el estudiante transite por los diferentes procedimientos de este, los autores elaboraron una alternativa metodológica para los docentes, que contiene cuatro etapas:

Etapa 1: De formulación de problemas y planteamiento de hipótesis.

En esta etapa se recurrió a la elaboración conjunta profesor-estudiante de la formulación del problema y, gradualmente, se les otorgó un mayor grado de independencia.

Según la complejidad del problema se procedió a su descomposición en otros más elementales, cuya solución tributa al problema principal.

Del mismo modo se procedió con la elaboración de las

hipótesis. La utilización de simulaciones sirvió para el entrenamiento de los estudiantes en esta fase [2].

Etapa 2: De diseño experimental.

A partir del problema asumido, cada equipo de estudiantes elaboró el diseño experimental.

Este procedimiento se realizó en un momento previo a la práctica de laboratorio de modo que los estudiantes se presentaron con un diseño experimental adecuado.

Etapa3: De ejecución del experimento, procesamiento de la información y elaboración de conclusiones.

Esta etapa se desarrolló siempre en el tiempo planificado para el laboratorio y fue necesario adiestrar a los estudiantes en el montaje experimental, sobre todo en las primeras prácticas donde este procedimiento se desarrolló de forma conjunta con el profesor. Para la ejecución del procesamiento de la data se indicó a los estudiantes la utilización de hojas de cálculo.

Etapa 4: De comunicación de los resultados.

En esta etapa se consideraron dos elementos: el primero, la redacción del informe de la práctica y, el segundo, la comunicación oral de los resultados en el aula, para lo cual se orientó la utilización de presentaciones electrónicas.

A continuación se expone la manera en que fueron aplicadas las ideas expuestas anteriormente en una clase de laboratorio de Física relacionada con el estudio de la fuerza de fricción por deslizamiento.

Durante este estudio se arribó, de forma conjunta con los estudiantes, a la interrogante siguiente: ¿De qué factores depende la fuerza de fricción entre dos superficies? Este constituye el problema principal, para cuya solución se descompone en los siguientes problemas a investigar:

Problema # 1:

¿Depende la fuerza de fricción entre dos superficies del área

de apoyo del cuerpo que se desliza?

Problema # 2:

¿Depende la fuerza de fricción que actúa sobre un cuerpo de la naturaleza de las superficies en contacto?

Problema # 3:

Dado un cuerpo que se desliza por una superficie horizontal, es necesario hallar la relación funcional que existe entre la fuerza de fricción y la fuerza normal (N) que actúan sobre dicho cuerpo.

A continuación se procedió a delimitar qué equipos de estudiantes investigarían cada problema por separado y al planteamiento de las posibles hipótesis.

Los siguientes procedimientos se desarrollaron según la secuencia: problema, objetivo, hipótesis, diseño del experimento, variable independiente y dependiente, variables ajenas a controlar, materiales y equipos, instrumentos de medición, condiciones del experimento, acciones a realizar sobre el objeto, procesamiento de la información y conclusiones del experimento.

Al comparar los valores de la fuerza de fricción para ambas áreas en la solución del primer problema, se encontró que la diferencia entre las fuerzas de rozamiento por ambas caras era mucho menor que el error de la diferencia de dichas fuerzas: $|\vec{F}_{R1} - \vec{F}_{R1}| << E_d$, por tanto, es válida la hipótesis según la cual dicha fuerza no depende del área de apoyo del cuerpo.

Finalmente, se puede plantear que resulta impostergable transformar la concepción del proceso de enseñanza aprendizaje de la Física en las asignaturas de ciencias, particularmente en lo concerniente a la realización de la actividad experimental y, por otra parte, la aplicación de la alternativa metodológica dirigida a los docentes permite dotarlos de una vía que propicia la adquisición de manera creciente del método científico experimental.

REFERENCES

[1] L. Landa, "La superación postgraduada en Física para los profesores del municipio de Camagüey". Tesis de maestría, Universidad de Camagüey, 2002.

[2] M. Legañoa, M. Hernández y L. Pérez, Revista Transformación **11**(1), 38 (2015).

METODOLOGÍA PARA FAVORECER EL DESEMPEÑO INVESTIGATIVO EXPERIMENTAL COMPETENTE EN ESTUDIANTES DE INGENIERÍA
METHODOLOGY FOR FAVORING COMPETENT EXPERIMENTAL OF INVESTIGATIVE PERFORMANCE IN ENGINEERING STUDENTS

C. Alvarez[a†], A. Mena[b] y R. Márquez[b].

a) Departamento de Física, Universidad de Camagüey, 70100 Camagüey, Cuba; carlos.alvarez@reduc.edu.cu[†]
b) CECEDUC, Universidad de Camagüey, 70100 Camagüey, Cuba
† autor para la correspondencia

En el presente trabajo se presentan resultados parciales de la aplicación de la metodología para la formación-desarrollo de la competencia investigación experimental en la Física para estudiantes de ingeniería (IEF), la misma está orientada al perfeccionamiento del desempeño de dichos estudiantes durante la realización de las prácticas de laboratorio de Física [1, 2] (consultar en http://www.reduc.edu.cu/siscomfis/index.html).

La metodología para la formación-desarrollo de la competencia IEF contempla cuatro etapas: I.- Diagnóstico; II.- Organización; III. Ejecución y IV. Evaluación de la metodología. Donde:

I Diagnóstico, persigue comprobar las potencialidades cognitivas referidas a las habilidades experimentales y tecnológicas.

II Organización: el profesor considerará:

- Seleccionar problemas experimentales afines al modelo de profesional.
- Capacitar a estudiantes y profesores en esta competencia.
- Incorporar la realización de prácticas de laboratorio virtuales contextualizadas.
- Considerar diversidad de equipos, instrumentos y accesorios para cada una de las prácticas de laboratorio.

III Ejecución: los estudiantes actuaran en correspondencia con los desempeños acordados para cada criterio:

a) Analizar el problema a investigar y actuar según el criterio 1.- Identifica el conocimiento.

b) En el laboratorio de Física, montar su experimento, cumplimentarán el criterio 2.- Emplea la estrategia pertinente.

c) En tiempo extra clase, individual o por equipos, cumplimentarán lo indicado en el criterio 3. Interpreta la información experimental.

d) Presentar y argumentar el resultado investigativo experimental siguiendo lo acordado en el criterio 4.- Comunica los resultados del proceso desarrollado.

e) Se autoevalúa, lo coevalúan y heteroevalúan su desempeño experimental.

Como procedimiento para llevar a efectos la metodología se elaboró el **método para el desempeño investigativo experimental**, entendido este como el proceso en que partiendo del problema en estudio se predice la evolución del mismo y se elabora el diseño investigativo experimental requerido para la solución del referido problema, ello demanda la utilización de equipos, instrumentos y accesorios así como de diferentes recursos tecnológicos lo cual aportará la información pertinente, ésta será analizada con los recursos necesarios, debiendo el estudiante comunicar de forma oral y escrita los resultados alcanzado ello permitirá reestructurar o sistematizar el conocimiento que posee como expresión del desempeño investigativo experimental alcanzado (ver Fig. 1)

La implementación parcial de la metodología se llevó a efecto con los 55 estudiantes del grupo de ingeniería Mecánica de la Universidad de Camagüey mientras cursaban las asignaturas Física I (curso 2014-15) y Física II (curso 2015-16).

Los resultados alcanzados por los estudiantes fueron analizados con la prueba de hipótesis con pares igualados de Wilcoxon [4] aplicada a las prácticas de laboratorio (PL):

I. Hipótesis de nulidad. (Ho): no habrá diferencia entre el nivel de desempeño investigativo experimental (DIEF) de estudiantes inicial y final.

II. Hipótesis alterna (Ha): el nivel de DIEF de estudiantes es menor al comienzo de las PL de Física respecto al alcanzado cuando se realiza la última.

III. Nivel de significación. Sean $\alpha = 0.01$ (probabilidad) y N el número de pares diferentes de cero.

Además se tuvieron en cuenta los resultados en cinco PL reales en cada asignatura.

Tabla I   Estadísticos de contraste

			PL5_FI - PL1_FI	PL5_FII - PL1_FI
Z			-6.435(a)	-6.492(a)
Sig. asintót. (bilateral)			.000	.000
Sig. Monte Carlo (bilateral)	Sig.		.000	.000
	Intervalo de confianza de 99%	Límite inferior	.000	.000
		Límite superior	.000	.000
Sig. Monte Carlo (unilateral)	Sig.		.000	.000
	Intervalo de confianza de 99%	Límite inferior	.000	.000
		Límite superior	.000	.000

a. Basado en los rangos negativos.
b. Prueba de los rangos con signo de Wilcoxon

Figura 1. Método para el desempeño investigativo experimental.
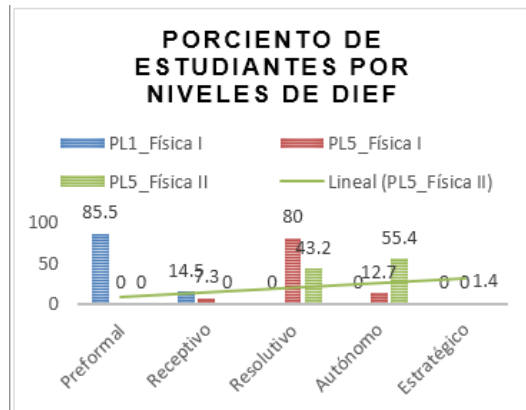
Figura 2. Resultados del desempeño investigativo experimental de los estudiantes de ingeniería mecánica.

Resultado del estadístico muestra el rechazo a la prueba de nulidad Ho, al ser el resultado final en cada etapa superior al que presentaron estos estudiantes en la primera práctica de laboratorio de Física, al constatarse que la probabilidad correspondiente a los valores de Z son menores $\alpha = 0.01$ (ver Tabla I).

Se reconoce que la metodología empleada permitió adoptar las medidas pertinentes para atender las carencias cognitivas y procedimentales que evidenciaron los estudiantes, lo cual fue viabilizado a través de lo acordado en la caracterización de la competencia IEF.

BIBLIOGRAFÍA

[1] C. Alvarez, "Formación-desarrollo de la competencia investigación experimental en la física para estudiantes de carreras de ingeniería". Tesis doctor, Universidad de Camagüey, 2016.

[2] C. Alvarez, A. Mena, y R. Márquez, Revista Transformación [ISSN: 2077-2955], I, 5, (2016) (https://transformacion.reduc.edu.cu/index.php/transformacion/article/view/203).

[3] S. Tobón, Trillas **378**(1), T629c (2014).

[4] S. Siegel, Estadística no paramétrica aplicada a las ciencias de la conducta, (Trillas, México DF, 1994).

SCIENTIFIC RESEARCHERS: THE SUCCESS STORY OF A UNIVERSAL COMMUNITY

INVESTIGADORES CIENTÍFICOS: LA EXITOSA HISTORIA DE UNA COMUNIDAD UNIVERSAL

W. Bietenholz[†]

Instituto de Ciencias Nucleares, Universidad Nacional Autónoma de México, A.P. 70-543, 04510 Ciudad de México, Mexico; wolbi@nucleares.unam.mx

PACS: PACS words

Albert Einstein is world-famous as a symbol of physics, and of science in general. In particular, the General Theory of Relativity might be the last truly epoch-making breakthrough, which was achieved by an individual scientist (although Einstein needed assistance by mathematicians [1]); meanwhile science is more and more an issue of collaborations.
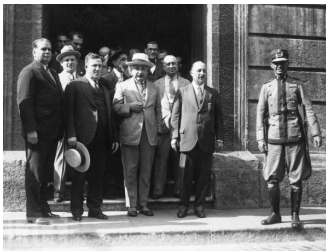
En la Sociedad Cubana de Ingenieros.

Figure 1. Albert Einstein during his visit to Havana. The picture bellow shows him writing in the *Golden Book*.

During his life Einstein was also a media star, and he is still frequently quoted in all kind of contexts, often beyond science, even though these citations have to be taken with caution (his lifetime of 76 years was hardly sufficient to make all the statements quoted by him).[1]

Here we refer to one citation by Einstein, which is not among the most famous ones, but which is well documented. In 1930, while in transit in Havana, he wrote in the guest book of the Geographic Society, the *Golden Book*, the following two sentences:

"The first truly universal society was the society of researchers. May the coming generations establish a political and economic society which insure us against catastrophes."

This message is cited in a historical account by José Altshuler [3], who questions "What exactly did he mean by this?". Although the interpretation certainly requires some speculation, it does not appear all that mysterious to me. Here I am going to comment on these two statements one by one.

I. THE SCIENTIFIC COMMUNITY

Let us first sketch the society, or community, of researchers that Einstein referred to — what does it look like today? UNESCO defines researchers as "professionals engaged in the conception or creation of new knowledge. They conduct research and improve or develop concepts, theories, models, techniques, instrumentation, software or operational methods". According to this definition, there are today about *8 millions of researchers* [4], which represent 0.1 % of the world population. This is far more than in past periods, not only as an absolute number, but also as a fraction of humanity.

We assume that Einstein had *natural science* in mind, which is more specific, but which still includes astronomy, biology, chemistry, geoscience and physics. Hence we are going to refer to natural science, which describes Nature in a systematic manner, based on observation and logical reasoning.

Of course, the scientific community is divided into numerous sub-communities and sub-sub-communities. If we particularly focus on *physics*, the community shrinks below 1

---

[1]For instance the authenticity of the famous citation, according to which Einstein denoted the introduction of a Cosmological Constant as his "biggest blunder" (or "größte Eselei" in German), is controversial [2]. In any case, this constant is now appreciated as the most obvious explanation for the accelerated expansion of the Universe.

[2]The estimate of 1 million physicists in Ref. [5] refers to the members of national physics societies around the world. It includes, however, some members, who are not researchers, in particular physics teachers.

million [5],[2] and even within physics nobody has an overview over all branches anymore. This is a facet of *specialization*, a generic trend of human history. Enrico Fermi was one of the last researchers who was very successful both in theory *and* experiment, and Lev Landau was perhaps the last physicist to contribute outstandingly to practically all branches of theoretical physics.

Figure 2. Top left: Enrico Fermi (1901-54), top right: Lev Landau (1908-1962) and bottom: Satyendra Bose (1894-1974), three pioneers in statistical mechanics.

As an example of a specialized sub-sub-community, the author works in Quantum Field Theory in the Lattice Regularization, a field which involves $O(1000)$ researchers. A significant part knows each other in person, in particular from the annual Lattice Conferences, and people involved over a long period know each other at least by name. This is not a *collaboration* in the usual sense; only small groups of up to $O(10)$ persons work directly together, and publish papers jointly. Still, the entire community does collaborate in the sense of aiming at the same goal, to elaborate results in Quantum Field Theory beyond the perturbative expansion, *i.e.* results that are computed — by means of Monte Carlo simulations — directly at finite field couplings, which is the realistic setting. The most prominent aim is to solve Quantum Chromodynamics at low energy, which is expected to be the fundamental theory underlying nuclear physics.

In this sense, the entire "lattice community" does represent *some kind of collaboration*, working on a common goal, although the work is performed in small groups, even with occasional rivalries. Nevertheless the general atmosphere at the annual conferences, where several hundred members of this community meet, is friendly. There is some mentality in common, along with a specific *jargon*, similar working experience and ways of thinking.[3]

These characteristics can basically be extended to the entire physics community, and even to all scientific researchers. The

unifying elements become less detailed when we consider a broader community, where most associates do not know each other, but the fundamental point persists: it is a worldwide community, embracing all continents, which shares a common conceptual approach and methodology of their work, along with a common goal. Scientists assume Nature to behave in a systematic manner, following a logical scheme, which they explore. This is opposed to sudden irregular jumps ("miracles"), or obviously absurd correlations, as they are claimed *e.g.* in astrology. The core of the methodology are systematic observations on the one hand, and the derivation of Laws of Nature and their implications on the other hand. Physics describes the world most directly in *mathematical terms,* an approach, which is tremendously successful (the question *why* this works so well [6], however, is rather philosophical).
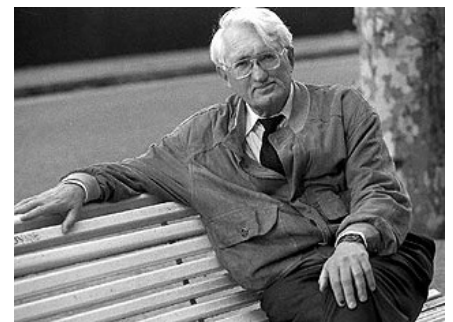
Figure 3. On the left: poster of 37th International Symposium on Lattice Field Theory, 2019, in Wuhan. On the right: Jürgen Habermas, contemporary philosopher interested in the social impact of science and technology.

An essential "common denominator" of natural science are (relatively) clear criteria for deciding whether or not some work is valid (unlike *e.g.* art, literature or philosophy): it must agree with observations, and be consistent. For a postulate to be significant in science, it must be non-trivial and withstand stringent falsification, as Karl Popper emphasized [7]. Then it will be recognized and — if it is very important — it enters the textbooks. A non-falsifiable statement is not scientific, and a claim, which is disproved, or does not prove useful, will be dismissed; this was the fate of the aether, for example, and currently supersymmetry is in danger of this destiny.

Based on these clear-cut criteria, science overcomes by its own dynamics any frontiers of nations or ethnic groups. It therefore forms a *global community,* concerned with the Laws of Nature, which hold worldwide, at any time (unlike juridical laws). This leads to joint efforts beyond any borders: for instance, when Einstein received a letter from the Indian physicist Satyendra Bose on quantum statistics, he translated it into German and submitted it on Bose's behalf to the renowned journal *Zeitschrift für Physik* [8]. Today technology drastically simplifies global communication, and even the editorial process of international journals is globalized.

The scientific criteria imply that it does (ideally) not matter *who* postulates something, and where he/she comes from; it just matters whether the postulate is correct and scientifically

---

[3]A rigorous analysis of the social behavior at scientific conferences might be a project for modern ethnologists. My impression is that a friendly atmosphere generally dominates.

relevant. Moreover, the concept of science is independent of any particular ideology, unless one considers the scientific way of thinking itself as an ideology, as discussed by Jürgen Habermas [9].

These are points in common, which characterize the scientific community, a minor fraction of humanity: we have mentioned an estimated number of 8 millions of researchers, similar to the population of Papua New Ginea, Switzerland or Sierra Leone, but less than the one of Cuba. This community is tiny compared to the four largest religions, each of which claims over 500 millions of members, but science has nevertheless a significant impact on humanity. It is not unusual that a small minority enjoys wide-spread attention: for instance the FC Barcelona consists of very few people, but it has over 100 million followers on Facebook. Worldwide we estimate some 130 000 professional soccer players (the world's most popular sport), which are given much more media attention (and higher salaries) than scientific researchers. The impact of science, however, is more profound than sport news:

- First, science is the foundation of technology, which is generally appreciated as a source of wealth and comfortableness. However, the impact of technology is not under the scientists' control, and it is not always beneficial for society but occasionally ambivalent, as we discussed elsewhere [10]. Still, even people with a mentality far from science are happy to benefit from technological achievements, for instance in health care, transport and communication (even the retired pope Benedict XVI uses a cardiac pacemaker, and the FC Barcelona could not attain such a huge number of followers without modern communication technology).

- Second, science has a strong influence on the public view of the world by shedding light on the mechanisms of Nature. For instance, the modern understanding of a thunderstorm replaces mythological pictures of the past. A practical benefit is that we now know how to protect ourselves from lightenings.

  In the 19th century, philosophy had a powerful impact on humanity, but nowadays the aforementioned Habermas is probably the only widely known contemporary philosopher. Since the 20th century, despite some persistent scepticism, it is natural science that shapes the established view of the world. This is amazing, in particular since science spreads its insight just by presenting facts, without tricks of mental manipulation (which are standard in commercial advertisements, making people buy useless things),

nor does it employ missionaries and mass psychology (which are common practice for religious groups).

School education gives increasing importance to science. Of course, the vast majority of school children won't become scientists, and won't remember much *e.g.* of their physics classes in their later lives, but many do internalize the method of logic reasoning to approach a question and solve a problem. In this sense, science and mathematics carry on the efforts of the Age of Enlightenment.[4]

Still there is sometimes fierce resistance against scientific insight. This can be based *e.g.* on religious dogmas, or on a psychological bias against accepting scientific facts: the famous insights by Galileo and Darwin both deprived our planet and humanity of its very special rôle, which people assumed and liked before. These paradigm shifts were not easily welcomed, and even in 2017 a Gallup poll revealed that 38 % of US citizens keep believing that "God created humans in their present form at one time within the last 10 000 years" [12].[5] An even more striking example is the flat-earth community,[6] which is still present all around the globe, and horoscopes keep appearing in countless newspapers and magazines.
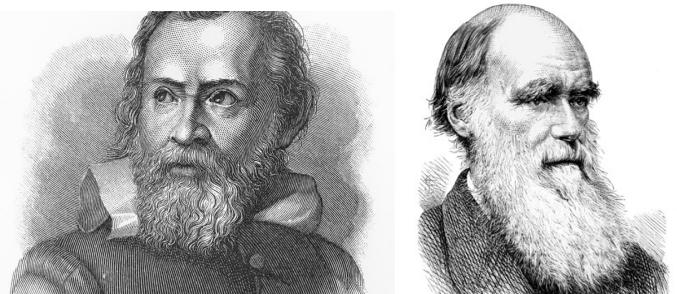
Figure 4. Galileo Galilei (1564-1642) and Charles Darwin (1809-1882): two great scientists who achieved paradigm shifts in different fields, with impacts on the public view of the world.

Despite such resistance, changes of scientific paradigms do occasionally take place [13], but in our era scientific progress is difficult to disseminate: research literature is only readable to specialists, and it is not easily communicated by popular science in a correct manner. For instance quantum physics — a major scientific revolution of the 20th century — is accurately expressed by mathematical formulae, but it is only painfully captured in terms of everyday language, which is designed for macroscopic objects, but which must be used in popular science. Hence its impact on society's vision of the world is not comparable to Galileo and Darwin, although for instance the awareness that randomness exists — in an objective sense — would be of interest to everybody.[7]

---

[4]This task is far from completed: for instance, a study in Mexico in 2017 [11] among third year secondary school students (age around 15) revealed that only 35.5 % are able to solve problems by performing basic operations with decimal numbers, and to express a simple relation in terms of an unknown variable. New pedagogical approaches, such as the Singapore and Shanghai method, raise hope for more effective mathematics teaching.

[5]This attitude is even present among highest authorities, as revealed in recent statements by Satyapal Singh and Damares Alves, ministers of India and Brazil, respectively (the former is responsible for Higher Education).

[6]Actually their viewpoint was already disproved by Aristotle, based on the Earth's shade observed during lunar eclipses.

[7]Einstein was much concerned with this question. He was never comfortable with this conclusion from quantum mechanics ("God does not play dice"), which has later been demonstrated by the violation of Bell's inequalities [14].

More than ever, it is a formidable challenge to produce high quality popular science; the importance of this issue is often not sufficiently recognized within the scientific community.

We conclude that Einstein's first statement appears fully transparent and correct: the researchers in natural science around the world do form a kind of community (or society) with common concepts and methodologies, which they apply to work on a common goal. The broader definition by UNESCO might include academic disciplines beyond natural science, like medicine and history, but it does still not reach out to the most powerful decision-makers on this planet, which Einstein addressed in his second sentence.

II. THE SCIENTIFIC SUCCESS STORY AS A MODEL FOR DECISION-MAKERS

Figure 5. Left: CERN from a bird-eye perspective, with white circles for the Super Proton Synchrotron and the Large Hadron Collider (small and large circle, respectively), and a dotted line for the Swiss-French border. Right: Tim Berners-Lee, the CERN employee who played a central rôle in the creation of the World Wide Web. Bottom: an illustration of ATLAS, one of the two CERN experiments that found the long sought Higgs boson in 2011/2012.

In 1986 the author had the pleasure to spend time at CERN, first as a "summer student", and again for a longer period in 1989. I experienced CERN as a multinational village, outside Geneva, with collaborators and visitors from all around world. It was impressive to see how well communication and collaboration works, and even social life is shared, simply ignoring the "cold war", or resentments between countries like Greece and Turkey; today India and Pakistan readily cooperate as Associated Member States. This spirit led CERN to tremendous success in research of high energy elementary particle physics; today it is without competition worldwide. At the "side-line" it provided numerous technical inventions, with applications ranging

from medicine to the World Wide Web (WWW).[8] Since 1998, over 100 countries contributed to the Large Hadron Collider. An important tool is its Worldwide Computing Grid, which enables joint computational work in over 170 computing centers in 42 countries. This is truly a success story, which rises the question: *why does the rest of the world not follow this example?*

Extending the view beyond CERN, the collective efforts in science are generally successful: year after year progress is achieved and further questions are solved. There are exceptions — for instance, since Einstein's visit to Havana there is no substantial progress in the unification of quantum theory and gravity, despite desperate efforts. Nevertheless, the overall advancement in natural science is a success story indeed.

This takes us to the question how far all this is actually *useful,* in particular regarding Einstein's desire to *"insure us against catastrophes"*. Our protection from natural disasters, like tropical cyclones, has improved thanks to technology. However, technology is still short of really insuring us of catastrophes, as the 2004 tsunami in the Indian Ocean and the 2010 earthquake in Haiti showed; these were the worst catastrophic events in recent times, each one left about 200 000 casualties. However, I assume that Einstein was also concerned with *human-made catastrophes.*

Figure 6. Pictures of the most catastrophic events in recent times: the 2004 tsunami in the Indian Ocean, and the 2010 earthquake in Haiti.

Science can help in some of these cases: the rescue of the ozone layer in the stratosphere is a prominent example. In this case, scientific warning [15] was finally heard — in the last moment — by decision-makers in politics and economy: the production of the destructive chlorofluorocarbon gases was finally banned in 1995. Regarding global warming, this awareness has only been achieved in part so far, which is *not* sufficient. For instance in the USA, a country which is particularly harmful in air pollution,[9] the public is by no means sufficiently informed to understand the necessity of changing its habits: just 27 % of adults know that nitrogen is the dominant gas in the Earth's atmosphere [17], and the incompetence of its leadership [18] even led to the retreat from the Paris Climate Agreement.

More scientific competence in political and economic leadership, along with ethical consciousness, would be

---

[8]In 1993 CERN made the WWW, which had mostly been created by its employee Tim Berners-Lee, publicly accessible, free of any charge, *i.e.* it was *donated to the world.* This would hardly have happened if it were developed by a private company, and even the University of Minnesota wanted to charge a license fee for the Gopher protocol, which was considered as an alternative to the WWW at that time.

[9]In 2014, the CO_2 emission amounted to 4.97 tons per capita worldwide [16], with substantial regional differences: Subsaharan Africa 0.84, South Asia 1.46, Latin America and Caribbean 3.06, Arab World 4.86, European Union 6.47, China 7.54, USA 16.49.

highly welcome. Worldwide only few politicians have any scientific background,[10] and since the leaders appoint their advisors, the latter are unlikely to alert them when it would be strictly necessary. Apparently nobody is in a position to alert the new Brazilian government to the severe danger for life on the entire planet due to the destruction of the Amazon rainforest, the lungs of our planet.[11]
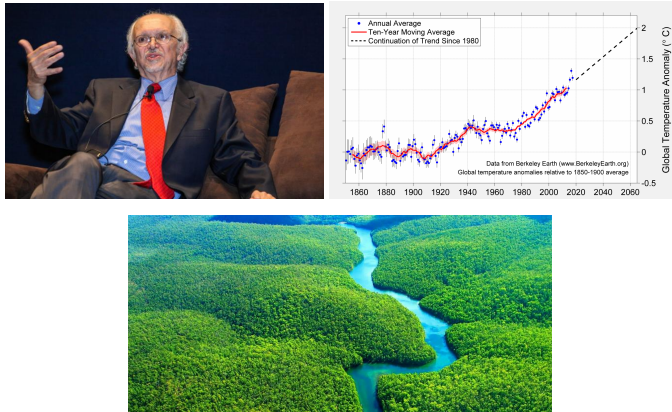

Figure 7. Left: Mario Molina, the Mexican chemist who played a key rôle in the discovery of the Antarctic ozone hole. Right: time-line of the global temperature, illustrating the rapid global warming since the 1980s. Bottom: the Amazon rainforest, where it is still intact.

Moreover there are *ongoing human-made disasters.* In particular, even in 2017 a total of 821 millions of persons suffered from hunger and malnutrition, *i.e.* one in every nine people [21]. This number keeps rising, despite massive food overproduction,[12] and millions die of preventable and treatable diseases; *e.g.* diarrhea kills more than 2000 children every day [23]. If decision-makers would be able and willing to collaborate at an international level to prevent such catastrophes, with the same harmony, efficiency and rigor as physicists at CERN, these problems would have been overcome long ago. Along these lines, a global collective effort could also do away with other evils, like illiteracy; it is hard to understand why this should be technically more difficult than discovering the gauge bosons of the weak interaction, $W^{\pm}$ and Z^0, and finally the Higgs boson.[13]

The United Nations constitute a step towards the formation of a global community which could address such urgent issues. It has proved useful at some occasions, for instance alleviating conflicts, and institutions like UNESCO, UNICEF and FAO are doing good jobs. However, the United Nations remain far below the effectiveness that would be required; in particular, it is not capable to eradicate military and economic aggression, which break international laws and cause suffering to millions and millions of humans.

In this sense, the community of scientific researchers represents a *vanguard,* an example to be followed in politics and economy. Here we finally arrive at the core of Einstein's second sentence, which he wrote in the Golden Book of the Geographic Society: he expressed it as his vision and hope for the future. Unfortunately nine decades after Einstein's visit to Havana, this is still not achieved: "globalization" takes place, but in a different sense. A collective worldwide effort to overcome ongoing disasters like malnutrition and wars should follow the examples of the scientific community's collective work to disclose the secrets of Nature. At this point, we can only iterate Einstein's vision and hope for it to finally materialize in yet future generations.

REFERENCES

[1] A. Pais, Subtle is the Lord: The Science and the Life of Albert Einstein, Oxford University Press, 1982.

[2] M. Livio, Brilliant Blunders: From Darwin to Einstein, Simon & Schuster (2013).
C. O'Raifeartaigh and S. Mitton, Physics in Perspective **20**, 318 (2018).

[3] J. Altshuler, Las 30 horas de Einstein en Cuba / Einstein's 30 hours in Cuba, Sociedad Cubana de Historia de la Ciencia y la Tecnología & Publicaciones Acuario, Havana, 2005.

[4] L. Soete, S. Schneegans, D. Eröcal, B. Angathevar and R. Rasiah,
UNESCO science report, towards 2030: executive summary,
https://unesdoc.unesco.org/ark:/48223/pf0000235407

[5] C. Day, Physics Today, April 2015.

[6] E.P. Wigner, Commun. Pure Appl. Math. **13**, 1 (1960).

[7] K. Popper, The Logic of Scientific Discovery, Hutchinson & Co., 1959.

[8] S.N. Bose, Z. Phys. **26**, 178 (1924).

[9] J. Habermas, Technik und Wissenschaft als "Ideologie", Suhrkamp, 1968.

[10] W. Bietenholz, Ciência e Sociedade, CBPF, Brazil, v.2, n.1, 33 (2014).

[11] http://planea.sep.gob.mx/ba/prueba_en_linea_2017/

[12] https://news.gallup.com/poll/21814/evolution-creationism-intelligent-design.aspx

[13] T.S. Kuhn, The Structure of Scientific Revolutions, University of Chicago Press, 1962.

[14] J.S. Bell, Physics **1**, 195 (1964). A. Aspect *et al.*, Phys. Rev. Lett. **47**, 460 (1981).

[15] M.J. Molina and F.S. Rowland, Nature **249**, 810 (1974) .

[10]Exceptions with a background in physics are Germany's long-term federal chancellor Angela Merkel, and Mexico City's new mayor Claudia Sheinbaum. In the past, we only know of one president and four prime ministers who had a degree in physics [19].

[11]Minister Santa Rosa denotes it as "unproductive" and "desert-like", and Jair Bolsonaro lamented "It's a shame that the Brazilian cavalry wasn't as efficient as the Americans, who exterminated the Indians" [20].

[12]FAO estimates that 1/3 of the food worldwide, about $1.3 \cdot 10^9$ t per year, ends up in garbage [22], while 20 000 persons starve to death every day.

[13]A popular science account is given in Ref. [24].

[16] https://data.worldbank.org/indicator/EN.ATM.CO2E.PC

[17] Pwe Research Center, http://www.pewresearch.org/science/2016/10/04/public-knowledge-about-science-has-a-limited-tie-to-peoples-beliefs-about-climate-change-and-climate-scientists/

[18] S. Kaplan, The Washington Post, November 10, 2016. For instance, it quotes Trump's statement "I think climate change is just a very, very expensive form of tax".

[19] https://de.wikipedia.org/wiki/Liste_bekannter_Physik er_in_anderen_Berufsfeldern

[20] F. Watson, The Independent, April 10, 2019.

[21] UNICEF Report, The State of Food Security and Nutrition in the World 2018, http://www.fao.org/3/I9553EN/i9553en.pdf

[22] http://www.fao.org/food-loss-and-food-waste/en/

[23] Centers of Disease Control and Prevention, Global Diarrhea Burden https://www.cdc.gov/healthywater/global/diarrhea-bur den.html

[24] W. Bietenholz, Rev. Cubana Fis. **30**, 109 (2013).

SOS FÍSICA: OCHO DESAFÍOS PARA LA FÍSICA CUBANA CONTEMPORÁNEA

SOS PHYSICS: EIGHT CHALLENGES FOR CONTEMPORARY CUBAN PHYSICS

C. Cabal-Mirabal

Facultad de Física, Universidad de La Habana, 10400 La Habana, Cuba; cabal@fisica.uh.cu

"...Los peligros no se han de ver cuando se les tiene encima, sino cuando se pueden evitar. Lo primero en política es aclarar y prever... Ver después no vale, lo que vale es ver antes y estar preparados..."

José Martí Pérez, 1889.

Los desafíos que enfrentan la Física y los físicos cubanos, son parte de los retos que tienen la Ciencia y la sociedad cubanas. Muchos están asociados al propio desarrollo de la Física en Cuba, otros son consecuencia de un deterioro de los ritmos de avance de la Ciencia en las pasadas décadas. No obstante, estos y otros factores se entremezclan. Su abordaje requiere alianzas, recaba de la acción mancomunada de sectores de la Ciencia, la Educación incluyendo la Superior, de los medios masivos de comunicación y otros actores sociales, ya que los problemas a resolver sobrepasan el marco estricto de la Física. Los retos que tienen la Física y los físicos en nuestro país, podrán enfrentarse exitosamente solo si esas interconexiones son efectivas y se logra movilizar al resto de la sociedad a corto plazo bajo conducción de políticas nacionales acertadas. Es ineludible resaltar asimismo, que algunos de estos desafíos son similares a la de otros países, incluyendo los desarrollados. Estar al tanto de sus experiencias puede vislumbrar caminos, opciones y alianzas internacionales para su solución.

Mencionar solo los desafíos no es lo seductor; sí lo seria trazar los posibles caminos para la solución. Sin embargo, esta compleja tarea no está al alcance de estas líneas. Seguramente se podrán mencionar otros retos más allá de los que aquí nos referimos. No obstante, la enumeración de estos ocho, que nos parecen esenciales, tiene cierta utilidad ya que invitan a pensar (ojalá a la acción), reavivan la inquietud y constituyen una alerta más.

La comunidad de los Físicos se ha expresado casi de todas las formas posibles, a través de artículos publicados en revistas científicas, en la prensa, en debates públicos dentro y fuera de los contextos académicos, en sus pasados Congresos... e intentan, una y otra vez, a irse por encima de las adversidades. Seguro estoy que los físicos estamos dispuestos a discutir a fondo los problemas y ser pro activos en su abordaje. La visión optimista es indispensable. Ella se fundamenta en los logros indiscutibles de la ciencia y de los otros sectores de la sociedad cubana. La agudeza de la situación, unida a la persistencia, las convicciones firmes, la objetividad en el debate y en el quehacer, deberán ser factores de éxito que conduzcan las posibles acciones transformadoras.

La exposición de los retos no responde a un orden de prioridad por lo que su enumeración es solo a los efectos ya que están estrechamente interconectados.

1. Enseñanza de la Física. Es imprescindible rescatar la enseñanza de la Física, como ciencia básica, amena, moderna y con rigor, en todos los niveles de enseñanza. El énfasis deberá hacerse en las siguientes direcciones:

   - La formación de los Profesores de Física para la enseñanza Media, Preuniversitaria y Tecnológica.
   - En la enseñanza Preuniversitaria, secundaria y Tecnológica.
   - La enseñanza de la Física en las carreras universitarias de ciencias Básicas e Ingenierías.
   - En las carreras de perfil Médico.

2. Sostener una "masa crítica" de físicos motivados, comprometidos, con alto nivel científico, cultural y académico en las Universidades cubanas, sobre todo en las carreras de Física en las tres universidades existentes. Fortalecer la interrelación activa y dinámica entre los claustros de Física de las universidades; aun cuando sean departamentos docentes de otras carreras, con énfasis en los Institutos Pedagógicos donde se forman los profesores de Física para la enseñanza precedente.

3. Establecer un sistema de selección temprana de jóvenes estudiantes de pregrado y post grado para acelerar su formación utilizando todas las posibilidades nacionales e internacionales.

4. Rescatar, modernizar, ampliar la base material de los laboratorios docentes y de investigación. Lograr que la experimentación tenga el lugar ineludible que le corresponde en la formación en todos los niveles de enseñanza. Es la Física Experimental una de las vías más efectivas para la comprensión de los fenómenos de la naturaleza y para entender el desarrollo tecnológico contemporáneo, base del progreso socioeconómico.

5. Conectar las investigaciones en Física con las demás ramas de las Ciencias Naturales y Técnicas, con los sectores científicos y productivos más importantes del país, mediante un plan coherente, intencionado, de mediano y largo plazo. Encontrar los mecanismos para garantizar su sostenibilidad y desarrollo de estar interconexiones.

Instituir como prioridad el direccionamiento de los esfuerzos hacia las Ciencias de la Vida, dada las tradiciones y logros de la Medicina y la Biotecnología autóctonas, retadas por la actual Tercera Revolución en la Biología, que se edifica en la convergencia de las Ciencias Básicas, fundamentalmente la Física y las Ciencias Técnicas con las Ciencias Biológicas.

6. Contribuir a la divulgación científica, creando un sistema que permita incrementar la motivación por esta rama de la ciencia, reforzando el pensamiento, el método y las tradiciones científicas en toda la sociedad, y así restringir el espacio para las manifestaciones seudocientíficas. Ampliar la comprensión del papel decisivo de la Física y el desarrollo del país en círculos de decisores, profesionales y el resto de la sociedad. Esta difusión, entre los expertos y el resto de la población, deberá incluir los logros, conflictos y desafíos de la ciencia contemporánea. La divulgación científica deberá estar acompañada de un sistema de vigilancia científico- tecnológica donde se vislumbren los derroteros más generales y los particulares de los avances científicos a nivel mundial, y las revoluciones que tiene lugar en la ciencia y la tecnología. Acrecentar el conocimiento y divulgación de la historia de la Física mundial como sustento cultural y ético para conocer las regularidades e individualidades de la creación científica, experimental y teórica. Fortalecer la Revista Cubana de Física elevando su nivel, ampliando sus opciones y visibilidad. Ella debe ser un punto de apoyo efectivo para seguir afrontando los desafíos.

7. Resulta vital para el éxito ante los desafíos incrementar la diversidad, estabilidad, dinamismo, efectividad y coherencia de las conexiones de la Física en Cuba con el resto de los países.

8. Preservar a los físicos y el patrimonio creado por ellos en Cuba y en el exterior: tesis, libros, laboratorios, equipos, apuntes importantes, fotos, resultados, estadísticas. . .

La Física; los físicos, debemos reclamar nuestra participación activa e intencionada en ese decisivo y trascendente reto. Nos corresponde.


ARBELIO SE DESPIDE

En marzo de 2019 terminó oficialmente el período como Decano de la Facultad de Física de la Universidad de La Habana del doctor Arbelio Pentón–Madrigal; una responsabilidad que había comenzado a desempeñar casi 5 años antes, en julio de 2014.

Bajo la dirección de Arbelio se materializó el retorno de nuestro claustro y nuestros estudiantes a su edificio, a pesar de que la planta baja del inmueble aún no ha sido terminada, y a contrapelo de que muchas de las reparaciones ejecutadas por la brigada de "Puerto Carenas" a cargo de la obra resultaron deficientes. Este "retorno a la tierra prometida" constituye la respuesta a quienes pensaron que nunca volveríamos, cuando alrededor del año 2006 la dirección de la facultad tomó la decisión de vaciar el edificio para que la reparación capital pudiera materializarse, y para proteger las vidas de estudiantes y profesores ante el posible colapso de columnas y techos, especialmente en el último piso.
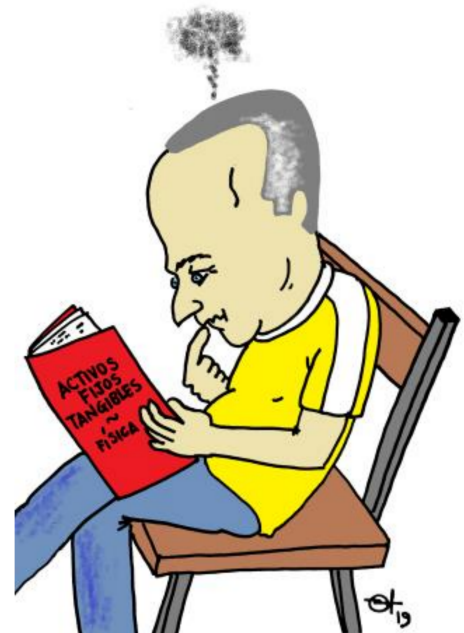
Un adiós con sentido del humor. Izquierda: En un acto celebrado en la Facultad de Física el día 21 de marzo de 2019, el decano saliente Dr. Arbelio Pentón recibe una caricatura de manos de la decana entrante, Dra. Aimé Peláiz. Derecha: detalle de la caricatura realizada con motivo de la ocasión (Foto: E. Altshuler)

Podemos discutir una eternidad sobre hasta qué punto el altruismo está o no condicionado por las circunstancias. Pero existe un hecho incontestable: a costa del lacerante sacrificio profesional y personal de Arbelio durante un lustro, el edificio ha crecido y ha ido saliendo de los baches de su crecimiento, algunos hemos podido avanzar profesionalmente; hay quien ha podido disfrutar de una vida personal más o menos sosegada. Mientras ello sucedía, el decano estaba en una reunión insulsa de 8 horas, o discutiendo con una brigada de albañiles, o hablando alemán con un premio Nobel de visita, o "dando trapeador" en un laboratorio docente a las 6 de la tarde un día cualquiera. Y, casi siempre, con una sonrisa en los labios… O, como máximo, con alguna frase mordaz escapando de ellos. Cierto: ese no es el concepto de un decano "de libro de texto". Pero es el concepto de un decano cubano cuando realmente le importa la responsabilidad que tiene entre manos. Cuando no se habla de sacrificio, sino que se practica el sacrificio.

Su lugar ha sido ocupado por la doctora Aimé Peláiz-Barranco, una colega de probada trayectoria profesional que pertenece a una generación más nueva. En sus manos hemos colocado la difícil tarea de incrementar el "orden y concierto" en nuestra institución, haciendo malabares entre el término del edificio de Física y la batalla que la Comisión de Carrera de Física libra para lograr un plan de estudios E verdaderamente digno de la historia de nuestra carrera.

Sea cual fuere nuestro derrotero final, debemos dormir tranquilos pensando que Física ha tenido la suerte y la entereza de mantener su estirpe con dirigentes que, de un modo u otro, son el fruto de nuestra propia formación, y de nuestra propia decisión.

E. Altshuler

8 DÉCADAS DE MELQUÍADES

El 20 de diciembre de 2018 se celebró el Mini-Taller "Celebración de los 80 años del Profesor Titular, Dr.C. Melquiades de Dios Leyva" en la Facultad de Física de la Universidad de La Habana. El taller, organizado por Arbelio Pentón Madrigal, Leo Diago Cisneros y María Teresa Pérez Maldonado, contó con la presentación de ponencias de Carlos Rodríguez Castellanos, José Marín Antuña, Leo Diago Cisneros, y la colaboración de Jorge Portelles Rodríguez (video, fotos) y Dayana Valdés Radillo.

Celebrando los 80 de Melquiades. Izquierda: foto de grupo de los participantes (Melquiades es el quinto de la fila delantera, contando de izquierda a derecha). Derecha: Caricatura entregada al homenajeado por el entonces decano Arbelio Pentón-Madrigal.

A continuación, se esboza una reseña biográfica de Melquiades de Dios-Leyva, basada en las palabras pronunciadas por Carlos Rodríguez durante el taller.

El profesor Melquiades de Dios Leyva se graduó como Licenciado en Física en 1968. Entre 1968 y 1972 transcurre una primera etapa de formación especializada, en parte autodidacta, en parte mediante la asistencia a cursos cortos de profesores extranjeros invitados a las escuelas de verano. Esta etapa culminó con la defensa de su tesis de Maestro en Ciencias Físicas sobre la aplicación del método de factorización a la solución de problemas de Mecánica Cuántica. Esta fue la primera tesis de maestría que se defendió en la Universidad de la Habana. Entre 1972 y 1975 se inician sus trabajos sobre Teoría Cuántica de Sólidos, primero sobre interacción electrón – fonón y luego sobre propiedades ópticas de sólidos. Entre sus 4 publicaciones de esta etapa se destaca una en la revista alemana "Physica Status Solidi-b", que es la primera publicación internacional producida en la entonces Escuela de Física.

A partir de 1975 desarrolla sus estudios de doctorado en la Facultad de Física de la Universidad Estatal de Moscú, donde investiga los estados electrónicos de semiconductores de gap estrecho. Sobre este tema publicó dos artículos en la Revista Cubana de Física.

A partir de 1981 comienzan sus trabajos sobre heteroestructuras semiconductoras, que es el tema central de su carrera científica, en el que ha publicado más de ochenta trabajos en revistas arbitradas. Aquí se incluye una amplia diversidad de sistemas: superredes periódicas, finitas y de Fibonacci, pozos cuánticos simples y dobles, hilos y puntos cuánticos, generalmente basados en materiales semiconductores de los grupos II-V y II-VI. Son objeto de estudio los estados electrónicos en las bandas e impurezas y los excitones, se analiza su comportamiento en campos magnéticos paralelos o perpendiculares a la dirección de crecimiento de la heteroestructura, los efectos de la presión, la temperatura y la radiación luminosa. Estos estudios se enfocan hacia la discusión de las propiedades ópticas y magneto-ópticas, así como las relacionadas con el transporte de carga y espín en estos sistemas. En estos trabajos se despliega un amplio arsenal de métodos exactos y aproximados de la mecánica cuántica de una partícula, explotando al máximo las propiedades de simetría de los sistemas estudiados. Mención aparte merecen sus trabajos sobre la aplicación del método de la dimensión espacial fraccionaria al estudio de los estados de electrones ligados a impurezas.

A partir de 2007 se inicia un ciclo de trabajos sobre cristales y estructuras fotónicas que hasta el momento ha producido 10 publicaciones. Aquí se incluye el cálculo de relaciones de dispersión, el estudio las condiciones de gap nulo y el transporte de energía en estos sistemas. Desde 2015 ha publicado cinco artículos acerca del efecto de los campos magnéticos sobre los estados electrónicos y las propiedades ópticas de superredes de grafeno.

Una característica relevante de los trabajos mencionados es el empleo de modelos realistas y la comparación de los cálculos

teóricos con los resultados experimentales.

En total, aparecen 106 publicaciones con 43 coautores, entre los que se destacan el profesor brasileño Luiz de Oliveira y el colombiano Carlos Duque. Ha dirigido seis doctorados y nueve tesis de licenciatura. Seis de sus trabajos han recibido premios de la Academia de Ciencias de Cuba, cuatro de la Universidad de La Habana y dos del Ministerio de Educación Superior. Ha sido Profesor Asociado del Centro Internacional de Física Teórica de Trieste, Italia. Recibió el Premio Nacional de Física la primera vez que se otorgó. Fue electo Académico de número para el ejercicio 2012-2018 y ha sido propuesto como Académico de Honor por la Academia de Ciencias de Cuba.

En general, los trabajos científicos del profesor Melquiades de Dios Leyva se caracterizan por el mismo rigor, la precisión, solidez, profundidad y detalle que apreciamos en sus clases aquellos que hemos tenido el honor de ser sus alumnos. Y la exigencia que recibimos la vemos reflejada en su labor científica como auto exigencia.

¿Cómo explicar tan extensa y valiosa obra de quien llegó relativamente tarde a la vida científica? ¿Cómo explicar que su productividad científica haya alcanzado un máximo a los setenta años y que, aún hoy, no presente síntomas de decaer? Los que hemos compartido la vida laboral con Melquiades sabemos que algunas de esas etapas de alta productividad han coincidido con momentos de serios problemas personales, que no han hecho mella en la autodisciplina, el tesón y la dedicación que, unidos a su sólida formación, lo han convertido en un ejemplo para varias generaciones de físicos cubanos.

L. Diago
Profesor, Facultad de Física
Universidad de La Habana

EJERCICIO DE COMPARACIÓN DE PIRANÓMETROS: EVALUANDO LA CALIDAD FOTOVOLTAICA DE CUBA

En el marco del proyecto INFRAESTRUCTURA DE LA CALIDAD PARA ENERGIAS RENOVABLES Y EFICIENCIA ENERGÉTICA, se realizó del **22 al 25 de Abril del 2019, en el Laboratorio de Investigaciones Fotovoltaicas de la Universidad de La Habana**, un ejercicio de comparación de piranómetros en el que participaron varias instituciones cubanas y extranjeras. El proyecto en cuestión se encuentra auspiciado por el PTB de Alemania, la Cooperación Alemana y la Agencia Mexicana de Cooperación Internacional para el Desarrollo (AMEXCID). La contraparte formal del proyecto en Cuba es la Oficina Nacional de Normalización (ONN).

Un piranómetro es un instrumento que permite medir la radiación solar con una gran exactitud. Estos dispositivos pueden ser utilizados en una gran variedad de aplicaciones donde la radiación solar juega un papel importante. En el caso de la fotovoltaica, una de las energías renovables con mayor potencial de desarrollo en nuestro país, la medición de la radiación solar es vital para poder estimar el rendimiento de los parques fotovoltaicos.

Piranómetros en la azotea del edificio de la Facultad de Física. Izquierda: foto de varios de los especialistas involucrados en el ejercicio. Derecha: detalles de los piranómetros.

El ejercicio de comparación de piranómetros se realizó en el techo de la Facultad de Física, organizado por el Laboratorio de Investigaciones Fotovoltaicas de la Universidad de La Habana y con la orientación del Centro Nacional de Metrología de México (CENAM). En este ejercicio se realizaron mediciones de radiación solar comparando un grupo de 12 piranómetros con dos instrumentos patrones pertenecientes al propio CENAM y al Observatorio de Radiación Solar del Instituto de Geofísica de la UNAM. Las instituciones participantes fueron: Centro Nacional de Metrología de México (CENAM), Instituto de

Geofísica-Servicio Solarimétrico Mexicano de la UNAM, Instituto de Biotecnología e Innovación Industrial (IIBI) de República Dominicana, Instituto Dominicano para la Calidad (INDOCAL) de República Dominicana, Laboratorio de Investigaciones Fotovoltaicas del Instituto de Ciencia y Tecnología de Materiales (IMRE) - Facultad de Física de la Universidad de La Habana, Unión Nacional Eléctrica (UNE) representada por las empresas ATI y EDIFRE, Centro de Estudio de Tecnologías Energéticas Renovables (CETER) de la CUJAE, Centro de Investigación de Energía Solar (CIES) de Santiago de Cuba, Instituto de Meteorología (INSMET), Grupo de Óptica Atmosférica de Camagüey (GOAC) perteneciente al INSMET y CUBAENERGÍA.

Este ejercicio es la primera comparación internacional de piranómetros que se realiza en Cuba y permitió Introducir a los participantes en los conceptos, condiciones, normativas, instrumentación, desarrollo, cálculos, estimación de la incertidumbre de la medición, análisis de resultados y documentación necesarios para la organización de una comparación de piranómetros en exterior.

Lídice Vaillant-Roca
Labortorio de Investigaciones Fotovoltaicas
Universidad de La Habana

CINCO DOCTORES EN CIENCIAS FÍSICAS, Y UNO EN CIENCIAS

Los días 11 y 12 de dicembre de 2018 fueron momento de recoger cosecha. Se defendieron exitosamente 5 jóvenes doctorantes en ciencias Físicas, barriendo temas en un amplio rango que abarcó desde la Superconductividad hasta la Biofísica.

La Superconductvidad sigue produciendo doctores. Imagen de la defensa de doctorado de M. A. Hernández-Wolpez (Universidad de Camagüey), que tuvo lugar el día 12 de diciembre de 2018 en la Facultad de Física, Universidad de La Habana.

Lídice Cruz-Rodríguez (Universidad de La Habana) presentó la tesis "Estudio de las propiedades físicas de clústeres atómicos: dinámica molecular cuántica". La tesis, tutorada por LL. Uranga y A. Martínez, fue defendida ante un tribunal internacional, desarrollándose en modo bilingüe durante parte de las respuestas a las preguntas del tribunal.

Nelia López-Marín (Universidad de La Habana) presentó la tesis "Una aproximación computacional a la terapia fotodinámica en células tumorales", bajo la turoría de R. Mulet.

Eduardo Domínguez-Vázquez (Universidad de La Habana), defendió la tesis "Extensiones del método variacional de clusters: sistemas cuánticos y dinámica de espines", tutorado por R. Mulet y A. Lage.

Alexey Cruz-Vázquez (Universidad de Oriente), defendió la tesis "Transporte eléctrico en muestras superconductoras policristalinas de $Bi_{1.65}Pb_{0.35}Sr_2Ca_{2+d}Cu_{3+d}O_y$", bajo la dirección de P. Muné y E. Altshuler.

Finalmente, **Manuel. A. Hernández-Wolpez** (Universidad de Camagüey) defendió la ponencia "Penetración, atrapamiento y relajación de vórtices Abrikosov-Josephson en cerámicas superconductoras de (Bi, Pb)-2223", tutorada por P. Muné, R. Figueroa y E. Gararo-Pérez.

Meses más tarde, el 4 de junio de 2019, el profesor **Ernesto Altshuler** (Universidad de La Habana) defendió la tesis de doctorado en ciencias "Vórtices, granos y hormigas: experimentos en sistemas complejos".

E. Altshuler

SE CELEBRÓ LA OCTAVA EDICIÓN DEL TALLER IBEROAMERICANO DE ENSEÑANZA DE LA FÍSICA

La Universidad de La Habana y la Sociedad Cubana de Física, en colaboración con la Universidad Nacional de Educación a Distancia (UNED) y la Universidad de Burgos, ambas de España, y el Karlsruhe Institute of Technology de Alemania convocaron la octava edición del Taller Iberoamericano de Enseñanza de la Física Universitaria (VIII TIBERO), que se celebró en la Facultad de Física de la Universidad de La Habana (Cuba) del 11 al 15 de marzo de 2019.

El tema central del taller fue: "Introducción de la Cosmología en los programas de la Licenciatura en Física". Además, durante todos los días que duró el evento, se impartió un curso de actualización sobre Elecricidad y Magnetismo para los participantes en el Taller. Otros temas tratados, fueron: Actualizaciones en temas fronteras de la Física, Experiencias en el Proceso de Enseñanza-Aprendizaje para mejorar las habilidades profesionales en las Carreras de Física. El Papel de la Enseñanza Experimental y el procesamiento de los datos en el Aprendizaje de la Física, Enseñanza de la Física en la Formación de Profesionales de otras Especialidades y Vías No Formales de Enseñanza de la Física.

En el taller se impartió un curso de actualización en electromagnetismo, se impartieron 13 conferencias magistrales, se realizó una mesa redonda, y se presentaron 14 comunicaciones cortas y 36 carteles. La conferencia inaugural, "Ciencia y

tecnología en la aventura espacial: el caso de Marte", fue impartida por el profesor Fernando Rull Pérez, Director de la Unidad Asociada Universidad de Valladolid (UVA) – Consejo Superior de Investigaciones Científicas (CSIC) al Centro de Astrobiología, asociado al NASA Astrobiology Institute, de España. La conferencia de clausura, "James Clerk Maxwell y las ecuaciones que cambiaron el mundo", estuvo a cargo del profesor Augusto Beléndez Vázquez, del Departamento de Física, Ingeniería de Sistemas y Teoría de la Señal de la Universidad de Alicante, España.

Imágenes del VIII TIBERO. Izquierda: un momento de la conferencia inaugural a cargo de Fernando Rull Pérez (Universidad de Valladolid, España). Derecha: Foto de grupo de los participantes en la entrada de la Facultad de Física de la Universidad de La Habana.

En el taller participaron 1 alemán, 4 colombianos, 33 cubanos, 6 españoles, 6 mexicanos y 1 puertorriqueño. Entre los resultados del taller, están: (a) Iniciar la formación de un grupo de trabajo entre varias universidades para elaborar un curso online gratuito, sobre el tema de Astrofísica y Cosmología, que podría estar disponible en las plataformas virtuales de las universidades, (b) Se valoró el criterio de estudiantes, que manifestaron que ellos entran a la universidad para iniciar sus estudios de Física ilusionados por temas de Astrofísica, Cosmología,… (que les habían introducido en preuniversitario);

y, sin embargo, se desilusionan al finalizar el primer año al ver que no se estudian esos temas y (c) Se creó un repositorio para el intercambio de información relacionada con la docencia: *https://unedo365-my.sharepoint.com/:f:/g/personal/jpsanchez_ccia_uned_es/Eo10l0MSZ-BHsCpgild4BckB-k39N95CGlTb96lur_5ffQ?e=51mn5g*

O. Calzadilla Amaya
Facultad de Física
Universidad de La Habana

LA BIOLOGÍA, SEGÚN LA FÍSICA ESTADÍSTICA

Del 4 al 15 de febrero de 2019 se celebró en la Facultad de Física de la Universidad de La Habana, la escuela "Statistical Physics Approaches to Systems Biology", dedicada al uso de las técnicas de la Física Estadística al estudio de sistemas biológicos complejos. El evento –organizado fundamentalmente por físicos cubanos y alemanes– puso especial énfasis en los desarrollos recientes del análisis de datos, así como en la comprensión de la

inmunología, el metabolismo y los procesos evolutivos generales en los procesos biológicos. Los últimos dos días de la reunión se dedicaron a un taller más avanzado que contempló un espectro más amplio de tópicos, incluyendo problemas inversos, redes biológicas, inmunología teórica, y evolución de tumores.

E. Altshuler

COSMOLOGÍA, FÍSICA NUCLEAR Y MUCHO MÁS EN 2019

Entre el 6 y el 12 de mayo pasado se celebraron en Cuba el Quinto Simposio Caribeño de Cosmología, Gravitación, Física Nuclear y Astropartículas STARS 2019 y el Sexto Simposio internacional de Campos Electromagnéticos Intensos y Estrellas de Neutrones SMFNS 2019. Este evento, organizado de manera bianual por la Sociedad Cubana de Física y el Instituto de Cibernética Matemática y Física (ICIMAF), reunió un total de 53 participantes, 37 extranjeros y 16 cubanos. Esta edición contó además con el auspicio del ICTP y del CLAF, lo cual permitió la participación de un gran número de estudiantes de Latinoamérica.

Las actividades relacionadas con el STAR/SMFNS2019 comenzaron desde los días 3 y 4 de mayo, con la realización en el ICIMAF de la escuela satélite de estos eventos: "Astrofísica relativista y problemas relacionados". Durante estos dos días, 23 estudiantes de pregrado y posgrado de la Facultad de Física de la Universidad de la Habana, del INSTEC, y de varias instituciones latinoamericanas, recibieron cuatro cursos cortos acerca de la modelación de objetos compactos, los experimentos dedicados a explorar el diagrama de fases de la QCD, la física de los discos de acreción, y la formulación matemática de la

magnetohidrodinámica relativista. Estos cursos contaron con profesores destacados, especialistas en cada uno de los temas.

La quinta edición del STARS (6-8 de mayo), dedicada al aniversario 500 de La Habana, tuvo como sede a la Casa Museo Árabe, sita en la Habana Vieja. Aunque durante sus sesiones se abordaron temas diversos, que abarcaron desde la arqueoastronomía hasta la física de altas energías, la mayoría de las discusiones se centraron en la detección de ondas gravitacionales y la primera foto obtenida de un agujero negro, dos logros observacionales recientes que se espera tendrán un gran impacto en nuestra forma de comprender el Universo.

Fotos de grupo. Izquierda: estudiantes y profesores de la escuela internacional Astrofísica Relativista y Problemas Relacionados, en la entrada de una de las dependencias del ICIMAF. Derecha: Participantes del SMFNS 2019 durante la clausura del evento, en Varadero.

Como ya es habitual, el SMNF2019 (8-12 de mayo) tuvo por sede al hotel Labranda Varadero en la provincia de Matanzas. Siendo este un evento de temática más específica, casi la totalidad de sus sesiones se dedicaron a los estudios teóricos y experimentales de los efectos del campo magnético en la materia nuclear y sus consecuencias a escalas macroscópicas, en particular en escenarios astrofísicos. No obstante, como ya se ha hecho en ediciones anteriores, se realizó una sesión dedicada a la Astrobiología.

Los eventos finalizaron con la entrega por segunda vez de los Premios Walter Greiner a los mejores trabajos presentados por estudiantes. Este premio fue instituido hace dos ediciones en honor al físico alemán Walter Greiner, fallecido en 2017, y quien fuera un entusiasta participante del STARS/SMFNS. En esta edición, 15 jóvenes optaron por el premio y cuatro resultaron premiados, las estudiantes de posgrado Gretel Quintero (Facultad de Física-UH-ICIMAF) y Diana Alvear (ICIMAF), y los estudiantes de pregrado Samantha López (Facultad de Física-UH-ICIMAF) y Víctor Alexander Torres Sánchez (Universidad Yachay Tech, Ecuador).

Gretel Quintero-Angulo
Facultad de Física,
Universidad de La Habana

CELÉBRASE VI TALLER DE ENSEÑANZA DE LA FÍSICA EN LA UNIVERSIDAD DE ORIENTE

Entre los días 6 y 8 de junio de 2019, convocado por los Departamentos de Física Aplicada (DFA) y Física (DF) de la Facultad de Ciencias Naturales y Exactas de la Universidad de Oriente (UO) y con el auspicio de la Sociedad Cubana de Física (SCF), se desarrolló el VI Taller de Enseñanza de la Física en la Universidad de Oriente.

En esta ocasión, fue dedicado a la conmemoración del centenario de los artículos "El eclipse total del 29 de mayo de 1919 y el efecto de la gravitación sobre la luz" por A. Eddington y "Colisiones de las partículas alfa con átomos ligeros", por E. Rutherford, que constituyen la primera corroboración de la Teoría General de la Relatividad y el reporte de la primera Reacción Nuclear, respectivamente. El Profesor Consultante del DF MSc. Luis M. Méndez Pérez –Vicepresidente de la SCF y Presidente del Grupo de la SCF en Santiago de Cuba– dictó una conferencia sobre ambos aniversarios trascendentales para el desarrollo de la física.

Participantes en el VI Taller de Enseñanza de la Física Universidad de Oriente.

En este Taller participaron profesores e investigadores de los departamentos coauspiciadores y de otras entidades de la UO como el Centro de Biofísica Médica (CBM) y la Facultad de Automática; y de otros centros del país, verbigracia: Universidad Central "Marta Abreu" de Las Villas (UCLV), Universidad "Vladimir Ilich Lenin" de Las Tunas, Universidad de Camagüey, Universidad de las Ciencias de la Informática (UCI), Universidad de Cienfuegos, Universidad "Oscar Lucero" de Holguín y en esta ocasión se tuvo la participación de un representante de la Universidad Nacional de Colombia.

El taller contó con 36 participantes, entre ellos, 3 estudiantes de tercer año de la carrera de Licenciatura en Física de la UCLV y se presentaron 36 ponencias orales en seis comisiones. Todos los trabajos coincidieron de una forma u otra en el análisis, desde distintas perspectivas, de los métodos en la enseñanza de la física, entre ellos métodos y medios durante el trabajo experimental y su influencia en el componente investigativo de los estudiantes, las tecnologías de información y las comunicaciones y su influencia en el proceso de enseñanza aprendizaje, el pensamiento sistémico

para contribuir al aprendizaje significativo, etc.

Se dictaron además las conferencias "Doctorado en Ciencia Básicas de la Universidad de Oriente" por el Dr. C. Pedro D. Muné Bandera, "Sobre la superación postgraduada" por la Dra. C. María Julia Rodríguez Saif y "Reflexiones sobre problemas interesantes" a cargo del Dr. C. Faustino Repilado Ramírez.

El Taller tuvo como colofón el homenaje a Fidel Castro-Ruz en el monumento donde reposan sus restos en el cementerio de Santa Efigenia. El saldo de este VI Taller se puede considerar positivo por las temáticas abordadas, la profundidad de los debates y el nivel de socialización alcanzado. Esperando que el VII Taller dedicado al L aniversario de la primera y única graduación de Ingenieros Físicos en la UO, el próximo año tenga iguales o mejores resultados.

Comité organizador
VI Taller de Enseñanza de la Física,
Universidad de Oriente

LA CUARTA OLIMPÍADA CENTROAMERICANA Y DEL CARIBE DE FÍSICA (OCCAFI) TUVO LUGAR EN LA UNIVERSIDAD DE LA HABANA

Profesores y estudiantes del equipo cubano. De izquierda a derecha: segundo, Frank Daniel Fonseca Rondón (mención), tercero Frank Eduardo Castel-Martín (medalla de plata), tercero y cuarto, René Alejandro Mirabal Rodríguez y Kevin Sarria Torres (medallas de oro). (Foto: A. Peláiz)

Del 17 al 21 de junio del 2019 se realizó en la Habana la IV Olimpiada Centroamericana y del Caribe de Física organizada por el Ministerio de Educación de Cuba (MINED). Este evento tuvo como sede permanente la Facultad de Física de la Universidad de La Habana.

En la OCCAFI participaron un total de nueve países: Costa Rica, Puerto Rico, Colombia, México, Honduras, Guatemala, El Salvador, Perú y Cuba. Más allá de la propia competencia, entre los

32 participantes se creó un espacio apropiado para el intercambio de experiencia, saberes y buenas prácticas entre profesores y estudiantes. La profundización de los elementos metodológicos y didácticos para la enseñanza de la física fue punto central de los intercambios entre profesores participantes en este evento.

El martes 18 de junio se desarrolló la prueba experimental y al día siguiente el examen teórico. Los resultados de la competencia fueron dados a conocer en el Aula Magna de la Universidad de La Habana. Fueron otorgados 25 premios, destacándose Cuba como el único país con medallas de oro.

Premios por países

País	Oro	Plata	Bronce	Mención
Cuba	2	1	-	1
México	-	2	2	-
Perú	-	2	2	-
Costa Rica	-	1	-	2
Colombia	-	-	4	-
El Salvador	-	-	2	1
Honduras	-	-	2	1

A.Pentón-Madrigal
Facultad de Física,
Universidad de la Habana

ROLAND GRÖSSINGER
(14 de mayo de 1944 - 25 de diciembre de 2018)

Grössinger en Cuba. De izquierda a derecha: sentados Rolando Grössinger, Arbelio Pentón, parados: Ernesto Estévez y Reiko Sato Turtelli. Foto tomada en la UCI en el mes noviembre del 2009. (Foto: A. Pentón)

El profesor Roland Grössinger falleció el pasado diciembre 25 a la edad de 75 años. Roland estudió Física en la Universidad Tecnológica de Viena culminando sus estudios iniciales en 1870 con uns tesis sobre el efecto Mössbauer. Como parte de ese trabajo participó en la construcción del primer espectómetro Mössbauer en Austria. En 1975 culminó sus estudios doctorales sobre trabajos en materiales magnéticos intermetálicos. En 1983 se le otorgó el la condición Venia Legendi como docente universitario y en 1993 el Ministerio de Ciencias de su país le otorgó la condición de Profesor universitario extraordinario. Pionero en los estudios de materiales en altos campos magnéticos fue el inventor de diversos sietmas de obtención de ultraltos campos magnéticos pulsados y reconocido mundialmente por sus aportes en este campo. Publicó más de 400 artículos científicos, más de 100 conferencias invitadas en eventos internacionales y participó en al menos 10 patentes de invención. Bajo su supervisión se formaron más de 20 doctores y 50 tesis de diploma.

Roland fue un amigo probado de Cuba y en particular de la Universidad de la Habana de la que fue Profesor Invitado. Bajo su supervisión se formaron varios doctores de nuestra universidad. Su apoyo rebasó tales marcos y donó a nuestro centro diversos equipos científicos a la vez que permitió la construcción de otros en su laboratorio, libre de costo, para ser traídos a nuestros laboratorios. Nos visitó regularmente por más de dos décadas, participando en eventos, escuelas de verano, proyectos conjuntos y visitas de trabajo. En más de una ocasión manifestó su admiración por Cuba y su gente, por la calidad de nuestra educación y por nuestra persistencia frente a las adversidades. El y su esposa, la también física Reiko Sato, demostraron en tiempos difíciles su amistad irrevocable y una voluntad permanente por ayudar al desarrollo de la física experimental en Cuba. Su fallecimiento es motivo de gran pena para todos aquellos que tuvieron la suerte de conocerlo y compartir su amistad sincera.

E. Estévez y A. Pentón
Facultad de Física,
Universidad de La Habana

ZHORES IVANOVICH ALFEROV
(15 de marzo de 1930-1 de marzo de 2019)

Zhores Alferov en el anfiteatro de la Facultad de Física de la Universidad de la Habana durante su visita en mayo de 2006 para recibir el título de doctor Honoris causa de la Universidad de la Habana.El entonces decano, Osvaldo de Melo, le entrega un pullover con el logotipo de la facultad de Física de la Universidad de La Habana.

Alferov nació el 15 de marzo de1930 en Bielorrusia y murió el 1 de marzo de 2019 en San Petersburgo. Nació al comienzo de la era de la electrónica, que de manera tan significativa ha cambiado nuestras vidas y fue precisamente a desarrollar la tecnología de esta nueva época, que estaba destinado al graduarse en el Departamento de Electrónica del Instituto Electrotécnico Ulianov de Leningrado (hoy San Petersburgo) en 1952. Una vez terminada su carrera, obtuvo una posición en el famoso Instituto Físico-Técnico Ioffe de esta misma ciudad, uno de los centros líderes en la investigación en Rusia. Años más tarde Alferov se refirió a su entrada allí como "la suerte que habría de determinar su feliz carrera científica".

Sin dudas su mayor resultado científico fue la modelación y fabricación de las "heterostructuras" semiconductoras. La mezcla de semiconductores con propiedades electrónicas diferentes permitió crear materiales con propiedades que no existían en la naturaleza dando origen a lo que se conoce como ingeniería de bandas, proceso que permite controlar o alterar los parámetros fundamentales de un semiconductor, como el ancho de la banda prohibida, la masa efectiva de los portadores de carga, la movilidad, el índice de refracción, etc, variando la composición de las aleaciones o fabricando estructuras "sándwich" que combinan capas de semiconductores diferentes.

Las heteroestructuras semiconductoras revolucionaron la física del estado sólido y pavimentaron el camino para la fabricación de los dispositivos que hoy son la base de sistemas de comunicaciones y la tecnología de la información como las celdas solares que se usan hoy en las estaciones espaciales y los transistores que integran por ejemplo los teléfonos celulares. Ya para el año 1968 Alferov había obtenido varios dispositivos basados en heterostructuras, del cual el más importante sería un láser semiconductor de doble heteroestructura capaz de operar en régimen continuo y a temperatura ambiente gracias a la mayor eficiencia en la inyección y confinamiento de los portadores y la luz que proveen estas estructuras. Estos trabajos se realizaron en el marco de una enconada competencia con grupos de científicos de Bell Telephone y RCA en los Estados Unidos y que Alferov ganó al publicar sus resultados un mes antes que sus competidores.

Alferov recibió su primer premio internacional en 1971, la Medalla del Instituto Franklin en los Estados Unidos. En 1972 fue condecorado con el Premio Lenin, la más alta distinción científica de la Unión Soviética. En 1987 fue electo Director del Instituto Ioffe de Leningrado y en 1990 Vicepresidente de la Academia de Ciencias de la Unión Soviética. Como director del Instituto Ioffe fundó la Escuela Secundaria Especial Físico Técnica de Leningrado adjunta a dicho instituto que fue uno de sus principales orgullos y satisfacciones. En ella él ha puesto su empeño y ha aplicado su íntima convicción de que la educación y la ciencia deben andar de la mano.

En 1987, la Universidad de La Habana a propuesta de la Facultad de Física, acordó entregar el título de Doctor Honoris Causa a este destacado científico. Por diferentes circunstancias que iban más allá de los deseos del galardonado y de los organizadores de la entrega del título, este acto no pudo realizarse sino hasta el 24 de mayo de 2006. Pero la demora fue muy provechosa, ya que hizo ver que la propuesta de la Universidad había sido acertada e incluso previsora. En el ínterin, Alferov recibió el Premio Nobel de Física de 2000 "Por el desarrollo los fundamentos básicos de la tecnología de información y comunicaciones modernas, en particular por el desarrollo de las heteroestructuras semiconductoras usadas en la electrónica de alta velocidad y la optoelectrónica".

Sus estudios, publicados en más de 500 artículos, 4 libros y 50 invenciones, son la base de las nuevas tecnologías de que disfrutamos hoy. Pero además han sido la semilla para una nueva rama de la ciencia: la nanotecnología, pues de hecho fueron las heteroestructuras semiconductoras las que permitieron crear dispositivos que confinan los electrones en regiones muy pequeñas como los llamados pozos, alambres y puntos cuánticos.

El Instituto Físico Técnico Ioffe fue un pilar del desarrollo de la física en Cuba. A inicios de la década de los 1970's, cuando la Física cubana comenzaba su despegue, Alferov nos trajo un conjunto de propuestas que significaron para los físicos de la Universidad de La Habana un avance importante: se inició un programa de colaboración gracias al que según un cálculo conservador, solamente de la Universidad de La

Habana pasaron por los laboratorios del Instituto Ioffe unos 25 físicos. Muchos fueron también los científicos del Ioffe que vinieron a ofrecer su experiencia, ayuda y colaboración. Así aprendimos a hacer láseres semiconductores y celdas solares en nuestros laboratorios. Alferov también facilitó el envío de importantes donaciones de materiales y equipos que nos permitieron avanzar substancialmente en el desarrollo de la física del estado sólido con un nivel superior en aquel momento al del resto de los países de América Latina.

En 2015 con motivo de su cumpleaños número 85 se establecieron en la Facultad de Física las "Zhores Alferov named lectures", ciclo de conferencias en reconocimiento a su destacada contribución al desarrollo de la optoelectrónica y por la introducción de la investigación en este campo en Cuba. Las conferencias con carácter anual han sido impartidas por un distinguido grupo de científicos de diversos países.

El apoyo que dio Alferov al desarrollo de la Física cubana, muestra la proyección humana de un hombre que luego de haber enseñado a los electrones a recorrer caminos inexplorados en el interior de los semiconductores, de modo que en su andar desaparecieran, generando luz coherente; vive hoy en esa otra luz, también coherente, con la que nos iluminó.

M. Sánchez-Colina y O. de Melo
Facultad de Física,
Universidad de La Habana